TESIS DOCTORAL

Radial velocity fiber-fed spectrographs towards the discovery of compact planets and pulsations on M stars

Zaira Modroño Berdiñas

Memoria presentada para optar al grado de
Doctor en Física y Matemáticas

Directores:
Dr. Pedro José Amado González
Dr. Guillem Anglada Escudé

Universidad de Granada
Programa de Doctorado en Física y Matemáticas

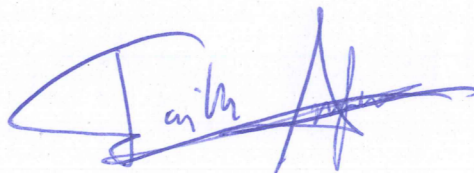A mis disparatados Berdiñas.

A Rubén.

Declaración

El doctorando, Zaira Modroño Berdiñas, y los directores de la tesis, Pedro José Amado González y Guillem Anglada Escudé, garantizamos, al firmar esta tesis doctoral, que el trabajo ha sido realizado por el doctorando bajo la dirección de los directores de la tesis y, hasta donde nuestro conocimiento alcanza, que en la realización del trabajo se han respetado los derechos de otros autores a ser citados cuando se han utilizado sus resultados o publicaciones.

Granada, a 19 de Octubre de 2016

Pedro José Amado González   Guillem Anglada Escudé

Zaira Modroño Berdiñas

Resumen en castellano

Esta tesis se desarrolla en el marco del paradigma de la búsqueda de un planeta análogo a la Tierra. En la actualidad, el estudio de las estrellas de baja masa, y en particular las estrellas de tipo espectral M, son elementos clave para este objetivo. A lo largo de esta tesis he estudiado en profundidad como se comportan las estrellas enanas M a corto plazo con el objetivo de buscar planetas de corto periodo, así como también de detectar por primera pulsaciones estelares en este tipo espectral. Estos objetivos se corresponden con los del proyecto "Cool Tiny Beats" (CTB) en el que se basan los datos de esta tesis. Es decir, medidas Doppler de alta resolución y alta cadencia obtenidas con los espectrógrafos HARPS o HARPS-N.

En primer lugar, esta tesis comprende un profundo estudio de la respuesta del espectrógrafo que tiene por objetivo caracterizar las fuentes de ruido en nuestro rango de estudio. Nuestra primera aproximación consistió en diseñar un experimento observacional con el fin de ahondar en la respuesta de HARPS-N durante el transcurso de la noche. Los resultados revelaron que la variabilidad del continuo de los espectros está correlada con las inestabilidades de la iluminación del espectrógrafo, la cuales están asociadas a variaciones de la masa de aire. Estas distorsiones, dependientes de la longitud de onda, están también presentes en una de las series generadas por el software de reducción de HARPS-N: el ancho del perfil promedio de las lineas del espectro (es decir, el índice FWHM), un índice comúnmente utilizado como indicador de la actividad estelar. Debido a estos resultados, nos vimos en la necesidad de buscar un índice alternativo para medir la anchura del perfil. En particular, utilizamos los momentos del perfil promedio de las líneas del espectro, el cual calculamos con una técnica de deconvolución por mínimos cuadrados. Como parte de este estudio también corroboramos

que las medidas de velocidad radial obtenidas por el software TERRA (que ajusta el espectro a una plantilla para obtener el desplazamiento Doppler) no se ven afectadas por inestabilidades en la iluminación. Además, este trabajo reveló un posible fallo en el funcionamiento del corrector de dispersión atmosférica (o ADC) de HARPS-N. Finalmente, se propusieron dos posibles soluciones: o bien se decorrelan las medidas del FWHM de las variaciones cromáticas del flujo del espectro, o bien se corrigen los espectros de manera muy precisa antes de calcular los indices de los perfiles promedio de las líneas.

En la segunda parte de esta tesis, y tras haber caracterizado la respuesta sub-noche del instrumento, se presentan los primeros resultados de CTB en relación a la búsqueda de pulsaciones estelares en estrellas de tipo espectral M. La detección de dichas pulsaciones abriría un nuevo campo de estudio: la astrosismología. Las herramientas astrosismológicas permiten calcular de forma muy precisa los parámetros físicos de la estrella y en consecuencia mejorar la determinación de las principales propiedades de los planetas que la orbitan. Esta parte está centrada en dos de las enanas M más estables observadas con HARPS y también por otros proyectos de alta precisión: GJ 588 y GJ 699 (estrella de Barnard). Al comienzo de esta parte se detalla la corrección del otros efectos instrumentales ya conocidos, como por ejemplo el efecto transferencia de carga, el efecto del *seeing* o los saltos de $1 - 2\,\mathrm{m\,s^{-1}}$ en la solución de la calibración en longitud de onda. Una vez corregidos nuestros datos utilizamos periodogramas de máxima verosimilitud para descubrir señales periódicas embebidas en el rango de periodos en el que se predicen las pulsaciones estelares. Sin embargo, ni las velocidades radiales, ni tampoco las series temporales de los momentos del perfil mostraron señales con un nivel de confianza suficiente como para considerarse como señales reales. Por otra parte, nuestro estudio utilizando señales sinusoidales sintéticas reveló que una señal por encima del umbral de $\sim 0.5\,\mathrm{m\,s^{-1}}$ sería detectada en el 90% de los casos. En otras palabras, hemos obtenido un límite superior para la sensibilidad del instrumento, lo que demuestra que las pulsaciones estelares podrían ser detectadas en el

rango de periodos predicho entre 20 minutos y 3 horas si se observan cuatro noches consecutivas y siempre y cuando sus amplitudes sean mayores a $\sim 0.5\,\mathrm{m\,s^{-1}}$. Este resultado, combinado con indicios de señales bajo este umbral, motivan la continuidad de nuestra búsqueda de pulsaciones estelares en enanas M.

La tercera parte de esta tesis presenta nuestros principales resultados en relación a la detección de planetas extrasolares en torno a estrellas cercanas de tipo M. La baja temperatura de las atmósferas de las enanas M, así como su baja masa en comparación con otros tipos espectrales, propician por un lado que la zona de habitabilidad (es decir, el rango de órbitas donde un planeta podría albergar agua líquida en su superficie) esté más cerca de la estrella, y por el otro que los planetas de tipo terrestre en esa zona sean detectables con la instrumentación actual. Además, la abundancia de enanas M de nuestro entorno solar ($\sim$70%) hace que los sistemas planetarios entorno a estrellas M cercanas sean únicos por las oportunidades de caracterización que ofrecen de cara a futuras misiones. Estas son las principales razones que motivan la búsqueda de planetas alrededor de enanas M. Al principio de esta parte de la tesis se detalla la detección de dos posibles planetas candidatos de masa terrestre orbitando en torno a la estrella de Luyten. Las masas mínimas calculadas para los posibles planetas fueron respectivamente 11.1 y 2.13 $M_\odot$ para Luyten b y Luyten c. Luyten b orbita muy cerca de la estrella con un periodo de tan solo 4.7 días, sin embargo, Luyten c, que tiene un periodo orbital de 18.6 días, se encuentra dentro de la estimación optimista de la zona de habitabilidad. En esta misma parte también se describe el descubrimiento de Kapteyn b y c, dos súper-Tierras entre las cuales el Kapteyn b está considerado potencialmente habitable. Finalmente, se detalla el reciente descubrimiento de un planeta de masa similar a la Tierra orbitando en la zona de habitabilidad de nuestra vecina estelar más cercana Proxima Centauri: Proxima b. En dicho estudio se incorporó la experiencia adquirida durante esta tesis en todo lo relacionado con la caracterización de los efectos instrumentales en el dominio de tiempos cortos en estrellas enanas M. De hecho, en este estudio se aplicaron por primera vez los momentos de los perfiles de deconvolución por mínimos

cuadrados como índices para caracterizar la forma de los perfiles promedio de las líneas espectrales de Proxima.

Finalmente, la última parte de esta tesis comprende un estudio puramente instrumental con el objetivo de mejorar el límite de precisión de las velocidades radiales que se puede alcanzar con un espectrógrafo. En particular, se centra en corregir las distorsiones causadas por inestabilidades del patrón de iluminación en espectrógrafos alimentados con fibras ópticas. En particular, se describe nuestro primer prototipo, el "Radiance Characterizator in two dimension" (RadiCa2D), diseñado específicamente para corregir medidas Doppler del espectrógrafo CAFE. El concepto principal del corrector RadiCa2D se basa en monitorizar simultáneamente tanto las observaciones como las distorsiones en el patrón de iluminación dentro del espectrógrafo, para así corregir, en tiempo real, errores generados en la medida de la velocidad radial. Sin embargo, este proyecto está aún en desarrollo y el rendimiento final del corrector aún no ha sido confirmado.

Abstract

This thesis is developed in the framework of the paradigm that seeks for the discovery of an Earth analog. Nowadays, low mass stars, and in particular M dwarf stars, are key targets towards achieving this goal. In this thesis, I focus on the study of the short-time domain of M dwarf stars with the aim of searching for short period planets, but also for the first detection of stellar pulsations on this spectral type. Both science goals are the primary objectives of the "Cool Tiny Beats" (CTB) survey, which has produced most of the data used in this thesis. CTB data consist in high-resolution and high-cadence spectroscopic Doppler measurements taken either with HARPS or HARPS-N spectrographs.

First of all, a thorough understanding of the spectrographs response in the short-time domain was performed to characterize the sources of noise in our range of study. Our first approach to the goals of this thesis consisted in the design of an observational experiment to delve into the HARPS-N sub-night performance. Results unveiled variability of the spectra continuum correlated with instabilities of the spectrograph illumination associated to the airmass. Such distortions, which are wavelength and time dependent, are also present in at least one of the data-products given by the HARPS-N reduction software: the width of the mean-line profiles (i.e. the so-called FWHM index), an index commonly used as a proxy of the stellar activity. As a consequence, we searched for an alternative approach to measure the width index. In particular, we calculated the mean-line profile of the spectrum with a least-squares-deconvolution technique and we obtained the profile indices as the moments of the profile distribution. As part of this study, we also corroborated that the radial velocities calculated with our template matching algorithm TERRA are not affected by the illumination

stability. This work unveiled a possible failure of the HARPS-N atmospheric dispersion corrector (or ADC) and outlined two possible solutions: either the FWHM measurements need to be decorrelated with the changes of flux on the spectra as a function of wavelength, or the spectra need to be corrected very precisely before deriving proxies for the mean line profiles.

In the second part of this dissertation, and taking advantage of the above characterization of systematic effects in the sub-night domain, I present the first CTB results regarding the detection of stellar pulsations in M dwarfs. The detection of such pulsations would open a new field of study for these stars, namely the field of asteroseismology. The asteroseismology tools allow to calculate very precisely the star physical parameters, thus improving the calculation of the bulk properties of any orbiting planet. This part of the thesis is focused on GJ 588 and GJ 699 (Barnard's star), two of the most long-term stable M dwarfs observed by HARPS and other high-precision surveys. Firstly in this section, I detail the procedures applied to correct the CTB data from known instrumental effects such as the charge transfer efficiency, the seeing effect, or the wavelength calibration $1-2\,\mathrm{m\,s^{-1}}$ night-to-night jumps produced by the wavelength calibration. Later, we used likelihood periodograms to unveil periodical signals embedded in the range of periods where stellar pulsations are predicted. Neither the radial velocities nor the time-series of the second order moment of the mean-line profile showed confident detections. In spite of that, our study with injected sinusoids indicates that signals above the $\sim 0.5\,\mathrm{m\,s^{-1}}$ threshold would be detected in 90% of the cases. In other words, this is an upper limit of sensibility showing that stellar pulsations in the predicted range of periods from 20 min to 3 h can be detected with four consecutive nights of observations provided that their amplitudes are larger than $\sim 0.5\,\mathrm{m\,s^{-1}}$. This result combined with some tentative detection of some signals below this threshold motivates us to keep searching for stellar pulsations in M dwarfs.

The third part of this thesis presents our main results regarding the detection of extrasolar planets around nearby M dwarfs. The low temperatures

of the M dwarfs atmospheres, as well as their intrinsic low masses compared with other spectral types, result in closer habitable zones (i.e. the range of orbital distances where a planet could maintain liquid water on its surface) and in Earth-mass rocky planets within this zone detectable with the current instrumentation. Moreover, planetary systems around M dwarf stars are rather unique for the interesting follow-up opportunities they offer. These characteristics motivate our search for planets around M dwarf stars. Firstly in this part, I describe the detection of two Earth-mass planet candidates hosted by Luyten's star. The minimum masses of the planets are 1.11 and $2.13\,M_{\oplus}$ for Luyten b and c, respectively. Luyten b orbits very close to the star with a 4.7-day period, while, Luyten c, with a 18.6-day period orbit, lies within the optimistic estimation of the habitable zone. Later in this part, I detail our discovery of Kapteyn's star b and c planets. They correspond to two super-Earth mass planets of which planet-b is considered as potentially habitable. Finally, I also describe our more recent discovery of an Earth-mass planet orbiting in the habitable zone of our closest neighbor Proxima Centauri: Proxima b. This study incorporated the experience acquired during this thesis regarding the characterization of the instrumental effects in the short-time domain of M dwarfs. In fact, we used for the first time in this study the moments of the least-square-deconvolution profiles as indices to monitor the shape of the mean-line profiles of Proxima.

Finally, the last part of this dissertation comprises the development of an astronomical instrumentation project, with the aim of improving the radial velocity precision limit attained by an spectrograph. In particular, we focus on correcting the distortions caused by illumination instabilities in fiber-fed spectrographs. I describe our first prototype, the *Radiance Characterizer in two dimensions* (RadiCa2D), which was specifically designed to correct the Doppler measurements of the CAFE spectrograph. The main underlying idea of RadiCa2D consists in simultaneously monitoring the illumination distortions inside the spectrograph, to correct, in real-time, the effects generated in the final radial velocity measurements. This project is still under development and the final performance of the corrector needs yet to be confirmed.

Contents

List of Figures

List of Tables

If you look at it, you see a dot. That's here. That's home. That's us.

Carl Sagan (1934-1996)

1

Introduction

RAISE your eyes, gaze at the star-packed sky and wonder which is your place in the vast Universe. We live in Carl Sagan's "pale blue dot", our home, our Earth, but up there, the starry night is full of twinkling dots waiting to be unveiled. Since ancient times, astronomy has inspired humankind to answer this and other questions. Whether we are alone in the Universe is still unknown. However, the myriad of worlds already discovered in the Milky Way make us think that life could have arisen in other corners of the Universe. This thesis is focused on the study of M dwarf stars and their planetary systems. Additionally, and because science is always driven by technical breakthroughs, it deepens also into the performance of the instruments used with this aim. Through this chapter, I firstly give an insight of the exoplanets field, then I describe the main formation theories, later I focus on the description of M dwarf stars as hosts of small planets, and finally, I describe the Cool Tiny Beat project and the outline of this thesis.

1.1 From the first attempts to the future prospects

1.1.1 A tale with a moral

Using the astrometric technique, which measures small wiggles in the location of a star, Friedrich Wilhelm Bessel first found in 1844 that Sirius was moving around an unseen companion. However, we had to wait until Alvan G. Clark's huge refracting telescope[1] to finally confirm the faint Sirius B in 1862. Throughout history, science has move forward thanks to technical advances like this one that allowed us to reach new milestones.

In 1938, Van de Kamp, who was an expert on the astrometric technique, started a long-term program to unveil star companions. He used the telescope at the Sproul Observatory, a bigger version of Clark's refractor. Very soon, Van de Kamp swapped from searching binary stars to lead the race to find extrasolar planets. In 1963, he announced that Barnard's star was surrounded by an object 60% more massive than Jupiter (van de Kamp, 1963). The wobble of the star in the photometric plates was hundred of times smaller than the size of the star itself, and it was discovered by painstakingly scrutinizing under a microscope the 2400 plates collected with the telescope during 46 years of observations[2] (see Fig 1.1). However, the refutation of two "planets" orbiting 70 Ophiuchi (Reuyl & Holmberg, 1943) and 61 Cygnus (Strand, 1943) a few years earlier, made the community to be cautious about Van de Kamp's claim.

After six years collecting new data, Van the Kamp's realized that the eccentric orbit of the 1.6 Jupiter mass object was indeed better explained by two planets with circular orbits (van de Kamp, 1969). Regardless of this change in the interpretation, the underlying story was that his claim was still on in 1969, and the community began to listen attentively. But the tempest was about to start. In 1973, Van de Kamp's colleague John L. Hershey was analyzing 30 years of observations of GJ 793, carried out also from the Sproul Observatory, when he realized that the resulting wobble was very similar to that of Barnard's star. The explanation was clear, either both stars hosted two identical planets, a very improbable case, or something was wrong with the data. Soon after, Hershey noted that the main displacements measured in the

---

[1]Alvan G. Clark's telescope had a diameter of 18 inches, 46 cm approximately.

[2]The first observations of Barnard's star from the Sproul Observatory date from 1916, 22 years before Van de Kamp started his long-term program.
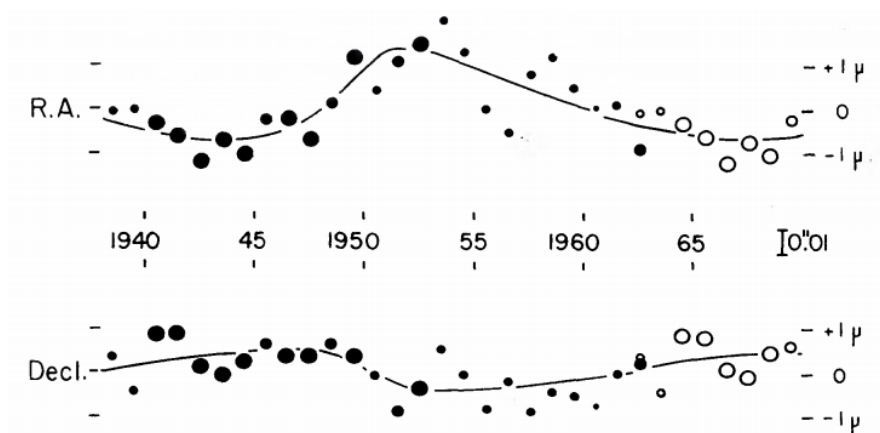
Figure 1.1: Van the Kamp's 1963 claim of a Barnard's star companion - Astrometric curves showing the displacement of Barnard's star during 46 years. Open circles are early yearly means moved 24-years forward. The solid line is the best fit to the data and was claimed to correspond to a a 1.6 Jupiter mass companion. The size of the dots accounts for their uncertainty. *From van de Kamp (1963).*

astrometric curves fitted several updates carried out in the telescope in 1949 and 1957 (e.g. a replacement of the photographic plates and other adjustments of the telescope lenses).

The case was now clear: the most promising planets discovered so far turned out to be instrumental systematic effects. Hershey did not mentioned Barnard's star in his paper (Hershey, 1973). However, before Van de Kamp had enough time for reanalyzing his data, Gatewood & Eichhorn (1973) announced that they could not find any planet orbiting Barnard's star using their more precise and independent astrometric dataset (see Fig. 1.2). In 1975, Van de Kamp recognized *systematic effects* in the data prior to 1949, but he still claimed that there were evidences for two planets on circular orbits (van de Kamp, 1975). In fact, he stood by his statements in a book he published in 1986 (van de Kamp, 1986), and he continued claiming his discovery for the rest of his life. But there was no way back: nobody could reproduce his results. Nowadays, Barnard's star is not only known to have no planets, it is known to be so stable that many instruments use it as reference for calibration purposes. Thus, the moral is to always keep a close eye on your instrument.
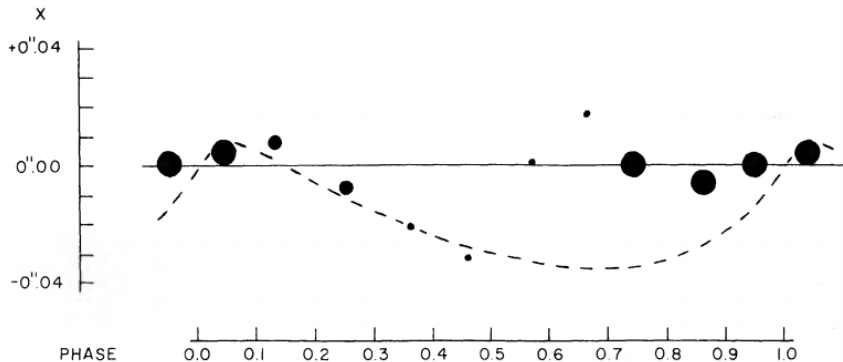
Figure 1.2: Gatewood & Eichhorn refutation in 1973 of Barnard's star planets - Disagreement between the Gatewood & Eichhorn data (black dots) and the model fitted by Van de Kamp using the data from the Sproul Observatory (dashed line). *From Gatewood & Eichhorn (1973).*

1.1.2 The 90's boom

In the early 80's it was clear that finding Jupiter-like planets would require new instrumentation. The high-precision radial velocity technique had been proposed as a method to infer the presence of Jupiter-like planets for a long time (Struve, 1952), but it was in the mid-80's when échelle spectrometers started to reach the required precision.

In 1988, David Latham was using a sample of stars to calibrate the échelle spectrometer CORAVEL (Baranne *et al.*, 1979) when he realized the star HD 114762 was behaving in a different way than the others. A year later, he announced the discovery of an object with 11 Jupiter masses that eventually resulted to be the first genuine detection of a brown dwarf star (Latham *et al.*, 1989). The first extrasolar planet was detected three years later by Wolszczan & Frail (1992). However, contrary to what it was expected, this discovery did not attract much attention. The reason was the planets were thought to be "dead worlds" because the host star was a pulsar, the hostile aftermath of a supernova event. But, if pulsars had planets, why regular stars couldn't?

The moment of glory arrived in 1995 when the Swiss Mayor & Queloz stunned the world with the discovery of a half-Jupiter-mass planet circling the solar-type star 51 Pegasi b (Mayor & Queloz, 1995). The method they used was the radial velocity one, and the instrument used was the échelle spectrometer ELODIE (Baranne *et al.*, 1996), at the Observatoire de Haute-Provence. ELODIE could reach the astounding level accuracy of $13\,\mathrm{m\,s^{-1}}$, a value far below the $\sim 60\,\mathrm{m\,s^{-1}}$ of the 51 Pegasi b signal

(see Fig. 1.3). But the big surprise was the short planet's period: only 4.32 days. Theoretical models did not predict in-situ formation of gas planets at such short distances; 51 Pegasi b location was completely unexpected and it was so-called a "hot jupiter". It was Mayor & Queloz's previous experience with close binaries what encouraged them to scrutinize short periods. Soon after, Marcy & Butler, the American team leading the exoplanet race up to that time, re-analyzed their data and within three months they were able not only of confirming 51 Pegasi b (Marcy & Butler, 1995), but also of reporting two new exoplanets orbiting 47 Ursae Majoris and 70 Virginis (Marcy & Butler, 1996).
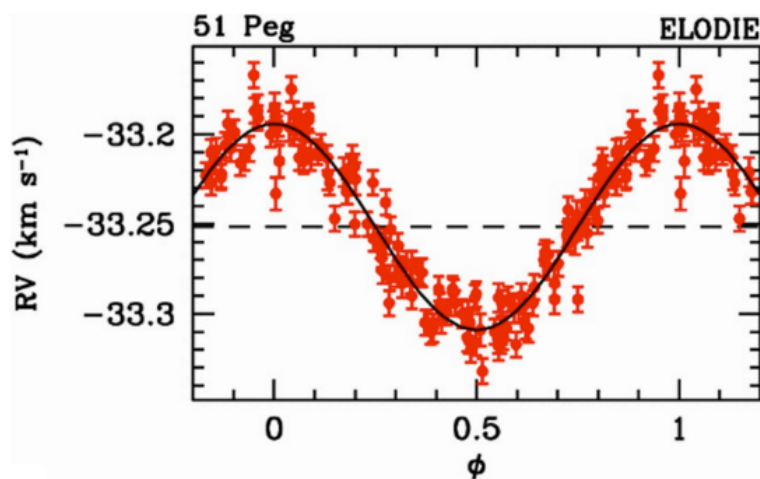
Figure 1.3: Mayor & Queloz's 1995 detection of the first exoplanet - Radial velocity curve showing the 51 Peg data obtained with the échelle spectrometer ELODIE. The best fit (solid line) corresponds to a planet half as massive as Jupiter in a 4.32-day period orbit. *From Mayor & Queloz (1995).*

1.1.3   The current plethora

Nowadays, 21 years after the discovery of 51 Peg b, we know more than 3500 new worlds (see Fig. 1.4). Exoplanets are very common in the Universe[1], and today we can study the whole population from a statistical point of view. In that way, we have learnt for example that gas-giant planets most likely form beyond the ice line (the distance from the protostar where volatiles can condensate into icy grains) and that they usually stay

---

[1]Recent studies point to ratios of at least one planet per half of the low-mass stars (Dressing & Charbonneau, 2013; Tuomi *et al.*, 2014).

there for the rest of their lives. Moreover, we know now that rocky planets are bigger and more eccentric the farther you get from the star (Marcy *et al.*, 2005).
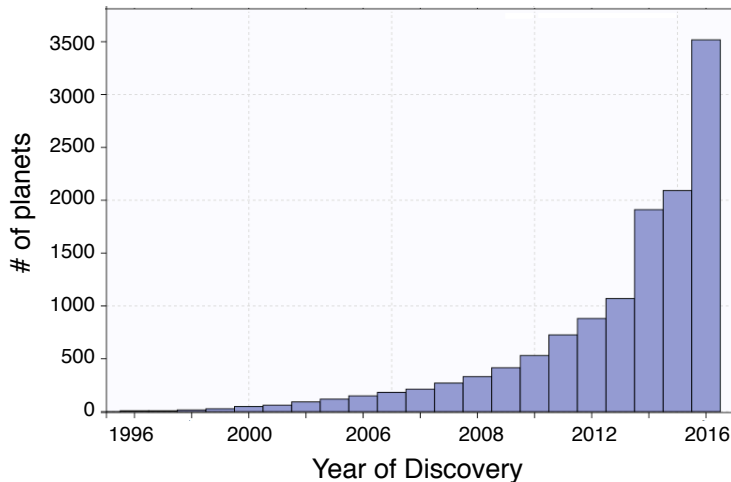
Figure 1.4: Exoplanets discovered since 1995 - Cumulative number of exoplanet known as of September 11, 2016. The number slowly increases with time due to the instruments precision improvement, the larger time-baselines, the large number of instruments or the more sophisticated data analysis techniques. The 2013 bump corresponds to the release of the *Kepler* data. The 2016 bump is due to the validation of 1284 new exoplanet among the *Kepler* database of possible candidates. *Source: http://exoplanets.eu/*

The population of exoplanets is usually illustrated with the diagrams in Fig. 1.5 and 1.6, that show respectively the mass–radius and the mass–semi-major axis distributions. Particularly, in Fig. 1.5 we can clearly see how the gas giants accumulate in the upper right corner while rocky planets populate the bottom left part. The gap between both types is supposed to be a remnant of the protoplanetary disk dissipation phase that takes place during the formation process (see Section 1.2). On the other hand, Fig. 1.6 shows the mass distribution as a function of the distance to the star. Here we can see how massive planets are more prone to be at large distances from the star. This is thought to be related with either the low efficiency of the massive planets to travel inwards (e.g. short period objects of 0.5-1 M_J can open gaps in the disk that act like a natural barriers), or, for those which migrate, with the probability of being engulfed by the host star (see e.g. Trilling *et al.*, 1998). Contrarily, there is a lack of low mass planets at large distances. However, this could be just an observational bias. The different techniques used to detect exoplanets (see a description in Chapter 2) are

sensitive to different areas in this diagram, and low-mass long-period planets are the most challenging targets for most of them.

Since the first discoveries of exoplanets we have learnt that they are very diverse. Frequently, new discoveries challenge the formation and evolution theories that have to be refined afterwards. This was the case of 51 Peg b, that made the inceptive formation models based on the Solar System to account for migration theories that could explain the new "hot jupiters". Other example could be the case of Kepler-10 c, the so-called "Godzilla Planet", a mega-Earth (a heavy terrestrial exoplanet with a mass of 17 $M_\oplus$ a radius of only 2.35 $R_\oplus$) orbiting in just a 45-day period that suggested that rocky planets could form much earlier than we thought (Fressin *et al.*, 2011; Dumusque *et al.*, 2014). But this is still happening, more recently, new discoveries such as the TRAPPIST-1 b and c planets, which are hosted by a cool brown dwarf star (Gillon *et al.*, 2016), or K2-33 b, a completely formed planet orbiting a very young star (David *et al.*, 2016), keep setting the state-of-the-art of the formation and evolution theories.
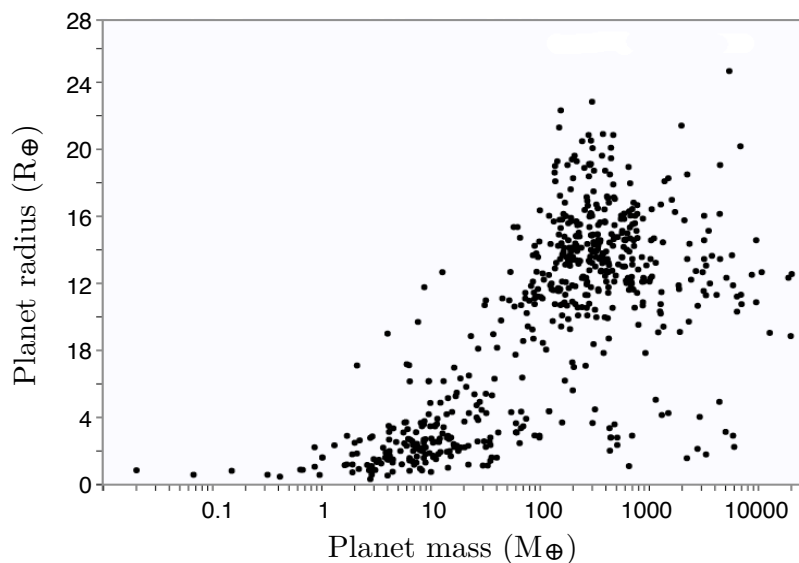
Figure 1.5: Mass – radius diagram of the current exoplanet population - Radius versus mass of the known extrasolar planets as of September 11, 2016. Gas giants are in the upper corner whereas rocky planets populate the bottom left part. The gap in-between is thought to be an evidence of the formation processes. This plot only includes exoplanets with mass measurements (∼600 exoplanets among a total of ∼3500 in the case of the transit method). *Source: http://exoplanets.eu/*
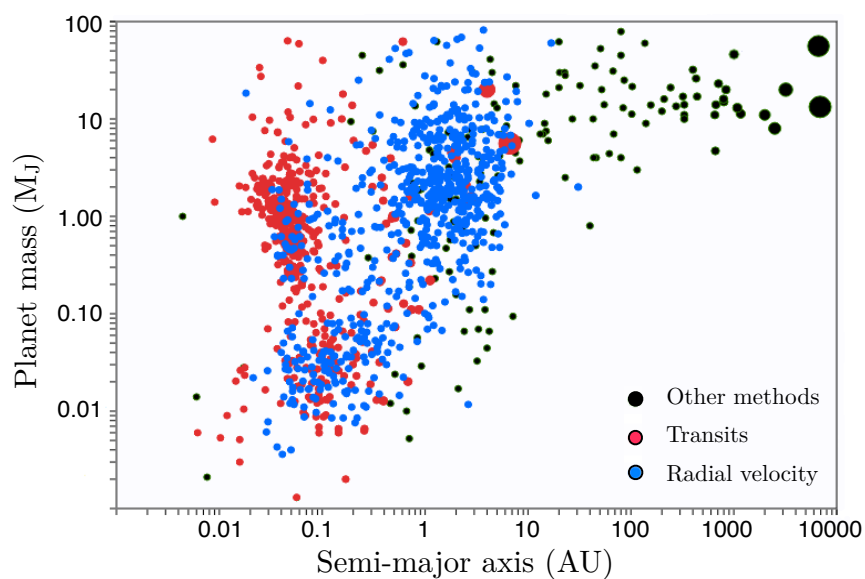
Figure 1.6: Mass – semi-major axis diagram of the current exoplanet population
- The different techniques are sensitive to different areas of the diagram. Planets discovered with the transit method are highlighted in red. Radial velocity planets are indicated in blue. Black dots are objects from either astrometry, direct imaging, microlensing or pulsar timing. The size of the dots accounts for the planet radius when the parameter is know. Planets as of September 11,2016. *Source: http: // exoplanets. eu/*

1.1.4 Next steps

In the roadmap for finding a inhabited Earth-twin, we are now moving from a pure detection phase, focused on finding new exoplanets, towards a characterization stage, in which we will determine bulk densities and analyze the composition of the exoplanet atmospheres.

Regarding the detection, we are now close to probe Earth-like planets orbiting Sun-like stars. Since the first exoplanets detection, radial velocity spectrometers have not stopped to develop, reaching now a few $\mathrm{m\,s^{-1}}$ (e.g. SOPHIE/OHP, HIRES/Keck or CAFE/CAHA), or even sub-$\mathrm{m\,s^{-1}}$ (e.g. HARPS/La Silla 2.2-m telescope or HARPS-N/TNG). This precision allows to detect Earth-mass planets, but only in the favorable case of orbiting stars smaller than the Sun. However, the forthcoming instruments such as ESPRESSO/VLT (first light in 2017) or HIRES/E-ELT (estimated for > 2024) will reach the required precision needed to discover Earth-like planets around solar stars, of tens of $\mathrm{cm\,s^{-1}}$, using bigger telescopes that will additionally allow to monitor fainter targets. Moreover, brand new near-IR spectrographs such as CARMENES/CAHA or GIANO/TNG are also expected to reach precisions of a few $\mathrm{m\,s^{-1}}$ in the short term.

In the field of high-precision photometry, new cutting-edge instruments are about to come too. Space missions like *JWST, TESS, PLATO* or *CHEOPS* will be the *Kepler* next generation. This will benefit, a better knowledge of long-orbit planets, which is necessary to better constrain the formation theories. New instruments like *Gaia* (launched in 2013 and first data release just happened in September 2016), SPHERE/VLT (in operation since 2015) or *EUCLID* (expected for 2021) will study this range using astrometry, direct image and microlensing techniques, respectively (see Chapter 2). Figure 1.7 summarizes the roadmap of the principal next generation exoplanet instruments.

Regarding the characterization of exoplanet atmospheres, the detection of biomarkers like water, molecular oxygen or methane will have to wait for larger telescopes like HIRES/E-ELT to be available. However, recent studies (e.g. Wyttenbach *et al.*, 2015) have demonstrated that we can already perform some atmospheric studies using high-resolution spectrographs on 4-m-class telescopes. For example, we can study other chemical such as the Na_I D1 and D2 lines. Two lines for which the wings and centers give different information about the atmosphere pressure and temperature profiles
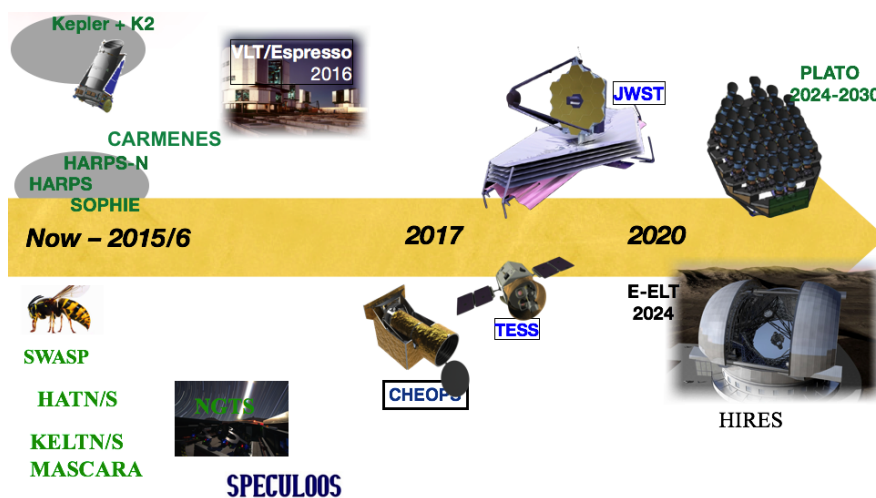
Figure 1.7: Present and future instruments - Some of the current and future facilities to characterize exoplanets. Instruments like *JWST* or HIRES/E-ELT will be used to characterize planet atmospheres.*Source: `https://palereddot.org/`*

(Redfield *et al.*, 2008; Wyttenbach *et al.*, 2015). The most common technique used nowadays is the high-resolution spectroscopy of transiting exoplanets. It allows to obtain both the transmission spectrum (the starlight filters through the planet atmosphere during the primary transit leaving its fingerprint in the spectrum) and the reflected spectrum (using the secondary transit to compare the spectrum without the planet counterpart). Nevertheless, even when we can attempt some atmospheric studies, the new instrumentation will have a lot to say about the planet atmospheres.

1.2 Planet formation and evolution models

Planets are the by-product of the star formation. By 1796 Laplace speculated about the possibility of the Sun and the Solar System been formed from the same cloud nebula [1]. This scenario was not new, the philosopher Immanuel Kant had the same idea earlier in 1755, but Laplace arguments were stronger since he argued that the same direction, coplanarity and nearly circular orbits of the Solar System planets should be related to a single rotating disk of material around the Sun. The Kant-Laplace *nebular hypothesis* evolved until today to derive in the *solar nebular model*.

---

[1]Nebulae were discovered by the astronomer William Herschel a just a decade before

The *solar nebular model* summarizes the formation of planetary systems within four stages (see Fig. 1.8). The first one is the *molecular collapse*, in which a molecular cloud, containing gas and dust particles, fragments due to an external factor[1]. This break-up derives in small cloud aggregations that later collapse by gravitational instabilities. The aggregations create cores wrapped with material and, in a second *protostar* stage, this material starts to be accreted by the protostellar core. However, in order to conserve the initial angular momentum of the cloud, the dust and gas moves to a flat protostellar disk that rotates around the protostar. Once the enveloping material has run out, the *protoplanetary disk* containing all the planet raw ingredients has formed (see a review of star formation in McKee & Ostriker 2007).
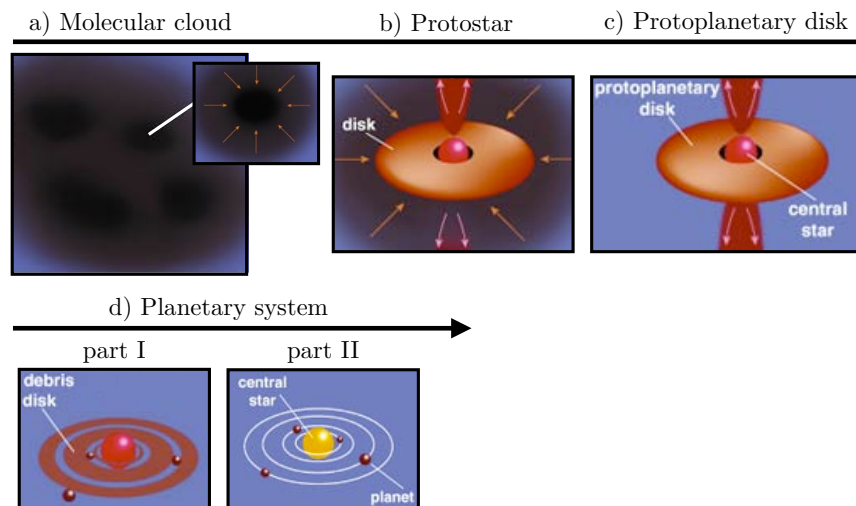
Figure 1.8: Planet formation diagram - Four principal stages of the planet formation: from the initial cloud collapse to the debris disk dissipation. *Adapted from Greene (2001).*

Two theories compete in the last stage for the formation of the final *planetary system*: the core-accretion and the gravitational instability theories. The core-accretion is the leading model because it can explain the formation of most exoplanets [2]. The forefather of this theory was Safronov (1969), who, leaving the obstacle of the Sun formation problem aside, described the solar system formation from the protoplanetary disk in four main steps: 1) the dust grains of the protoplanetary disk coagulate un-

---

[1]The source that triggers the molecular fragmentation is still under debate. A hypothesis gaining observational strength is a close supernova causing shock waves able to break the cloud stability.

[2]Matsuo *et al.* 2007 find that 90% of the exoplanets can be explained through core-accretion.

til forming kilometer-scale planetesimals[1], 2) the planetesimals collide to form planet embryos, 3) the remaining debris disk of gas and dust dissipates, and 4) the planet embryos gravitationally interact, colliding and forming the final almost circular planets orbits (see an schematic view in Fig.1.9).
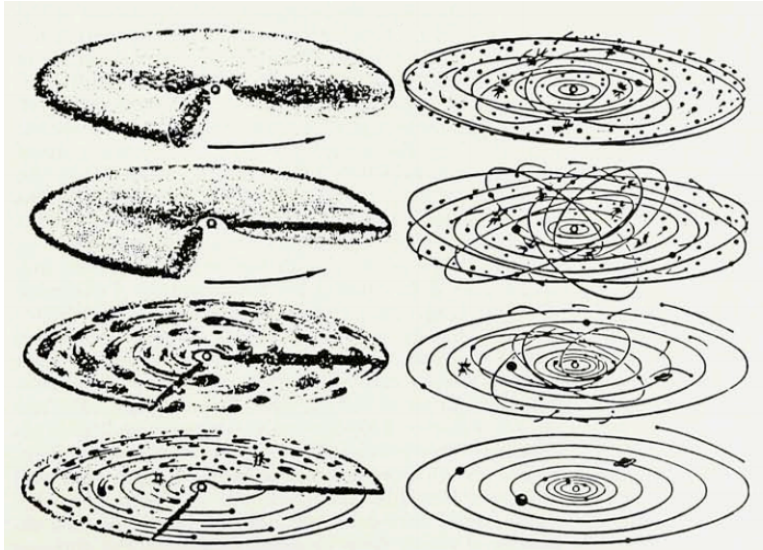
Figure 1.9: Safronov's Solar system scenario - Evolution of the Solar system from the formation of a thin disk of particles at the disk center to the final circularization of the orbits. *From Ahrens (1994).*

Safronov knew that the formation of giant gas planets would require an additional step in which the planet embryos accrete gas from the disk, but the timescale he calculated for that resulted to be larger than the age of the Solar System. A few years later, Perri & Cameron (1974) suggested that cores of $10\,\mathrm{M_{\oplus}}$ beyond the *ice line* would be massive enough to accrete gas[2]. This hypothesis was later described in detail by Mizuno (1980), who suggested that such cores would attach a thin layer of gas that would condensate, reaching the critical mass required for a runaway gas accretion onto the core. Today, we know that giant planets continue to accumulate dust and gas from their surrounding until the debris disk dissipates after $\lesssim 10$ Myr (Pollack *et al.*, 1996) and the planet formation is complete (see the last formation stage two parts in Fig. 1.8).

---

[1]The aggregation mechanism to grow meter-size bodies is well understood, but the evolution to kilometer-size planetesimals is still unclear. See a review of the problem in Levison *et al.* (2010).

[2]The *ice line* highlights the distance from the star where volatiles can condensate into solid grains. Thus, forming bigger cores is easier beyond this limit.

However, the massive planets at wide orbits discovered through direct imaging were a challenge for the core-accretion theory. In the outer parts of the protoplanetary disk, the coagulation process slows down because of the short supply of dust grains. Consequently, the core-accretion gives unrealistic timescales for the formation of cores with the critical mass required to ignite the runaway gas process (Kenyon & Bromley, 2008). In 1997, Boss (1997) described how massive planets can form directly from the fragmentation of the protoplanetary disk, i.e. without an initial accretion phase. This gravitational instability theory worked well forming planets at large distances ($\gtrsim$100 AU) and reducing the timescales for the formation of gas giants in the outer disk ($\sim$ 1000 yr; Boss 1997). However, it failed in forming rocky planets in the inner part of the disk. Nevertheless, the huge diversity of exoplanets suggests that both mechanisms have to be present in the formation of the planetary systems (see reviews of both formation models in Matsuo *et al.* 2007 or in Mordasini *et al.* 2010).

Still, from time to time, new discoveries keep challenging both formation theories. The proximity of 51 Peg b to its host star caused the introduction of the migration theories. Migration allows the planets to travel inwards or outwards from their birthplace and is driven by three mechanisms: i) the planet-disk interaction, that forces the planet inwards while it grows, in order to conserve the angular momentum while the disk is present, ii) the planet-planet scattering, that cause inwards or outwards migrations due to gravitational instabilities between the bodies[1], and that can still be active after the disk dissipation, and iii) the planet-star tidal forces, that carry the planets inwards as the star evolves, thus lasting for timescales of Gyr.

1.2.1 Observational constrains on planet formation

In the same way that observing stars at different evolutive stages allows us to outline the details of the Hertzsprung-Russell diagram, observational evidences of planetary systems at different ages are required to constrain the formation and evolution models. Technological advances are required to better understand the evolution of deceptive bodies such as evaporating close-in planets (e.g. GJ436 b, Butler *et al.*, 2004; Ehrenreich

---

[1]The "Grand tack" hypothesis proposes a Jupiter inwards travel through a type-II migration with the consequent Solar System reconfiguration. How it exactly happened is still a matter of debate (Raymond & Morbidelli, 2014).

et al., 2015), free-floating planets (e.g. PSO J318.5-22, Liu *et al.*, 2013), or even planets around dead stars (e.g. PSR 1257+12, Wolszczan & Frail, 1992).

The recent start of operations of the radio interferometer ALMA has allowed to study in detail planetary systems in early evolutionary stages (see in Fig. 1.10 how in a few decades images have improved to be able to resolve gaps in the debris disk, possibly created by planet embryos accreting disk material). Nowadays, we can not just obtain debris disks images, we can even directly observe young planetary systems (see Fig. 1.11). In a decade, we expect also to be able to detect elder completely formed planetary systems like for example that of our closest neighbor Proxima b (Anglada-Escudé *et al.*, 2016a).
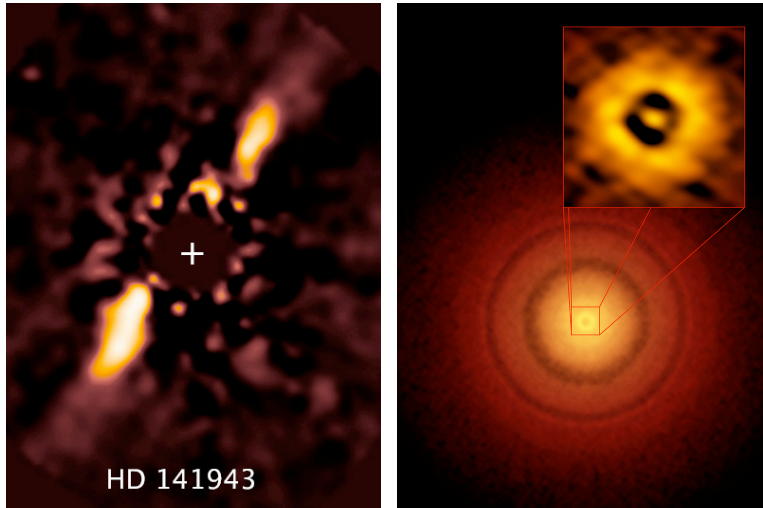
Figure 1.10: Debris disk observed with *HST* and ALMA - (Left) A debris disk observed in the star HD 141943. The discovery was done applying a new image processing to *HST* archive images (Soummer *et al.*, 2014). (Right) Planet-forming disk around the young Sun-like star TW Hydrae. Original Image obtained this year with the Atacama Large Millimeter/submillimeter Array (ALMA) (Andrews *et al.*, 2016). The image resolves the disk's gaps that are thought to be caused by the planet embryos.

1.3   Planets around M dwarfs

Low-mass stars, and in particular M dwarf ($\sim$ 0.075 to 0.6 M $_\odot$), have recently become the focus of interest of exoplanetary studies (see Fig. 1.12). There are several reasons for this, but the main one is we can detect with the current instrumentation an Earth-mass
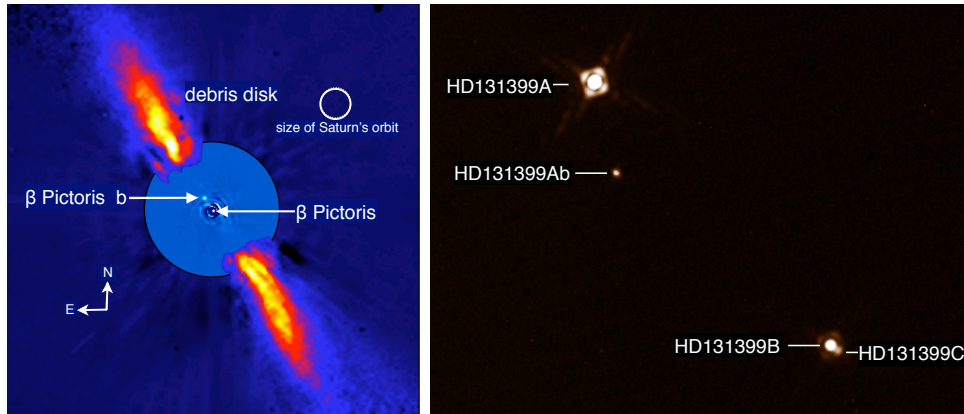
Figure 1.11: Direct images of exoplanets - (Left) Image of Beta Pictoris b, a super-Jupiter orbiting in the debris disk of a A-type star. The image was taken with NACO/VLT in 2003, but the planet was discovered in 2008 thanks to a new processing tool (Lagrange *et al.*, 2009). (Right) Recent Wagner *et al.* (2016) discovery using SPHERE/VLT of a Jovian planet (HD 131399Ab) orbiting in a triple-star system.

rocky planet in a temperate orbit around the star where liquid water on the planetary surface would be stable over the life-span of the star.

The habitable zone (HZ) depends on the star bolometric luminosity and it is defined as the range of orbital distances in which a planet can possible maintain liquid water on its surface (Kasting *et al.*, 1993; Kopparapu *et al.*, 2013; Leconte *et al.*, 2013; Yang *et al.*, 2013; Kopparapu *et al.*, 2014, 2016). M-type star low temperatures (2300-3800 K) make their HZs to be closer to the star (see Fig. 1.13), and thus, a planet like the Earth will produce a larger gravitational influence on the star than in the case of a warmer spectral type star. This influence is amplified by the smaller star/planet mass ratio of M dwarfs. This scenario makes the Doppler shift caused in the spectrum of $\sim 1\,\mathrm{m\,s^{-1}}$ in radial velocities, roughly ten times larger than the gravitational pull that the Earth imprints on the Sun. Such signal can be resolved by the precision limit of the state-of-the-art spectrographs (e.g. HARPS and HARPS-N ; Pepe *et al.*, 2011) and gives us an estimation of the exoplanet period and minimum mass. But, not only the Doppler technique benefits from close-in HZs. Both the probability of transit and the amplitude of the transit signature increase due the proximity to the host star and to the favorable star/planet size. Consequently, another advantage of studying compact planetary systems around M dwarfs is our greater chances of accurately measuring the
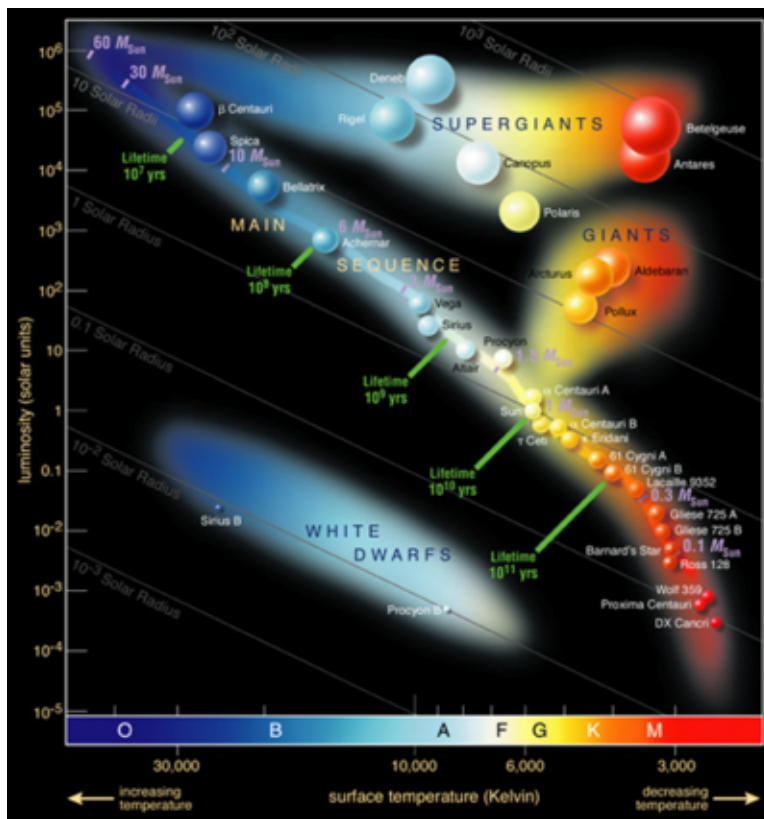
Figure 1.12: Hertzsprung-Russell Diagram - M dwarf stars are cool low-mass stars and are placed at the bottom right of the main-sequence. *Source: ESO*

planet radius (and thus the planet density and composition if the mass is known), and even of characterizing the planet atmosphere.
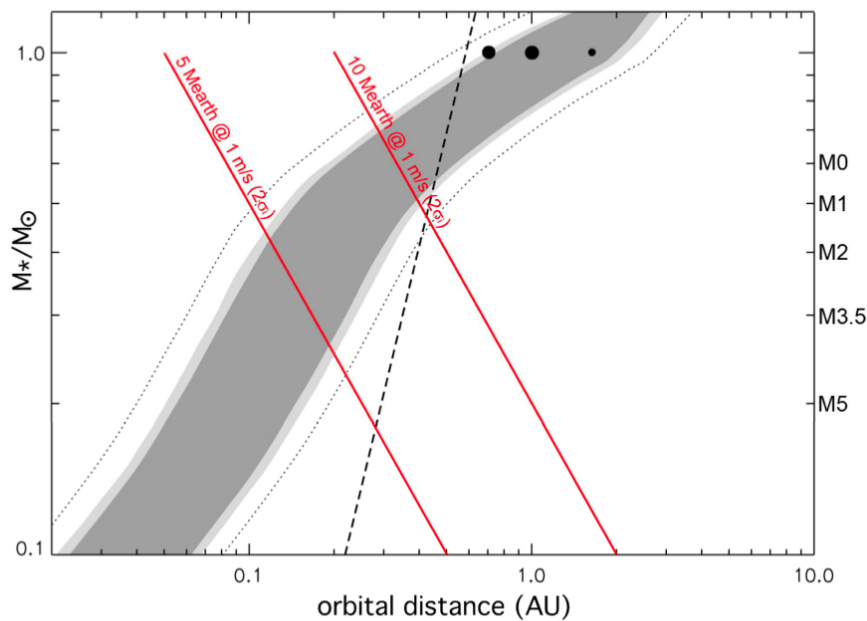
Figure 1.13: Habitable zones on M dwarf stars - Distance of the habitable zone (grey shaded area) as a function of the stellar mass. The plot is centered at the low-mass M dwarfs regime. The Solar System is shown in the upper part of the plot for comparison purposes. Objects to the left of the black solid line are in synchronous rotation (tidal-locked). Planets with masses up to 5 and 10 M$_\oplus$ can be detected with a $1\,\mathrm{m\,s^{-1}}$ precision limit if they have orbital periods below the respectively red solid lines. *From: CARMENES.*

From an observational point of view, the large abundance of M dwarfs compared with other spectral types (roughly 70% of the stars in the Milky Way are M-type stars assuming a Kroupa initial mass function Kroupa 2001; see Fig. 1.14) and their propensity to host planets (half of M-stars host a 1.5-2.0 R$_\oplus$ planet in an orbit shorter than 50 days; Dressing & Charbonneau 2015) make them ideal targets to study the physics of planet formation and evolution in the low mass regime of the Hertzsprung-Russell diagram. The initial conditions of planet formation change with the stellar mass (e.g. Ida & Lin, 2005; Kennedy & Kenyon, 2008; Alibert *et al.*, 2011), consequently, parameters such as the initial disk mass or the gas dissipation and migration timescales model the final architecture of the planetary system. In fact, the increasing amount of planets discovered around M dwarfs, allowed to unveil some observational constrains.

For example, we now know that giant planets are rare around less massive stars, and that the population is in average less massive than for FGK stars (e.g. Bonfils *et al.*, 2007; Udry & Santos, 2007; Bonfils *et al.*, 2013). This result agrees with the core-accretion model which predicts that protoplanets do not have enough time to grow a massive solid core able to accrete gas before the disk dissipation (e.g. Ida & Lin, 2005; Kennedy & Kenyon, 2008). However, other theories such as the disk gravitational stability or the fast accretion and migration theories claim that forming gas giants is viable also in low mass stars (Boss, 2006a,b; Alibert *et al.*, 2005).
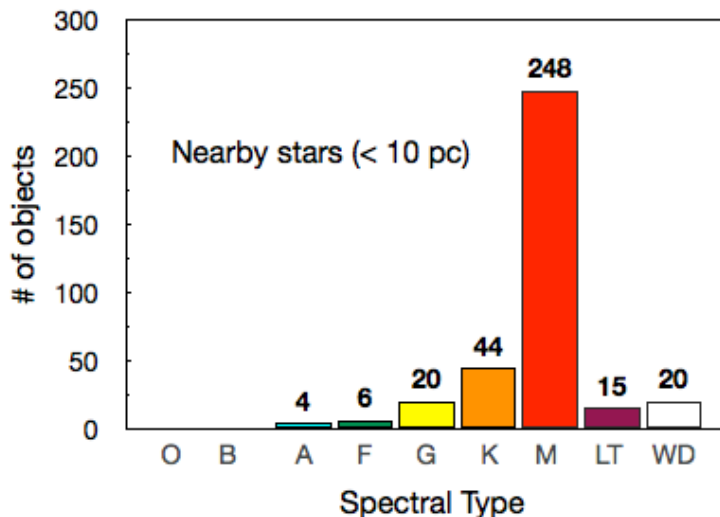
Figure 1.14: Census of M dwarf stars in the solar neighborhood - $\sim 70\%$ of the main-sequence stars within 10 pc are M dwarf stars. *Source: http://www.recons.org/census.posted.htm*

Besides the mass, another example of the accumulated observational evidence is the weak metallicity correlation detected for low mass planets around low mass stars (Jenkins *et al.*, 2013). Since the discovery of the first exoplanets, we know that metal-rich stars are more prone to host planets (e.g. Gonzalez, 1997; Santos *et al.*, 2004; Fischer & Valenti, 2005). This tendency is well explained by the core-accretion theory which predicts that dust rich environments will faster grow faster the core required to form giant planets. However, the metallicity-correlation vanish for low-mass planets since they do not have to reach any minimum mass. In fact, more low-mass planets are expected in metal-poor stars since the less dusty reservoirs should result in the grow of

smaller planets by the disk dissipation time. The typical longevity of the low mass stars favors the observational testing of this and any other planetary system architectures predicted by the models because most of the planetary systems observed are completely formed already. Moreover, longevity works in favor of the habitability, since planets around M dwarfs would have had more time to develop life.

1.3.1   Habitability conditions of planets around M dwarfs

Despite the reasons given above, M dwarf stars have not been historically as well studied as other spectral types. Besides their intrinsic faintness in visible wavelengths, the main reason was their complex spectra[1]. Nowadays, M dwarfs are in the spotlight and many teams work to better characterize them.

Early-type M dwarfs have a radiative core that decreases in size with the stellar mass, being late-types fully convective (cut-off at M4, $\sim 0.35, M_\odot$; Chabrier & Baraffe 1997; Reid & Hawley 2005). Several studies agree with the fact that partially convective early-types are slow rotators, and it has been shown that slow rotators are significantly less active (Browning *et al.*, 2010; Reiners *et al.*, 2012; West *et al.*, 2015). Even though, the stellar magnetic activity can be a big challenge for the habitability in M dwarfs systems. The habitability of a planet requires water, but also an incoming stellar flux low enough to permit the existence of an atmosphere able of keeping a certain surface pressure and possibly a greenhouse effect. Planets in the HZs of M dwarfs are close to the star and thus are generally highly exposed to magnetic fulgurations. Whether planet habitability is possible in the presence of UV and X-ray flares is still a matter of debate[2]. However, recent studies suggest that there are mechanisms to conserve the habitable properties even when the planet receives high UV/X-ray flux ratios (e.g. see several studies for the M5.5V host star Proxima Centauri in Ribas *et al.*, 2016; Turbet *et al.*, 2016; Barnes *et al.*, 2016).

Exoplanets in the habitable zone of M dwarfs are generally in a tidal-locked configuration, i.e. they rotate synchronously with their host star in a 3:2 resonance like the Moon and the Earth do. For many years, the large temperature gradients between

---

[1]The low surface temperatures characteristic of M dwarfs result in crowded spectra where atomic lines and molecular bands blend and depress the continuum complicating the spectral analysis.

[2]Segura *et al.* (2010) showed that a single flare do not compromise the planet habitability. However, planets may have suffered frequent and strong flares at younger ages (Armstrong *et al.*, 2016).

the day and night sides were thought to prevent the planet habitability. However, recent studies indicate that the runaway greenhouse of the day-side and the atmospheric collapse of the dark-side can be avoided with heat transportation (see several possible scenarios in Fig.1.15). The efficiency of the redistribution would depend on the total amount of water initially available as well as of the atmosphere mass, thickness and composition (e.g. Pierrehumbert, 2011; Yang *et al.*, 2014; Goldblatt, 2016). Therefore, observational proofs are required to constrain the climate model solutions, characterize in better detail the composition of the planet atmospheres, and shed light on the climatic effects of a tidal-locked configuration and of a high UV/X-ray irradiation.
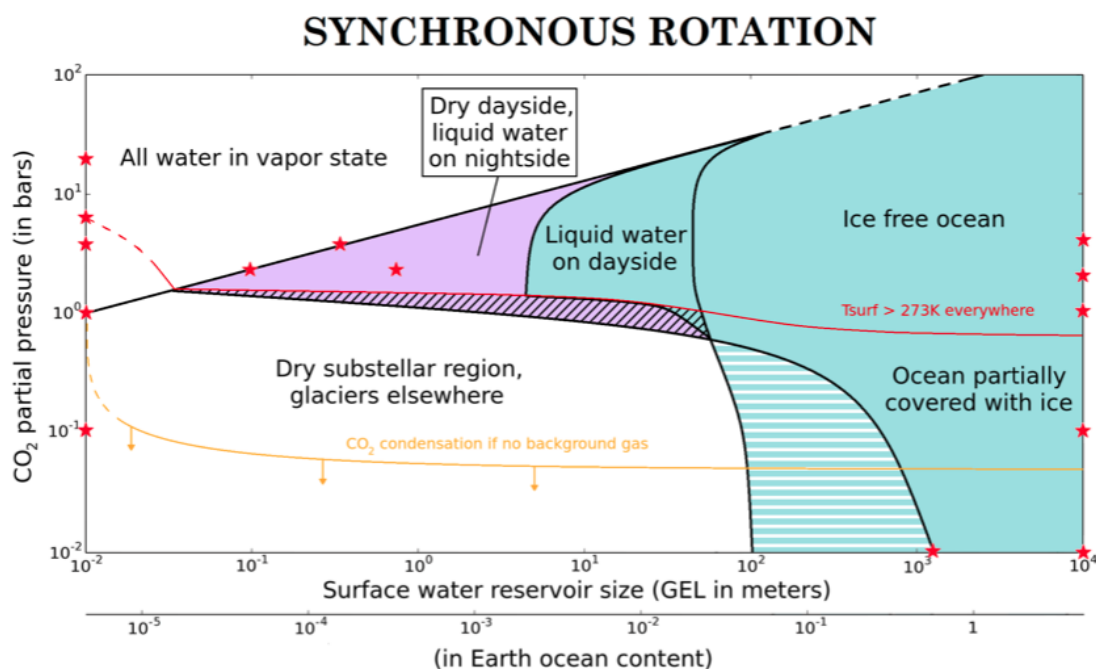
Figure 1.15: Possible climates in a synchronous rotation - Possible atmospheres as function of the CO_2 and water content in the planet surface. The units of the water content (GEL) account for the globally averaged layer depth that would result from putting all the water reservoirs in the planet surface. Simulations done for Proxima b parameters. *From Turbet* et al. *(2016).*

1.4 The Cool Tiny Beats project

Exoplanetary studies on M dwarfs have to evolve hand in hand with our understanding of stellar physics. With this aim, we started in 2013 the "Cool Tiny Beats" (CTB) project (Berdiñas *et al.*, 2015). CTB makes use of the high-precision radial velocity spectrographs HARPS and HARPS-N (see Chapter 2) to study the short time domain of nearby M dwarfs. In particular, the survey objectives are threefold: (1) to detect potentially habitable rocky planets, (2) to increase our knowledge about the stellar magnetic activity in M dwarf stars and, (3) to search for the predicted, but still undetected, stellar pulsations of M dwarfs (see Fig. 1.16)
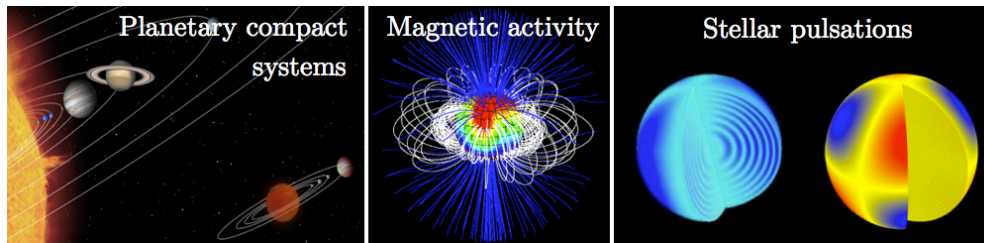
Figure 1.16: Cool Tiny Beats science goals - The three main goals of the CTB project are: search for planetary compact system (left), study the star magnetic activity (middle), and detect stellar pulsations in M dwarfs (right). *Sources: NASA, Jardine* et al. *(2009) and NASA/Kepler.*

1.4.1 Goal 1 – short period planets

By 2013, the photometric space mission *Kepler* had gathered several transit signals that were thought to correspond to small short-period planets ($P \lesssim 3$ days and $R \lesssim 1.5\,R_\oplus$). However, no plausible formation scenario could explain their presence at that time. Today, we know that *Kepler* had indeed discovered a new kind of compact planetary systems around M dwarfs (e.g. Kepler-42, Kepler-80, KOI 1843; Muirhead *et al.*, 2012; Ragozzine & Kepler Team, 2012; Ofir & Dreizler, 2013), and current models can explain their formation through core-accretion and migration (Coleman & Nelson, 2016). Doppler spectroscopy had also detected planets at short periods, but they were typically super-Earth or Neptune mass planets (e.g. GJ 436 b, GJ667 C b-c-d; Butler *et al.*, 2004; Anglada-Escudé *et al.*, 2012a). However, detections such as that of GJ 581 e (Mayor *et al.*, 2009), with twice the Earth-mass and ∼3 day period, demonstrated that

we were close to reaching the Earth-mass domain with HARPS. CTB was designed to explore the short time domain of M dwarfs with the aim of detecting Earth-mass planetary compact systems as those first unveiled by *Kepler*.

1.4.2 Goal 2 – activity on M dwarfs

The stellar activity can be a limiting factor in the search for Earth-like planets. It can induce RV signals that do not necessarily vanish over time, producing apparent signals that can be mistaken as planets (e.g., Queloz *et al.*, 2001; Hatzes, 2002; Bonfils *et al.*, 2007). The stellar rotation couples with the convective motion of the star envelope creating magnetic fields which generate starspots and plages on the star through a magnetic dynamo mechanism[1]. Such starspots produce a modulation of the starlight that can be mistaken for a Doppler shift caused by a planet. Furthermore, M dwarfs, like other stars with external convective envelopes, can present long-term activity cycles caused by either the oscillation of the global level of activity or by the spatial rearrangement of the active regions (e.g. Gomes da Silva *et al.* 2012 found RV variations up to $\sim 5\,\mathrm{m\,s^{-1}}$ due to long-term activity). Both rotation and activity cycles are the two events which more efficiently induce RV signals (Dumusque *et al.*, 2011). Regarding timescales, stellar rotation induces activity signals of days while activity cycles typical induce signals of years (Suárez Mascareño *et al.*, 2015, 2016). CTB monitors simultaneously with the RVs several chromospheric indices that are supposed to originate in the active regions (e.g. CaII H+K, Hα, NaI D1+D2; Gomes da Silva *et al.*, 2012). Also, indices accounting for the spectral line shapes (e.g. the bisector span or the FWHM provided by the HARPS-Data Reduction Software) are measured. In that way, we can better understand the chromospheric activity and test if any correlation with the Doppler variability is present.

1.4.3 Goal 3 – oscillations to probe M dwarfs' interior

Recent theoretical studies from Rodríguez-López *et al.* (2012, 2014) predict that low-mass M dwarf stars can oscillate. That is, they can start, drive and maintain stellar pulsations. Stellar pulsations have demonstrated to be a powerful tool to infer the properties of the star interiors and thus, to derive their global parameters very accurately.

---

[1]M dwarfs' magnetic dynamos can last several Gyr (West *et al.*, 2008; Zuluaga & Bustamante, 2016).

Consequently, planet properties such as the mass, the radius, the age, or even the average surface temperature or the spin-orbit angle (through the Rossiter-Mclaughlin effect) can be measured at a very high precision if the host star pulsates (e.g. Kepler-10, Kepler-56 or Kepler-419; Fogtmann-Schulz *et al.*, 2014; Huber *et al.*, 2013; Dawson *et al.*, 2014).

However, before applying the asteroseismic tools to M dwarfs, pulsations have to be observationally confirmed. Rodríguez-López *et al.* (2014) predict two main regions where M dwarfs may maintain pulsations: one comprises young pre-main sequence stars, and the other mainly partially-convective M dwarfs in the main-sequence[1]. Regarding the range of predicted periods, the ϵ *driving mechanism*, caused by the burning of He[3], is thought to excite mainly very short periods from 20 to 60 min. On the contrary, the *flux-blocking mechanism*, caused by the periodic block of the radiative flux at the tachocline (i.e. the transition layer from radiative to convective) should drive pulsations ranging from 20 min to 3 h. The CTB project monitors this range of predicted periods with the aim of detecting stellar pulsations in main-sequence M dwarfs.

1.4.4 The sample selection and observational strategy

CTB performed high-cadence observations, meaning that we continuously monitored the same target with exposures shorter than 20 min during several consecutive nights. This observational strategy is one of the key points, since it allows us to combine all the scientific cases in a single observational run (see Fig. 1.17). The CTB initial sample was comprised of $\sim$25 M dwarfs. The targets were mostly selected to lie within the boundaries of the instability region formed by main sequence M dwarfs, as well as on criteria of long-term Doppler stability (RMS $< 2.5\,\mathrm{m\,s^{-1}}$), low activity levels, and slow rotation. That is, to satisfy the requirements of both the exoplanetary and the asteroseismology science cases (see the sample in Fig. 1.18). To date, more than 13 M dwarfs of the sample have been observed during 49 high-cadence nights spread over 7 runs. For a future CTB phase II, we plan to extend our sample to targets from the two instability bands predicted by Rodríguez-López *et al.* (2014). Moreover, we plan to update our observational strategy to include simultaneous photometry and to broaden out the search with near-IR Doppler measurements.

---

[1]This study includes the fundamental radial mode as well as non-radial and non-fundamental *p*-modes and *g*-modes.
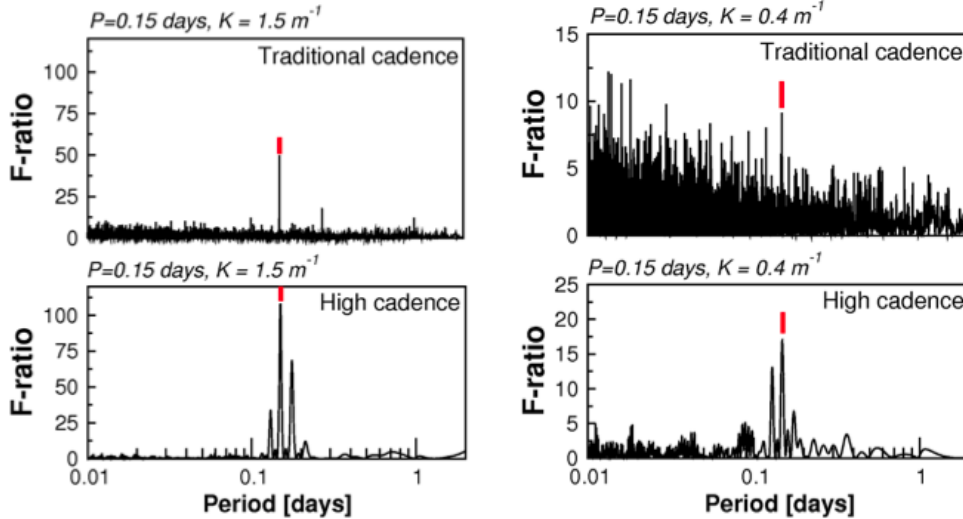
Figure 1.17: Cool Tiny Beats sampling cadence - Periodograms of synthetic datasets showing the fatal effect of the traditional sampling cadence (upper panels) in case of searching for short-period low-amplitude signals. Most of the aliases vanish when we use a suitable high-cadence strategy (lower panels).

1.5   Thesis outline

The goal of this thesis is to detect compact planetary systems around M dwarfs using radial velocity measurements. This objective requires both a global understanding of the host star and deep knowledge of the instrumentation used. From a scientific approach, besides searching for short-period planets around M dwarfs, I have searched for stellar pulsations that, if detected, would allow to constrain the star (and planets) physical parameters. From an instrumental point of view, I have studied the not-very-well-known performance of the radial velocity spectrometers in the sub-night domain. Additionally, in the last part of this thesis I present a prototype which, from an instrumental approach, aims at increasing the precision in radial velocity.

The thesis structure is as follows: In Chapter 2, I summarize the instruments and methodology used in this thesis. Chapter 3 delves into the HARPS-N instrumental response within the sub-night regime. In Chapter 4, I present the first Doppler-search attempts in the search for stellar pulsations in M dwarfs. Chapter 5 focuses on the discovery of planetary compact systems on M dwarfs. In Chapter 6, I present RadiCa2D, an instrumental alternative to the classic scrambling methods. I draw the conclusions
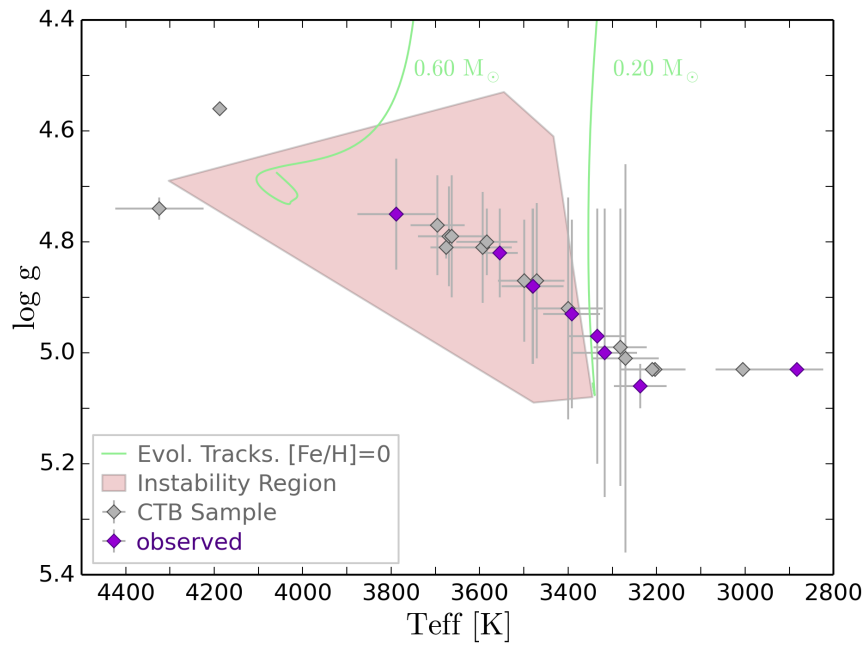
Figure 1.18: Cool Tiny Beats targets - T_{eff} - $\log g$ diagram showing the M dwarf stars comprising the initial CTB sample (grey diamonds). Purple diamonds are observed targets. The pink area corresponds to the instability region predicted for main-sequence M dwarfs. The solid green lines are the evolutionary tracks that delimit the region.

in Chapter 7 and finally, Chapter 8 states the future perspectives of this thesis.

2
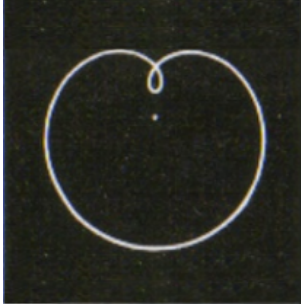
Radial velocities: From theory to observation

WHILE there are several techniques to detect exoplanets, the radial velocity method has demonstrated to be one of the most fruitful regarding the search for low-mass exoplanets. This thesis is mainly focused in the analysis of radial velocity data. Thus, the current Chapter delves into the details of the method, describing the fundamental theoretical aspects in Section 2.1, the basis of the radial velocity instruments in Section 2.2, and how to extract the radial velocity curve and the methods involved in the analysis in Sections 2.3 and 2.4, respectively. A review of other techniques is given in Appendix C. See in Lovis & Fischer (2010) further details about the radial velocities and in Fischer *et al.* (2016) the field state-of-the-art and the main future prospects.

2.1 Theory of radial velocities

In this section I describe the fundamental concepts involved in the detection of a planet though radial velocities.

2.1.1 Gravitation and Doppler effect

The radial velocity method is based on two main effects. The first one was described by Isaac Newton (Newton, 1687) and refers to the mutual gravitational forces that massive bodies exert on each other. Suppose we have a star-planet system. Today, it is very well known that both the host star and the planet (or any other gravitationally linked body) orbit around the barycenter of the system (i.e. the center of gravity where the total sum of the mutual forces is zero). Therefore, the presence of a planet can be inferred by measuring the star's velocity in the line of sight with the Earth (i.e. the radial velocity). Moreover, since the less massive a planet is, the closer the barycenter is to the star, then the radial velocity also gives us hints about the relative planet mass.

The second effect refers to how to measure the star's velocity and it is the very well-known *Doppler effect*. This effect accounts for the change in frequency that a wave suffers when the source is moving. A wave emitted at a frequency f would be received by the observer at $f + \delta f$; where δf is positive if the source is approaching the observer, and negative if the source is receding. In our case, the wave is the light emitted by the star, which is the source, and δf is the periodic shift the spectrum suffers to bluer (if the star approaches) or redder (if receding) wavelengths, as the star moves around the barycenter of the system (see an schematic view in Fig 2.1). Thus, the observed wavelength (λ) is a function of the original wavelength (λ_0) and a term accounting for the relativistic velocity of the star light:

$$\lambda = \lambda_0 \sqrt{\frac{1 - V_r/c}{1 + V_r/c}}, \tag{2.1}$$

where V_r is the radial velocity of the star and c the speed of light in vacuum. Then, we can derive the star's velocity from:

$$\frac{\Delta\lambda}{\lambda} = \frac{V_r}{c}, \tag{2.2}$$

where $\Delta\lambda = \lambda_0 - \lambda$ is the total wavelength shift measured in the spectrum.
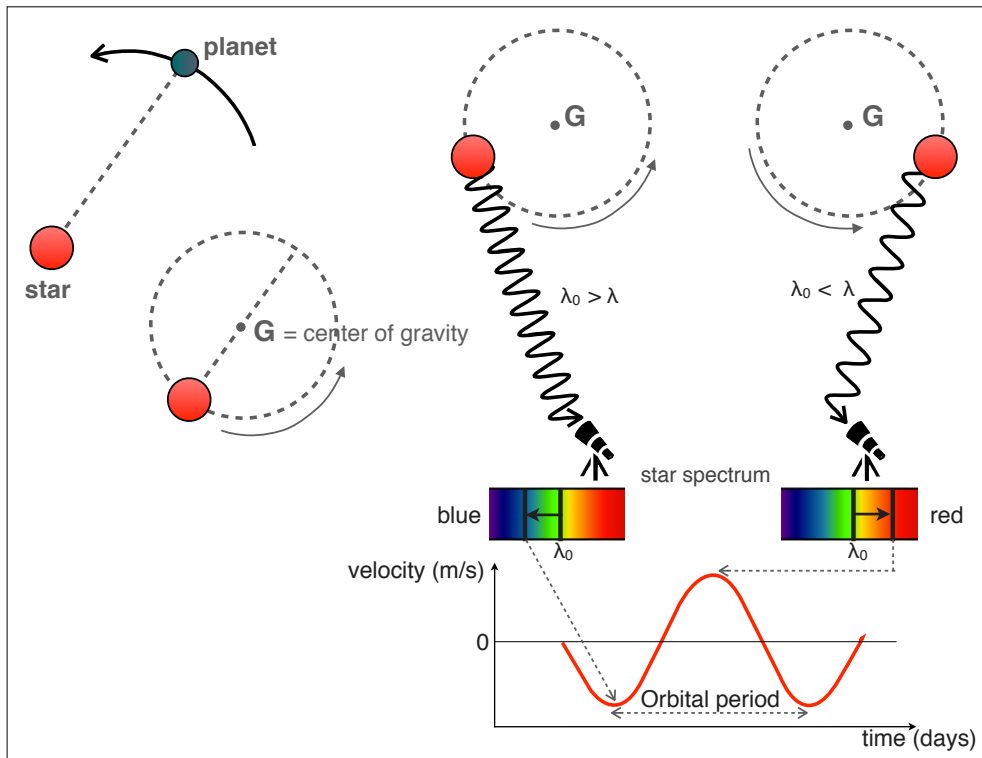
Figure 2.1: Doppler effect - Schematic view of the Doppler effect produced by the movement of the star around the center of gravity of the star-planet system. This movement causes the spectrum lines to periodically shift in wavelength. *Adapted from Ollivier* et al. *(2009).*

2.1.2 Orbital mechanics

Once we know how to measure the radial velocity of the star through the *Doppler effect*, we will delve into the analytic definition of the orbital equations with the aim of obtaining some of the planet parameters. In a two dimensional reference frame, if we place the system's origin at the barycenter and we make the x-axis positive towards the periapsis, the Cartesian coordinates of an orbiting body (the star) are:

$$x = r \cos \nu$$
$$y = r \sin \nu$$
$$z = 0 \tag{2.3}$$

where r is the relative star-barycenter distance and can be written from the ellipse analytic function as

$$r = a \frac{1 - e^2}{1 + e \cos \nu} \tag{2.4}$$

In these equations, e is the eccentricity of the orbit and ν measures the angle to the star since the last passage by the periastron. This angle is known as the *true anomaly* and is related with the *eccentric anomaly* (E) as

$$\tan \frac{\nu}{2} = \left(\frac{1 + e}{1 - e} \right)^{1/2} \tan \frac{E}{2} \tag{2.5}$$

From this equation, we can easily see that ν and E would be equal if the orbit was circular ($e = 0$). In fact, the *eccentric anomaly* accounts for the non-circularity of the orbit (it is the angle between the periastron and the star, as if it was in a circular orbit of radius equal to the semi-major axis of the ellipse; see Fig. 2.2).

To obtain the *eccentric anomaly* we first have to calculate the *mean anomaly*, M, both being related through the *Kepler's equation of movement*:

$$M = E - e \sin E \tag{2.6}$$

The *mean anomaly* is not a physical angle. It is related to a fictitious mean motion that allows to calculate the position of the orbiting body as a phase since the last periastron passage (t_p). Thus, being the *mean anomaly* given by

$$M = \frac{2\pi}{P}(t - t_p) \tag{2.7}$$
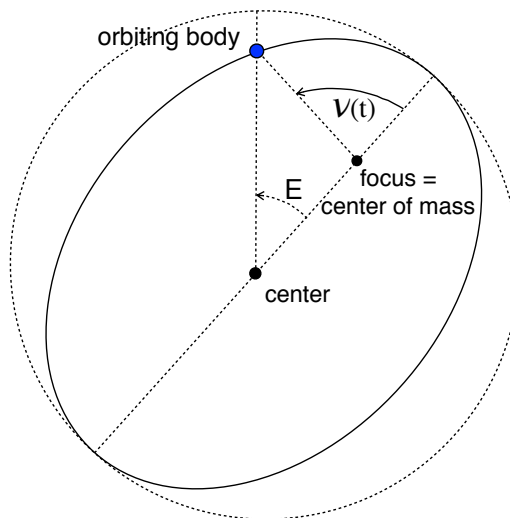
Figure 2.2: Orbiting body – 2D reference system - The orbiting body (e.g. the star) orbits around the focus of the orbital ellipse (e.g. the star-planet system barycenter). The conventions for the *true* and *eccentric anomalies* angles are described in the diagram.

we can redefine it in terms of a known time t_0, for example the first observed epoch. In that case we obtain M as

$$
\begin{aligned}
M &= \frac{2\pi}{P}(t - t_p + t_0 - t_0) = \\
&= \frac{2\pi}{P}\Delta t + M_0
\end{aligned}
\tag{2.8}
$$

where M_0 is the *mean anomaly* at t_0. Consequently, we can use the equations 2.5, 2.6, and 2.8 to write the *true anomaly*, and the orbital equations, as a function of e, P, and Δt.

Nevertheless, the reference frame given in Eq. 2.3 corresponds to the projection of the orbit in the plane of the sky. In the real case, the probability of seeing the system face-on (i.e. $z = 0$) is very low and rotation angles have to be included to consider other orientations. If we define the Cartesian z-axis as the direction to the observer, the system coordinates are described by:

$$
\begin{aligned}
x &= r\left[\cos\Omega\cos\left(\nu + \omega\right) - \sin\Omega\sin\left(\nu + \omega\right)\cos i\right] \\
y &= r\left[\sin\Omega\cos\left(\nu + \omega\right) + \cos\Omega\sin\left(\nu + \omega\right)\cos i\right] \\
z &= r\,\sin\left(\nu + \omega\right)\sin i
\end{aligned}
\tag{2.9}
$$

where i is the *inclination* of orbit, Ω the *longitude of the ascending node*, and ω the *argument of the periastron*. See in Fig. 2.3 the angle conventions.
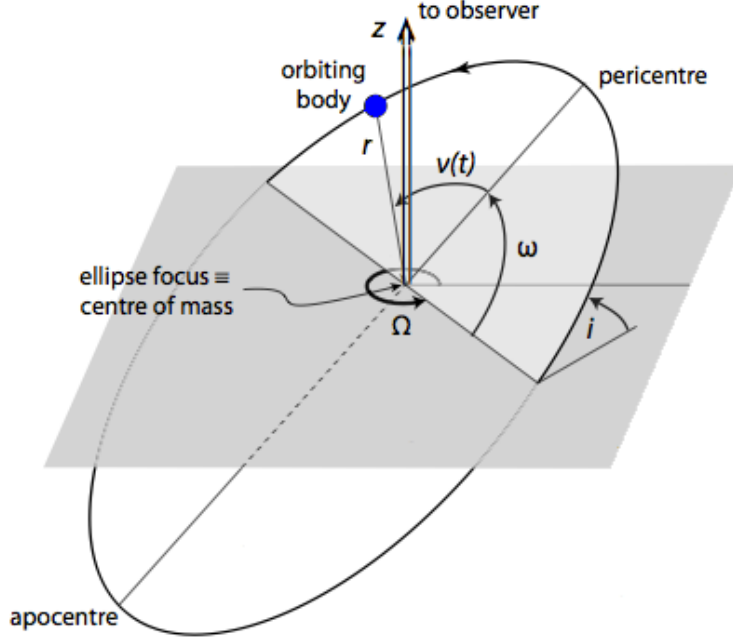
Figure 2.3: Orbiting body − 3D reference system - Description of the orbit elements when the direction of the observer (z) is considered.

Therefore, the radial velocity of the star (V_r) can be obtained by deriving the z-axis as a function of time. The only time-dependent parameter in the z-axis coordinate is ν. Then, we can use *Kepler's Second Law* (the law of areas) expressed by

$$\frac{d\nu}{dt} = \frac{2\pi}{P\,r^2}a^2\sqrt{(1-e^2)} \tag{2.10}$$

to obtain the star's radial velocity:

$$V_r = V_{\mathrm{cm}} + K_\star\left[\cos\left(\nu + \omega\right) + e\cos\omega\right] \tag{2.11}$$

where V_{cm} is the velocity of the system as a whole (the velocity of the center of mass), and $K_\star$, which corresponds to:

$$K_\star = \frac{2\pi}{P}\frac{a_\star\sin i}{\sqrt{(1-e^2)}}, \tag{2.12}$$

is the module of the star's velocity in the radial axis (note that it depends on the inclination angle i and on the star's position along the orbit). In other words, $K_\star$

is the semi-amplitude of the radial velocity signal detected by the observer (e.g. the amplitude of the curve at Fig. 2.1).

2.1.3 Planet parameters from radial velocities

Getting the period (P) and the semi-amplitude (K) from the *Doppler effect* signal is straightforward. However, a planet in a non-circular orbit will produce a Doppler signal which is not sinusoidal. Modeling $V_r(t)$, the radial velocity curve, enables the determination of other parameters such as the eccentricity of the planet orbit, the position of the periapsis, or even the planet minimum mass or its orbital semi-major axis. The last two can be obtained as follows:

Using *Kepler's Third Law* for a star-planet system orbiting the barycenter we get:

$$\frac{P^2}{a^3} = \frac{4\pi^2}{G(M_\star + M_p)} \tag{2.13}$$

which using the identities:

$$a = a_\star + a_p$$

$$M_\star \, a_\star = M_p \, a_p \tag{2.14}$$

allows us to redefine K as

$$K_\star^3 = \frac{2\pi G}{P \, (1-e^2)^{3/2}} \left[\frac{M_p^3 \sin i^3}{(M_\star + M_p)^2} \right] \tag{2.15}$$

where the term in brackets is known as the *mass function*. Thus, assuming we know the star's mass, $M_\star$, from other method and that $M_p << M_\star$, the minimum mass of the planet is defined by:

$$M_p \sin i = \left(\frac{P}{2\pi G} \right)^{1/3} K_\star \, M_\star^{2/3} \, \sqrt{1-e^2} \tag{2.16}$$

or in Earth mass units by:

$$\left(\frac{M_p \sin i}{M_\oplus} \right) = 11.19014 \, \text{m/s} \, K_\star \, \sqrt{1-e^2} \left(\frac{M_\star}{M_\odot} \right)^{2/3} \left(\frac{P}{1yr} \right)^{1/3} \tag{2.17}$$

From Eq. 2.13 and 2.14 we can also obtain the semi-major axis of the planet orbit as

$$a_p = \left(\frac{G}{4\pi^2} \right)^{1/3} M_\star^{1/3} P^{2/3} \tag{2.18}$$

which, again in more intuitive units is:

$$\left(\frac{a_p}{\text{AU}}\right)^3 = \left(\frac{M_\star}{M_\odot}\right)\left(\frac{P}{1yr}\right)^2 \tag{2.19}$$

Note that, from Eq. 2.16, the radial velocity method provides only a lower limit to the planet mass if the inclination is unknown. That is, the value from Eq. 2.16 would be the real planet mass only if the orbit is edge-on ($i = 90°$). We can use, for instance, astrometric measurements to get the inclination. However, since the astrometric signal is larger for massive planets at wide orbits, it is generally the transit method the approach used to obtain most of the inclinations, but not all planets discovered with radial velocities are transiting planets. Despite the difficulty in the determination of the inclination, we know that the probability of observing an almost face-on configuration is very low. For comparison, integrating over all possible inclinations and assuming that $\cos i$ is uniformly distributed over the $i = 60° - 90°$ range, we we find the mass of the planet would be typically <15% larger than the minimum mass. See more details about the astrometry and transit methods in Chapter C.

Additionally, from Eq. 2.16 we can also infer the amplitude dependence with the planet mass and period: the Doppler signal will be larger for massive short-period planets around low-mass stars. However, as the radial velocity precisions given by the current echelle spectrographs increase, the detection of lower mass planets also becomes possible. In fact, from Eq. 2.16, a precision of a few cm s^{-1} (the goal of ESPRESSO/VLT) is required to detect the signal of an Earth-like planet orbiting a 1-year period around a Sun-like star.

2.2   Fiber-fed échelle spectrographs

Fiber-fed cross-dispersed échelle spectrographs are the most successful instruments in detecting planets through the radial velocity (RV) method. These planet hunters have increased their RV precision from several tens of m s^{-1} down to $\sim 0.8 - 1\,\text{m s}^{-1}$ (HARPS; Pepe *et al.*, 2011), in the course of about two decades. The high stability of the current instruments is responsible for the precision increment. Most precise spectrographs are placed in independent-ground rooms, where they can be isolated inside both a vacuum

vessel and a thermally stabilized cryostat[1] and the light is carried by an optical fiber from one of the telescope's focus to the spectrograph (see Fig.2.4).
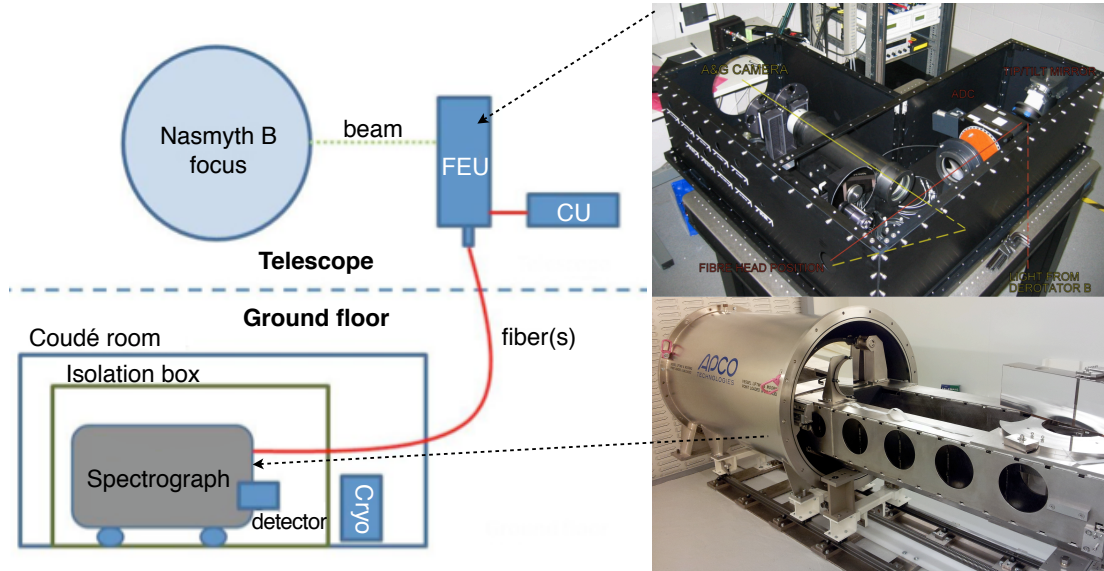
Figure 2.4: HARPS-N schematic view - The spectrograph is vacuum and thermally stabilized in the Coudé room. An optical fiber carries the light from the telescope to the spectrograph (science fiber). The front-end unit (FEU) connects the telescope beam with this fiber. Besides the science fiber, another calibration fiber gets to the spectrograph. The calibration fiber injects the light from the lamps placed at the calibration unit (CU). Again, the FEU connects the CU with the spectrograph. *From Cosentino* et al. *(2012)*.

Regarding the RV precision, another fundamental element is the calibration system. The use of fibers also allows to record, simultaneously with the science object, the light from a stable source (e.g. a ThAr lamp, a Fabry-Pérot or the newer laser frequency combs). The light from this reference source, placed at the calibration unit (CU), is injected into a secondary identical fiber through the front-end unit (FEU). Therefore, both the star and the reference light share almost the same optical path. In that way, we can measure the RVs of the star relative to the reference source. See in Fig. 2.6 panel (b) the spectra from a laser frequency comb recorded over the star spectra in the detector.

The main sub-system of course is the spectrograph itself, where the optical bench has a similar layout as in Fig. 2.5. Here, the fiber with the starlight coming from the

---

[1]HARPS-N operates at the Coudé room of the TNG with pressure and temperature variations below 0.001 mbar and 0.001 K, respectively.

telescope is injected into the spectrograph and collimated before reaching the échelle grating. Afterwards, the different splitted wavelengths come back to the same off-axis collimator to be diverted through an intermediate slit which helps in removing stray light. Finally, the beam is collimated once again before being cross-dispersed and entering into the camera. See Fig. 2.6 for an schematic view of the échelle grating & cross-disperser concept as well as its relation with the final image appearance on the CCD.
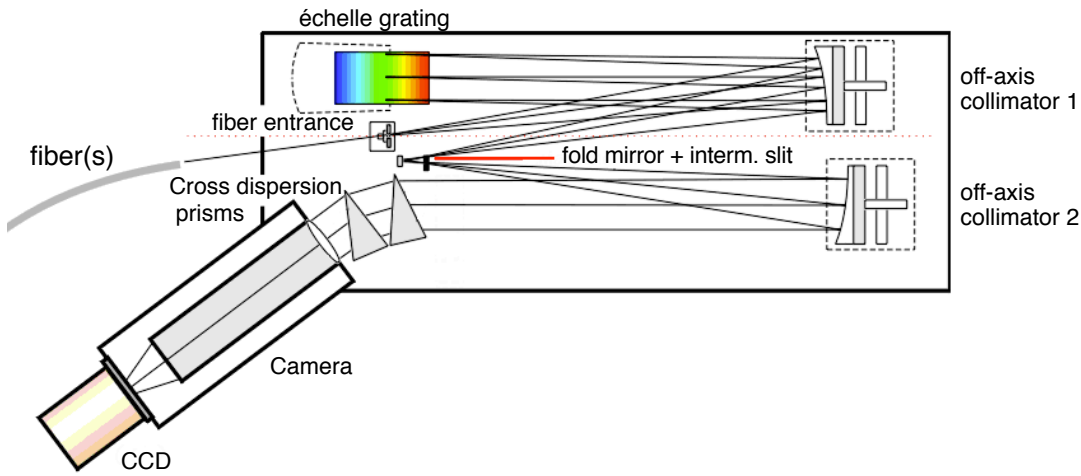
Figure 2.5: Optical layout of a typical échelle spectrograph. - Optical design of classic échelle spectrographs. The light from the fiber is dispersed first by the échelle grating and later by the cross-dispersion prisms. This diagram in particular corresponds to FOCES, the CAFE precursor at the 2.2 m telescope of CAHA. *Adapted from* `http://www.usm.uni-muenchen.de/people/gehren/foces.html`

The échelle grating is the element that ensures a wide wavelength coverage and a high-resolution spectra and deserves further explanation. In a regular grating (see panel *a* in Fig. 2.7) the rays are reflected at the different grooves of the grating following the equation:

$$\frac{n\lambda}{d} = \sin\alpha + \cos\beta \tag{2.20}$$

where n is the diffraction order, d the width of the grooves, and α and β the angles of the incident and reflected rays, respectively. As a consequence, we obtain an interference pattern with consecutive maxima at $n\pi$. However, this pattern is superimposed to a second one produced by the reflection of the rays inside the groove. This secondary
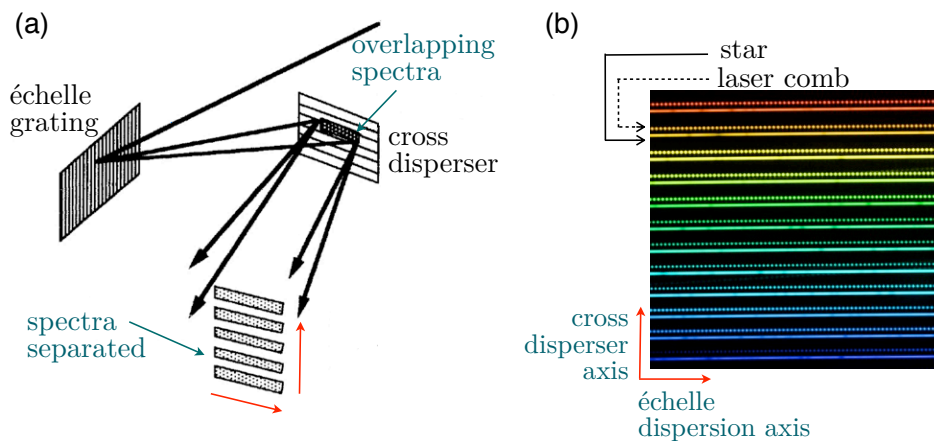
Figure 2.6: Échelle grating & cross-disperser - (a) The cross-disperser adds a low dispersion in the opposite direction to the échelle to disentangle its overlapping high-resolution spectra (overlapping is typical of gratings working at high-diffraction orders). (b) Raw image taken with HARPS while testing a laser frequency comb. The star and the reference spectra are recorded simultaneously (the science and calibration fibers are both coupled at the spectrograph). *Sources: (a) adapted from Kitchin (1995); (b) ESO.*

pattern is known as the blaze function and it dramatically reduces the throughput at orders different than zero (see panel *b* in Fig. 2.7). Consequently, from Eq. 2.20, we can conclude that there is no dispersion at $n = 0$ (we inject and recover white light). This problem is solved by "blazing" the grating, that is, tilting the grooves to shift the blaze function to higher orders (see panels *c* and *d* in Fig. 2.7). The tilt angle is known as the *blaze angle* (ϕ), and échelle gratings are characterized for having $\phi > 45°$ (i.e. the light is reflected at the short part of the groove). In fact, échelle gratings of instruments like HARPS and HARPS-N are in a *quasi-Littrow configuration*, that is, the incident and the diffracted rays are auto-collimated (i.e. $\alpha = \beta = \phi_L$). Such condition ensures large blaze angles while simplifying the optical design. Therefore, échelle gratings work at high-resolution as we can infer from the angular dispersion equation:

$$\frac{\delta\beta}{\delta\lambda} = \frac{n}{d\cos\beta} = \frac{2}{\lambda}\tan\phi_L \tag{2.21}$$

that indicates how the angular dispersion (i.e. the resolution) increases with the order n and the angle ϕ_L.

Therefore, the interference pattern shown at panel *d* of Fig. 2.7 corresponds to the shape of the spectrum that results from sticking together the different apertures (or
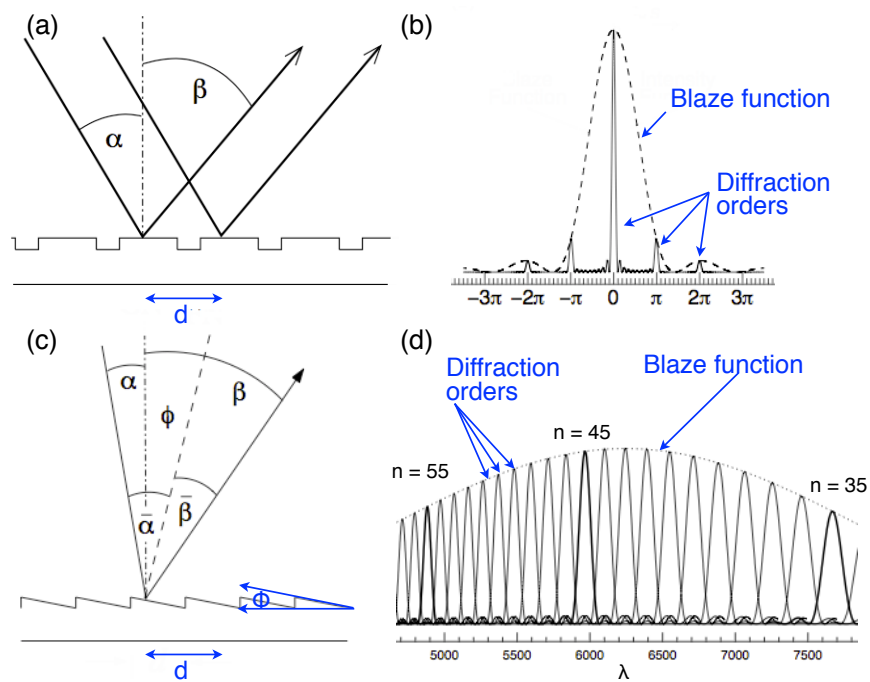
Figure 2.7: Diffraction gratings - (a) Schematic view of the reflection in a regular grating (b) Interference pattern of a regular grating. The blaze function destroys the diffraction at diffraction orders $n \neq 0$. (c) Blazed grating with a blaze angle ϕ. The grating's grooves are tilted to shift the maximum of the blaze function at higher orders. (d) Typical interference pattern of a échelle grating. *Adapted from Churchill 2016, in prep. (book "Cosmological Absorption Line Spectroscopy"; private communication).*

spectral orders) recorded at the detector (see Fig. 2.8).

Figure 2.8: Raw échelle spectra - (Left) Raw cross-dispersed échelle spectra in 2D. The wavelength increases from left to right (échelle diffraction axis) and from bottom to top (cross-dispersion axis). Each row corresponds to a spectral order n (given on the vertical left scale). (Right) 3D raw spectra. The blaze function modules the flux inside each spectral order. Sticking together the spectrum at each row with increasing wavelength gives panel d in Fig. 2.7. *Source: `http://www.gemini.edu/` and `www.astro-spec.com`*

2.2.1 HARPS and HARPS-N

The vast majority of the data used in this thesis were obtained observing either with HARPS or HARPS-N as part of the "Cool Tiny Beats" (CTB) project. Both instruments are descendants of the first planet-hunters ELODIE (Baranne *et al.*, 1996) and CORALIE (Queloz *et al.*, 2000) and share a very similar optical design; they are stabilized high-resolution fibre-fed cross-dispersed échelle spectrographs. HARPS (Mayor *et al.*, 2003; Pepe *et al.*, 2004), that stands for High Accuracy Radial Velocity Planet Searcher, operates from the 3.6 m telescope at La Silla Observatory (Chile), while HARPS-N (Cosentino *et al.*, 2012) is a very similar concept installed in the northern hemisphere, in particular, at the 3.6 m Telescope Nazionale Galileo (TNG) at Roque de los Muchachos Observatory (Spain). Concerning the photon noise, the large telescope apertures allow to gain radial velocity precision. The HARPS and HARPS-N large telescope apertures combined with their high-resolution powers (R $\sim$ 110000) and their high stability (0.001 mbar and 0.001 K) allow to reach long-term precisions of $0.8 - 0.9\,\mathrm{m\,s^{-1}}$ (Pepe *et al.*, 2011), also on M-dwarfs (Anglada-Escudé *et al.*, 2012b).

In the short-term (i.e. within a night), the precision can increase to even $0.2\,\mathrm{m\,s^{-1}}$ (Lovis & Fischer, 2010) a fact that favors our search of stellar pulsations in M dwarfs. The goals of the CTB project, as well as of this thesis, require of very precise RVs. Therefore, HARPS and HARPS-N, which provide the current highest RV precisions, are the most suitable instruments currently available to carry out our task.

2.2.2 Near-IR spectrographs & CARMENES

The current most precise spectrographs (i.e. HARPS and HARPS-N) operate at optical wavelengths ($\sim$380–690 nm). However, M dwarfs are faint in this range as their emission peak is within the near-IR[1] (see panel *b* in Fig. 2.9). The lack of high-resolution RV spectrographs operating in the near-IR (NIR) is one the reasons for the small population of exoplanets discovered around late-type M dwarfs (see shaded area in Fig. 2.9 panel *a*), as studies with HARPS and HARPS-N are restricted to close bright M dwarfs[2].
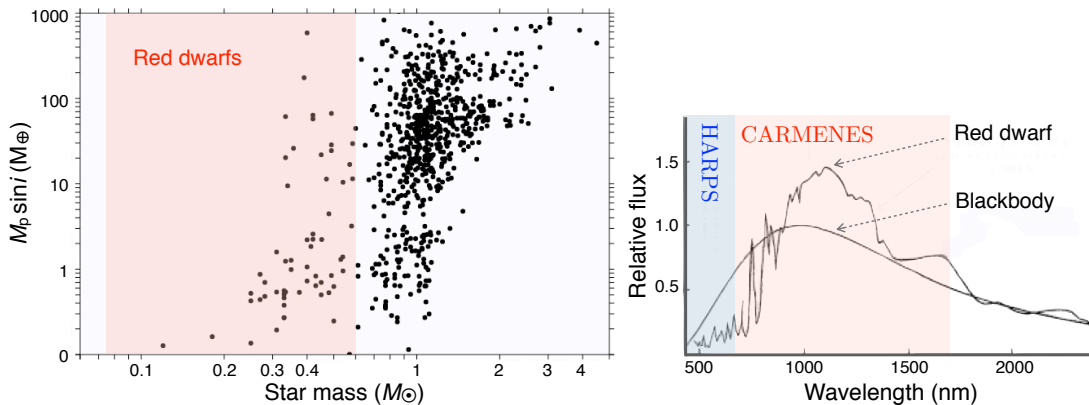
Figure 2.9: The niche of near-IR spectrographs - (Left panel) Population of exoplanets as a function of their minimum mass (y-axis) and the mass of the host star (x-axis). The red area highlights the M dwarfs regime. There is a clear scarcity of exoplanets around stellar hosts with low masses. (Right panel) Comparison of a red dwarf synthetic spectrum with the HARPS and CARMENES wavelength coverage. *Source: www.exoplanets.eu.*

High-resolution NIR spectroscopy is challenging in terms of detector technology,

---

[1]Assuming a blackbody emission, the Wien's displacement law: $\lambda_{\mathrm{max}} = \frac{2900\,[\mu\mathrm{m\,K}]}{T}$ indicates M dwarfs ($T \sim 2900 - 3800$ K) peak at $\sim 0.76 - 1.26\,\mu\mathrm{m}$. HARPS and HARPS-N, which are optimized for Solar-like stars, cover up to $0.69\,\mu\mathrm{m}$.

[2]A M5.5V star like Ross 258 at only 3 pc has a J-band magnitude of 7, whereas in the V-band it is 12.28. HARPS would require a long exposure of 50 min to get a SNR of 50 at 600 nm.

thermal control, wavelength calibration, telluric lines identification and sky background (Plavchan *et al.*, 2013a,b; Anglada-Escudé *et al.*, 2012b). However, the advantages of working at NIR wavelengths make the necessary efforts to develop the technology worthwhile. Bean *et al.* (2010) previously achieved $\sim 5 \, \mathrm{m \, s^{-1}}$ using CRIRES/VLT (Käufl *et al.*, 2004) on a sample of M dwarfs. However, CRIRES is an slit-fed spectrograph and, whereas this favors the sky subtraction, the intensity scrambling is more challenged and the spectrograph has variable illumination. The new instrument CARMENES (Quirrenbach *et al.*, 2014; Amado & CARMENES Consortium, 2015) has overcome many of the NIR technical challenges and aims at reaching $\sim 1 \, \mathrm{m \, s^{-1}}$ precision.

CARMENES (Quirrenbach *et al.*, 2014) has been recently installed[1] at the 3.5-m telescope of CAHA observatory (Spain). CARMENES operates in the optical–NIR[2] and was designed to detect low-mass planets in the habitable zone of late-type M dwarfs. As the rotational broadening and stellar activity typical of late-type M dwarfs (see Chapter 1) can limit planet detections, CARMENES will survey 300 late-type M dwarfs which were previously checked to be slow-rotators (Alonso-Floriano *et al.*, 2015).

2.2.3   Other slit-fed spectrographs

HARPS and HARPS-N were the main instruments used along this thesis. However, in Chapter 5 we also used data from CARMENES and from other three échelle spectrographs. One of the main differences of these instruments, compared with HARPS, HARPS-N and CARMENES, is that they are slit-fed spectrographs calibrated with iodine cells instead of lamps (Marcy & Butler, 1992). Below, I detail their main characteristics. A comparison is also shown in Tab. 2.1.

- **HIRES** (Vogt *et al.*, 1994): The slit-fed High-Resolution Échelle Spectrograph, settled at the Keck-1 10-m telescope (Mauna Kea, Hawaii), covers the 364 - 797 nm range with a resolution power of 55,000. However, the iodine cell system, used to give a wavelength reference, reduces the operative range for Doppler analysis to a 510 - 620 nm range. From a scientific point of view, HIRES is mainly focused in characterizing stellar populations along with detecting planets.

---

[1] CARMENES was installed by the end of 2015 and started its *Guaranteed Time Observations* in January 2016.

[2] A beam splitter diverts the light towards two spectrographs operating in the VIS ($0.52 - 0.96 \, \mu$m) and NIR ($0.96 - 1.71 \, \mu$m) with R~80000 and 100000 resolutions, respectively.

In 2004, its RV precision was improved from 3 to 1.5 m s^{-1} thanks to a detector upgrading. HIRES is not in a vacuum enclosure like HARPS, HARPS-N or CARMENES, which coupled to other instrumental issues, cause the RV rms of HIRES to be typically greater than $2\,\mathrm{m\,s^{-1}}$.

- **PFS** (Crane *et al.*, 2006): The Planet Finder Spectrograph (PFS) is installed at the 6.5-m Magellan telescope settled at Las Campanas Observatory, Chile. This is also a high-resolution (R∼76,000) slit-fed échelle spectrometer for which the total 390 - 670 nm range is also restricted to 510 - 620 nm for Doppler measurements, due to the iodine cell system. The main goal of the PFS survey is to detect low mass companions hosted by nearby stars (closer than 50 pc). The single measurement RV precision (SMP) of the PFS is about $1.2\,\mathrm{m\,s^{-1}}$ while the typical rms is $2-4\,\mathrm{m\,s^{-1}}$. The PFS grating is vacuum sealed and the instrument temperature can be actively controlled. It is planned to increase its resolution in 2016 by upgrading the detector and by adding a pupil slicer which will be fed by six optical fibers.

- **APF** (Radovan *et al.*, 2010; Vogt *et al.*, 2014): The relatively small size Automated Planet Finder telescope, which has a 2.4-m aperture and is located at Lick Observatory, California, operates with a spectrograph. An advantage of the APF is that it is fully robotic and thus it can be operated in remote mode. This spectrometer uses a narrow slit that can yield a resolution power up to 150,000. However, the iodine cell limits its RV precision to about $1\,\mathrm{m\,s^{-1}}$ since the Doppler measurements are restricted to a subsection of the original 374 - 950 nm wavelength range. Its main goal is the discovery and characterization of extrasolar planets through high-cadence RVs, and in the future it will provide follow-up support for TESS targets.

2.3 Extracting radial velocities

In the roadmap for detecting an exoplanet (see Fig. 2.10), the next step after observing and getting the spectra[1] is to extract the radial velocities. Several approaches can be

---

[1]HARPS and HARPS-N spectra analyzed in this thesis were extracted and wavelength calibrated with the Data Reduction Software (DRS). The details of this pipeline are out of the scope of this thesis.

Table 2.1:   Doppler instruments summary.

Spectrograph (1)	Slit or fiber (2)	Spectral resolution (3)	Wavelength range [nm] (4)	Wavelength calibrator (5)	SMP [$\mathrm{m\,s^{-1}}$] SNR=200 (6)	First light (7)	N (8)
HARPS	f	115,000	380 - 690	ThAr & FP	0.8	2003	276
HARPS-N	f	115,000	380 - 690	ThAr & FP	0.8	2012	5
CARMENES-V	f	94,600	520 - 960	ThNe & FP	< 1.0	2015	42
HIRES	s	55,000	364 - 797	Iodine[†]	1.5	1996	63
PFS	s	76,000	390 - 670	Iodine[†]	1.2	2010	34
APF	s	150,000	376 - 940	Iodine[†]	1.5/2.0*	2013	15

Note. — This table summarizes some of the main parameters of the Doppler instruments used in this study. Col. 1: Instrument; Col. 2: Light coupling method, fiber or slit; Col. 3: Spectral resolution; Col. 4: Wavelength coverage; Col. 5: Wavelength calibration methods where FP refers to Fabry-Pérot; Col. 6: Single measurement radial velocity precision (SMP) at SNR=200 and for an equivalent pixel bin of $3\,\mathrm{km\,s^{-1}}$ at 550 nm; Col. 7: Starting of operations date. Col. 8: Number of exposures used in this study. [∗] the Lick-Carnegie Planet Search (LCPS) and the California Planet Search (CPS) teams share the APF observing time and give slightly different SMP values. [†] The iodine cell system restricts the range of spectra useful for Doppler analysis to 510 - 620 nm.

used with this aim. Here I describe the widely used cross-correlation method as well as the template matching technique. The first one is the method used by HARPS and HARPS-N Data Reduction Software (DRS). However, the RVs of this thesis were extracted with the TERRA template matching algorithm since it gives better results for M-stars (Anglada-Escudé & Butler, 2012).

2.3.1   Cross-correlation approach

The cross-correlation technique was first described by Fellgett in 1953, but Griffin (1967) was the first one materializing the idea. This technique is based on obtaining a mean-line profile of the spectrum by cross-correlating the star's spectrum with a mask. Later, the RV curve is calculated as the variability of the profile's centroid. Today, the cross-correlation process is done computationally a posteriori, but the first spectrographs actually cross-correlated a masked negative located in the focal surface of the instrument[1]. In any case, the underlying concept is equivalent.

The HARPS and HARPS-N pipeline, the DRS, uses this approach to calculate the

---

[1]This was for example the case of CORAVEL (Baranne *et al.*, 1979), the instrument involved in the discovery of the first brown dwarf (Latham *et al.*, 1989).
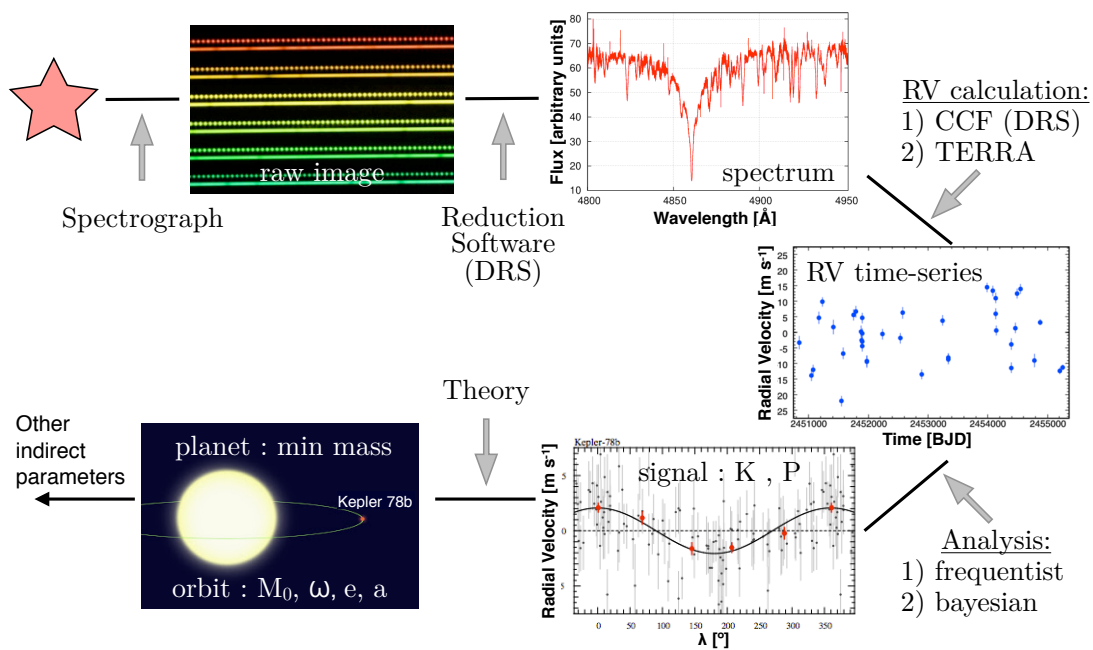
Figure 2.10: Planet detection scheme - Diagram of the main steps involved in an exoplanet detection using RVs: from the observations to the different analysis tools through the extraction of the spectrum and the RV curve. *Sources: Raw image from ESO. RV curve from Meschiari et al. (2011). Kepler-78 b RV curve from Pepe et al. (2013). Artistic impression by David A. Aguilar (CfA).*

RVs. Schematically, it consists in creating an opaque mask with holes at the positions of the spectral lines (i.e. holes of $\lambda_0 \pm \Delta_{\text{width}}$ depending on the observed spectral type, where λ_0 is the rest wavelength of Eq. 2.2). Then, we calculate the total flux that is not blocked by the mask while we continuously shift the mask Δ_{v} steps until we obtain the cross-correlation function (see a diagram in Fig. 2.11).
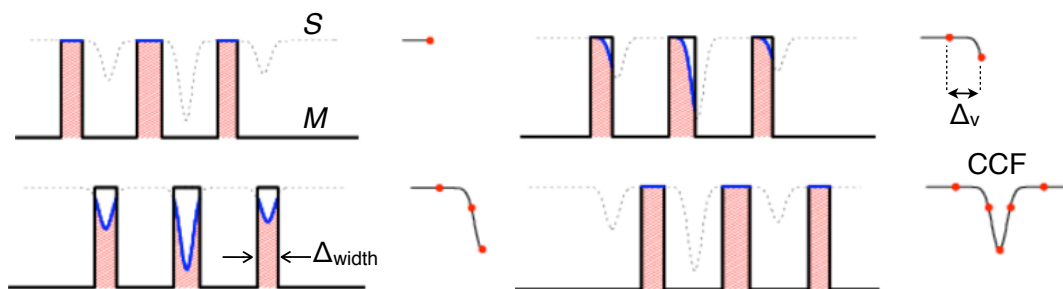
Figure 2.11: Cross-correlation method - Illustration of the construction of the cross-correlation function. *Adapted from Eggenberger & Udry (2010)*

Mathematically, the mask (M) is a binary function defined to be 1 if $\lambda = \lambda_0 \pm \Delta_{\text{width}}$ and zero otherwhise. Therefore, if S is the observed spectrum, the cross-correlation function (CCF) would be:

$$\text{CCF(v)} = S(\lambda) \times M\left[\lambda(1 + \text{v}/c)\right] w \tag{2.22}$$

In practice, each CCF can be calculated by: 1) defining an array of velocities $\text{v} = [-\text{v}_A, \text{v}_A]$ with step Δ_{v}, 2) computing the observed spectra in the range $\lambda_0(1 + \text{v}/c) \pm \Delta_{\text{width}}$ where v refers to the velocity element, and 3) correlating S with M for the different velocity elements for which w will be either 0 or 1.

Then, the RV is obtained as the centroid of a Gaussian function fitted to the CCF profile. The DRS gives a CCF per spectral order. However, the RV of a specific observation is obtained as the average value weighted by the SNR of each individual spectral order. One of the advantages of the cross-correlation approach is that not only the RVs are obtained, but also the whole mean-line profiles are extracted. Planets cause shifts of the spectral lines centroids, but magnetic activity effects such as co-rotating temperature spots cause distortions of the line shape. The CCFs allows to measure other indices such as the line asymmetry (e.g. the bisector span, BIS) of the full-width-at-half-maximum (FWHM) accounting for changes driven by stellar activity.

The good performance of the cross-correlation method relies on the appropriate Δ_{width} and Δ_{v} definition, as well as in creating an accurate mask. The large amount of spectral lines typical of the M dwarfs cause blends between adjacent lines, complicating the continuum determination and the mask definition. Consequently, the CCFs calculated by the DRS using an M-type mask present wing distortions that can complicate the final RV calculation, i.e. a Gaussian function could not resemble the profile any more (see Chapter 4 for more details).

2.3.2 The template matching technique

The RVs obtained in this thesis were extracted using a template matching approach. In particular we used the Template-Enhanced Radial velocity Re-analysis Application (TERRA; Anglada-Escudé & Butler, 2012).

This method is based in building a high-SNR template by combining all of the observed spectra, and in finding later the parameters that minimize the difference between the observed spectrum (f) and the template (T). That is, to minimize R, the residuals at each pixel i defined as:

$$R(\lambda_i) = F\left[\alpha_v\,\lambda\right] - f[\lambda]\sum_{m=0}^{M}\alpha_m\,(\lambda - \lambda_c)^m \tag{2.23}$$

where the parameter α_v is the Doppler shift between the template and the observed spectrum (i.e. the radial velocity, $\alpha_v = 1 - V_r/c$), and α_m are the parameters of the *flux normalization function*: an M-degree polynomial that accounts for time-dependent observational and instrumental effects (e.g. atmospheric differential refractions, differential absorption or telescope tracking errors). Thus, the Doppler shift and the other α_i are obtained for each aperture (i.e. spectral order) from minimizing:

$$\chi^2 = \sum_{i=1}^{N_{\text{pixel}}} \omega_i R^2\,(\lambda_i) \tag{2.24}$$

where ω_i is the pixel weight (i.e. the weight at each λ_i). Since α_v is a non-linear parameter the system is solved iteratively for different $\delta_{\hat{\alpha}}$ increments[1]. The final RV is the weighted mean of the values obtained at each aperture. Additionally, a second and more realistic mean is calculated by including a *zero point correction*. This new

---

[1]We solve the covariance matrix $A_{lk}\,\delta_{\alpha_k} = b_l$, that is equivalent to minimizing χ^2. The initial parameters are $\alpha_v = 1$, $\alpha_0 =< f >$, $\alpha_{1,..,M} = 0$, $\omega_i = \sqrt{f_i}$.

mean accounts for the dispersion at the apertures during the run, while it preserves the common offsets to all apertures that are indicative of real signals (e.g. a planet signal).

This method, while giving similar precision to the cross-correlation method on G- and K-type stars, has demonstrated to work better for M dwarfs. The main disadvantage of the template-matching is that it does not provide a mean-line profile along with the RVs. Thus, in this thesis we obtained the RVs from the template matching algorithm TERRA, whereas we used a least-squares deconvolution (LSD) approach to obtain the mean-line profiles (Donati *et al.*, 1997; Barnes *et al.*, 1998). Then, the classic Gaussian indices (e.g. FWHM/BIS), but also the *moments of the distribution* (m_i; Press, 1992) were calculated for these LSD-profiles.

2.4 Extracting the Keplerian signal

Having obtained the RV-curve, the next step is to search for Keplerian periodic signals embedded in it (see Fig.2.10). Several Bayesian or frequentist methods can be used with this aim. Some time ago, detecting a planet meant finding a model that could explain the RV curve, and to reject that a simpler model (i.e. a model without planet) could explain the data. In case of doubt, more observations were performed. Nowadays, gathering more observations is not sufficient to search for low-mass planets. Their intrinsic low-amplitude RVs require more complex models, as well as statistical assessments of the signal significances through methods using model comparison and global optimization. On the one hand, *global* means that we do not search for signals over the residuals of any model (classic pre-whitening procedures) but all the free parameters of the model are re-adjusted within a new search. On the other hand, *model comparison* means that a model is accepted only if it is statistically preferred compared to an initial (null) hypothesis, e.g. if the difference between the χ^2 of a model with a Keplerian signal and a model without planets exceeds a threshold; generally a false alarm probability (FAP) threshold.

In any case, even when using appropriate analysis techniques, the model incompleteness (i.e. precise models for stellar activity or instrumental effects are unknown) can result in spurious significant signals. Often, the particular characteristics of a planetary signal (e.g. the long-term stability, the constant velocity shift regardless the wavelength range, the lack of line distortions different from centroid shifts, etc) or an

alternative analysis with independent instruments help confirming the Keplerian origin of a signal. In this thesis, we use frequentists procedures to assess the statistical significance of detections (likelihood periodograms; Baluev, 2009) and Bayesian Monte Carlo Markov chain methods to assess the credibility intervals of each parameter (i.e. derive uncertainties for each parameter; Ford, 2005). See below a description of the likelihood periodograms. For a review of Bayesian methods see Tuomi & Jones (2012) and Tuomi *et al.* (2014).

2.4.1 The likelihood periodograms

Assuming an instrument INS and a time reference t_0, we can model the radial velocities as

$$v_{i,\text{INS}} = \gamma_{\text{INS}} + \dot{\gamma}(\Delta t_i) + \mathcal{K}_p(\Delta t_i) + [c_{\text{I,INS}}\, \text{I}_{\text{INS}} + \text{MA}_{i,\text{INS}}] \tag{2.25}$$

where γ_{INS} is the *zero-point velocity*, a *velocity offset* accounting for different RV averages depending on, for example, the wavelength reference of each instrument. The term $\dot{\gamma}(\Delta t_i)$ is a *linear trend* accounting for long-term signals (e.g. magnetic activity cycles of the star, long period planets, etc.). $\mathcal{K}_p(\Delta t_i)$ accounts for a single ($p = 1$) or a superposition ($p > 1$) of *Keplerian signals*. Each *Keplerian signal* depends on five parameters: P, K, M_0, e, w, that are the period, amplitude, mean anomaly with respect to the periastron at t_0, eccentricity, and the argument of the periastron, respectively. Terms between brackets are optional: $c_{\text{I,INS}}\, \text{I}_{\text{INS}}$ accounts for *linear correlations with activity indices* (e.g. FWHM, BIS, chromospheric indices), and $\text{MA}_{i,\text{INS}}$ is the *moving average term* that performs a simple parametrization of possible correlated noise. The *moving average term* can be written as:

$$\text{MA}_{i,\text{INS}} = \phi_{\text{INS}}\, \exp\left\{\frac{t_{i-1} - t_i}{\tau_{\text{INS}}}\right\}\epsilon_{i-1,\text{INS}} \tag{2.26}$$

where $\epsilon_{i-1,\text{INS}}$ correspond to previous measurements residuals, τ_{INS} is the time-scale, and ϕ_{INS} is the correlation coefficient that quantifies the strength of the correlation between i and $i - 1$. ϕ_{INS} is bounded between -1 and 1 to guarantee a stationary process. That means that the MA does not arbitrary grow over time. In fact, the exponential term decreases the correlation strength as the difference between t_i and t_{i-1} increases. Like for the other parameters of the model related to noise, we assume the MA depends of the instrument.

Periodograms are plots which represent a *reference statistic* in the y-axis versus the period in the x-axis (see Fig. 2.12). The *reference statistic* accounts for the improvement of a *model* compared to a null-hypothesis. Classic Lomb-Scargle periodograms (Lomb, 1976; Scargle, 1982) use the F-ratio statistic which is defined by:

$$\text{F-ratio} = \frac{(\chi^2_{null} - \chi^2_p)/(k - k_{null})}{\chi^2_p/(N - k)} \tag{2.27}$$

where N is the number of observations, k is the number of free parameters of the model, and χ^2_{null} and χ^2_p are the chi-square functions of the null hypothesis and a model with p Keplerian signals, respectively. Then, if $m_i \pm \sigma_i$ are the measurements and χ^2_p is:

$$\chi^2_p = \sum_i^N \frac{(m_i - v_{i,\text{INS}})^2}{\sigma_i^2} \tag{2.28}$$

the model parameters are obtained by minimizing $\delta\chi^2_p/\gamma_p$ at each P.
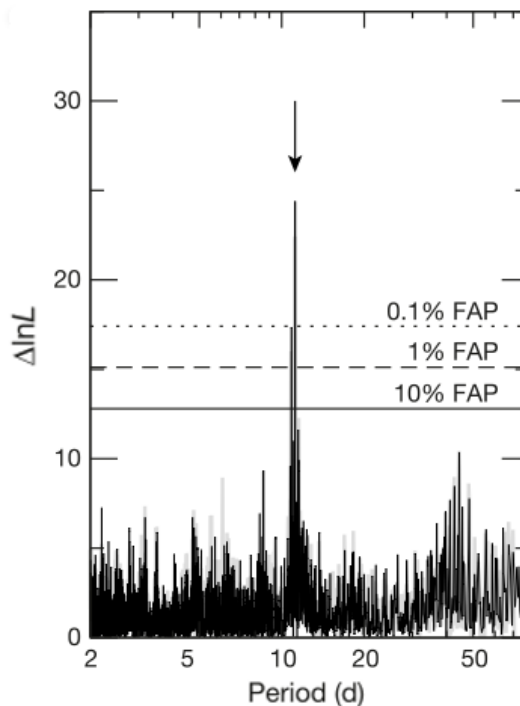
Figure 2.12: A ln-likelihood periodogram - Example of a $\Delta \ln \mathcal{L}$ periodogram (black lines). The grey line corresponds to a Bayesian posterior density. The horizontal lines represent the FAP thresholds of the frequentist analysis. *From Anglada-Escudé et al. (2016a)*

2. RADIAL VELOCITIES: FROM THEORY TO OBSERVATION

Instead, the *reference statistic* of the likelihood periodograms is $\Delta \ln \mathcal{L}$. Assuming Gaussian errors we can write the probability of each measurement with a likelihood function as:

$$l_{i,\mathrm{INS}} = \sqrt{\frac{2\pi}{(\sigma_i^2 + \sigma_{\mathrm{INS}}^2)}} \exp\left[-\frac{1}{2}\frac{(m_{i,\mathrm{INS}} - v_{i,\mathrm{INS}})^2}{(\sigma_i^2 + \sigma_{\mathrm{INS}}^2)}\right] \qquad (2.29)$$

where σ_i accounts for the uncertainty of the i-th measurement and σ_{INS}, the *jitter*, for the excess of white noise not included in σ_i. Thus, the total probability can be obtained as the multiplication of the individual i-th probabilities by:

$$\mathcal{L} = \prod_i l_i \qquad (2.30)$$

whose natural logarithm is:

$$\ln \mathcal{L} = \sum_i \ln l_i = N \ln\left(\sqrt{2\pi}\right) - \langle \ln\left(\sigma_{i,l}\right)\rangle - \frac{\chi^2}{2} \qquad (2.31)$$

Consequently, maximizing the likelihood function is equivalent to minimizing the χ^2 when all the free parameters are included in χ^2. The prescription used here allows to fit the *jitter* (extra-noise term) as a model parameter. As a result, the maximization of the $\ln \mathcal{L}$ is obtained by resolving the system defined by:

$$\frac{\delta \ln \mathcal{L}}{\gamma_p} = 0, \quad \frac{\delta \ln \mathcal{L}}{\sigma_{\mathrm{INS}}} = 0 \qquad (2.32)$$

Therefore, the difference between the best-fitted model and the null model gives $\Delta \ln \mathcal{L}$; the *reference statistic* of the likelihood periodogram:

$$z = \ln \frac{\mathcal{L}_{\mathrm{p}}}{\mathcal{L}_{\mathrm{null}}} = \Delta \ln \mathcal{L} \qquad (2.33)$$

Compared with the classic Lomb-Scargle periodograms, the likelihood periodograms have several advantages. The most important one is that the likelihood is a global statistic in the sense that all parameters are optimized (including noise parameters such as the *jitter*) at the period search level. Contrarily, the classic Lomb-Scargle periodograms fit for a sinusoid to residual data. See a detailed revision of the likelihood periodograms in Baluev (2009).

2.4.2   The false alarm probability

Once we have calculated the periodogram, a criterium is required to assess whether a signal is significant or not, i.e. if a peak could have arisen by a random combination of noise only. The tool commonly used is the false alarm probability (FAP). For example, a periodogram peak at FAP=1% means this peak has 99% probability of not being caused by noise. The FAP criteria are generally indicated with horizontal lines in the periodograms (see Fig. 2.12).

The FAP can be estimated analytically but it requires knowing the total number of independent frequencies M in the range studied. Cumming (2004) indicates that the probability of obtaining a power z greater than the observed z_0 can be obtained as:

$$P(z > z_0) = -\ln\left(\frac{\text{FAP}}{M}\right) \tag{2.34}$$

In practice, M is not known a-priori[1] and the FAP is usually calculated with bootstrap Monte Carlo simulations. This statistical test consists in first calculating the $\ln \mathcal{L}_{obs}$ of our observations and later scrambling the RV data while maintaining the time sampling of the observations and the data errors. Then, we calculate the $\ln \mathcal{L}_{boots}$ and compare it with the value from the observations. If the observed dataset has a real Keplerian signal embedded, we expect the $\ln \mathcal{L}_{obs}$ to be much larger than $\ln \mathcal{L}_{boots}$. The FAP can be defined as the fraction of Monte Carlo tests that yielded $\ln \mathcal{L}_{boots}$ values lower than the original observations (see Cumming (2004) for further details).

---

[1]Each peak at the periodogram corresponds to a independent frequency, so we could obtain an approximate value of M by counting. However, M highly depends of the range of periods that is being analyzed (the higher the frequency under study the larger the number of peaks).

z

Systematic effects in line profiles

<div style="text-align: right;">3</div>

A thorough understanding of the response of your spectrograph and of your analysis techniques is essential in order of take the most out of your science. The "Cool Tiny Beats" survey studies the limits of precision of Doppler spectroscopy in the short period domain of M-type dwarfs. This time-domain has not been extensively explored in the past. As a consequence, the CTB survey constitutes a performance test for the instrument itself. This Chapter details the instrumental systematic noise effects found in the intra-night regime and shows our efforts to explain their origin. Additionally, we check if such effects lead to variability of the spectra or the data-products. Section 3.1 introduces the work, while Sections 3.2 and 4.2 detail the targets characteristics and the observational strategy, respectively. In Sections 3.4 and 3.5, I present the common variability detected among different indices, while later in Section 3.6 I check for correlations between them. Section 3.7 is a test of the performance of our analysis tools. Section 3.8 proposes a correction method and Section 3.9 analyzes the performance of the cross-dispersed direction of the spectrograph. An unveiled Doppler signal is later discussed in

Section 3.10. Finally, in Section 3.11, I present the discussion and conclusions of this Chapter.

3.1 Introduction

Nowadays, $1\,\mathrm{m\,s^{-1}}$ precision is being enough to identify the emerging population of potentially habitable planets around M dwarfs. Nevertheless, there are active discussions on whether this reported long-term precision limit is caused by stellar processes, instrumental effects or both. Whereas certain stars are intrinsically more Doppler variable than this limit, it is unlikely that $0.8 - 1\,\mathrm{m\,s^{-1}}$ (Pepe *et al.*, 2011) is an universal limit for Doppler measurements.

From the analysis of the CTB high-cadence data, it was obvious that some kind of instrumental or reduction-process effect was producing intra-night variability common to several targets[1]. In this study, we alternated observations of the well-suited pair of M dwarfs GJ 725A+B to delve into the sub-night HARPS-N response.

3.2 The targets: GJ 725A+B

Our targets were the bright nearby stars: GJ 725A and GJ 725B[2]. We selected this binary system for being a bright (V=8.91, V=9.69, for A and B respectively, Jenkins *et al.*, 2009; Cutri *et al.*, 2003), nearby (d=3.57 pc, d=3.45 pc, Anderson & Francis, 2012), and a common proper motion pair of almost identical spectral type (M3V and M3.5V, Reid *et al.*, 1995). The targets have no previous reports of intense magnetic activity or planets. At epoch 2000, their projected separation was 13.3 arcseconds, implying a minimum separation of 47.5 AU (Hipparcos, van Leeuwen, 2007).

3.3 Observations and data reduction

We used HARPS-N to observe GJ 725A+B during two high-cadence different runs: one in 2013 and another one in 2014. In August 2013, GJ 725A was the only target of a five-day run with a total of 314 high-cadence data points[3]. In 2014, we observed both GJ 725A and B during four consecutive nights,alternating exposures between the two stars. In total, we obtained 101 spectra for GJ 725A and 116 for B[4]. Exposure times were set to be between 240 and 480 s. The

---

[1]Night-to-night variability is also present in the time-series from both HARPS and HARPS-N. However, these effects are better known because the time-domain has been widely explored. After the first runs, we could identify the main night-to-night effects, which are explained in greater detail in Chapter 4.

[2]Check `http://www.pas.rochester.edu/~emamajek/spt/M3V.txt` and `http://www.pas.rochester.edu/~emamajek/spt/M3.5V.txt` for a thorough review of both stars properties.

[3]We rejected data with SNR<45 and with airmasses above 2.5, the operational limit of the atmospheric corrector (*F. Pepe, private comm.*).

[4]Except for the first night, we halted the alternating sequence between A and B at the meridian passage to better sample this part of the night.

Table 3.1:   **Observational parameters of the HARPS-N 2014 run.**

Nights	Night 1	Night 2	Night 3	Night 4
N_A	27	40	16	18
N_B	27	21	31	37
AM_{max}	1.55	1.64	1.59	1.65
Seeing	0.86	0.87	0.74	0.78
$Seeing_{min}$	0.58	0.60	0.48	0.59
$Seeing_{max}$	2.83	1.47	3.64	1.20
SNR_A	78	54	59	71
SNR_B	63	49	53	59

Note. — Subindices A and B refer to targets GJ 725A and GJ 725B. N indicates the number of exposures. The SNR and seeing values are median measurements of the nights. SNR values correspond to the spectral order 60 (centered at 631 nm). The TNG seeing monitor was out of order, so the shown values are from the nearby Isaac Newton Telescope. The minimum airmass (AM) of all nights was 1.17.

main observational parameters of the 2014 run are shown in Table 3.1.

The spectra were processed and extracted with the standard HARPS-N/TNG Data Reduction Software (DRS) and the RVs were obtained with TERRA (Anglada-Escudé & Butler, 2012). Additionally, in this study we used the FWHM index given by the DRS, i.e. the full-width-at-half-maximum of the Gaussian function fitted to the mean-line profiles (or CCFs) that produce the DRS. See more details about these and other reduction strategies in Chapter 2.

3.4   Systematic effects in the time-series

3.4.1   First evidences in 2013

The 2013 observations, of which GJ 725A was the primary target, showed a clear ~ 1 day Doppler signal present in both the RVs and the FWHM time-series (see Fig. 3.1). However, this signal resulted to be highly correlated with the airmass. We suspected an instrumental origin, but with only one observed star, we could not distinguish systematic effects from astrophysical ones.

3.4.2   The observational experiment of 2014

As a consequence, we designed a second observational run in 2014 to separate astrophysical from instrumental effects: given that GJ 725A+B is a common proper motion pair of almost identical components, obtaining alternating observations of both components is a simple and efficient way to point out common trends. Correlated variability, common to both stars, can
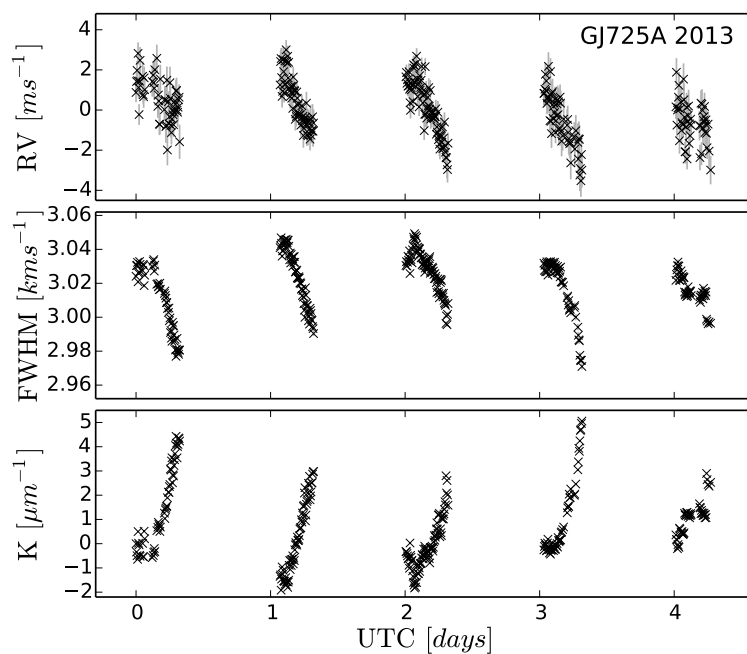
Figure 3.1: Time-series of the 2013 run - RV (top) and FWHM (middle) time-series of GJ 725A during 2013. The bottom panel shows the κ-index (see Sec. 3.5.1). The FWHM and RV vary peak-to-peak tens of $\mathrm{m\,s^{-1}}$ and $\sim 4.5\ \mathrm{m\,s^{-1}}$, respectively.

readily be spotted by direct inspection of the time-series (e.g. see the first night of the run in Fig. 3.2).
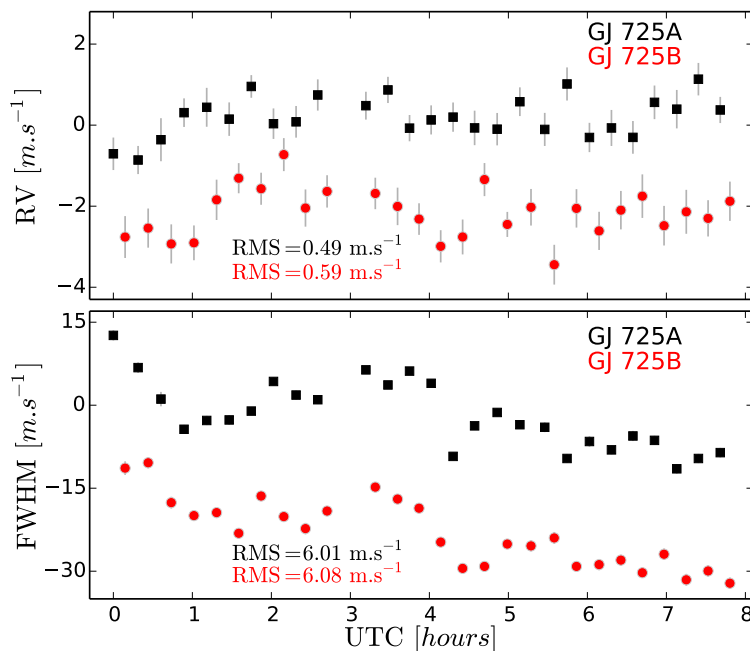
Figure 3.2: Time-series of the first night of the 2014 run - RVs (upper panel) and FWHM (lower panel) time-series for the first HARPS-N night of the 2014 run. For the sake of clarity, we subtracted the FWHM mean velocities (2989.97 and 2975.62 $\mathrm{m\,s^{-1}}$ for GJ 725A and B, respectively), and we shifted the FWHM (-20 $\mathrm{m\,s^{-1}}$) and the RVs (-2.3 $\mathrm{m\,s^{-1}}$) of GJ 725B.

Periodograms of the difference - To isolate real signals arising from either star, we computed periodograms of the time-series of the individual stars, together with periodograms of their difference. Periodograms in Figure 3.3 follow the procedures outlined in Zechmeister & Kürster (2009) [1]. To compute the differential periodograms, we calculated the difference between the GJ 725A and B RVs. With this aim we firstly evaluated B at the A observing epochs, i.e. we linearly interpolated the GJ 725B time-series. The RV and FWHM periodograms of the individual stars showed common peaks (see black and red lines in Fig. 3.3). However, most of these peaks disappear in the differential periodograms (blue lines)[2]. This result suggests

---

[1]We used the F-ratio statistic to find the period of the sinusoid best-fitting the data. We used these periodograms because, while being formally equivalent to the Lomb–Scargle periodograms (Scargle, 1982), they are less susceptible to aliasing and provide more accurate frequencies.

[2]Note a promising signal arising over the 0.1 per cent of the false alarm probability (or FAP, Cumming, 2004) threshold at ~3 d in the RV differential periodogram. This signal may correspond to some real variability of GJ 725B as discussed later in Section 3.10.

common instrumental variability on the data-products of both stars.
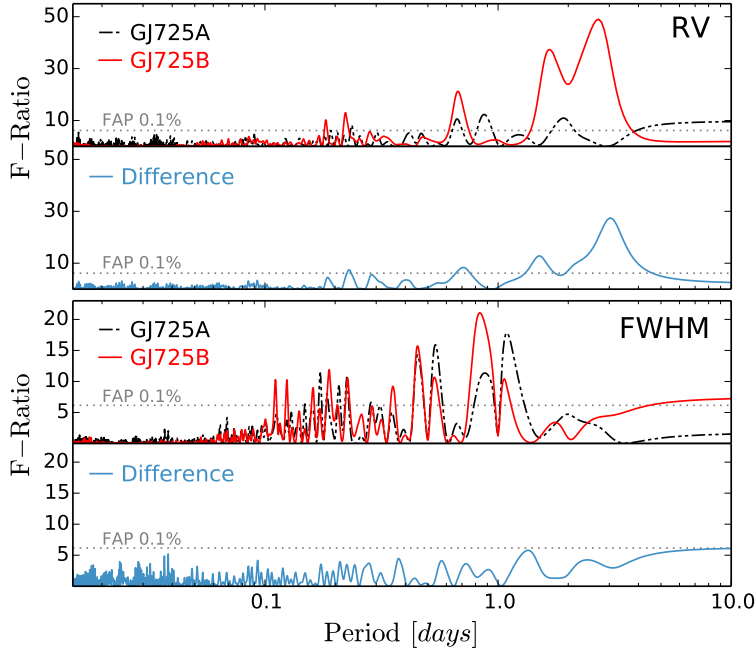
Figure 3.3: - Periodograms for the RV (upper panel) and the FWHM (lower panel) for the GJ 725A (black line) and GJ 725B (red line) data of the 2014 run. The blue line corresponds to the periodogram of the two stars' differential time-series. Common variabilities result in common peaks. These common peaks disappear on the difference periodograms, the remaining ones being real signals from either GJ 725A or GJ 725B.

3.5   An insight into the instrument response

Once the common instrumental variability was confirmed, we concluded that we needed extra indices to delve into the response at different parts of the instrument. With this aim, we studied the stability of both the images of the autoguide camera and the spectral energy distribution (SED). In that way, while the autoguide images give us hints about the illumination stability at the spectrograph input, the SED accounts for the stability of the distribution of the flux across the detector. Several indices were defined to indicate their degree of stability. The detailed calculation of these indices, as well as the main variabilities detected in both the SED and the autoguide images are described below.

3.5.1   Spectral energy distribution *and* the κ-index

In this section we analyzed the variability of the SED. We obtained the distribution of the flux across the spectra by calculating how the total flux at each spectral order varies compared to

a reference one. With this aim we used the spectra as given by the DRS (the so-called e2ds data-products). Firstly, we added the flux of all pixels in each spectral order; and secondly, we normalized these measurements to the total flux at the spectral order 56 (selected for having low telluric contamination). We named it the normalized *pseudo spectral energy distribution* (pSED).

The resulting pSED is shown in the upper panel of Figure 4.6 (for GJ 725A in 2014). Here we see how the pSED pivots around the normalization order (R). Consequently, we see a pSED wavelength and time-dependent. Changes relative to the first co-added spectrum (T) are shown in the lower panel of Figure 4.6. The pSED is expected to vary for a number of environmental effects coupled with the instrument, as for example: i) the *atmospheric dispersion*, which increases with the air density at low altitudes splitting the star image in its blue-red components in the zenithal direction, ii) the *atmospheric extinction*, which is caused by the Rayleigh scattering and by the molecules and dust absorption; or iii) the *seeing*, which also increases at low altitudes, being the blurring more severe for shorter wavelengths[1]. However, this variability has to be corrected at some stage (i.e. at the instrument or by post-processing the spectrum) in order to produce independent data-products. HARPS-N includes an atmospheric dispersion corrector (ADC) to correct for the *atmospheric dispersion*, but it only corrects either the pupil or the telescope image. Regarding the *atmospheric extinction*, we corrected it using the method outlined by Hayes & Latham (1975)[2]. Results indicate the pSED varied less than a 4.5 per cent due to *atmospheric extinction*. Finally, the *seeing* is very difficult to correct due to its random behavior, and often adaptive optics is used with this goal.

The *spectroscopic chromatic index* (κ) - To quantify the impact of changes in the pSED, we defined a spectroscopic chromatic index (κ). This index accounts for the variability of the slope of the pSED/T as a function of wavelength. To calculate κ we only considered a linear region around R. That is, we only account for the pSED/T in a region of ± 8 spectral orders from R (see blue area in Fig. 4.6). Then, κ_i is obtained from:

$$\mathrm{pSED_i}\left(\lambda\right) = \left[1 + \kappa_i\left(\lambda_c - \lambda_{cR}\right)\right]\mathrm{T}(\lambda) \tag{3.1}$$

where i indicates the observations, λ_{cR} is the central wavelength of the reference order 56, λ_c refers to the central wavelength of any other order, $\mathrm{T}(\lambda)$ corresponds to the initial $\mathrm{pSED_{t_0}}(\lambda)$ for each star. Finally, κ_i is a coefficient with units of $1/\lambda$, that we named as the chromatic index (κ). The κ-index accounts for wavelength and time-dependent pSED variability.

---

[1]All these effects worsen the higher the airmass is. The *atmospheric dispersion* dominates below $\sim 50\,\mathrm{deg}$ on nights with good seeing ($\sim$1 arcsecond in the zenith).

[2]See ORM atmospheric extinction values for a dust-free atmosphere at `http://www.ing.iac.es/Astronomy/observing/manuals/ps/tech_notes/tn031.pdf`. To correct from aerosol scattering we used the V-band extinction measurements for the month of July from table 1 of García-Gil *et al.* (2010).
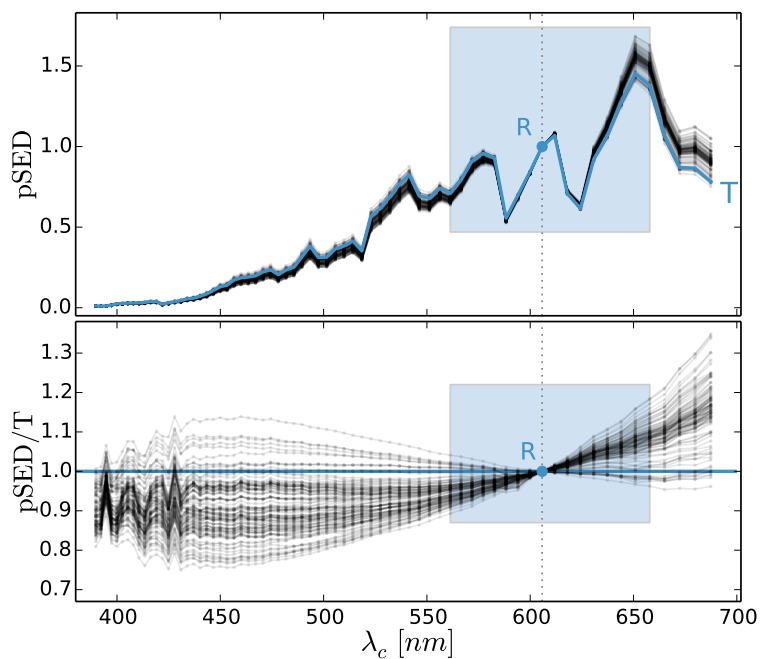
Figure 3.4: Pseudo-spectral energy distribution - (Upper panel) Sum of the flux of the 69 spectral orders of GJ 725A plotted versus wavelength (pSED). λ_c is the central wavelength of each spectral order. R is the normalization point (order 56). The blue line (T) is the initial pSED of the run. (Bottom panel) pSED relative to T. The index κ measures the relative changes in the slope of the pSED. It is calculated within the blue area where we assume a linear behaviour of the pSED slope variability. Fluxes were corrected from atmospheric extinction.

3.5.2   The autoguide camera images *and* the Φ, and Θ indices

The images obtained by the autoguide camera were additional products that were used for trying to find an explanation for the systematic effects. In HARPS-N, the star light that is not injected into the fiber is reflected towards the autoguide camera. To do this, the fiber head is fitted in the central hole of a slightly tilted flat mirror. Therefore, the images recorded by this camera show the shape of the star at the fiber entrance. Two kind of images are stored, the acquisition images, taken with the star off-fiber before the science exposure, and the autoguide images, which are the average of the short images (~ 100 ms) taken during the science exposure to guide the telescope.

It must be realized that, in an equatorial telescope (or in a de-rotated field of view in an altazimuthal telescope), the direction of the dispersion of the atmosphere changes during the night (following the zenithal direction), whereas in a non-de-rotated field of view (the case of HARPS-N) the zenithal direction remains constant while the field rotates (see Fig. 3.5).

It is important to note that, as a result of the flat mirror tilt, a stable distortion of the images was expected, i.e. we expected the images to be elongated in the same proportion and direction as the measured ones for the circular hole of the mirror (see the shape of the central hole in Fig. 3.6). However, the autoguide images presented a variable elliptical elongated shape of the star that did not fit the distortion of the mirror hole and did not rotate with the field (within a maximum error of $4°$), keeping always aligned with the zenithal direction. This result, together with the correlation of the elongation with the airmass (see three autoguide images taken at the beginning, middle and end of one night, with airmasses 1.30, 1.17, and 1.33 respectively, in Fig. 3.6), led us to hypothesize that the elongated shape was produced due to an insufficient correction of the atmospheric chromatic dispersion by the ADC. To validate our hypothesis, we fitted an ellipse to the autoguide images[1], and we checked that the elongation was compatible with the zenithal axis. In particular, we measured maximum differences of only $7.8° \pm 6.2°$ between p_r (the real parallactic angle), and p_h (its analogous in case the semimajor axis of the ellipse fitted to the image and the zenithal direction were coincident)[2]. Consequently, if this is so, the resulting image is consistent with a superposition of wavelength dispersed images of the star caused by the atmosphere.

The *semimajor axis module* (Φ) and the *circularity index* (Θ) -   In order to account for the distortions of the autoguide images we decided to monitor the module of the semimajor axis resulting from fitting an ellipse to the autoguide images, that is, the *semimajor axis module index* (Φ). Moreover, we defined the *circularity index* (Θ) as the seeing difference, in arcseconds, between the x- and y-axis, obtained from the autoguide image headers.

---

[1]Only the outermost pixels with fluxes within ± 1 per cent of the half value between the maximum and the background were considered.

[2]After accounting for the field rotation and the fix angle of the derotator, we measured a good agreement of p_h –the angle subtended by the north axis N, and the ellipse semimajor axis Z'– with p_r, the real parallactic angle (or angle subtended by the north-zenith axis).
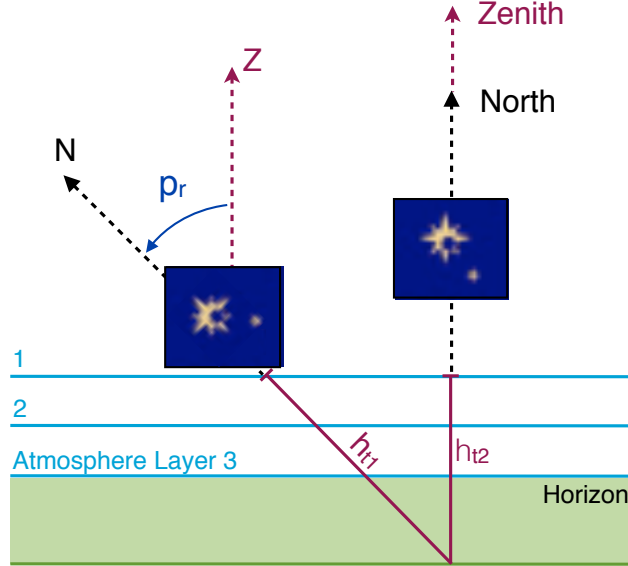
Figure 3.5: FOV orientation in a non-de-rotated altazimuthal telescope - During the night, the field rotates following the celestial north axis direction (N), while the zenithal axis (Z) remains perpendicular to the atmosphere and does not rotate with the field. The atmosphere chromatically disperses the light more efficiently when the atmospheric layers are thicker (e.g. for h_{t_1} compared with h_{t_2}). p_r refers to the parallactic angle, the angle subtended by Z and N.
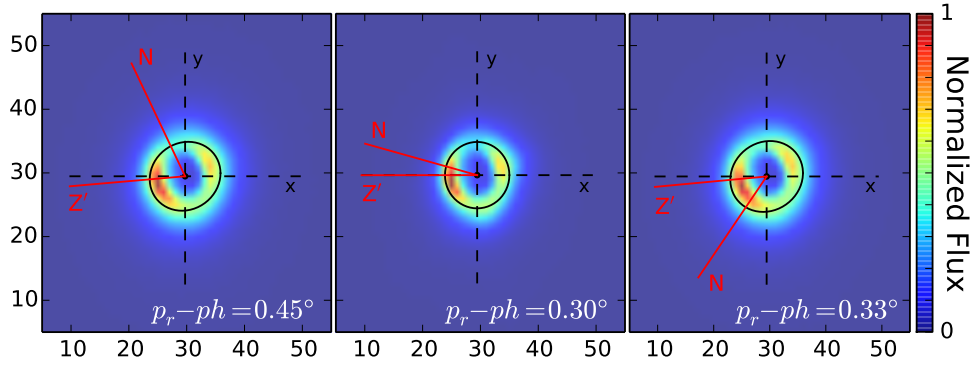
Figure 3.6: Autoguide camera images - Images of GJ 725A taken at the beginning (left), close to the meridian crossing (middle), and at the end (right) of the first night of the 2014 run. The central hole corresponds to the science fiber position. It seems to be elliptical due the slight tilt of the flat mirror that carries the light to the camera. However, while the central hole has the same shape, the image elliptical distortion (solid black ellipses) varies with the atmospheric dispersion axis (Z), that is, with the airmass.

3.5.3 Time-dependences of pSED and autoguide images

The time-series of the new pSED and autoguide images indices revealed, as for the case of the RVs and FWHM (see Fig. 3.2), a common behavior between both stars in the alternating run (see Fig. 3.7). Despite GJ 725A was the only target in 2013 run, we can see in Figure 3.1 how the time-series of κ share the same night trends that those of the RV and FWHM. Unfortunately, most of the acquisition and some of the guiding images from 2013 were lost due to an error in the acquisition software[1] (later solved in March 2014). As a result, we could not obtain consistent measurements on the 2013 autoguide images.
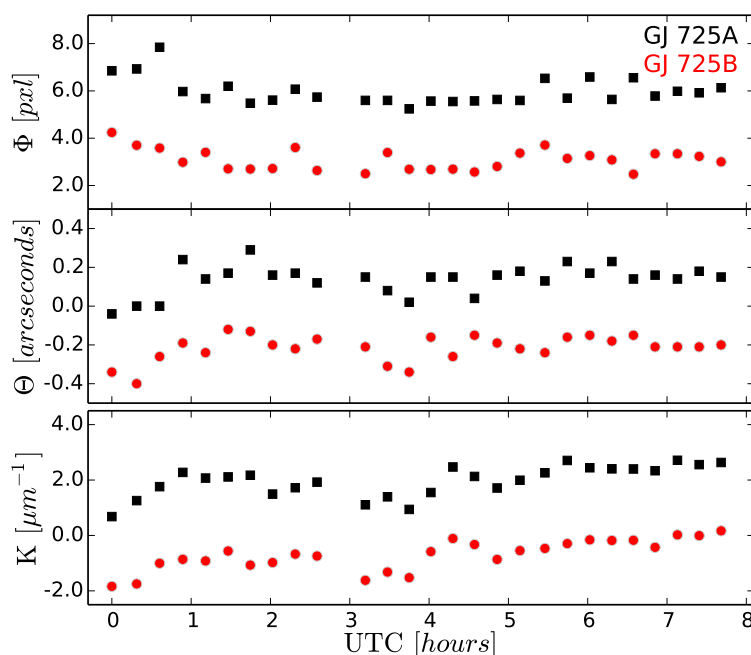
Figure 3.7: Time-series of Φ, Θ, and κ - The first night of the 2014 run is shown here. For the sake of clarity, we displaced GJ 725B -3 pixels for Φ, -0.35 arcseconds for Θ, and -2.5 $\mu\mathrm{m}^{-1}$ for κ.

3.6 Correlated variability between indices

In this section I analyze the correlation between all the above indices, summarized in Table 3.2. In particular, to check if two indices are correlated, we used the following procedure. Given two indices x_i and y_i, we modeled the existence of correlations by fitting a linear relation between them: $y_i = a + bx_i$, where a and b are the free parameters. Assuming that the null model containing no correlation is $b = 0$ and $a = \bar{y}$, our significance assessment consists in obtaining

---

[1] Instrument upgrades can be consulted in `http://www.tng.iac.es/instruments/harps/`.

3. SYSTEMATIC EFFECTS IN LINE PROFILES

Table 3.2: Summary of used measurements

Index	Name	Definition/Source
RV	radial velocity	Extracted with TERRA
FWHM	full-width-at-half-maximum	Given by the DRS pipeline
κ	Spectroscopic Chromatic Index	Quantifies the changes in the slope of the pSED
Φ	Semimajor axis module	Module of the semimajor axis of the ellipse fitted to the AI*
Θ	Circularity index	From AI headers, seeing difference between the x- and y-axis.

Note. — For the sake of clarity, we summarize here the measurements that will be use in this study. [∗] AI stands for autoguide images.

the improvement in the χ^2 statistic as

$$\Delta\chi^2 = \sum_i \left(\frac{y_i - (a + b x_i)}{\sigma_{yi}} \right)^2 - \sum_i \left(\frac{y_i - \bar{y}_i}{\sigma_{y_i}} \right)^2 \qquad (3.2)$$

Then we can determine whether such an improvement could be caused by a fortunate arrangement in the noise. Instead of using analytic expressions for the expected distribution of $\Delta\chi^2$ in the presence of noise, we obtained its empirical distribution using a Monte Carlo approach. For each correlation under investigation, we generated a large number of synthetic datasets by randomly swapping the y_i values while keeping the same x_i. The false alarm probability (or FAP) is empirically defined here as the number of these random experiments which give a $\Delta\chi^2$ larger than the one obtained from the real data divided by the total number of experiments. We performed enough experiments (in all cases $10^3 - 10^4$ depending on the obtained FAP) to ensure that the FAP estimates were accurate enough (see more details about the FAP in Chapter 2).

The correlation analysis for the 2014 measurements (which include both stars) are shown in Figures 3.8 and 3.9. The two squares in the top right corners of the individual plots indicate the FAP (ticked green squares mean FAP < 1%, dotted orange mean 1% ≤ FAP < 10%, and crossed red mean FAP ≥ 10%) for GJ 725A (black squares data) and GJ 725B (red dots data). We excluded five Φ outliers (three for having a dispersion above 4.5, the measured standard deviation of the sample, and two produced by sudden seeing increases and corresponding SNR in the spectra below 40).
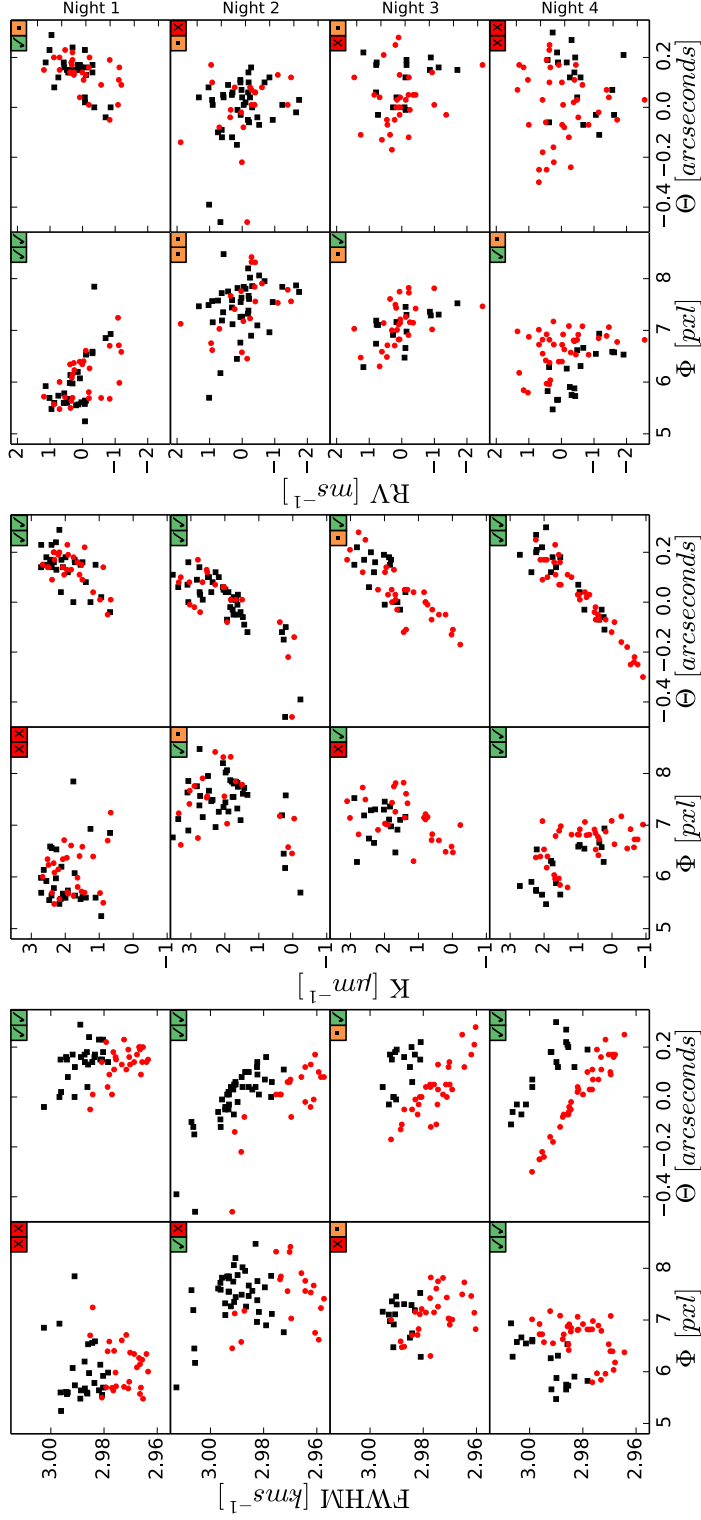
Figure 3.8: Correlations between indices - The spectroscopic indices FWHM (left panel), κ (central panel), and RV (right panel) versus the image indices, Φ and Θ. Each row matches one night. Black squares correspond to GJ 725A and red dots to GJ 725B. Two squares in the top right corners of each plot indicate the FAP for GJ 725A and B, respectively from the left: ticked green squares means FAP < 1%, dotted orange $1\% \leq$ FAP < 10% and crossed red FAP $\geq$ 10%. Main correlations are: FWHM-Θ, κ-Θ and RV-Φ. GJ 725B RVs are residuals to the Doppler signal discussed in Sec. 3.10.

The strongest correlations correspond to the FWHM and the spectroscopic κ-index (see Fig. 3.9, first column). The correlation is so strong that all nights tested resulted in compatible fitted parameters for both stars. This dependence, together with the correlation of κ with the image index Θ (see Fig. 3.8, first panel), seems to indicate that the issues at the fiber coupling are propagating all the way down to the science spectrum and affecting its SED and its mean-line profile. In other words, the instrumental profile of the spectrograph seems to vary with wavelength and time. It is important to note that variable seeing necessarily increases the autoguide image radius momentarily, but it will increase proportionally in both the x- and y-axis. As a result, Θ will remain a good measurement of the asymmetry in the fiber injection.

We also measured a less strong correlation between the RVs and the image index Φ (Fig. 3.8, third panel). We used the GJ 725B RVs after subtracting the Doppler signal discussed in Section 3.10. The correlation is not as strong as that of the FWHM with κ, however both stars have the same qualitative behavior. The FAP of all observed nights remains below the 10 per cent threshold.
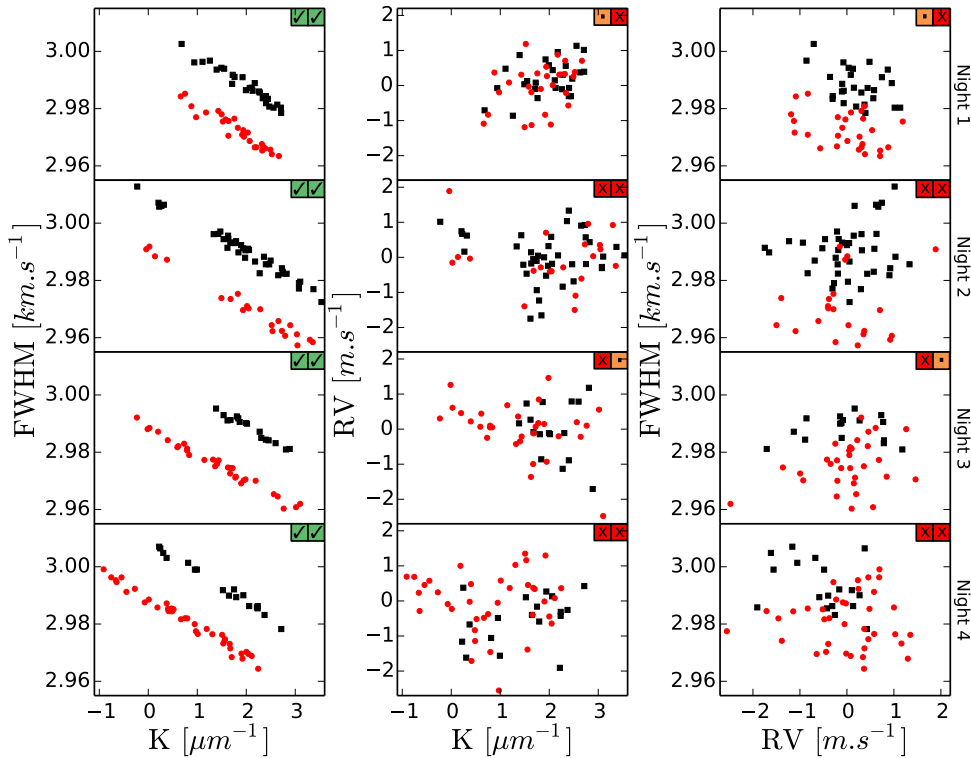
Figure 3.9: Correlations between spectroscopic indices - FWHM $- \kappa$ (left panel), RV $- \kappa$ (central panel), and FWHM $-$ RV (right panel). Markers and top right corner squares are coded as in Figure 3.8. Among these indices FWHM-κ was the only correlation detected.

3.6.1 The 2013 single star run on GJ 725A

As for the 2014 alternating run, the analysis shows that the κ-index clearly correlates with the FWHM (see Fig. 3.10). During this run we covered a wider range of airmasses (up to 2.5 in airmass) compared with the 2014 alternating run (which covered up to 1.6 in airmass). This might have been the cause of the larger span of κ values measured in 2013, but a punctual under-correction of the ADC can not be ruled out. The slope of the correlation law is equivalent to the value measured on the differential run. The offset could be due to a focus realignment carried out in between the two runs (during the technical run of March 2014[1]). Unfortunately, we had to discard the autoguide images indices in the analysis of this run (see Sec. 3.5.3).
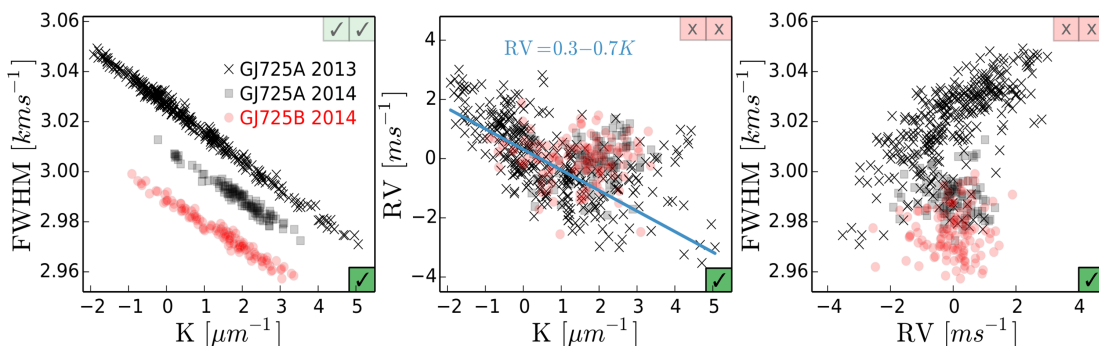
Figure 3.10: Correlation between spectral indices in both runs - Black crosses correspond to GJ 725A data taken in 2013. The 2014 alternating run is shown for comparison (black squares and red dots). The FAP is coded as in Figure 3.8, but here the squares at the bottom right corners refer to 2013. The blue line and equation correspond to a tentative correction (see Sec. 3.8). The similarity between the slope in 2013 and 2014 (particularly evident in the first panel) points to a common origin.

The wider range of variability in κ seems to better support the existence of a relation between this index and the RVs as well (see Fig. 3.10, central plot). The variability in both the FWHM and the RV suggests that the mean-line profile was changing during the night. However, we could not rule out a problem in the measurements themselves (i.e. in the algorithms) producing spurious variability in the time-series. To address this, we performed a number of tests and applied profile measurements independent from the DRS in the next section.

3.7 Independent measurements and validation experiments

Systematic variability in the measurements can be caused by *intrinsic* changes in the line profile (i.e. instrumental), by sub-optimal procedures in the measurement of these quantities (i.e. algorithmic), or both. For example, even if the line-profile is perfectly stable, inaccuracies in the fitting of the flux or background subtraction will produce apparent variability of measurements of the line shape. In particular, the cross-correlation profiles are obtained by computing some

weighted mean of the profiles of the individual spectral orders (see Chapter 2).

Because the effective line profile of each individual order is different, changes in the weights (e.g. if the weights are computed using Poisson statistics from the photon counts) will produce spurious variability correlated with these changes. In other words, a different SED implies a different local SNR for each order. On the other hand, an inaccurate continuum or background subtraction will cause different mean-line profiles at each spectral order. As a result, we can obtain a modified final mean-line profile when we combine a variable weight distribution with different profiles at each order. Furthermore, the RV and FWHM values obtained from the final profile will be also different with the SED. Thus, if our methods do not perform a good continuum or background subtraction, we may be measuring spurious RV or FWHM variabilities even when the instrument is stable.

A similar effect was earlier reported by Bourrier & Hébrard (2014) on 55 Cancri. Following their findings, the DRS flux-normalizes the continuum of all the spectra with respect to a reference spectrum for F, G and K stars. However this has not been yet implemented for M dwarfs, because, as it was defined, some zero division problems may occur in the bluer part of the spectra (*F. Pepe, private comm.*). In order to validate if the algorithms we used could be the cause of the observed variability in the measurements, we have performed the two experiments detailed below.

3.7.1   Experiment 1 : RV measurement against pSED variability

TERRA simultaneously fits the Doppler shift (α_v) and the shape of the continuum (α_m) at each order m (see a detailed description in Chapter 2). As a consequence, the α_m parameters are also modeling instrumental flux variations effects such as the atmospheric differential refraction or tracking errors. In order to validate if this simultaneous continuum fitting technique prevents the RVs from being affected by chromatic correlations, we performed the experiment detailed below.

We selected three epochs, one for each star and run, and we changed the flux of their spectra as:

$$f_{\mathrm{new}}(\lambda, t) = f_{\mathrm{orig}}[\lambda, t] \cdot [1 + S(t) * (\lambda - \lambda_{\mathrm{cR}})], \tag{3.3}$$

where $S(t)$ randomly takes values in the 0 to 2.086 $\mu\mathrm{m}^{-1}$ range[1]. We repeated this calculation several times, and, in total, we obtained 100 new synthetic spectra for each of the three selected epochs. Afterwards, we post-processed these synthetic spectra with TERRA, recovering in all cases a RV with and RMS below $2 \times 10^{-6}\,\mathrm{m\,s^{-1}}$ for the three epochs (see right panel in Fig. 3.11).

This result indicates that the RVs measured with this template matching algorithm are mostly insensitive to changes in the SED. TERRA is properly fitting the flux of the spectra. Therefore, our intentionally introduced wavelength distortions cannot be the cause of the ob-

---

[1]This range was selected to ensure positive new fluxes at least for the last 31 orders that were used in the second experiment (detailed in Section 3.7.2), and to result in flux distortions below 20%, as this is approximately the SED distortion measured in the linear range used to calculate κ (see Fig. 4.6).
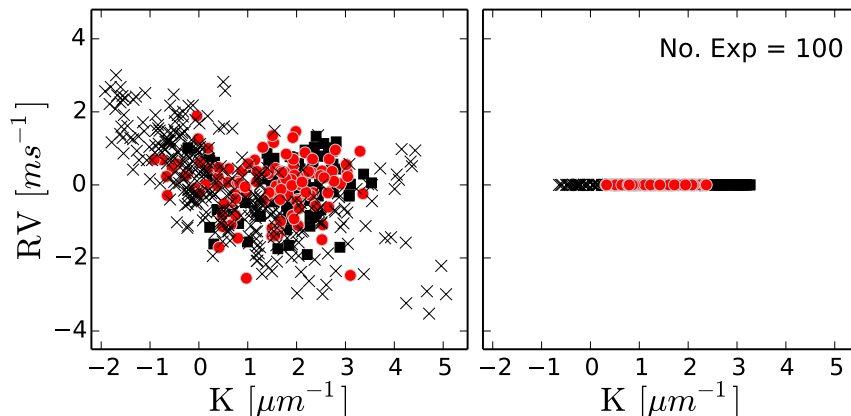
Figure 3.11: Testing the RV-κ correlation - RV versus κ when the input corresponds to the real observations (left plot) or to a set of 100 flux-distorted spectra calculated from an observed epoch (right plot). TERRA measures relatives values and centers the RV at $0\,\mathrm{m\,s^{-1}}$. The zero-values (RMS below $2 \times 10^{-6}\,\mathrm{m\,s^{-1}}$) on the right plot indicate that the normalization carried out by TERRA ensures RVs independent on the flux distortions deliberately included to perform this experiment.

served RVs variability in general; neither of the RV$-\kappa$ correlation in particular (see left panel in Fig. 3.11).

3.7.2 Experiment 2 : line profile width against pSED variability

TERRA provides an independent measurement of the RV, but we do not have any equivalent for the FWHM. With the aim of checking if the strongest FWHM$-\kappa$ correlation could be due to a software issue related with the weighting of the orders (see detailed explanation at the beginning of this section), we estimated the profiles using an independent least-squares deconvolution technique (LSD; Donati *et al.*, 1997). In particular, we used the implementation given by Barnes *et al.* (1998, 2012).

The least square routine involves solving the mean-line profile which, when optimally convolved with a line list, gives the best match to the observed spectrum. Generally, the line list used is just a theoretical identification of wavelengths and depths. Instead, we used the high SNR template computed by TERRA to obtain a more realistic empirically determined list of lines. This template is built by co-adding all the observed 2-dimensional spectra given by the DRS (the so-called e2ds). Those regions of the spectrum with strong telluric absorption or strong stellar molecular bands were not used for the deconvolution.

Like the DRS, the LSD discards some wavelengths in the blue part of the spectra[1]. However, in contrast to the DRS, the LSD does not calculate one profile per order. The deconvolution

---

[1]Only those corresponding to the last 31 orders were used, while the DRS uses the reddest 51 orders.

is performed on each spectrum using all lines (including those repeated in adjacent orders) to obtain one single LSD profile per exposure. Our LSD method normalizes each spectrum to a template to obtain an individual continuum. That is, each spectrum in turn is divided by the template spectrum and a cubic order polynomial is fitted to the residuals. Later, the continuum of each spectrum is obtained by multiplying this cubic polynomial fit by the template continuum, which was previously obtained by iteratively fitting a 5th degree polynomial to the template. Because each spectrum is normalized to an individual continuum, we did not expect variability related with weighting problems arising from the algorithm or background issues (see beginning of this Section).

The output of the LSD technique is a mean-line profile in absorption. These $F_i(t)$ profiles can be inverted (sign changed) after having subtracted their residual continuum $w(t)$, producing a normalized (positively defined) probability distribution function $f(t)$. Then, the moments of $f(t)$ can then be computed as:

$$f_i(t) = w(t) - F_i(t) \tag{3.4}$$

$$m_0(t) = \sum_{i=1}^{N} f_i(t) \tag{3.5}$$

$$m_{n \geq 1}(t) = \frac{\sum_{i=1}^{N} [f_i(t)] \cdot v^n}{\hat{m}_0(t)} \tag{3.6}$$

Before calculating the moments with Eq. 3.6, we truncated the profiles in a range of $\pm\, 20\,\mathrm{kms}^{-1}$ around the estimated zero-velocity (the velocity of the co-added barycentric corrected high SNR template from which we obtained the line list applied during the deconvolution process), and we excluded the negative values resulting after the continuum inversion. This truncation was done to avoid including wing distortions in the moment calculation. The profiles were calculated with a mean velocity increment of $0.81\,\mathrm{kms}^{-1}$ –value that corresponds to the pixel size of the HARPS-N detector– and later interpolated by a factor 10 using a spline function. The order zero moment, m_0, corresponds to the integral of the normalized profile. m_1 is equivalent to its centroid (all spectra are aligned to zero-velocity before computation of the LSD profile), and m_2 corresponds to the profile variance and can be related with FWHM, (i.e. with a measurement of the line profile width).

With the aim of testing the LSD performance, we calculated the LSD profiles of the flux modified spectra that we used in the previous section to test the TERRA software; i.e. we took the same three spectra (one for each star and run) and we modified their flux following the Eq. 3.3. In this case, the second order moment (or m_2) calculated from these contaminated profiles, correlated with κ in an analogous way to the observations (see Fig. 3.12). This implies that, even with our method, that fits the continuum of each spectrum individually, we find a strong correlation of the measurement of the line width (through m_2) with the artificially introduced slope of the pSED. In other words, the changes in the distribution of the flux along the CCD can drive the FWHM variability. Then, the largest correlation involving the FWHM$-\kappa$ relation can be explained as an inaccurate computation of the profile by the algorithms. Neither the DRS nor the LSD method produce accurate enough measurements. Actually, the fact that

we need to correct a residual continuum $w(t)$ for each deconvolution profile may arise from a non perfect description of the continuum.
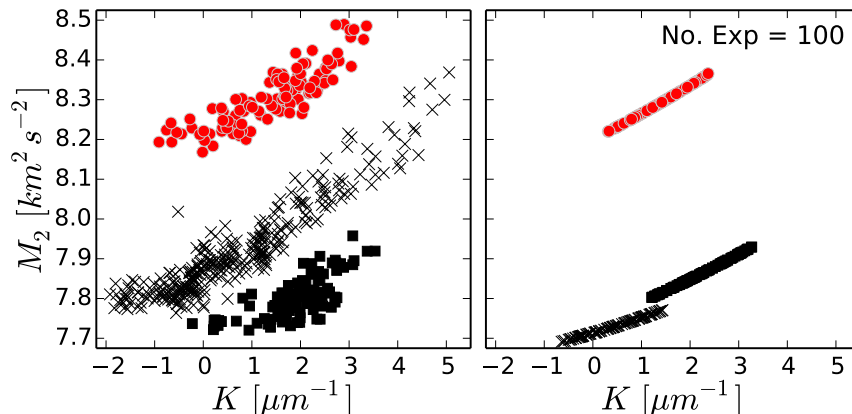
Figure 3.12: Testing the correlation of the line-profile shape with κ - Plot of the moment of second order (m_2) of the LSD profiles versus the κ-index. The trend for the synthetic data (right plot) reproduces the observational trend (left plot) indicating a software issue.

According to our experiment, only the RV measurements obtained by the TERRA algorithm seem to be insensitive to the SED variability. This result indicates that new algorithms that simultaneously fit the continuum of each echelle order and the line profile need to be developed, or the current methods refined to account for this.

To use the FWHM index produced with the M-dwarf mask of HARPS-N, one should -at the very least- apply some decorrelation procedure. Otherwise, this index is only tracing small changes in the measured SED produced by the expected flux loses in fiber-fed spectrographs.

3.8 Detrending strategies

Once we clarified that the strongest FWHM-κ correlation has an algorithmic origin, we aimed at defining an empirical function to detrend the FWHM time-series from chromatic effects. The function should be valid for (at least) the GJ 725A+B pair and other stars with similar spectral types (note that the chromatic nature of the effect will likely affect different spectral types differently). We made use of both 2013 and 2014 data to compute the detrending law.

The FWHM contains additional contributions from other effects. In particular, since the observations span over a finite amount of time, the FWHM will be broadened by the change in the barycentric velocity of the observer. The following procedure was designed to remove the effect of this barycentric broadening (which can account for several $\mathrm{m\,s^{-1}}$ depending on integration time and coordinates of the star).

The central moments of a distribution can be denoted as $m_k = <(x_i - \bar{x})^k>$. Thus, m_2

= Var(x), the variance of the distribution which, for two independent distributions, satisfies the additive property: Var(x + y) = Var(x) + Var(x) (Press, 1992). The mean-line profiles of the spectral orders can be considered as a probability density function. In consequence, the FWHM should also be a variance.

The observed $\text{FWHM}^2_{\text{obs}}$ is the sum of three terms:

$$\text{FWHM}^2_{\text{obs}} = \text{FWHM}^2_{\text{real}} + \text{B}^2 + \text{I}^2 \tag{3.7}$$

where $\text{FWHM}_{\text{real}}$ is the true line profile we want to measure, and B and I are:

- The barycentric correction (B): It is a squared velocity value we have to subtract to the square of the observed FWHM to correct it from the movement of Earth in its orbit. Firstly, let us assume that the velocity v of the observer changes between the initial instant t_i, and the end-of-integration time, t_f, by dV. The effect of the barycentric broadening is then a convolution of the stellar profile with the double of the variance of a boxcar distribution ($F(v)$) of width dV:

$$\text{B}^2 = 2 \int_{-\infty}^{\infty} F(v) v^2 dv = 2 \frac{\text{dV}^2}{12} \tag{3.8}$$

where, C being a constant, $F(v)$ is the boxcar function $f(v)$ normalized to have unit area as follows:

$$F(v) = \frac{1}{\text{C dV}} f(v) \tag{3.9}$$

$$f(v) = \begin{cases} \text{C} & \text{if } \frac{-\text{dV}}{2} < \text{v} < \frac{\text{dV}}{2} \\ 0 & \text{if v} < \frac{-\text{dV}}{2} \text{ or v} > \frac{\text{dV}}{2} \end{cases} \tag{3.10}$$

This correction can be exactly computed using the observation, the exposure time, and a custom made code used to compute the barycentric correction (implemented within the TERRA software).

- Chromatic effect correction (I): This term contains the correlation with the chromatic κ index as computed in previous sections. We searched for the linear model which best-fitted the observed FWHM corrected from barycentric term (FWHM_{B}), and the κ-index series:

$$\text{FWHM}^2_{\text{B}} = \text{FWHM}^2_{\text{obs}} - \text{B}^2 = \alpha + \beta\,\text{K} \tag{3.11}$$

where α, the offset, is a nuisance parameter, equal to $(90.53 \pm 0.02) \times 10^5\,\text{m}^2\text{s}^{-2}$ for GJ 725A, $(89.34 \pm 0.01) \times 10^5\,\text{m}^2\text{s}^{-2}$ for GJ 725B, and $(91.620 \pm 0.004) \times 10^5\,\text{m}^2\text{s}^{-2}$ for GJ 725A observed in the 2013.

Thus, we defined the chromatic correction term as

$$\text{I}^2 = \beta\,K \tag{3.12}$$

where $\beta = (-0.620 \pm 0.003) \times 10^5\,\text{m}^2\text{s}^{-2}\mu\text{m}$ is the average of the values obtained for the three data sets independently. The low degree of scatter in the values (coefficient of

variation lower than 10 per cent) means that the average is representative and thus, we can define a common law which is the same for both stars and all observed nights (see Fig. 3.13, left panel).

Finally, the FWHM corrected from barycentric and chromatic effects can be written as

$$\text{FWHM}^2_{\text{real}} = \text{FWHM}^2 - 2\,\frac{dV^2}{12} - \beta\,K \tag{3.13}$$

and its error, obtained by applying simple error propagation functions by

$$\sigma_{\text{FWHM}^2_{\text{real}}} = \sqrt{4\,\text{FWHM}^2\,\sigma^2_{\text{FWHM}} + K^2\sigma^2_\beta} \tag{3.14}$$

Results are shown in Figure 3.13. The same slope for 2013 and 2014 data was expected as it is caused by the same instrumental effect. However, results indicated some systematic residual effects, specially in the 2013 data. This extra variability might be related to some lesser degree contributions specific to each run. However, as the main correlation may have the same origin, we still prefer to apply the same empirical law to detrend all the datasets. We also expected the zero-point offset (α) of the two runs to be the same for GJ 725A, but the change could be due to an instrument focus readjustment carried out between the two observational campaigns. In spite of these discrepancies, the improvement is obvious: the RMS is reduced a factor of 5: from 7.73 to 1.66 m s^{-1} for GJ 725A, from 9.52 down to 1.85 m s^{-1} for GJ 725B; and an 87 per cent for the 2013 run in GJ 725A, from 16.71 down to 2.15 m s^{-1}. I would like to point out that the RMS reduction comes from the presence of highly structured noise, which makes the new time-series of the FWHM a much more reliable tracer of the physics occurring in the photosphere of the star.

On the other hand, the intranight systematic effects in the RVs can be also modeled with a linear function. Bourrier & Hébrard (2014) detected a similar RV correlation for the 55 Cnc high-cadence data observed with HARPS-N. They used the SNR ratio of two orders as the detrending quantity, which is a simpler version of our chromatic κ-index. As discussed before, we did not find any significant correlation for the 2014 run. Therefore, we have only detrended the 2013 data, following:

$$\text{RV}_{\text{C}} = \text{RV} - \omega\,K \tag{3.15}$$

where $\omega = -0.7 \pm 0.2$ m s$^{-1}\mu$m^{-1}. This value of ω is obtained by fitting the linear correlation law to each night independently to avoid contamination by additional, longer term variability (e.g. planets or induced activity happening at time-scales of a few days) Finally, the fitting parameters (see equation in the central panel of Fig. 3.9) are the weighted mean of the i-th values.
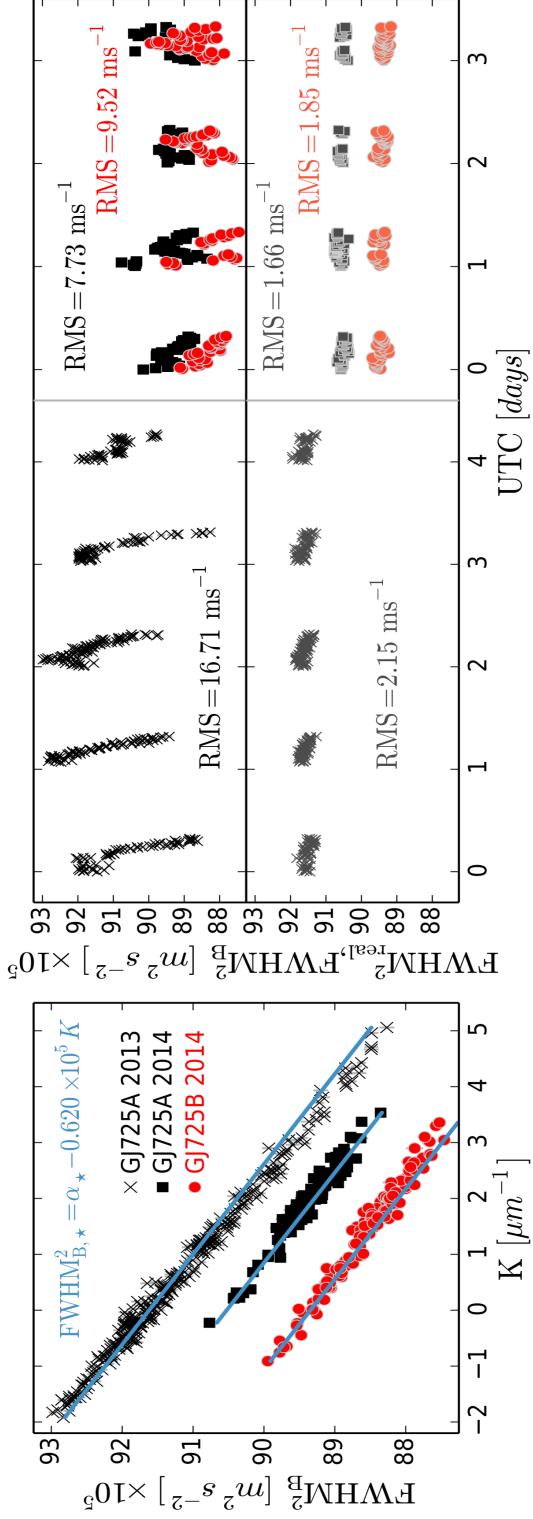
Figure 3.13: Correction of the FWHM - (Left panel) FWHM (barycentric corrected) and κ-index correlation. Blue lines and equation correspond to the best-fitting function. The chromatic correction consists in detrending the data by subtracting the slope term. Note that this empirical law is the same for all runs and both stars. (Right panel) Time-series before (top panel) and after (bottom panel) the chromatic correction. The RMS is reduced by a factor of 8 in 2013 and by a factor of 5 in 2014.

The detrended RVs, shown in the bottom panel of Figure 3.14, have a mean peak-to-peak difference of 3.3 m s^{-1}. The RMS is reduced from 1.29 down to 1.00 m s^{-1}, which is close to the photon noise of the HARPS-N observations.
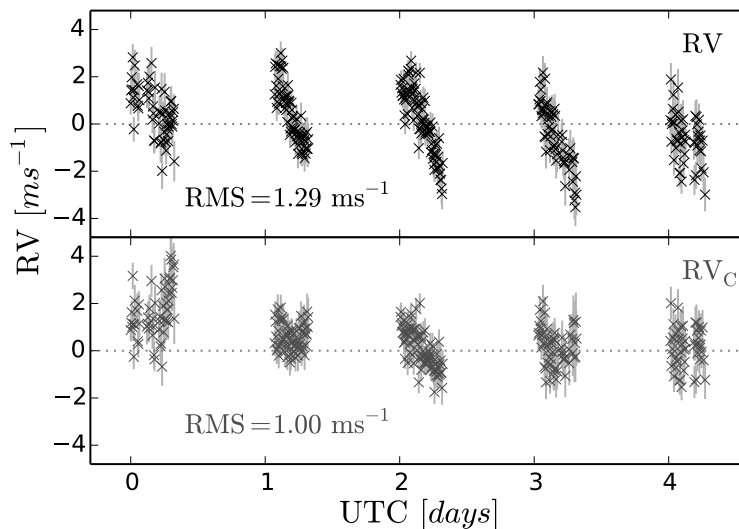
Figure 3.14: Correction of the 2013-run RVs - RVs of GJ 725A before (top panel) and after (bottom panel) applying the empirical function to detrend the RV-κ correlation. The RMS decreases by a factor 1.3.

We recommend caution when using the correlation laws defined here to detrend the FWHM and RVs from HARPS-N observations. As we have seen, instrumental updates and (possibly) spectral types might produce slightly different values for the correlation laws. As a general rule, in case of aiming at detrending archival data, firstly we strongly recommend to compute the chromatic κ-index, and secondly, verify if there are chromatic effects. That is, verify if there are correlations between the κ-index and the main data-products (e.g. RVs, FWHM or other indices). Finally, in case of detecting significant correlations, follow the detrending steps explained in this study. Another approach to this problem can also be found in next Chapter 4, where we directly corrected the spectra from the SED slope before calculate the LSD profiles.

3.9 Cross-dispersion profiles

We defined the cross-dispersion profile as the mean profile obtained from cutting the échelle spectrum perpendicular to the spectral direction. This profile is very sensitive to illumination distortions produced at the fiber input (e.g. telescope focus, seeing changes or pointing errors; see more details in Chapter 6). This is because each perpendicular cut corresponds to a section of the fiber image. In fact, the fiber size defines the width of the order in this direction.

Therefore, the cross-dispersion profile is by itself a measure of the instrumental profile and

can be used to measure the illumination stability in the detector. For example, if the wavelength dependence variations of the flux of the spectra were due to a non-perfect smoothness of the instrumental profile (i.e. due to an inefficient fiber scrambling system on HARPS-N; see Chapter 6), we would expect to find a correlation between the width of the cross-dispersion profile and the κ-index.

To measure this profile, we cut the raw images across the cross-dispersed axis, and we extracted the flux at each column of the reddest half of the κ CCD (see diagram in Fig. 3.15). After blocking the lamp emission (recorded with a secondary fiber simultaneously with the science exposure), we subtracted the floor level using a polynomial[1]. Then, we normalized each order to its maximum and we cross-correlated each column of the raw image with the corresponding flat column. After that, we obtain a *cross-dispersed mean profile*.

Then, in order to measure its shape, we fitted a Gaussian. We calculated the cross-dispersed FWHM at each column as:

$$\text{FWHM} = 2\sigma\sqrt{2\log 2}, \tag{3.16}$$

where σ corresponds to the width of the fitted Gaussian. I note that this function includes a fourth parameter (an offset) in an attempt to model the background flux variabilities.

Because the detector is flat, the image of the fiber onto the detector (and also the FWHM in the cross-dispersed direction) increases towards the detector edges. To avoid this effect, we took the differential cross-dispersed FWHM measurements of each column with respect to the first epoch. Furthermore, the detector edges are more sensitive to illumination changes (see table 7 of the HARPS-N User Manual[2]), and this cause the measurements at the edge columns to be more sensitive to SNR variabilities. Aiming at correcting the SNR dependencies of this origin, we detrended the cross-dispersed FWHM using the fitted offset parameter from the Gaussian model. The final measurement for each exposure (FWHM_{cd}) was obtained as the median along the column detrended values.

We have also calculated the centroids along the cross-dispersed axis. This measurement corresponds to the mean parameter of the Gaussian function fitted to the profile. The cross-dispersed centroid (or CEN_{cd}) of the exposure was directly defined as the median of all the column values. In this case, we could not use the background level to detrend this measurements because, as it was expected, the centroid of the Gaussian did not move with changes of the background flux level; as a consequence we still had some correlation of the CEN_{cd} with the SNR.

In spite of the corrections explained above, we detected the FWHM_{cd} to be more dispersed at low SNRs. Therefore, we performed an additional experiment to discard possible non-linearity effects of the detector as a source of variability. We let the values of the cross-correlated profiles of the 20% of the exposures with worse SNR to randomly vary $\pm 0.2\%$, total amount

---

[1] The counts obtained in between consecutive science orders were compatible with the bias level obtained during the standard calibration performed at the beginning of the night. However, we fitted a polynomial instead of subtracting a constant bias level to better account for other possible background effects that can introduce biases in the final width of the cross-dispersion profile.

[2] http://www.tng.iac.es/instruments/harps/
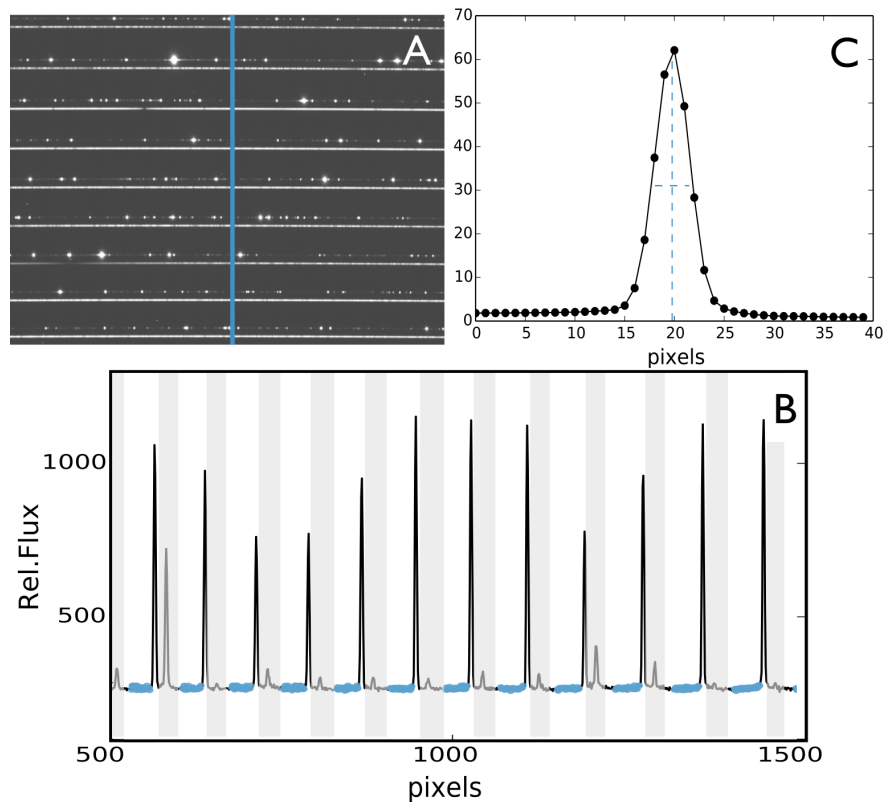
Figure 3.15: Diagram of the cross-dispersed profile calculation process - To extract the cross-dispersed profiles (B), the raw images (A) are cut in the cross-dispersed axis following the blue line. Simultaneously with the science observations, we recorded emission lines from a ThAr lamp (bright spots in A). We blocked the lamp lines (shaded areas in B) before selecting the points used to fit and subtract the floor level (blue dots, B). Finally, after normalizing each peak to its maximum, we cross-correlated the profile with that of the corresponding flat column to obtain the *cross-dispersed mean profile* (C).
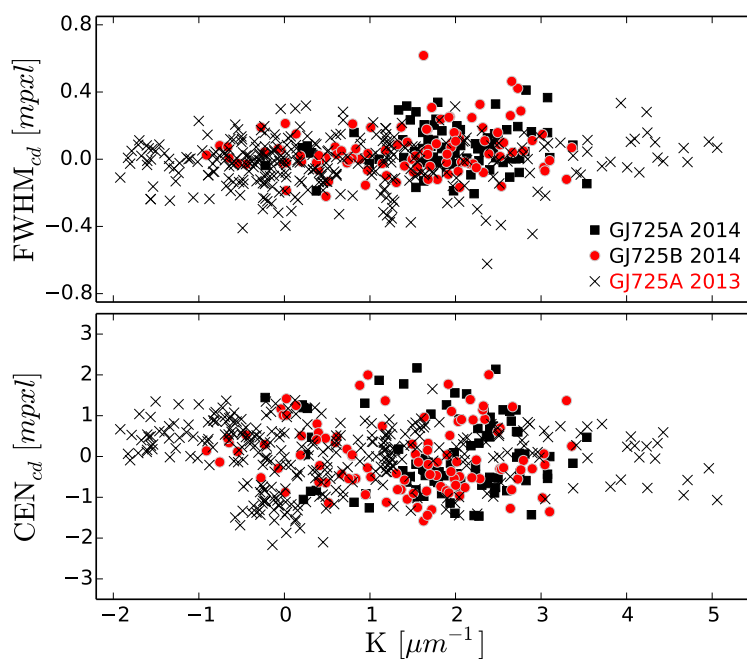
Figure 3.16: FWHM and centroids of the cross-dispersed mean profile - No significant correlation was measured between the $FWHM_{cd}$ (upper panel) or CEN_{cd} (lower panel) and the κ-index. This rules out a pure scrambling issue. The $FWHM_{cd}$ values are referred to the first exposure. The average values of the three CEN_{cd} series were subtracted to better compare its scattering.

that could be associated to a non-linearity effect[1]. However, we found no significant changes, discarding the non-linearity as responsible for any changes in the $FWHM_{cd}$.

If the spectral FWHM variability was due to illumination effects (instead of being a pure software issue), the variation of the cross-dispersed FWHM with κ would be significant. However, as I show in Figure 3.16, the scatter of the $FWHM_{cd}$ is below 1 millipixel (1 millipixel $\sim 0.8\,\mathrm{m\,s^{-1}}$). Moreover, we did not detect any significant correlation with κ. The cross-dispersed centroids, whose maximum RMS was only $0.8\,\mathrm{m\,s^{-1}}$, do not correlate with K either, opposite to what we detected for its spectral counterpart in the 2013 observations.

In consequence, we do not detect significant distortions of the image onto the detector through the measurements in the cross-dispersed direction. Bearing in mind that, in the case of the CEN_{cd} we still deal with some correlation with the SNR, this result indicates that, neither the large variability detected on the spectral FWHM nor the RV-κ correlation measured for the 2013 data, are due to a non-perfect smoothness of the inhomogeneities of the injected light spot. This result validates the use of the cross-dispersed profiles as a useful test to account for illumination issues.

3.10   Possible GJ 725B planet candidate?

In this section I discuss a possible planet hosted by GJ 725B. As I pointed out in Figure 3.3, the F-ratio excess detected in the RV differential periodogram could be compatible with a planet orbiting either GJ 725B or GJ 725A. To assess the significance of the variability and its possible fit to a Keplerian orbit, we used likelihood periodograms as described in Chapter 2. Results indicate that a 2.7 ± 0.3 day periodical signal with an amplitude of $1.2\,\mathrm{m\,s^{-1}}$ is the best fit to account for the variability of the differential time-series. The false alarm probability (FAP) of the signal (which represents a $\Delta ln\text{-}\mathcal{L} = 32.79$ improvement) is $< 1.5 \times 10^{-11}$; a result which exceeds by far the 1%- FAP threshold.

A compatible period is obtained when analyzing GJ 725B RVs independently, indicating that the variability may come from this star. Besides the common variability in both stars, no additional significant RV variability is detected on GJ 725A. However, even when the 2.7-day signal is statistically significant (i.e. a sinusoidal model is highly preferred over no signal at all), its nature cannot be fully confirmed. The reason is the short time-baseline of the observations compared to the period (see in Fig. 3.17 how most of the GJ 725B variability comes from the third night). Consequently, follow-up observations and/or transit searches will be needed to verify its strict periodicity. Nevertheless, if a planet candidate is confirmed with future observations, models indicate that it would correspond to a $1.2\,\mathrm{M_\oplus}$ Earth-mass planet orbiting at 0.024 AU almost circular orbit. This orbit would be inner to the classic habitable zone[2] (Kopparapu *et al.*, 2013).

---

[1]See the ESO report about the EEV44-82 CCDs at: `https://www.eso.org/sci/facilities/develop/detectors/optdet/docs/reports/EEV-report.html`

[2]The habitable zone is: 0.102 - 0.194 AU (assuming T_{eff}=3334 K, $m_\star = 0.25\,M_\odot$, and $L_\star = 0.009\,L_\odot$ for GJ 725B; Gaidos *et al.* 2014).
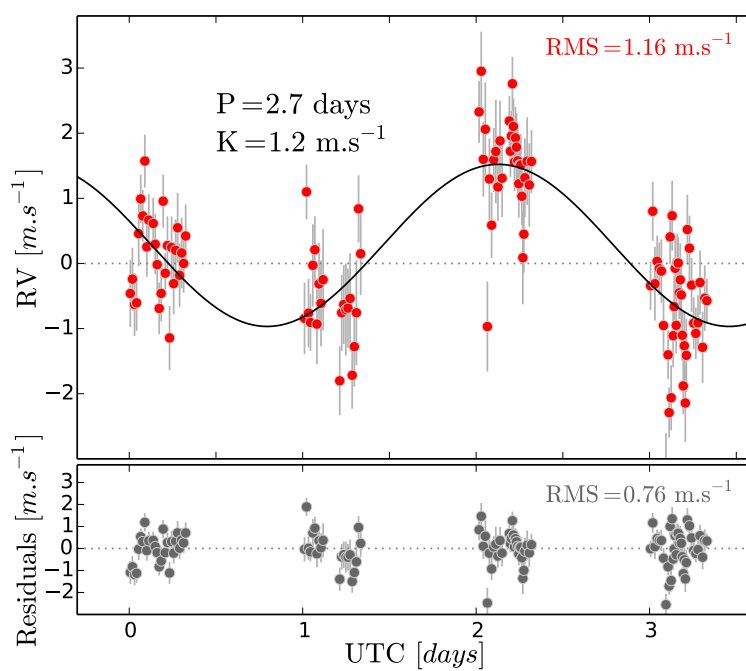
Figure 3.17: Doppler signal of GJ 725B. - (Upper panel) GJ 725B time-series in the 2914 run. The black line is the circular Keplerian model best-fitting the data (P = 2.7 d, K = 1.2 m s^{-1}). Residuals to this model are plotted in the lower panel. The RMS decreases from 1.16 to 0.76 m s^{-1} in the residuals.

3.11   Results and discussion

We obtained high-cadence observations using the HARPS-N spectrograph on the nearby M-dwarf binary system GJ 725A+B. The alternating observations strategy on the two stars unveiled common strong systematic effects in the measurements of the width of the mean-line profile (through the FWHM), and also in the RV measurements to a lesser degree. The presence of these systematic effects is a likely component of the floor noise observed in long-term Doppler programs of M-dwarf stars, and seriously affects the use of high-cadence observations for very low amplitude signal searches ($< 2\,\mathrm{m\,s^{-1}}$).

The systematic effects seem to be related to flux losses due to imperfect corrections of chromatic effects introduced by the Earth's atmosphere at the telescope-fiber interface. This suspicion is motivated by several measurements and correlations observed in pre-fiber images of the star compared to a number of measurements on the spectrum (most notably changes in the slope of the measured SED). The comparison of measurements between the two stars (and their almost identical systematic behavior) shows beyond reasonable doubt that the significant variability observed with high-cadence on M-dwarfs has an instrumental origin. While most variability in the width of the line profile is likely to be caused by the used algorithms, smaller residual RV variability remains unexplained.

HARPS-N includes an ADC which corrects the atmospheric dispersion; however other sources of error such as the atmospheric extinction or the wavelength dependence with the seeing remain uncorrected. A direct consequence of a non-optimal correction of the Earth's atmosphere is a superposition of wavelength-dispersed images of the star at the fiber entrance. This causes the light injected into the fiber to vary in wavelength as the energy peak (used for centering the image in the fiber during exposure) changes with the airmass. To measure whether this was causing distortions in the spectra, we defined the κ-index, which measures how the flux is distributed across the detector during the observations (i.e. accounts for the SED variability). Besides, we measured variability of the κ-index. This, as well as the airmass, resulted to be correlated with the distortions on the pre-fiber images. However, while these SED variabilities cause changes in the flux, this does not necessarily imply that the instrumental profile shape changes too (neither the data-products) due to illumination effects. In fact, to avoid illumination dependencies, all current high-resolution fiber-fed spectrographs apply scrambling methods (see Chapter 6). Therefore, a correlation of the SED variability with the data-products is not expected. Nevertheless, we found a strong correlation of the SED variability with the line-width (through the FWHM) and a correlation with the RVs only for our 2013 single star run on GJ 725A. Further measurements of the spectral order shapes in the cross-dispersed direction ruled out an inefficient scrambling as the origin for these correlations. These measurements also validate the use of the cross-dispersed profiles as a useful test to account for illumination issues on other echelle spectrographs.

We performed two tests to validate the algorithms used in this work. The results indicate that, whereas TERRA properly corrects and models the continuum, the DRS is sensitive to changes in the slope of the SED. This computational issue explains the strong FWHM-κ cor-

relation. Contrarily, the RV-κ correlation found in the 2013 run remains unexplained and has to be caused by another effect. Since the width of the mean-line profile is a parameter very sensitive to magnetic activity events (e.g. Reiners *et al.*, 2013), the FWHM is often used as an activity indicator and a tool to decorrelate Doppler time-series. Thus, it is essential to detrend this index. We outline a procedure to decorrelate the HARPS-N FWHM measurements using the slope of the SED. A tentative decorrelation law is also proposed for the 2013 RVs. The decorrelation laws are likely to be slightly different on each target (especially for targets of different spectral types), so we advise to obtain the specific SED slopes changes with the κ-index and perform similar verifications on all individual targets of a given program.

Ideally, new algorithms that simultaneously fit for the continuum and the line profile need to be developed to account for the FWHM variability. Other option is to refine the current methods, as it was already done in the last DRS version for F, G and K stars, where the continuum is re-normalized with respect to a reference spectrum. Regarding the variability of the RVs in the 2013 single run in GJ 725A, given the large correlation with the airmass, we suspect that the most likely explanation for it was the sub-optimal performance of the atmospheric correction. The possibility of a systematic ADC failure only during continuous mode observations (where the pointing procedure is not redone between same object exposures) was ruled out by the HARPS-N core team (*R. Cosentino, priv. comm.*). However, our in-situ monitoring of the ADC parameters during posterior HARPS-N campaigns showed that, under some unknown circumstances, the ADC values seem not to be updated. Therefore, we suspect that the ADC failed during this 2013 run.

Remaining correlations with the image distortions might be the origin for the noise floor level which popped up as common signals in the GJ 725A+B alternating run. As a by-product, we have shown that the GJ 725A+B pair is stable enough to be used as a benchmark case for commissioning of future high precision spectrographs, at least down to $\sim$1-2 m s^{-1}. Indeed, CARMENES spectrograph (Quirrenbach *et al.*, 2014) is planning to use this system for validation purposes. The $\sim 1 - 2$ m s^{-1} limit is possibly set by a low-mass companion orbiting GJ 725B, whose presence will be further investigated in future campaigns.

Long-term surveys (like the HARPS-GTO program) try to observe all the stars at the same airmass each night, minimizing sources of effects related to airmass and scrambling, and randomizing possible systematic shifts occurring within a night. However, this strategy is not possible for programs which require continuous high-cadence observations, as the CTB survey. Many science cases, such as the molecule detection on transiting exoplanets (Snellen *et al.*, 2010; Martins *et al.*, 2013), can benefit from an extremely stabilized instrumental profile and robust procedures to measure it. Concerning Doppler spectroscopy, I note that an extra effort should be put into the image stabilization and correction of chromatic effects such as those reported here (~ 1 m s^{-1}) in order to clean spurious signals and get the most of the new technologies for wavelength calibration at cm s^{-1} levels, like laser frequency combs (Probst *et al.*, 2014). This is the goal of our prototype RadiCa2D further explained in Chapter 6. The best wavelength determination is useless if systematic signals populate the periodograms.
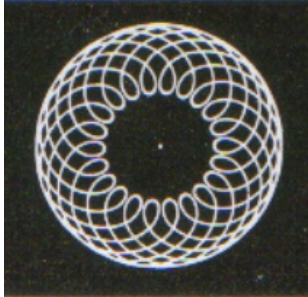
4

Searching for pulsations on M dwarfs

S TELLAR oscillations appear all across the Hertzsprung-Russell diagram. Recent theoretical studies also support the existence of seismic beats in the atmospheres of M-type stars. This opens the possibility for the application of asteroseismic tools to M dwarfs. Among the applications, asteroseismology techniques allow to have a better knowledge of the star interior and consequently enable an accurate determination of the properties of the hosted exoplanets. However, seismic signatures have not yet been detected for cool stars. In this Chapter, I present our first attempts for finding pulsations with the "Cool Tiny Beats" survey (CTB). The study is focused on GJ 588 and GJ 699 (Barnard's star), two targets known to be stable in the long-term. Section 4.2 details the observations and data reduction, whereas in Section 4.3 we correct the data from night-to-night and intra-night effects. Section 4.4 is the main part of the study and comprises the search for periodic signals and the definition of a HARPS precision limit in the high-cadence time domain. Finally, I present the main conclusions of the study in

Section 4.5.

4.1 Introduction

Rodríguez-López *et al.* (2014) (from now on RL14) predicted two main regions in the Herztprung-Russell diagram where M dwarfs may be able of maintaining pulsations. One is formed by young pre-main sequence stars and another by M dwarfs on the main sequence. The CTB sample is comprised by targets in the second region. RL14 predicts for them pulsation periods in the 20 min up to 3 h range (8 to 72 d^{-1} in frequency). Two driving mechanisms are at work to maintain the oscillations: i) the ϵ mechanism, caused by He^3 burning, that works on its own in the 20–30 min range for completely convective models (0.20–0.30$M_\odot$), and ii) the so-called *flux-blocking mechanism*, that acts periodically blocking the radiative flux at the tachocline[1] and is the main driver of the pulsations in the whole 20 min to 3 h period prediction for models in the 0.35–0.60$M_\odot$ range. RL14 is an extension of Rodríguez-López *et al.* (2012) to include the excitation of not just the fundamental radial mode, but also non-radial and non-fundamental p-modes and g-modes. Such a range of predicted periods gives us a starting point to begin the search for stellar pulsations in main sequence stars.

Even though the theory works well in predicting the expected periods, the current existing linear oscillation codes cannot predict the amplitudes of the oscillations. So far, photometric campaigns have only been able to establish upper limits on the amplitudes. Indeed, Rodríguez *et al.* (2016) have recently performed an extensive and exhaustive analysis of 87 M dwarfs observed at high-precision and short-cadence (1 min) with the Kepler spacecraft. Although they did not find any significant signal in the 10-100 d^{-1} range, they set up a new photometric detection threshold of tens of μmag. This photometric limit is very low, however, it does not imply that stellar pulsations are undetectable in RV using high-precision spectrographs. In fact, pulsations detected in both, photometric and spectroscopic observations for other spectral types, indicate that amplitudes can be up to 100 times larger in radial velocities. This indicates that a signal of 10 μmag can have a counterpart of 1 m s^{-1} in radial velocities; an amplitude that is detectable with HARPS (Lovis & Fischer, 2010 reported RV precision of 0.5 m s^{-1} in the short-term). This is supported by a number of studies on δ Scuti and also γ Dor oscillators, holding for radial and non-radial modes (e.g. FG Vir, RZ Cas, 9-Aur, HR 8799, gam Dor, and HD 49434; Zima *et al.*, 2006; Lehmann & Mkrtichian, 2004; Zerbi *et al.*, 1997, 1999; Krisciunas *et al.*, 1995; Uytterhoeven *et al.*, 2008). This favorable relation motivated the asteroseismology science case of CTB for which I present here our first results.

4.2 Observations and data reduction

The CTB initial sample was comprised of ~25 M dwarfs mostly selected to lie within the boundaries of one of the instability regions defined in RL14 (the one mainly comprised by main

---

[1]The tachocline is the transition layer from the radiative interior to the convective exterior.

Table 4.1:   **GJ 588 and GJ699 stellar parameters**

Parameters	GJ 588	GJ 699	Refs.
SpT	M2.5	M4	RE95
V_{mag}	9.31	9.51	KO10
Dist. [pc]	5.93 ± 0.05	1.82 ± 0.01	KO10
P_{rot} [d] [†]	61.3 ± 6.5	148.6 ± 0.1	SU15
$v \sin i$ [km s^{-1}]	< 3.0	< 2.5	RE12
[Fe/H] [dex]	0.06 ± 0.08	-0.51 ± 0.09	NE14
T_{eff} [K]	3555 ± 41^{1}	3237 ± 60	GA14
M [M$_{\odot}$]	0.43 ± 0.05	0.15 ± 0.02	GA14, BO12
R [R$_{\odot}$]	0.42 ± 0.03	0.187 ± 0.001	GA14, BO12
$\log g$ [cm s^{-2}]*	4.82 ± 0.08	5.040 ± 0.005	

Note. — References: [BO12] Boyajian *et al.* (2012), [GA14] Gaidos *et al.* (2014), [KO10] Koen *et al.* (2010), [NE14] Neves *et al.* (2014), [RE95] Reid *et al.* (1995), [RE12] Reiners *et al.* (2012), [SU15] Suárez Mascareño *et al.* (2015).

[∗] The $\log g$ values were obtained from this table parameters.

[†] SU15 used also CTB data to calculate the P_{rot} values.

sequence M dwarfs). Barnard's star (red dot in Fig. 4.1) is an extensively studied M dwarf which does not have any reported planets and it is known to be stable in the long-term[2]; in fact CTB used it as its RV standard. That is, in addition to the high-cadence observations presented here, we took at least one spectrum of GJ 699 per night when it was visible. For this reason, even when GJ 699 lies in the outer edge of the theoretical instability region, we decided to included it in this study[3]. On the other hand, GJ 588 (black square in Fig. 4.1) is both, stable and well within the predicted instability region. The relevant stellar parameters of GJ 588 and GJ 699 are shown in Table 4.1.

The GJ 588 and GJ 699 high-cadence data were obtained with HARPS during a CTB observational campaign carried out in May 2013 (see Fig. 4.2). Besides the high-precision spectroscopy, a continuous time monitoring is essential in asteroseismic studies. We monitored GJ 588 at high-cadence during four consecutive nights with exposure times of ~ 600 s, reaching a maximum airmass of 2.2. In total, we obtained 189 spectra with a mean signal-to-noise ratio (SNR) and seeing values of 63 and 1.03 arcsec, respectively. We acquired 108 high-cadence spectra for Barnard's star. Among them, two nights are consecutive and previous to

---

[2]Zechmeister *et al.* (2009) derived a RV stability of 2.70 m s^{-1} after subtracting the secular acceleration using UVES data. Later, Anglada-Escudé & Butler (2012) reduced the RV limit down to 1.23 m s^{-1} using HARPS. More recently, Choi *et al.* (2013) found no significant periodic Doppler signals with amplitudes above ~ 2m s^{-1} using 25 years of data from the Lick and Keck Observatories.

[3]The instability region gives us a starting point in the search for pulsations. However, we should not necessarily exclude targets close to its edge since its boundaries are not yet well defined.

the GJ 588 observations, while an extra third night of GJ 699 was observed just after the GJ 588 high-cadence run ended (see Fig. 4.2). In this case, the median exposure time was ∼ 500 s, the maximum airmass reached 2.0, and the mean SNR and seeing were and 63 and 0.64, respectively.
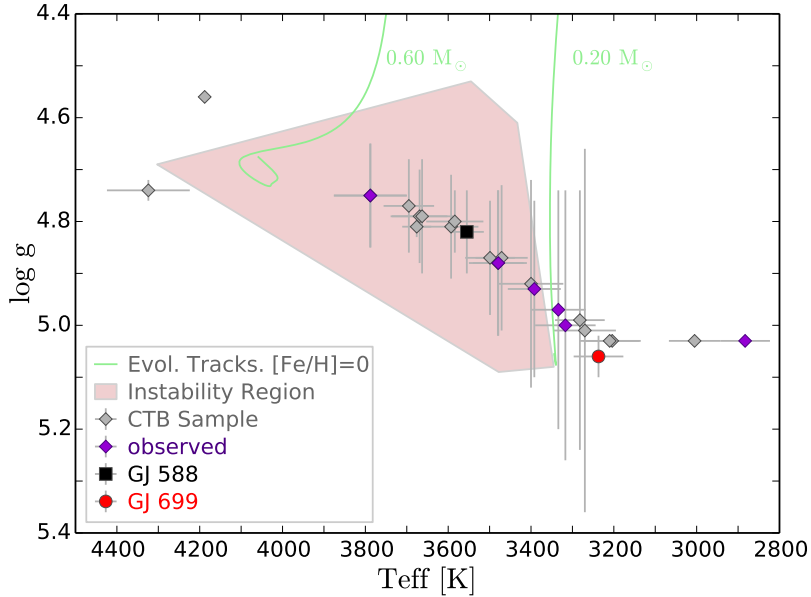
Figure 4.1: Instability region of main-sequence M dwarfs - Grey diamonds are CTB targets. Light green lines are evolutionary tracks (of solar metallicity, unity mixing parameter α) and 0.20 and 0.60 M$_\odot$ initial masses) delimiting the area. The black square and red dot correspond to GJ 588 and GJ 699, respectively. Physical parameters come from: Gaidos *et al.* (2014), Boyajian *et al.* (2012), Santos *et al.* (2013), Dressing & Charbonneau (2013), and Steffen & Farr (2013).

The spectra were extracted and wavelength calibrated with the standard HARPS Data Reduction Software (DRS). We used the Template Enhanced Radial velocity Reanalysis software (TERRA) to calculate the radial velocities (see Chapter 2). The mean-line profiles were obtained with the least-square deconvolution technique (LSD) outlined in Barnes *et al.* (1998, 2012) and by fitting a Gaussian we derived the full-width-at-half-maximum of the LSD profiles (FWHM-LSD, see Sec. 4.3.4).

4.3 Instrumental effects correction

The analysis of the CTB data revealed both intra-night and (possibly) night-to-night instrumental effects. The main intra-night effects have already been described in Chapter 3. Here, I show a more efficient correcting procedure. Additionally we identify other sources of systematic noise that need to be mitigated when dealing with high-cadence observations.
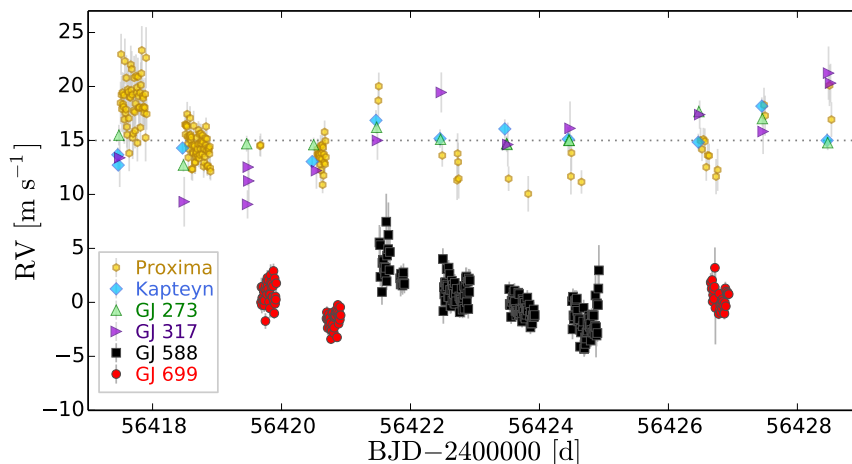
Figure 4.2: RVs of the May 2013 run from HARPS - Radial velocities time-series of the 6 targets observed during 11-nights. GJ 588 (black squares) and GJ 699 (red dots) are the focus of this study. The RVs of the other targets were shifted 15 m s^{-1} for visualization reasons.

4.3.1 Wavelength calibration jumps

One of the effects that we quickly identified were night-to-night RVs jumps of $\sim 0.5 - 2.0\,\mathrm{m\,s^{-1}}$. The stability of the RVs obtained with TERRA or any other reduction software relies on the calibration of the wavelength, which is given by a ThAr lamp measurement taken at the beginning of each night with HARPS. Since the wavelength solution has also an associated uncertainty, its random errors are bound to produce night-to-night jumps than can easily reach a $\sim$ 1-2 m s^{-1} level. Moreover, compared to the typical G & K dwarfs for which HARPS was designed, M dwarf stars have most of their flux and Doppler information in the redder part of the detector. As a result, night-to-night RVs become more sensitive to random errors in a smaller number of the redder diffraction orders. To calculate the night-to-night offsets in the wavelength solution, we selected one GJ 699 spectra per night[1] and we measured the effective Doppler shift as the wavelength difference against a reference (i.e. a theoretical list of lines). Normalizing the drift with respect to the first night (or t_0), we can compare the wavelength solution drift between nights as:

$$\mathrm{drift(m\,s^{-1})} = c\left(\left\langle\frac{\lambda_{t_i}}{\lambda_{t_0}}\right\rangle - 1\right) \tag{4.1}$$

where c is the speed of light and λ_{ti} accounts for the wavelength difference against the reference for the GJ 699 spectra observed at ti. This difference is calculated for each of the pixels of the 22 reddest spectral orders.

As a complementary wavelength reference source, a spectrum of a stabilized Fabry-Perot

---

[1]For nights with several GJ 699 spectra, we selected the one observed early after the beginning of the night.

(FP) interferometer is also obtained as part of the calibration procedure executed before the night starting. Using TERRA, we computed differential RV shifts of all the FP frames within each epoch, against the FP frame taken in the first night. In the upper panel of Figure 4.3, we compare the nightly FP and wavelength solution drifts[1]. Although these FP measurements also show some structure, the corresponding time-series are much more stable (rms $= 0.22\,\mathrm{m\,s^{-1}}$) than those derived from the wavelength solutions (rms $= 1.16\,\mathrm{m\,s^{-1}}$). Although they are likely to contribute to random noise over long time-scales, the jumps in the wavelength solution already cause serious issues in the consistency of our time-series in the high-cadence domain (signals in the P$<$ 2 d range). For example, see in Figure 4.3 the $3.6\,\mathrm{m\,s^{-1}}$ jump in the wavelength solution between the first and the second night of GJ 588 observations. As a comparison, the GJ 588 time-series look much flatter if we use the wavelength solution of the first night for all of the observations, instead of the individual night calibrations (compare grey and black squares in the bottom panel of Fig. 4.3).

This random variability of the wavelength solution is one of the causes of the spurious $\sim$1-day peaks (and integer fractions of it, like 1/2 and 1/3) that commonly appear in the periodograms of high-cadence data (e.g. the low frequency excess in the power spectra in Fig. 3 and Fig. 7 from Bedding *et al.* 2007 and Bouchy *et al.* 2005, respectively). Although we do not expect pulsations at such long periods, the window function can inject significant correlated noise at other frequencies, which is undesirable. We use the strategy of using a common wavelength solution for all the run to mitigate this source of noise. The long term stability of the FP ($>$week) has not yet been established (*Pepe & Lovis, priv. comm.*) so we advise against using this technique to improve the consistency of time-series with a time-span longer than a few days.

4.3.2 Charge Transfer Inefficiency

Doppler shifts have been reported to correlate with the signal-to-noise ratio (SNR) of the observations (Bouchy *et al.*, 2009). This is in part due to the *charge transfer inefficiency* (CTI) effect. The CTI gets worse at low fluxes and it is associated with an inefficient transference of charge between adjacent pixels during the readout process in charge-coupled devices (CCD). The CTI can produce effective changes in the position and the shape of the HARPS spectral lines (Lo Curto *et al.*, 2012; Zhao *et al.*, 2014), and thus, cause RV offsets of several $\mathrm{m\,s^{-1}}$(Bouchy *et al.*, 2009) as a function of the SNR. Bouchy *et al.* (2009) proposed a method to assess the charge lost in the pixels of the SOPHIE spectrograph (Perruchot *et al.*, 2008). Using similar methods, the raw frames of HARPS-N are corrected for CTI since 2013. However, such a correction was not implemented in HARPS (*Lovis, C., Pepe, F., priv. comm.*).

As a consequence, to mitigate CTI effects in our campaign, we implemented an empirical post-processing correction: during the December 2014 CTB campaign we observed GJ 887,

---

[1]The datapoints of the wavelength solution and FP do have the same acquisition time (i.e. they do not fit in the x-axis of Fig. 4.3) because while the FP is recorded before the start of the night, the GJ 699 spectra used to obtain the wavelength solution were observed all throughout the night.
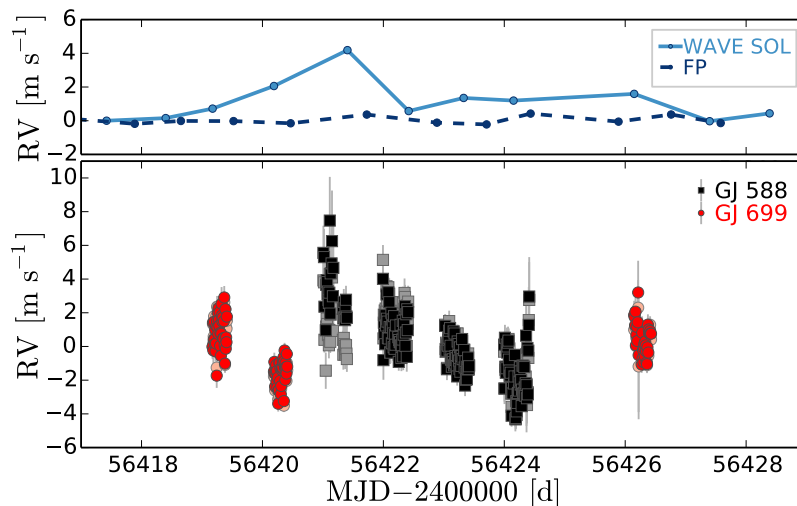
Figure 4.3: Wavelength solution drift - (Upper panel) Comparison of the wavelength solution (light blue solid line) and FP (dark blue dotted line). The wavelength solution, that relies on the ThAr reference lamp, is less stable. (Bottom panel) GJ 588 and GJ 699 RVs obtained for the same wavelength solution (light color symbols) and for individual night calibrations (dark color symbols). The wavelength solution drift causes night-to-night RV offsets.

a very bright M2V spectral type star, with different exposures times, i.e. at different SNRs. Similarly to what Santerne *et al.* (2012) did for SOPHIE, we used these spectra to fit a relation between RVs and SNRs which is valid for, at least, M dwarf stars observed with HARPS. This relation is:

$$\Delta RV(m\,s^{-1}) = 4.92 - 1.31 \ln SNR_{60} \,, \tag{4.2}$$

where SNR_{60} refers to the SNR measured in the spectral order 60. Figure 4.4 shows the CTI empirical calibration function together with the de-trended RVs of GJ 588 and GJ 699.

4.3.3 Seeing Effect

We observed that when atmospheric conditions were excellent (i.e. seeing < 1") the Doppler measurements of several stars were correlated with it (see Fig. 4.5). Such effect was firstly described by Boisse *et al.* (2010a,b) and it was pointed out as the main limiting factor of the SOPHIE spectrograph (Perruchot *et al.*, 2008). The effect can be understood as a vignetting of the telescope pupil. Such vignetting causes instabilities of the pattern illuminating the grating, which ultimately produce small shifts of the spectral lines and measured RVs. HARPS has a *double image scrambler* to stabilize the image and to homogenize the illumination. Since this system interchanges the fiber near and far fields (see more details in Chapter 6), vignetting the pupil results to be equivalent to reduce the size of the image of the star. That is, equivalent
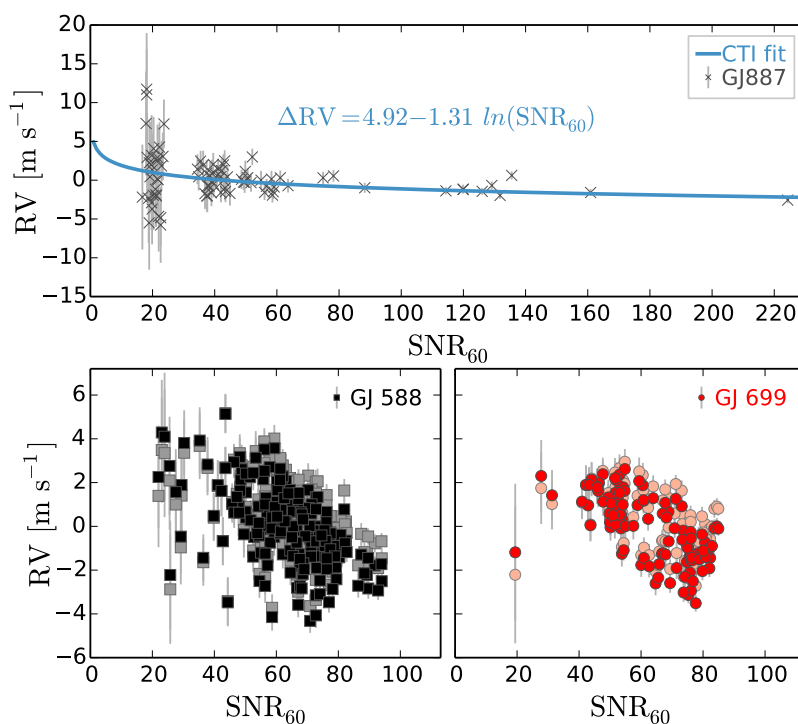
Figure 4.4: Charge Transfer Inefficiency (CTI) effect - (Upper panel) GJ 887 observations taken with different exposure times (from 10 up to 600 s) to obtain the CTI calibration function in blue. (Bottom) Dark symbols are the original RVs for GJ 588 (black squares) and GJ 699 (red dots) while the light ones correspond to their CTI-corrected counterparts.

to have good seeing conditions. When the seeing is below 1 arcsecond, the telescope image is sharper than the HARPS fiber width, and thus, if the light scrambling is not perfect, the far field fluctuations cause RV shifts up to $\sim 3\,\mathrm{m\,s^{-1}}$ (Boisse *et al.*, 2010a).

The effect described above is known as the *seeing effect* and was demonstrated for SOPHIE by Bouchy *et al.* (2013). In that study it was also shown that using octagonal fibers, instead of circular ones, improves the scrambling efficiency and the resulting RV precision by a factor of ~ 6. In May 2015, an octagonal fiber link was introduced in HARPS. However, the data used in this study were obtained before this upgrade. Therefore, we applied a post-processing empirical correction based on our observations.

We used as a proxy for the seeing the value given in the data headers[1]. Then, we fitted and subtracted a linear function to the observations with seeing < 0.75 arcseconds (see Fig. 4.5). This value is below the HARPS fiber width (1 arcsecond) and was chosen in terms of the May 2013 data variability. Moreover, our 0.75-arcsecond cut-off resulted to be in good agreement with the 0.7 arcseconds quality image given by the 3.6-m telescope (Boisse *et al.*, 2010a).
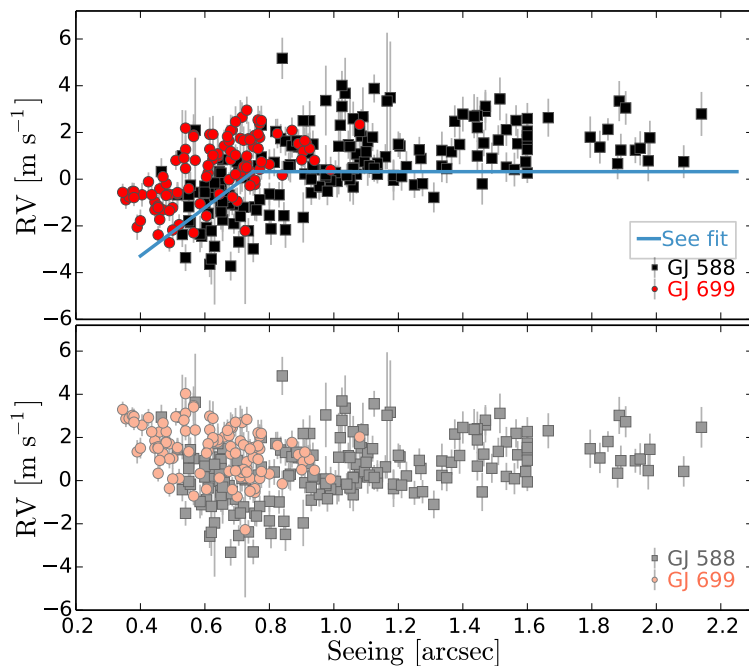
Figure 4.5: Seeing effect - The upper panel shows the RVs uncorrected from the *seeing effect*. Datapoints clearly decrease when they are observed at seeing values below the fiber size (i.e. 1 arcsecond in HARPS). Based on dispersion criteria, we only corrected with a linear fit the RVs below 0.75 arcseconds. Corrected series are shown at the bottom.

---

[1]This value is obtained as the FWHM of the acquisition image taken by the autoguider camera.

4.3.4 SED normalization effect

Our previous studies using CTB high-cadence data revealed systematic effects within the night in HARPS-N (see Chapter 3). Such systematic effects (we will call them *SED normalization effect* hereafter, where SED stands for spectral energy distribution) consist of wavelength dependence of the flux losses caused by small illumination changes at the fiber entrance. Wavelength and time dependencies in the SED function of GJ 588 and GJ 699 revealed that this effect is also present in HARPS spectra (see Fig. 4.6). Then, the HARPS DRS pipeline does not account for the *SED normalization effect* producing uncorrected cross-correlation functions (or CCFs). That means that the mean-line profile proxies, along with the indices derived from them, are affected by the *SED normalization effect*. They should be treated before being used for scientific purposes.
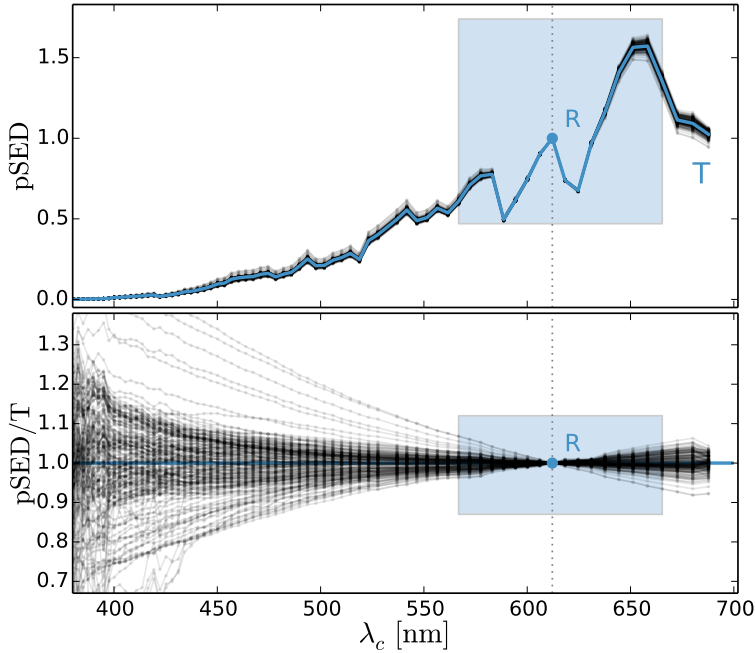
Figure 4.6: SED normalization effect - The upper panel shows the GJ588 pSEDs (pseudo spectral energy distribution function; see Chapter 3). The wavelength and time-dependence is clearly in the bottom panel, where I show the pSEDs normalized by T (the function at t_0). The index κ measures the relative changes in the pSED slope. It is calculated for the range of wavelengths in the blue area.

In order to measure un-contaminated mean line profiles we have to correct their variable slope. To this end, we re-scaled the flux at each order and observation to match that of our template spectrum (highest SNR). Once we corrected the spectra from the SED normalization effect, we calculated the mean-line-profile measurements with a LSD approach (Barnes *et al.*, 1998, 2012). Compared to the CCFs from the DRS, our LSD approach better treats the

continuum of M dwarfs spectra resulting in more realistic mean-line profiles. As a proof, in Figure 4.7 I show a CCF and a LSD mean-line profiles for the same GJ 588 spectrum. The side lobes present in the CCFs[1] increase the uncertainty of the Gaussian fit as well as of the derived measurement from it such as the FWHM (the line width), the RV (the line centroid), and the BIS (the line asymmetry).
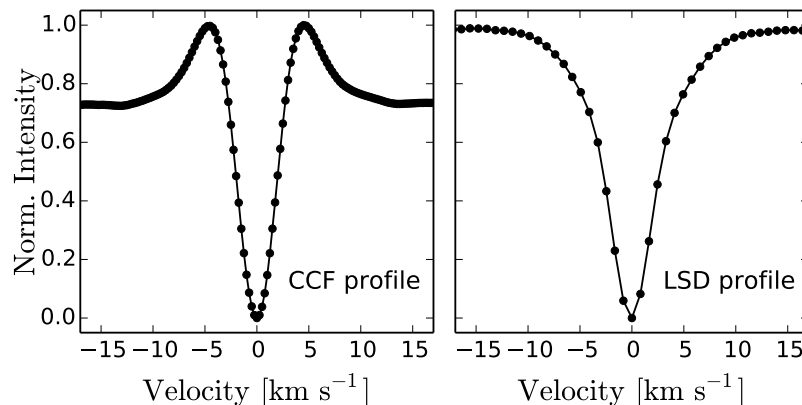
Figure 4.7: Comparison of a CCF and a LSD mean-line profiles - For the same GJ 588 spectrum I show in the left panel the cross correlation profile from the DRS pipeline (CCF) and on right panel the profile obtained with a least-square deconvolution (LSD) approach. For visual reasons, both profiles were shifted to zero-velocity and normalized by its minimum intensity.

The LSD method consists in finding the convolution kernel applied to a list of lines to reproduce the observed spectrum in a least-squares sense thus naturally accounting for the blends. As in Chapter 3, to create such a list of lines, we used a co-added high-SNR spectrum generated with all the observations. This processing consists in matching the continuum and Doppler shift of each spectrum to the highest SNR spectrum, and then co-adding all of them. When selecting lines for the LSD, chromospheric emission lines (such as H_α and NaI D1 and D2 lines) or any telluric lines deeper than 0.05 compared to the normalized continuum are excluded. The LSD profile is obtained using the reddest HARPS apertures only (from order 32 to 72) and it is sampled at $0.821\,\mathrm{km\,s^{-1}}$, which matches the effective average pixel size of the HARPS CCD in Doppler space[2]. Then, for each LSD profile in absorption, we produce a normalized positively defined probability distribution function by subtracting their residual continuum and normalizing its area to unity. Finally, we calculate the FWHM-LSD index as the full width at half maximum of a Gaussian function fitted to the mean line profiles. The FWHM-LSD is a proxy of the profile width changes. Figure 4.8 shows how, in contrast to the FWHM of the CCFs (FWHM-CCFs), the FWHM-LSD measurements does not correlate with

---

[1]Side lobes are generally caused by blending between nearby lines. This is typical of cool stars which are crowded of lines that distort the star's continuum.

[2]The DRS oversamples the pixels size and calculates the CCFs with a velocity step of $0.25\,\mathrm{km\,s^{-1}}$.

κ, the index accounting for the SED variability[1].
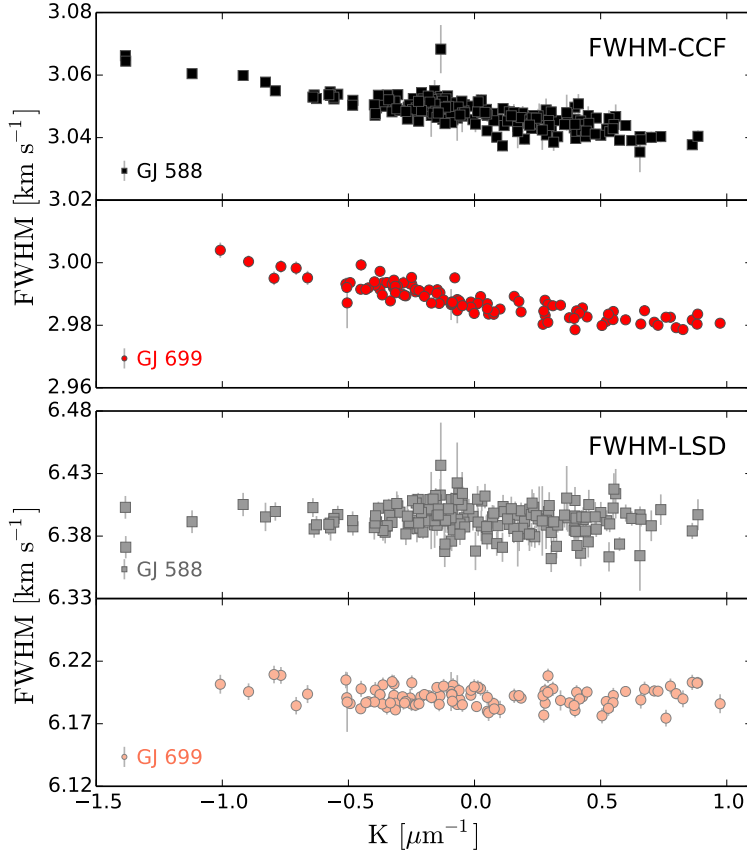
Figure 4.8: SED normalization effect - (Upper panel) the width of the CCFs given by the DRS (FWHM-CCF) correlates with κ, the index accounting for the *SED normalization effect*. (Bottom panel) after correcting the spectra and calculating a new mean-line profile proxy (the LSD profiles) we obtain a line width index (FWHM-LSD) un-correlated with κ.

Uncertainties in the LSD profiles, and thus in the FWHM-LSD are difficult to estimate analytically. Instead, we used an empirical procedure based on the fact that uncertainties follow the SNR of the observations. We assumed the standard deviation of the differences between FWHM-LSD data-points to be the $\sqrt{2}$ times the uncertainty of the mean SNR of each night (at reference échelle aperture number 60). I used as reference the first observed epoch of each night. Then, the error values of the other observations within the night were obtained by scaling this standard deviation by a factor of $<\text{SNR}>/\text{SNR}_{\text{obs}}$.

---

[1]The κ-index is calculated in the pSED slope in region of wavelengths were we use a linear approximation (see blue area in Fig.4.6). For more details see Chapter 3

4.3.5   Final time-series

The final measurement to be used for this study were the RV and the FWHM-LSD corrected as explained above. Figure 4.9 shows the final resulting time-series. The FWHM-LSD still shows patterns which seem to repeat themselves on different nights (e.g. the arc-shape of the FWHM-LSD in nights two and three of GJ 588). Since we have corrected the spectra from the *SED normalization effects*, such variability can not be driven by flux distribution changes. An explanation could come from the barycentric broadening of the spectral lines caused by changes of the star-Earth differential velocity during the observations. That is, by changes in the star-Earth relative RV between observations taken close and far from the Zenith[1]. However, our measurements indicate that the contribution of such effect is negligible at the HARPS precision level for these targets. Nevertheless, even when we cannot identify the origin, we know the periods associated to such pattern will be close to 1-day and/or sub-multiples in the periodograms. Therefore, our range of study ranging from 20 min to 3 h prevent us from misleading signals.

4.4   Analysis

4.4.1   Short time domain variability

We used *ln-$\mathcal{L}$* periodograms (Baluev, 2009) to search for periodic signals embedded in the RV and FWHM-LSD high-cadence time-series. The *ln-$\mathcal{L}$* periodograms search the best fit of the data to a likelihood model; which in this case is:

$$v_{i,\text{Night}} = \gamma_{\text{Night}} + \dot{\gamma}(\Delta t_i) + \mathcal{K}_p(\Delta t_i) \qquad (4.3)$$

where γ_{Night} is an *offset velocity* and $\dot{\gamma}(\Delta t_i)$ is a *linear trend parameter*. Note that we let each night to have a different offset, whereas a single trend is fitted to all nights. Finally, $\mathcal{K}_p(\Delta t_i)$ is in this case a sum of k sinusoids:

$$\mathcal{K}_p(\Delta t_i) = \sum_p^k A_p \sin\left(\frac{2\pi}{P_p} t_i\right) + B_p \cos\left(\frac{2\pi}{P_p} t_i\right) \qquad (4.4)$$

where each p-th sinusoid is defined by the A_p and B_p amplitudes and the period P_p. Therefore, the *ln-$\mathcal{L}$* periodogram fits only two non-linear parameters, those are the period and the *stellar jitter* (see Chapter 2 for more details).

In this study, we globally modeled the time-series considering each high-cadence night as an independent set (equivalently to the different instrument analysis performed inAnglada-Escudé *et al.* 2016a). We proceed in that way aiming at filtering out periodicities longer than 1 day in which we are not interested (remember 1-day periods and/or sub-multiples are expected due to uncorrected intra-night effects). In other words, this approach avoid a large superposition of p-th sinusoids in the model before studying sinusoids compatible with pulsations. It is important

---

[1]Bodies at the Zenith seem to move faster for a fixed observing time, thus causing a broadening of the spectral lines.
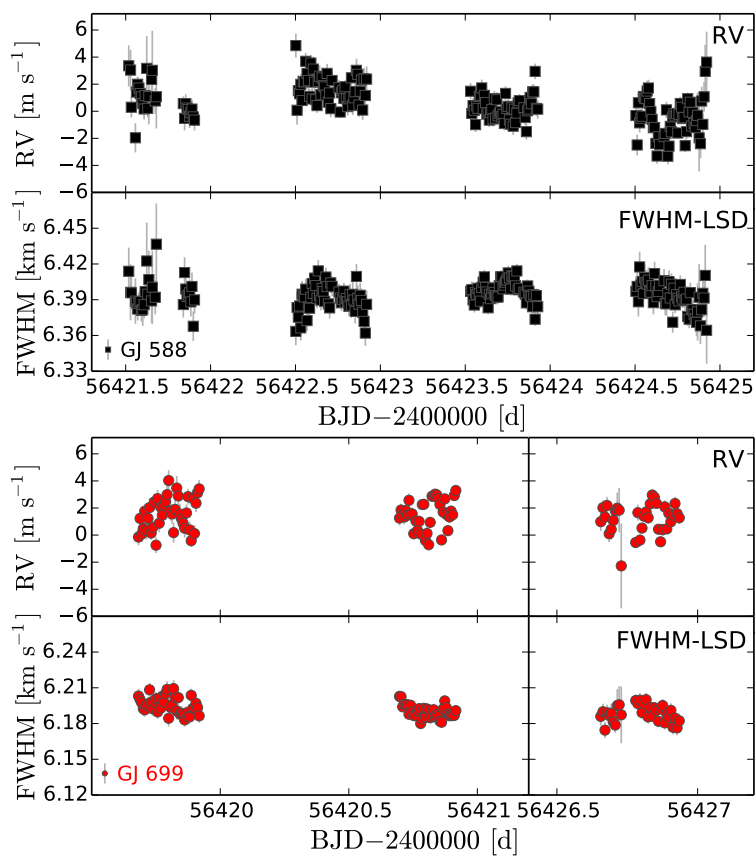
Figure 4.9: Final time-series of this study - RV and FWHM-LSD time-series resulting after intra-night and night-to-night corrections. The upper and bottom panels show four and three high-cadence nights of GJ 588 and GJ 699, respectively. This are the data we will study in next sections.

to note that *ln-L* periodograms do not apply pre-whitening procedure. Instead, every time that a model with $p+1$ sinusoids (SOLp+1) is preferred against the p case (SOLp) a new sinusoid is added to the model. Then, all the model parameters are re-adjusted every time that we search for those of the new sinusoid.

I show the RV and FWHM-LSD *ln-L* periodograms of GJ 588 in the second and third panels of Figure 4.10, respectively. On the other hand, in the same panels of Figure 4.11 I show the *ln-L* periodograms of GJ 699. Grey areas highlight the range of periods where pulsations are not expected (i.e. periods out of the 8-72 d^{-1} range). In the upper right corner of *ln-L* periodograms I indicate the number of p sinusoids included in the model until find the first solution outside the grey area. For example, the SOL2 of the RV-periodogram of GJ 588 means the model contains two sinusoids, the first one corresponding to a large amplitude signal with a period different from 20 min-3 h.

As a figure of merit to quantify the significance of a detection we used the so-called *False Alarm Probability* (FAP hereafter), which is the probability of obtaining a peak by a random combination of the errors (Cumming, 2004). The grey dashed line at FAP 1% shown in the periodograms indicates that, above this threshold, the chance of obtaining a peak due to random noise if the null hypothesis were true is below 1%. In this study, and given the smallness of the sample (two stars), we established a FAP 1% as the threshold to claim a detection of a sinusoidal signal. Given that this is a new time-domain we estimated the FAP empirically. The goal was to establish how the maximum likelihood statistic is distributed in the presence of noise only. To do this, we generated synthetic data by randomly permuting the measurements among the given observed epochs (i.e we bootstrapped the time-series). Then we calculated periodograms over the resulting series and we recorded the maximum $\Delta \ln \mathcal{L}$ achieved in each of these test periodograms . After repeating this experiment $N = 10^3$ times, we derived the FAP as is shown in Figure 4.12. That is, the FAP of a signal is the number of synthetic experiments giving spurious $\Delta \ln \mathcal{L}$ larger than the original time-series divided by the total number of tests.

No signals were found with a FAP <1% in the range of frequencies where we expected to find pulsations. However, for the RVs, we can see some excess of power for both, GJ 588 and GJ 699, in the range of a few hours (or tens of d^{-1}) close to the 10% FAP. In particular, the preferred peaks have a corresponding frequency of 12.04 d^{-1} (indicated with a vertical solid red line in Fig. 4.10) in the case of GJ 588 and of 10.83 and 23.12 d^{-1} (vertical solid blue and dotted green lines in Fig. 4.11) in the case of GJ 699. Nevertheless, the presence of the 23.12 d^{-1} peak also in the FWHM-LSD periodogram of GJ 588 (highlighted in Fig. 4.10 also with a vertical dotted green line) lead us to suspect that it could be an instrumental artifact. The 12.04 d^{-1} is recovered regardless of the approach used to filter out the periodicities close to 1-day (and their aliases). However, we decided to consider each night as independent data sets because in this case the model requires fewer sinusoids and is simpler[1]. The FWHM-LSD periodograms

---

[1]For example, in the case of the GJ 588 RVs if we consider each night independently only one sinusoid is required to account for the long-term variability (SOL1 corresponds to ~ 0.5 days). On the contrary, if we consider the run as a whole the 12.04 d^{-1} period is recovered after fitting two $\sim$1.5 and $\sim$0.5 days sinusoids.
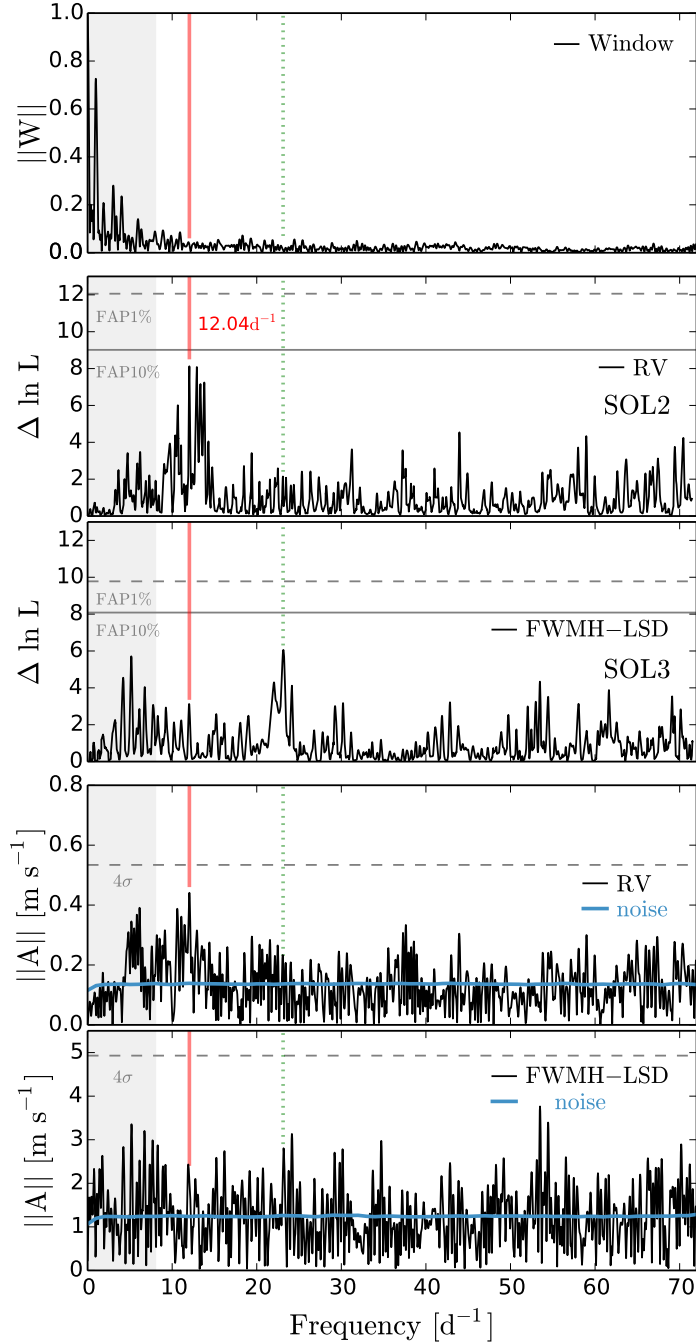
Figure 4.10: GJ 588 analysis of periodicities - GJ 588 Window function (panel 1), RVs and FWHM-LSD Likelihood periodograms (panels 2 and 3) and Power Spectra (panels 4 and 5). The vertical red line highlights a putative signal at $12.04 \, \mathrm{d}^{-1}$ appearing in both the RVs $ln\text{-}\mathcal{L}$ periodogram and Power Spectra. The vertical dotted green line highlights a peak found in the RVs of GJ 699 for which we detect a counterpart in the FWHM-LSDs of GJ 588 (panel 3). Horizontal lines account for different levels of significance. See text for details.
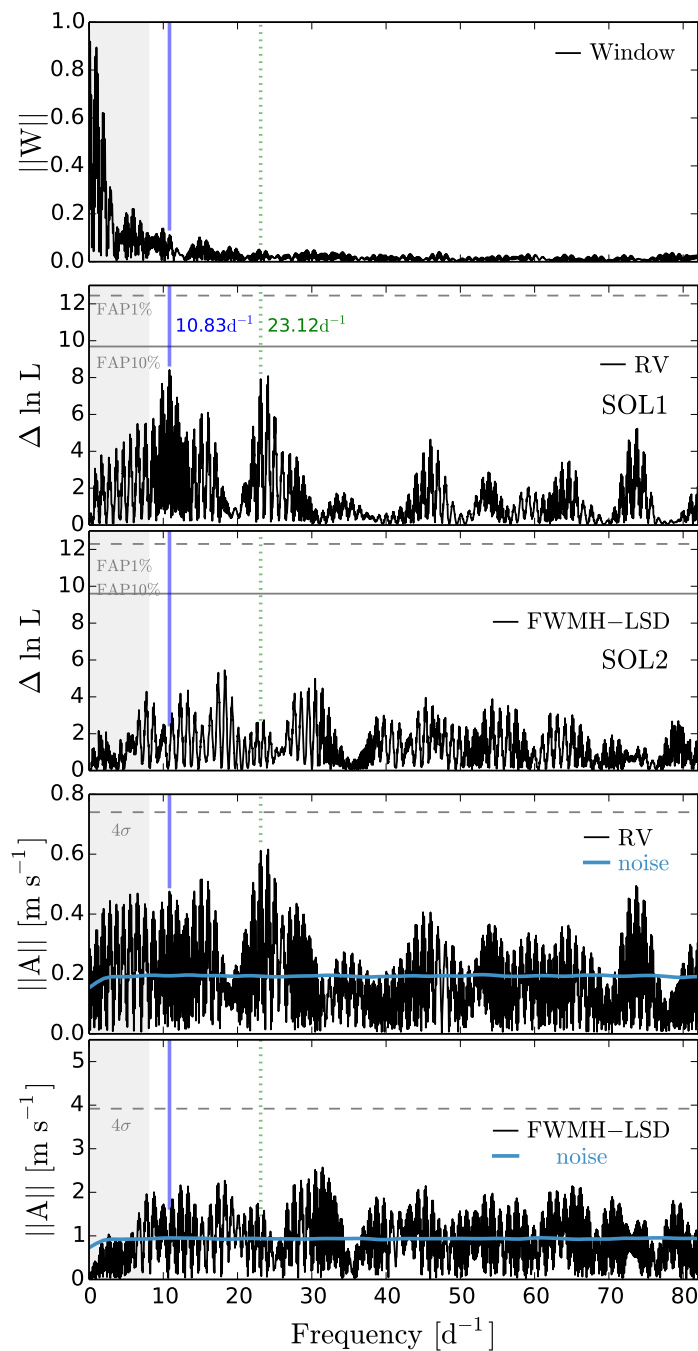
Figure 4.11: GJ 699 analysis of periodicities - Panels follow the same criteria as for GJ 588. The continuous night monitoring halted complicates the window function causing aliases. Like for GJ 588, no significant signals were detected but some structure is present. The two preferred peaks are: 10.83 (vertical blue line) and at $23.12\,\mathrm{d}^{-1}$ (vertical dotted green line), also present in the FWHM-LSD periodogram of GJ 588.
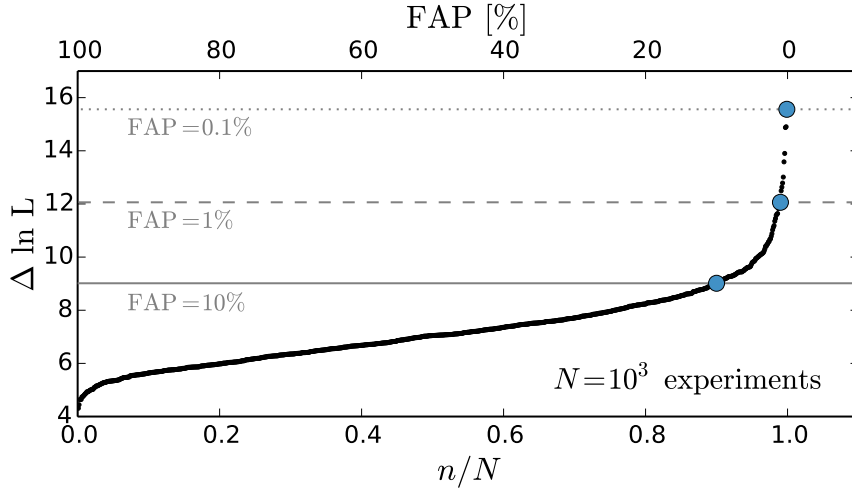
Figure 4.12: Empirical FAP estimation - Bootstrapping approach used to calculated the FAP of the residuals RVs at SOL1. The y-axis corresponds to the maximum $\Delta \ln \mathcal{L}$ resulting for each of the N=10^3 experiments performed. The x-axis accounts for n/N, the cumulative probability of obtaining a certain $\Delta \ln \mathcal{L}$. FAP thresholds are referred to the $n/N = 1$ experiment for which we assume FAP=0%. Horizontal line thresholds correspond to those in the second panel of Fig. 4.10.

do not present any other peak besides $23.12\,\mathrm{d}^{-1}$ for GJ 588, and even when some structure is present, any peak is not even close to the permissive threshold of 10% FAP, for either GJ 588 or GJ 699.

In order to perform an independent assessment, we have also computed the power spectra using the code SigSpec (Reegen, 2007). This code uses a pre-whitening methodology (i.e. it does not globally model all the solutions). As a consequence, in this case we used as input the time-series of the residuals to the best models found with the ln-$\mathcal{L}$ periodograms. That is the residuals to SOL1 ($\sim$ 0.5 days) for the RVs and to SOL2 ($\sim$ 1 and $\sim$ 0.4 days) for the FWHM-LSD of GJ 588; and in the case of GJ 699, the original RVs and the residuals to SOL1 ($\sim$ 0.3 days) for the FWHM-LSD. The power spectra relies on the discrete Fourier transform (DFT) and consists of plotting its amplitude (or the square root of the sum of its real and imaginary squared components) versus a grid of frequencies. In the last two panels of Figures 4.10 and 4.11 I show the RV and FWHM-LSD power spectra which correspond to the ln-$\mathcal{L}$ periodograms of the central panels two and three. The general criterion to consider a peak statistically significant is that it has to have an amplitude at least four times larger than the noise. The grey dashed line in the last two plots indicates this threshold, which was calculated as four times the mean amplitude of the peaks with frequencies higher than $8\,\mathrm{d}^{-1}$ (white area, pulsation range). Again, even when no peak reaches the threshold, we obtained a power excess in the range of a few hours with a preferred peak at $12.04\,\mathrm{d}^{-1}$ in the RVs. In the same way, the

power spectra of GJ 699 showed results comparable to those of the *ln-$\mathcal{L}$* periodograms.

We also calculated the window function (first panel of Fig. 4.10 and Fig. 4.11) using a DFT. This function helps us to identify misleading peaks arising from periodicities caused only by the sampling (e.g. the night-to-night spanning or the span between observations). The reason for the more complicated window function for GJ699 is the time gap between the second and the third night which causes more aliases. However, since the resolution of the individual peaks is inverse to the total time baseline, this is also the reason why in the GJ 699 periodogram the peaks are narrower. Additionally, the window function is a very useful tool because any peak corresponding to a real periodic signal in the time domain, rather than being a simple Dirac Delta function in the power spectra, is a convolution of it with the window function (Gray & Desikachary, 1973). In this case, the window function also indicates that the putative signal at $12.04\,\mathrm{d}^{-1}$ in the case of GJ 588 is far away from the range of influence of the window peaks.

Aiming at checking if the sampling could originate and excess of power in a certain zone, we generated the power spectra of the noise. That is, we calculated the averaged power spectra resulting from 10^3 bootstrapping experiments. Such power spectra were found to be almost flat, as indicate the horizontal blue lines of the bottom panels of Figures 4.10 and 4.11. This means that the sampling does not bias the spectrum of the noise in the absence of signals. Even when the $12.04\,\mathrm{d}^{-1}$ or the 10.83 and $23.12\,\mathrm{d}^{-1}$ peaks do not reach our threshold criterion, the sampling seems not be the cause.

4.4.2 Compatibility with pulsation models

The discussed putative signals may be caused by intrinsic oscillations of the star that might not be necessarily described as single frequency sinusoids. Therefore, as a first step, we have calculated where we could expect to find pulsations with these putative periods in the Hertzsprung-Russell (HR) diagram. This approach will allow us to know if some excited model is compatible with the star parameters, i.e. if the star and the model share the same position in the HR diagram. With this aim, we used the evolutionary tracks from RL14, which were calculated with different models for a range of masses of 0.10-0.60 $\mathrm{M}_\odot$ with 0.05 resolution (see more details about these models in Table 1 from RL14). Later, we perturbed models along these tracks and we explored their pulsation instabilities for modes of degree $\ell = 0$ to 3.

In Figure 4.13 black symbols show the stellar models which resulted to be excited with periods in the range of the observed one for GJ 588 ($\sim$12 d^{-1}). The physical parameters of those excited models set up the *asteroseismic box* of GJ 588 (see A box in Fig. 4.13 defined by $T_\mathrm{eff} = 3687 \pm 98$ K and $\log g = 4.80 \pm 0.03$)). The *photometric box* of GJ 588 was defined to know if the physical parameters of GJ 588 are compatible with those of the models comprised in the *asteroseismic box*. We used the T_eff and $\log g$ values given in the literature to define the box. In particular, we used T_eff=3555$\pm$41 K, and mass and radius determinations of 0.43$\pm$0.05 $\mathrm{M}_\odot$ and 0.42$\pm$0.03 $\mathrm{R}_\odot$ from Gaidos *et al.* (2014) to derived a $\log g$=4.82$\pm$0.08 (see Tab. 4.1)[1].

---

[1]Neves *et al.* (2013) and Bonfils *et al.* (2013) for GJ 588 $T_\mathrm{eff} = 3325 \pm 80\,\mathrm{K}$. However, for the evolutionary tracks in Baraffe *et al.* (1998) and RL14 this value is in clear contradiction with the mass
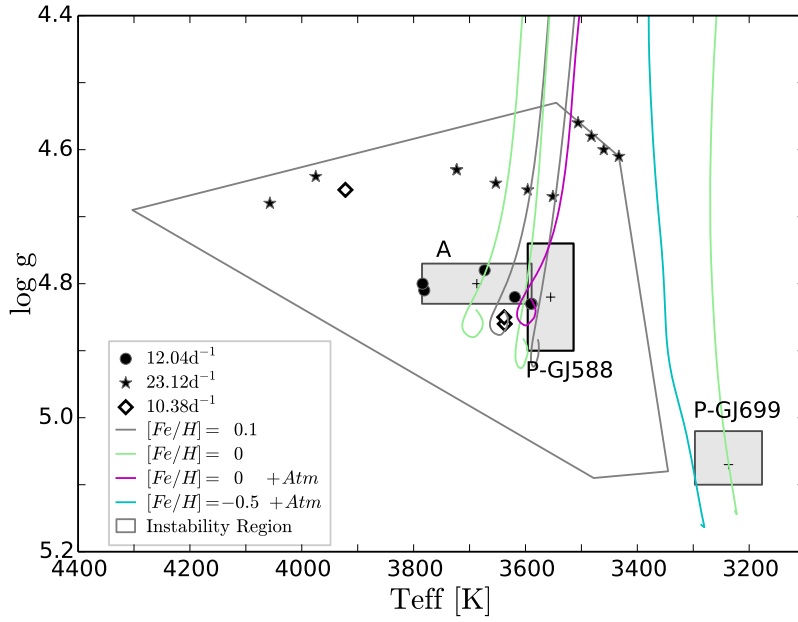
Figure 4.13: Compatible pulsation models - Photometric (P–GJ 588 and P–GJ 699) and asteroseismic (A) boxes in the T_{eff}-$\log g$ diagram. Among the models described in RL14, we only plotted the evolutionary tracks that cross any of these boxes and have metallicities and masses closer to the literature values (0.40 and 0.45 $M_\odot$ and super-solar metallicity for GJ 588, and 0.15 $M_\odot$ and sub-solar for GJ 699). Solar metallicity was also included for comparison purposes. Stellar models including an atmosphere are indicated with the label "Atm" in the legend. All tracks were calculated with a mixing parameter $\alpha = 1$. Solid black dots indicate models excited with a 12.04 d^{-1} period (putative signal of GJ 588). Stars and diamonds correspond to models with $23.12d^{-1}$ and $10.38d^{-1}$ periods (putative signals of GJ 699). The black dot in the intersection of the A and P–GJ 588 boxes (0.45 $M_\odot$ on the magenta track) give theoretical support to the GJ 588 putative signal.

Additionally, in Figure 4.13 I have included the *photometric box* of GJ 699 defined by T_{eff}=3237±60 (Gaidos *et al.*, 2014) and $\log g = 5.040 \pm 0.005$ derived from 0.15±0.02 $M_\odot$ and 0.187±0.001 $R_\odot$ (Boyajian *et al.*, 2012), along with the black stars pointing the models that excite periods at ∼10.83 d^{-1} and diamonds for periods at 23.12 d^{-1}. I also show the evolutionary tracks that cross the photometric or the asteroseismic boxes of GJ 588 and GJ 699. For the sake of clarity, I only show in this figure the evolutionary tracks that have similar metallicity and mass as the stars under study.

In the case of GJ 588, the *photometric box* resulted to be traversed by twelve tracks with masses between 0.15 and 0.50 $M_\odot$; while the *asteroseismic box* was traversed by 19 tracks with masses in the 0.20 to 0.50 $M_\odot$ range. Consequently, evolutionary tracks within the boxes encompass the 0.43 $M_\odot$ mass determination from the literature. The excited models within GJ 588 asteroseismic box have masses in the 0.45 to 0.50 $M_\odot$ range corresponding to low-radial, low degree, ℓ=1, and ℓ=2, *g*-modes. In particular, the excited model in the overlapping boxes has 0.45 $M_\odot$, which would give theoretical support to the putative signal.

On the contrary, results for GJ 699 point to a very different situation. In this case, even when the tracks falling within the *photometric box* are in good agreement with the mass in the literature (6 tracks with 0.10–0.20 $M_\odot$). The excited models at ∼23.12 d^{-1} (∼63 min) and ∼10.38 d^{-1} (∼2.3 h), indicated in Fig. 4.13 with stars and diamonds respectively, correspond to masses (0.40–0.60 M⊙) that do not comprise GJ 699 lower mass determination from literature. Therefore, our pulsation analysis does not support the presence of oscillations in GJ 699, which we recall was out (but close to the edge) of the instability region.

4.4.3 Completeness and signal detectability limit in the sample

In this section we set up an upper limit for the intra-night precision of the HARPS spectrograph. Therefore, if stellar pulsations on M dwarf stars exist and induce Doppler shifts in the spectra, such upper limits would indicate the amplitude threshold that we will be able to detect with a CTB-like campaign in either the RVs or other index.

We performed the following experiment using GJ 588 as reference. We preferred GJ 588 over GJ 699 because, even when they are equally stable, GJ 588 has more data points, and a simpler window function. Firstly, we randomized the measurements to create the time-series of the noise with the observed time span. Later, we added simulated sinusoids of increasing amplitudes (from 0.2 up to 0.8 $m\,s^{-1}$ in steps of 0.02 $m\,s^{-1}$) and random phases. Besides, we tested different frequencies ranging from 0 to 70 d^{-1} to sample the pulsation frequency domain and to measure the dependence of the threshold with frequency. Secondly, we calculated *ln-$\mathcal{L}$* periodograms and we checked when our method succeeded in recovering the amplitude and frequency injected ("positive experiment"). In particular, we performed one hundred experiments for each input amplitude and frequency, varying the noise in all cases. The criterion we chose to define an experiment as positive was to recover both an amplitude within ± 40% of the input value and

---

given by the same authors. Thus, if $M = 0.47\,M_\odot$ holds $T_{\mathrm{eff}} > 3400\,\mathrm{K}$, otherwise the mass would correspond to ∼ 0.2M⊙ models.

a frequency within the resolution range given by the inverse of T, the total time span of the observing run. Finally, we defined the completeness at a certain frequency as the percentage of positive experiments recovered at each input amplitude; thus, the completeness increases with increasing amplitude, as expected. Consequently, fitting a simple S-shape function (or sigmoid function) we could define the limiting amplitude required to reach a 90% completeness with HARPS (see Fig. 4.14).
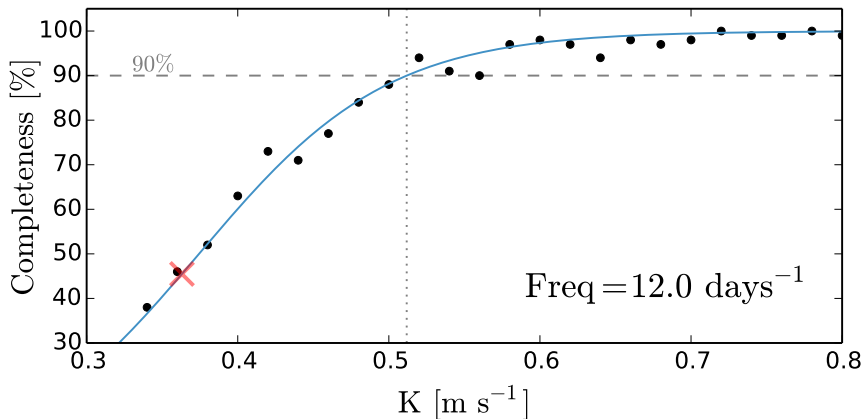
Figure 4.14: Completeness assessment a 12 c/d putative signal period - This plot indicates that a periodic physical phenomenon with a frequency of $12.0 \, \mathrm{d}^{-1}$ should produce a Doppler signal with a minimum amplitude of $0.51 \, \mathrm{m\,s}^{-1}$ (vertical grey dotted line) to be easily detectable with HARPS at with a 90% chance (horizontal grey dashed line). To find this value we fitted a S-shape function (blue solid line) to the black symbols resulting from the "positive experiments". The red cross points shows that the putative signal on GJ 588 is in a region where only a 45% completeness would be expected.

Results for different input frequencies within the stellar pulsation range shown in Figure 4.15 indicate that, in spite of the frequency dependence, if stellar pulsations exist and induce Doppler signals, we will not be able to detect them with HARPS if the induced signal has amplitudes below $0.5 \, \mathrm{m\,s}^{-1}$. The putative signal found in the GJ 588 RVs at $12.04 \, \mathrm{d}^{-1}$ (red solid vertical line in Fig. 4.10), for which we measure an amplitude of $0.36 \, \mathrm{m\,s}^{-1}$, lies in a region where the completeness is only a 45%, which is consistent with recovering tentative but inconclusive statistical evidence for such a signal (see red crosses in Fig.s 4.14 and 4.15).

The same experiment performed over the GJ 699 time baseline resulted in a more conservative detection limit ($\sim 1.20 \, \mathrm{m\,s}^{-1}$). That crucial impact on the detectability of the signal is the result of having three nights of high-cadence data instead of four, and of having consecutive or non-consecutive observing nights that tangle the window function. In other words, even when both GJ 588 and GJ 699 are comparable in terms of stability, the more complicated window function of GJ 699 as a result of the sampling cadence might have prevented us from reaching higher sensitivity.
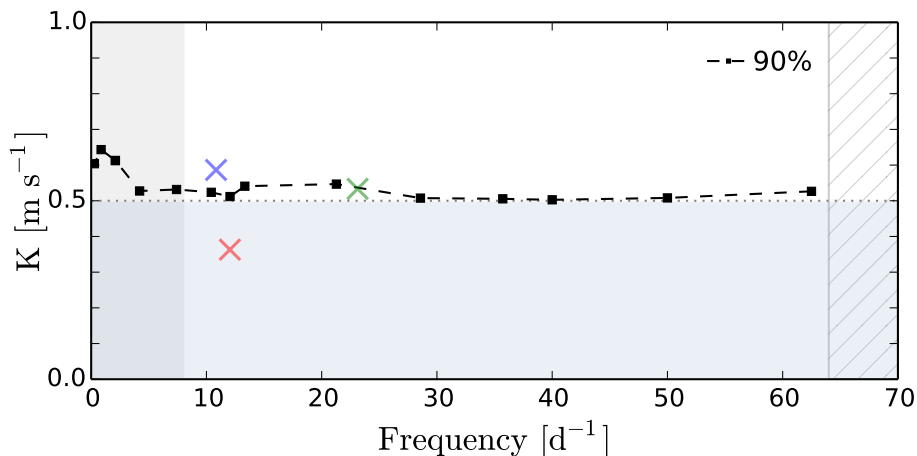
Figure 4.15: HARPS short-term Doppler limit - Limiting amplitudes detectable with a 90% completeness as a function of the frequency. Grey left area is out of the pulsation range. The stripped right area indicates frequencies non-accessible for being of the order of the exposure time. The red cross (GJ 588 putative signal) is below the detection limit. Blue and green crosses (GJ 699 putative signals) are above the limit but the poorer sampling of the GJ 699 observations degrade the completeness 90% limit up to $\sim 1.20\,\mathrm{m\,s^{-1}}$ seriously diminishing our sensitivity.

4.5 Results and discussion

Theoretical studies predict that main sequence M dwarfs can oscillate with periods ranging from 20 min up to 3 h. The detection of such pulsations will open the whole field of asteroseismology for this spectral type; but first stellar pulsation on M dwarfs have to be observationally confirmed. This is one of the goals of the Cool Tiny Beat program (CTB), which makes use of the high-precision spectroscopy given by HARPS and HARPS-N to explore the short time domain of a sample of M dwarfs with high-cadence observations.

The CTB thorough monitoring of the night through high-cadence observations deepens into a time domain which has not yet been widely explored by HARPS. As a result we had to deal with some not very well known instrumental effects. In this study, we detail the main corrections to be applied to deal with such effects and thus we set up a procedure for the analysis of the CTB data. We present here the first results of the survey in the search for stellar pulsations on M dwarfs. In particular, we focused in GJ 588 and GJ 699 (Barnard's star), two of the most long-term stable stars targets of the sample (i.e. with no planet or strong activity reported so far) for which CTB collected four and three whole data nights respectively.

Even when no signals compatible with pulsations were detected above the classical confidence thresholds (FAP=1% or 4 σ) we detected some excess of power in the periodograms and their power spectra for the two targets. More and higher precision data would be needed to confirm/refute them.

4. SEARCHING FOR PULSATIONS ON M DWARFS

Giving serious thought to the fact that the signals could be caused by stellar oscillations, we have checked their compatibility with pulsation models. Results indicate that the putative signal at 12 d^{-1} ($\sim$2 h) found for GJ 588 would be compatible with low-radial, low degree ℓ=1 and ℓ=2 g-modes produced in stellar theoretical models also compatible with the GJ 588 physical parameters in terms of mass, age, T_{eff} and $\log g$. On the contrary, GJ 699 was found not to be compatible with any pulsation mode excited with the period of its putative signals.

Finally, we derived an amplitude detection limit for the search of pulsations on M dwarfs with HARPS. Results indicated that no signal below $\sim 0.5\,\text{m\,s}^{-1}$ can be detected with a confidence level better than 90% on the most Doppler stable M-dwarf studied so far (GJ 588). To obtain this limit, we used the standard CTB observational strategy for the pulsations science case. The higher threshold derived for GJ 699 –for which we only get three non-consecutive nights– demonstrates the crucial impact of the observational cadence in the detectability of a pulsation signature. The success of any spectroscopic program searching for pulsations will ultimately rely on even higher precision but also on optimal sampling strategies.

Before solar-like oscillations were finally detected, many studies on different spectral type stars reported hints of power excess. This was the case of the G2V star α Cen A for which (e.g. Schou & Buzasi, 2001) reported excess of power before the solar-like oscillations were finally confirmed by Bouchy & Carrier (2001, 2002) using the spectrometer CORALIE. This final confirmation came hand by hand with the rapidly improvement of the spectrographs, which aimed at detecting the first exoplanets. This could be the case of M dwarfs oscillations. If theoretical studies are accurate and driving mechanisms can efficiently develop oscillations in M dwarf stars either: i) the amplitudes are very low thus requiring its confirmation of more precise spectrographs (e.g. ESPRESSO/VLT; Pepe *et al.* 2010, or HIRES/E-ELT; Zerbi *et al.* 2014) or, ii) the size of the sample combined with a possible non-pure instability region is preventing us from having an observational confirmation (e.g. only $\sim 40\%$ of the Delta Scuti within its instability region present oscillations (Balona & Dziembowski, 2011)).

In spite of this result, the "Cool Tiny Beats" survey takes us one step closer to the observational detection of M dwarf pulsations and illustrates the challenges of high precision experiments even with current state-of-the-art instrument like HARPS. Besides widening our observed sample with HARPS and HARPS-N we plan to extent the search with ESPRESSO in the near future to monitor both pulsation regions predicted by RL14 with a more targeted asteroseismology sample where models predict pulsations to be more conspicuous.
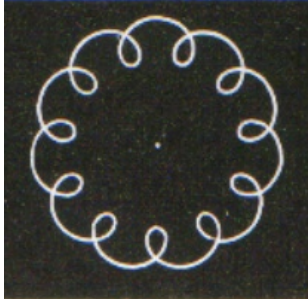
5

Compact orbit planets around M dwarfs

A FTER two decades exploring the sky in search for exoplanets, the huge exoplanet plethora is now a reality. Since the first breakthrough hot jupiters (e.g. 51 Pegasi b; Mayor & Queloz, 1995) new discoveries keep challenging the formation and evolution theories time and time again. Planets in extremely compact orbits around the host star (compact planets) were once considered non-feasible planetary systems by the formation and evolution theories. However, since the first discoveries carried out by *Kepler* (e.g. Kepler-42, Kepler-80, KOI 1843; Muirhead *et al.*, 2012; Ragozzine & Kepler Team, 2012; Ofir & Dreizler, 2013) a significative sample of short-period planets (<3 days) have been discovered. Once again the exoplanet diversity was wrecking our preconceived ideas. One of the "Cool Tiny Beats" (CTB) project goals is the discovery of such planetary compact systems around M dwarfs. This Chapter is organized as follows: In Section 5.1 I present the results of the study focused on Luyten's star (these results will be published soon after this PhD thesis). Additionally, Sections 5.2 and 5.3 focus on the detection of two planets orbiting the Kapteyn's star (Anglada-Escudé *et al.*, 2014),

as well as on our recently discovered Proxima b, a temperate Earth-mass planet around our closest neighbor Proxima Centauri (Anglada-Escudé *et al.*, 2016a).

5.1 Planet candidates orbiting Luyten's star

Luyten's star, also known as GJ 273, is a main-sequence mid-type red dwarf (M3.5V). This target was selected for our CTB high-cadence monitoring for being bright and nearby (9.87 V_{mag}, 3.8 pc or 12.4 ly; Koen *et al.*, 2010), and for not having planets reported so far (see the stellar properties in Tab. 5.2). These characteristics made it the focus of many studies in the past, such as those in the late 80's and early 90's attempting to detect a brown dwarf for the first time (e.g. Henry & McCarthy, 1990). More recently, these characteristics made GJ 273 to be part of surveys looking for low mass planets (e.g. the HARPS-GTO survey; Bonfils *et al.* 2013, or the newer CARMENES survey; Quirrenbach *et al.* 2014).

Up to day, only Bonfils *et al.* (2013) reported, using HARPS, a vague signal of 440 days in radial velocities of GJ 273. They associated this signal to a very eccentric orbit. The poor phase-coverage, along with the predicted high eccentricity of the signal, prevented them from giving a strong conclusion about the nature of the signal. Instead, they concluded it may be an alias of a long term trend.

The stellar activity can be the cause of such long term trends. Recently, Suárez Mascareño *et al.* (2016), using the All Sky Automatic Survey (ASAS), reported for GJ 273 a period of 6.6 ± 1.3 years thought to be due to a magnetic cycle. Furthermore, in a previous work from 2015, the same team reported the rotation period of the star (usually coupled with starspots or plage events) to be 115.9 ± 19.4 days (Suárez Mascareño *et al.*, 2015).

In this study, we have used radial velocity (RV) measurements from our CTB survey in combination with public data from the HARPS archive to search for periodic signals in Luyten's star. Additionally, and with the aim of ruling out signals driven by stellar magnetic activity, we have also monitored several photometric and chromospheric indices. Next sections present the indices and the analysis of the periodic signals.

5.1.1 Observations and measurements

5.1.1.1 Radial velocity datasets

The GJ 273 high-cadence observations were obtained with the CTB program and comprise data from both HARPS and HARPS-N (see more details about the instruments in Chapter 2). In total, we collected 58 spectra with HARPS during a run of nine nights between December 2013 and January 2014. From HARPS-N we obtained 52 spectra during five consecutive nights in March 2016. However, we had to discard two spectra for having low SNR, therefore only 57 and 51 spectra were used respectively from HARPS and HARPS-N (see a summary of the main observational parameters in Table 5.1, the corresponding RV time-series are shown in Fig. 5.1).

In addition to the CTB high-cadence data, we have also included in this study public observations available in the HARPS archive. Then, the complete HARPS dataset is comprised

Table 5.1:   Observational parameters of the high-cadence CTB runs.

Instrument (1)	Run (2)	Nights (3)	N (4)	$AM_{\max}$ [arcsec] (5)	Seeing [arcsec] (6)	SNR (7)
HARPS	30 Dec 2013 - 10 Jan 2014	9n	57	2.3	0.6 - 1.5	37 - 69
HARPS-N	3-8 Mar 2016	5n	51	2.1	1.4 - 2.7	29 - 72

Note. — Main observational parameters of the CTB high-cadence runs. Col 1: Instrument; Col 2: Date of the run; Col 3: Number of nights observed; Col 4: Number of spectra used in this study; Col 5: Maximum airmass reached during the run; Col 6: Minimum and maximum *seeing* values during the run; Col 7: Range of SNR values measured at order 60 ($\sim$ 631 nm).
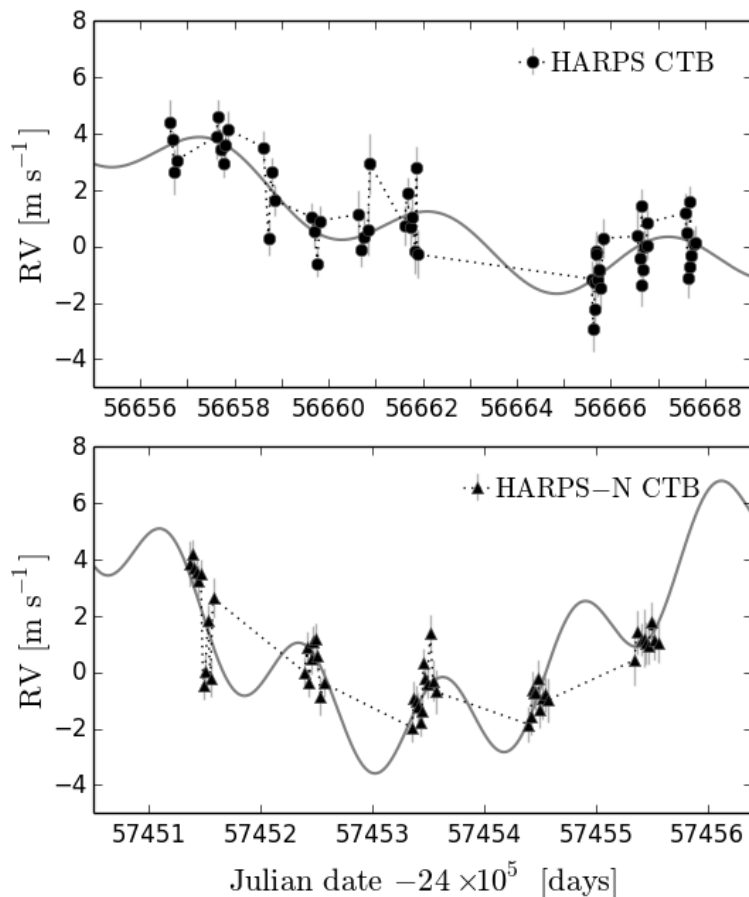
Figure 5.1: **RV time-series of the high-cadence runs observed with the CTB survey** - (Upper panel) data taken with HARPS between December 2013 and January 2014. (Bottom panel) observations performed from HARPS-N in March 2016.

of 276 spectra spread out over 12 years (from 2003 to May 2015). This dataset also includes nightly bins of our CTB high-cadence data. In the Figure 5.2 the black dots show the RVs time-series of the complete HARPS dataset, while the grey dots highlight the data obtained as part of the CTB survey.
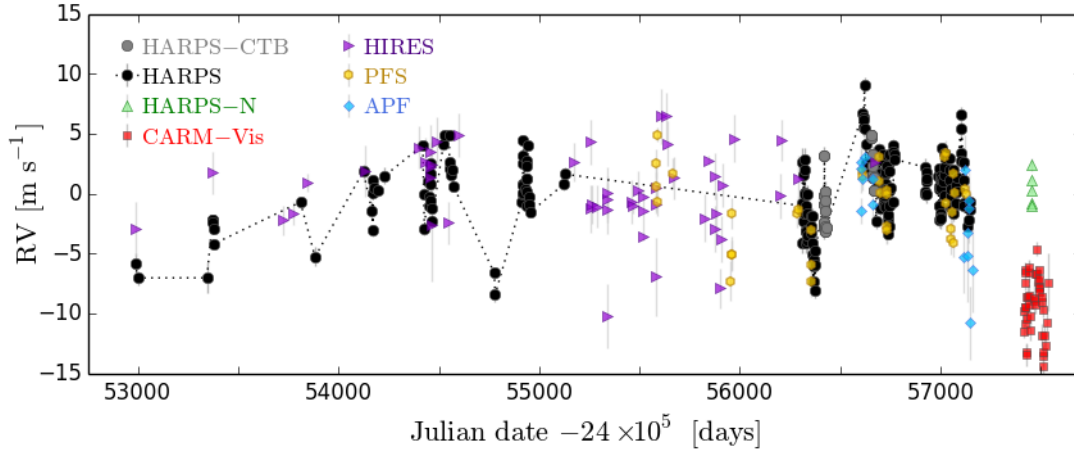
Figure 5.2: RV time-series from different instruments - These are the nightly binned RVs included in this study. Black dots refer to archival data from HARPS, while grey dots highlight those from our CTB program (two campaigns, one at high-cadence carried out in Dec 2013–Jan 2014 and a previous one at low-cadence in May 2013). We have also used RVs from HARPS-N and from four other instruments, including visible newly CARMENES data. The color code is: HARPS-N green up triangles; CARMENES, red squares; HIRES, purple right triangles; PFS, yellow hexagons; APF, blue diamonds.

Besides nightly bins RV time-series from HARPS (CTB + archive data) and HARPS-N (CTB data), we have also used in this study Doppler measurements from other four instruments, including the new CARMENES spectrograph. The CARMENES dataset comprises some of the first observations collected with the visible spectrograph. Among the 77 RVs measurements, only 66 datapoints remained after filtering clear outliers. The filtered data of each night were later binned resulting a final RV time-series of 42 measurements for CARMENES (see Fig. 5.3). We decided to nightly bin the observations taken during the same night to avoid statistical biases of the resulting signals caused by higher weights of the nights accumulating a large number of measurements. The RV time-series from the other three spectrographs correspond to: i) a dataset comprising 63 nightly binned data obtained from the initial sample of 75 spectra observed from 1997 to 2014 with the HIRES spectrograph, ii) 34 nightly binned RV data from a initial sample of 36 observed from 2011 to 2015 with PFS spectrograph, and iii) 15 nightly binned RVs for the original sample of 27 data observed during 2 years, from 2013 to 2015, with the APF spectrograph. More details about these instruments, as well as a comparison of their capabilities, can be found in Chapter 2. Figure. 5.2 shows the RV time-series from the different

instruments used in this study.
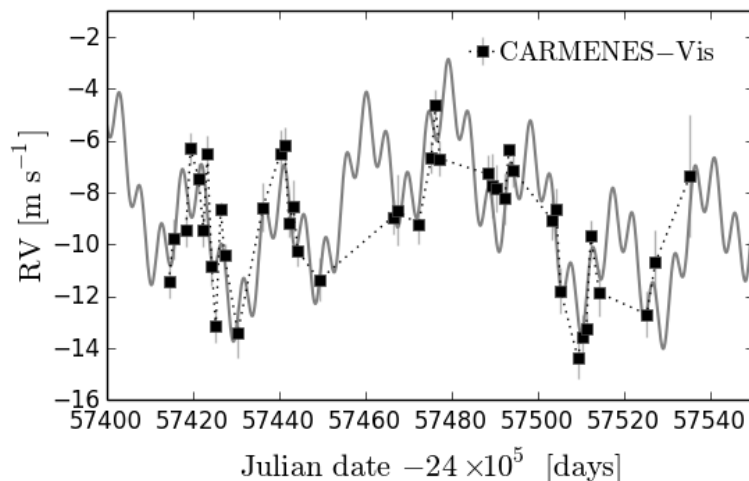
Figure 5.3: RV time-series from CARMENES - GJ 273 RVs observed with the CARMENES visible spectrograph since January 2016. The total sample of 42 datapoints results from filtering outliers and binning the RVs of each night.

The HARPS and HARPS-N spectra were extracted and wavelength calibrated using the standard Data Reduction Software (DRS). To calculate the RVs we used the template matching algorithm implemented in the TERRA software (Anglada-Escudé *et al.*, 2012a). See Chapter 2 for more details about the RV extraction and the method in which TERRA is based. The CARMENES spectra were extracted and wavelength calibrated using CARACAL[1], the first standard pipeline of CARMENES; the RVs were computed with the second pipeline SERVAL[2]. The RVs of the other instruments were obtained using the iodine cell technique as described in Butler *et al.* (1996).

5.1.1.2 Chromospheric activity indices

In this study we have investigated the variability of several chromospheric indices, which are supposed to originate in the active regions, with the aim of identifying tracers of spurious Doppler variability. Besides computing the HARPS and HARPS-N RVs, we used TERRA to calculate the equivalent width of certain individual spectral lines. In particular, we have analyzed the variability of the H_α, Na I D1 and D2 lines, and Ca II H+K lines, which are respectively proxies for the activity in the upper, middle-to-lower, and lower part of the chromosphere. See below a detailed explanation of the calculation of these chromospheric indices:

- **Ca II H+K *S*-index:** HARPS was designed to include in the spectrum the H and K lines of the Ca II that appear at 3968.47 and 3933.68 Å, respectively. In that way we can

---

[1]https://carmenes.caha.es/ext/conferences/CARMENES_TOEII2014_Zechmeister.pdf

[2]https://carmenes.caha.es/ext/conferences/CARMENES_SPIE2016_Caballero.pdf
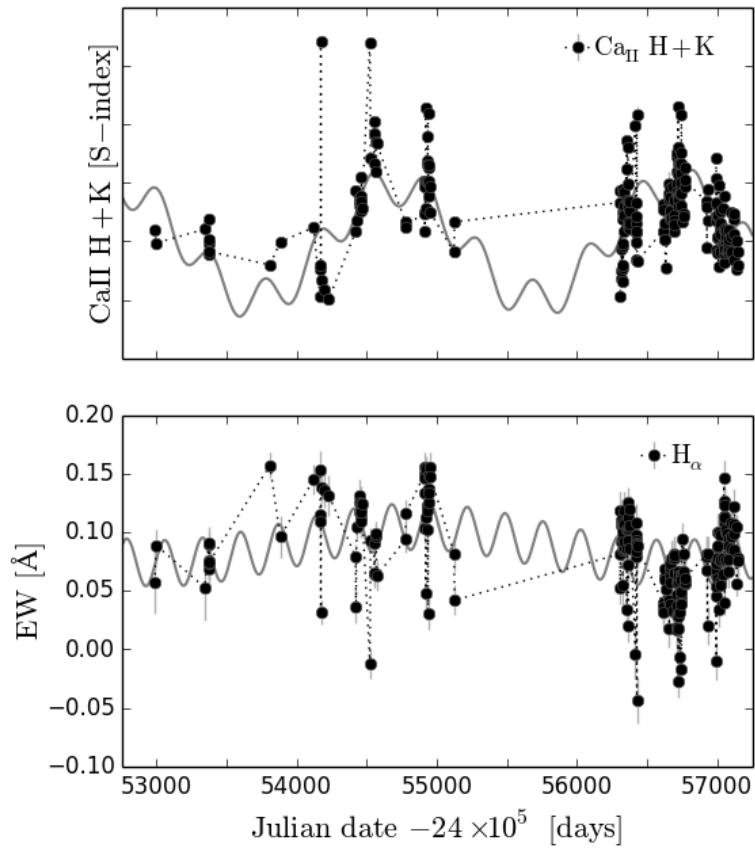
Figure 5.4: Chromospheric indices time-series I - S-index, obtained from the Ca II H and K lines (top panel), and H_α (bottom panel) time-series for the complete HARPS dataset. Both indices were cleaned from strong flare events.

monitor the Ca II variability simultaneously with the star Doppler shifts through the so-called S-index, calculated following Boisse *et al.* (2009). That is, firstly we summed the flux within two triangular bandpasses of 1.09 Å centered at the H and K lines and secondly we normalized them by the integrated flux obtained from two 20 Å width reference windows (one bluer than the doublet at at 3891 Å, and another redder at 4001 Å). The uncertainties were calculated as the sum of the variance of the data within each bandpass.

- **H$_\alpha$ emission index:** Similarly to the process used for the S-index, TERRA computes H$_\alpha$ by summing the flux within a square bandpass of 0.678Å centered at H$_\alpha$ (6562.808 Å), and later it normalizes the resulting value by the continuum level obtained from two windows centered at 6550.870 and 6580.309 Å of 10.75 and 8.75 Å widths. Again the uncertainties were calculated as the sum of the variance of the data within the bandpasses.

- **Na I D1 and D2 lines index:** TERRA computes this index in a similar way than Díaz *et al.* (2007). That is, it calculates the averaged flux in the core of the lines D1 (5895.92 Å) and D2 (5889.95 Å) using 1 Å bands, and later this value is normalized using two continuum bands of 10 and 20 Å centered at 5805.0 and 6090.0 Å . The uncertainties were calculated as for the other chromospheric indices.

For red M dwarfs such as GJ 273 the Na I D proxy is preferably compared to the S-index. The reason is that the Ca II lines appear in the blue part of the spectrum and thus have typically lower SNR compared with the Na I D lines (Gomes da Silva *et al.*, 2011). Between H$_\alpha$ and Na I, the latter is also preferred in the case of M stars. The reason is that H$_\alpha$ is more sensitive to stellar flare events, and the mid-M stars are common flare stars (Hawley *et al.*, 2014). However, aiming at comparing the different indices, all were included in this study. The large time coverage of the complete HARPS dataset made it the most suitable for recovering possible long-term activity signals. Thus, this was the only dataset for which we have analyzed the chromospheric indices. Figs. 5.4 and 5.5 show the corresponding time-series.

Flares and radial velocities − Removing the flare events from the chromospheric indices is necessary in order to search for periodicities in their time-series, otherwise the punctual flares events bias the parameters of the sinusoidal models used. We take advantage of the H$_\alpha$ flare sensitivity and of its correlation with Na I to filter out these events. A similar approach was used in previous studies (e.g. Robertson *et al.*, 2015). In particular, we have removed all datapoints beyond $\pm 3\,\sigma$ from the H$_\alpha$ - Na I D1 linear correlation (see Fig. 5.6). Flare events were removed from chromospheric indices but not from the RVs. Typical flares should not cause correlated shifts in the RVs as our simultaneous spectroscopic and photometric observations of Proxima Centauri concluded (Anglada-Escudé *et al.*, 2016a).

5.1.1.3   Mean line profiles indices

The gravitational pull induced by a planet causes all the spectral lines to move as a whole: it causes a pure Doppler shift. On the contrary, other effects such as the stellar pulsations,
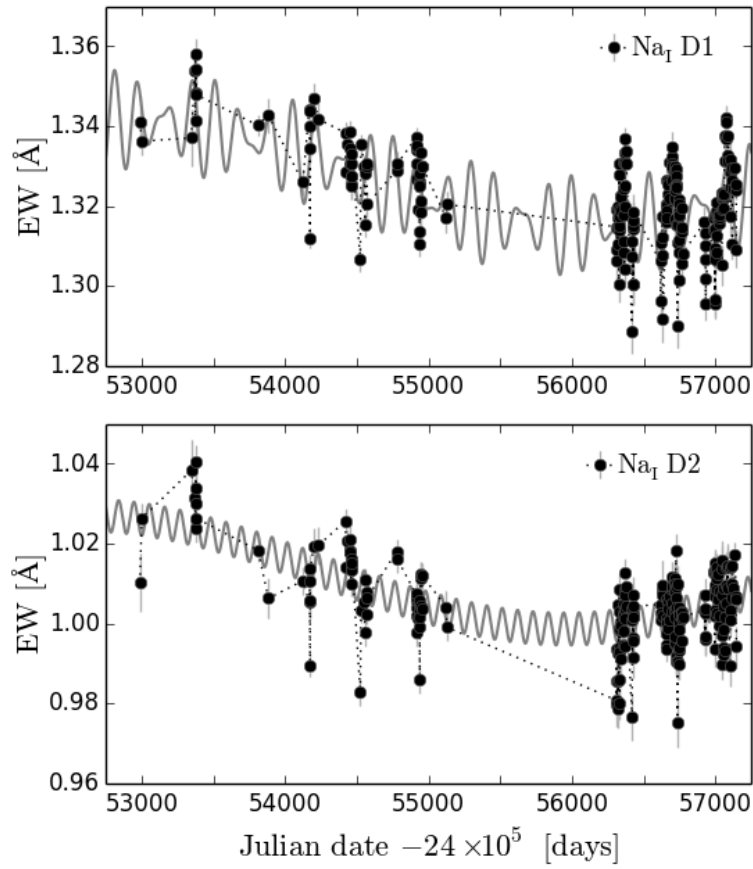
Figure 5.5: Chromospheric indices time-series II - Na I D1 (top panel) and D2 (bottom panel) time-series for the complete HARPS dataset. Flares were previously removed from both indices.
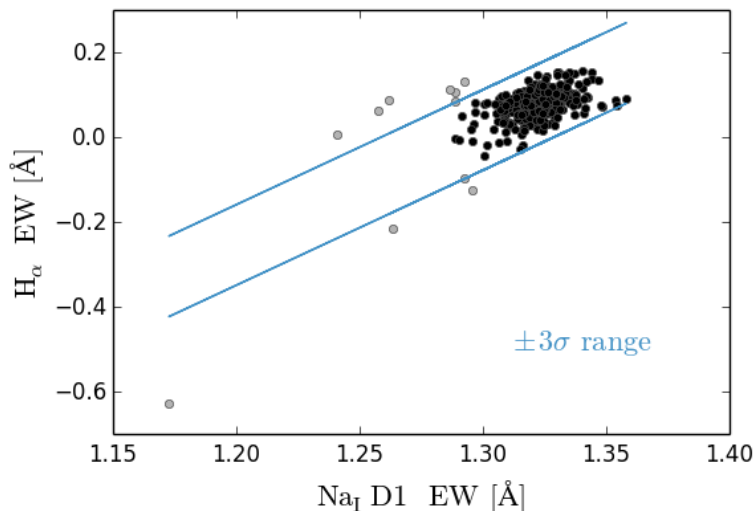
Figure 5.6: Linear correlation of H$_\alpha$ and Na I D1 chromospheric indices - Grey dots indicate the datapoints outside the range delimited by the two blue solid lines, i.e. the datapoints beyond $\pm 3\,\sigma$ from the H$_\alpha$–Na I D1 linear correlation. This was the criterium followed to filter out suspicious flare epochs in the chromospheric indices time-series.

the stellar activity or even instrumental effects can distort the shape of spectral lines besides producing Doppler shifts. This is the main reason to simultaneously monitor the spectral lines centroids (i.e. the RVs) together with other parameters accounting for the spectral line shape.

The standard DRS pipeline cross-correlates the observed spectrum with a binary mask to generate a mean-line profile (or CCF). From them two measurements of shape are derived: the bisector span (or BIS), that measures line asymmetries, and the full-width-at-half-maximum (or FWHM), that accounts for width and contrast changes. However, as stated in Chapters 3 and 4, these CCFs do not have trivial shapes in the case of M stars. The reason is the large quantity of spectral lines, typical of cool stars, which cause blending effects during the cross-correlation step. Consequently, besides the FWHM and BIS, we have also computed the indices m_2 and m_3 (see time-series in Fig. 5.7 and 5.8). These indices correspond to the second and third central order moments of a mean-line profile obtained with a Least-Squares Deconvolution (LSD) technique (Donati *et al.*, 1997). Such technique has demonstrated to be a better choice for M stars (Barnes *et al.*, 2012) and it is based in convolving the spectrum with a template formed by line positions and intensities. The resulting mean-line profiles can be assumed to be a probability distribution function and thus we can calculate their central order moments following Press (1992). In particular, in this study we have used m_2, which corresponds to the variance of the line and thus accounts for symmetric variabilities, and m_3, which accounts for line asymmetries. As for the chromospheric indices we only analyzed the complete HARPS dataset indices.

Before calculating the LSD mean-line profiles we have detrended the slope of the spectral
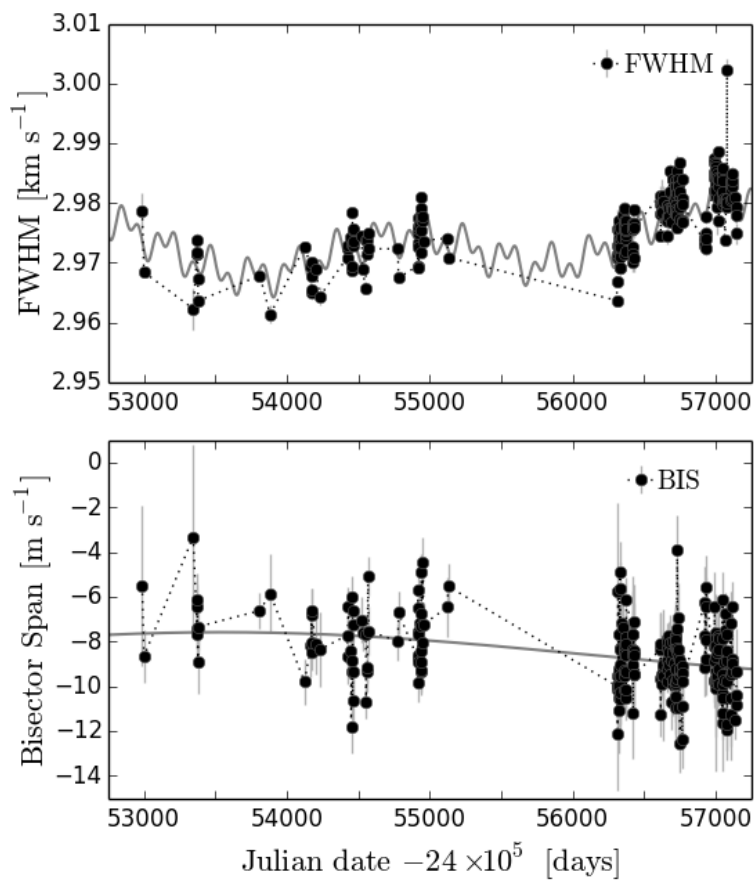
Figure 5.7: Shape indices from the DRS-CCFs: the FWHM and BIS - The FWHM (upper panel) and the BIS (bottom panel) are given by the HARPS-DRS pipeline and measure the width and the bisector span of the mean-line profiles obtained from a cross-correlation method. This series correspond to the complete HARPS dataset.

energy distribution (SED) discussed in Chapter 3. We applied the same procedure explained in Chapter 4, that is, we matched the blaze and SED slopes of all the spectra to the highest SNR spectrum. The central moments uncertainties were obtained empirically and correspond to the standard deviation of the difference between consecutive datapoints later scaled by the SNR of each measurement. We could have calculated the FWHM and the BIS of the detrended LSD mean-line profiles as we did in Chapter 4, instead we decided to use m_2 and m_3 to show that they are a valid alternative. Indeed, they were the only indices used in Proxima Centauri's work, where both, but in particular m_2, demonstrated to behave well (see Sec. 5.3 for more details).
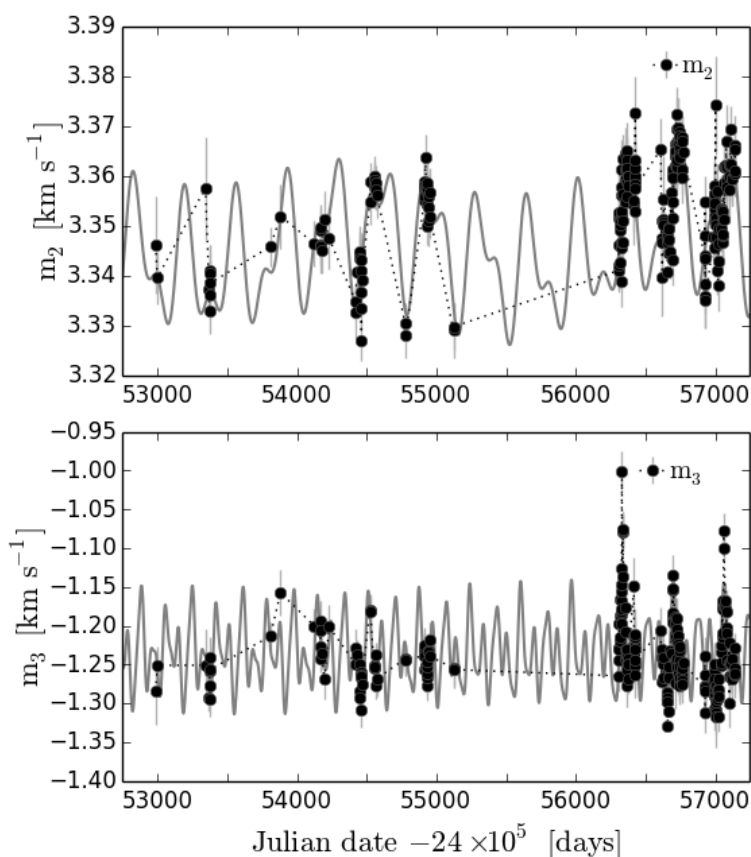
Figure 5.8: Shape indices from the LSDs profiles: m_2 **and** m_3 - The m_2 (upper panel) and m_3 (bottom panel) indices correspond to the central order moments of the mean-line profiles calculated with a LSD technique. They respectively account for symmetric and asymmetric changes in the profile shapes. The SED slope changes were removed from the LSD profiles before computing these indices.

5.1.1.4 Photometric datasets

Additionally to all the spectroscopic indices previously described in this Section we have also included two photometric datasets. On the one hand, we have checked the long-term variability of the GJ 273 absolute photometry using V-band data from the all sky survey ASAS (Pojmanski, 1997), and on the other hand, we used our observations from the 90-cm telescope installed at the Observatorio de Sierra Nevada (OSN) to obtain short-term differential photometry in V and R bands.

The ASAS survey runs from Las Campanas Observatory since 1998 and monitors targets up to DEC $< 28°$ with an average accuracy of ~ 0.05 mag. We used this series with the aim of monitoring sources of long-term signals that modify the star integrated flux such as the activity cycles. After filtering duplicated measurements and outliers[1], the final V-band dataset comprises 312 observations spread over 8 years since 2001.

The OSN observations were performed between January and February 2016. These observations are part of a campaign designed to catch the transits of the two planetary signal candidates we had at that time, those were signals with 18 and a 4.7 days periods. Among the 14 nights of observations six nights were within the $\pm 99\%$ probability transit window of the 4.7-day signal and one within the window of the 18-day signal. We did not detect any clear transit signature. However, the phase is not well covered yet (we will keep observing GJ 273 in 2017). In spite of this negative result, we used nightly bins of these time-series to check if any short-time signal is the RVs were also present in the photometry. In Fig. 5.9 I show the nightly binned photometrical time-series from the OSN V and R bands and from ASAS.

5.1.2 Search for periodic signals

In this section I show a homogeneous search for periodic signals in all the time-series previously described. For this goal, we used the likelihood-ratio periodograms described in Chapter 2. The model used for fitting the Doppler time-series includes, besides the Keplerian parameters, a *zero-point velocity* term, and a *linear trend* (see the whole model equation in Chapter 2). The first one accounts for constant offsets in the data, while the second one accounts for large velocity trends. Since long-term activity signals can look like linear trend in the short term, we did not include the linear trend term in the modeling of other indices different from the RVs. In all periodograms the black curve accounts for the first signal while the grey, orange, blue and green curves account respectively for signals from two to five. I want to note that we did not use pre-whitening procedures to search for the signals after the first one. Instead, when searching for a second signal, we included the first one in the model and let its parameters slightly change, i.e we refined the parameters of the previous solutions with every new search. The red vertical lines in the periodograms refer to the planet candidates, while the grey areas mark the range of periods predicted by Suárez Mascareño *et al.* (2015, 2016) for the Luyten'star rotation period and magnetic activity cycle.

---

[1]Data quality is flagged from "A" (best data) to "D" (worst data) in the ASAS database: `http://www.astrouw.edu.pl/asas/?page=aasc`.
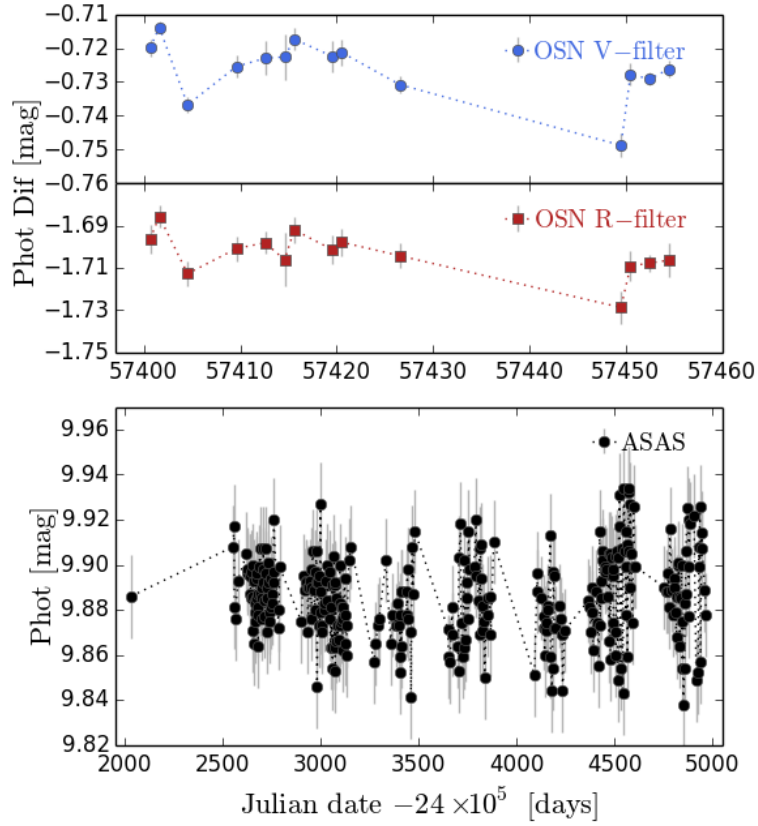
Figure 5.9: Photometrical time-series - OSN short-time differential photometry in V and R bands (top panel) obtained from the 90-cm telescope. The series are nightly binned. The original were used to search for transit signal without success. The negative measurements indicate that GJ 273 is weaker than the star field used to get the differential photometry. The V-band ASAS absolute photometry (bottom panel) was used to search for long-term stellar activity signals.

5. COMPACT ORBIT PLANETS AROUND M DWARFS

5.1.2.1 Radial velocities time-series

We present here the analysis of the Doppler time-series obtained with the different instruments. We obtained the early evidence from our CTB high-cadence program. Both, the HARPS-N and HARPS CTB time-series showed evidence for a $\sim 5 - 6$ day period signal. Additionally, we also got hints for a larger period when we do not include the *linear trend term* in the model. In Fig. 5.10 the black solid line corresponds to classic F-ratio periodograms, while the vertical black arrows indicate the likelihood maxima. In the upper panel, the periodogram of the RVs from HARPS, shows evidence for a signal longer than ~ 20 days, along with a peak of ~ 6 days. However, the short amount of data (not many datapoints comprise the nightly binned CTB series since the program was designed to sample the sub-day domain), combined with a short time baseline, prevent us from resolving these peaks. Despite that, we detected two peaks at 1.059 and 1.196 days that would correspond to 1-day aliases of signals with 17.949 and 6.102 days periods. In the same way, the periodogram for the HARPS-N RVs (bottom panel) indicates to a signal longer than ~ 5 days, that could be better constrained if the peak at 1.273 days is a 1-days alias of a 4.663 days peak.

With the aim of better delimiting these signals, we have analyzed the complete HARPS Doppler dataset (see likelihood-ratio periodograms in Fig. 5.11). Results show two clear signals at 4.72 and 18.64 days. These peaks are compatible exoplanetary signals and fits well with the CTB predictions. The peaks surrounding the 18.64 days signal correspond to its annual and daily aliases (see a zoom in Fig. 5.12). Although both signals are strongly detected (they are far over the conservative 0.1%-FAP threshold), we only recovered them after including into the model other long-term signals (see black, grey and orange periodograms maxima). These long-term signals could be due to stellar variability, long period planets or even instrumental long-term variability. Including the RV time-series of other instruments can allow us to confirm if the signals are real and stable. In other words, even if the data from the individual instruments can not confirm the signals by themselves, they can help in discarding spurious signals.

The analysis of the RV time-series observed with CARMENES revealed variability at $\sim$ 4.7 and 19.5 days (compatible with the 1-day alias of a $\sim$ 18.64-days periodic signal). This result However, we will have to get more data to gain significance and independently confirm the signals detected with HARPS. (see in Fig. 5.13 the predicted peaks below the 0.1%-FAP criteria). But the likelihood periodograms allow us to fit several instruments at the same time as independent datasets. When we combine the HARPS and CARMENES RVs the planet candidate signals stay and even increase in significance, while the distribution of the long-term signals slightly changes. The same happens when we combine all the instruments. In this case, the other instruments do not destroy the signals of the planet candidates (i.e. we obtain similar $\Delta \ln \mathcal{L}$ values that for HARPS only), but many other spurious signals are vanished. Still, two main long-term signals remained at 418 and 530 days. Moreover, the forest of signals with P > 30 days indicate that GJ 273 may be slightly active. In the next section we analyze the remaining indices to rule out that the signals of the planet candidates arise from stellar activity variability.
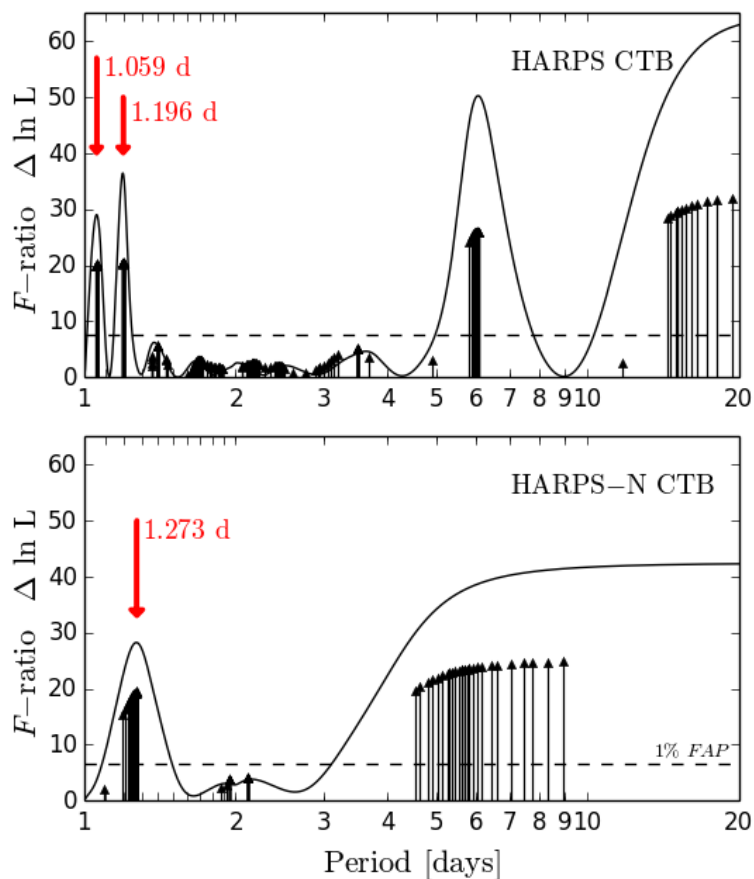
Figure 5.10: Likelihood periodograms of the RV time-series from the CTB high-cadence runs - The top panel illustrates high-cadence HARPS data, while the bottom panel corresponds to HARPS-N. Black solid lines correspond to F-ratio periodograms. Due to the short length of the nightly binned CTB time-series the likelihood-ratio periodogram do not sample well this range of periods. The vertical black arrows represent maxima of the likelihood function. We suspect that the peaks highlighted with red vertical arrows correspond to 1-days aliases of longer period signals.

121
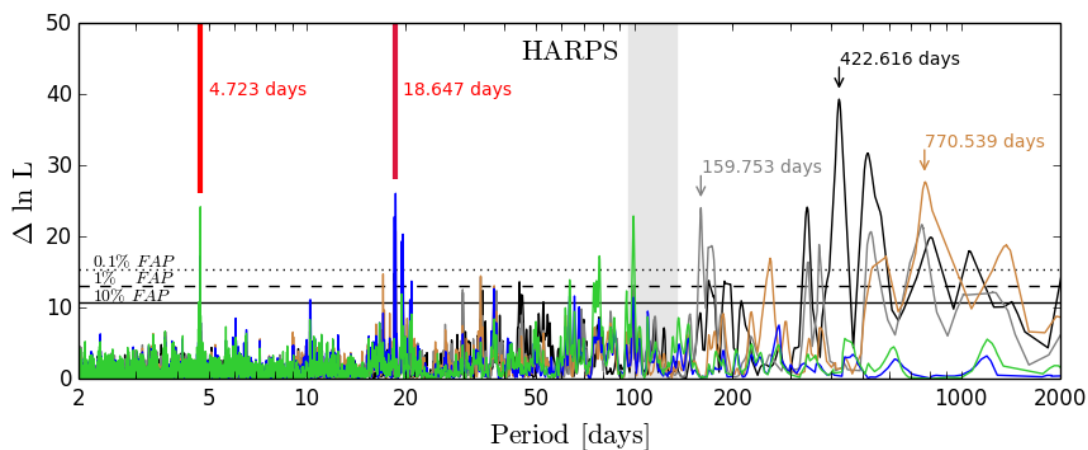
Figure 5.11: Likelihood-ratio periodogram for the complete HARPS RVs -
Nightly binned CTB data are also included in the analysis. Two signals at 4.72 and
18.65 days, compatible short period exoplanets, are detected after accounting for other
three long-term signals.
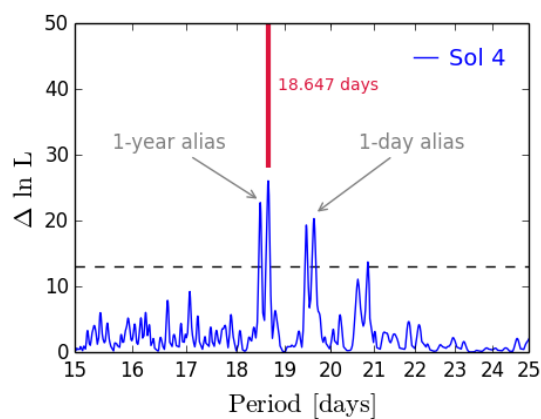
Figure 5.12: Zoom of the complete HARPS dataset periodogram - Detailed region
of the periods close to the ∼18 days signal. The adjacent peaks correspond to annual and
daily aliases.
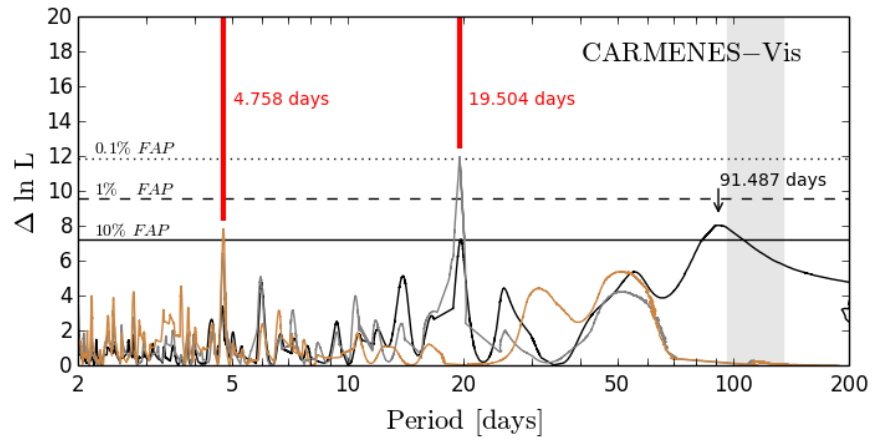
Figure 5.13: **Likelihood-ratio periodogram for CARMENES RVs** - The CARMENES RVs, observed with the visible spectrograph, agree with the result from HARPS. More observations are required to have a strong detection.
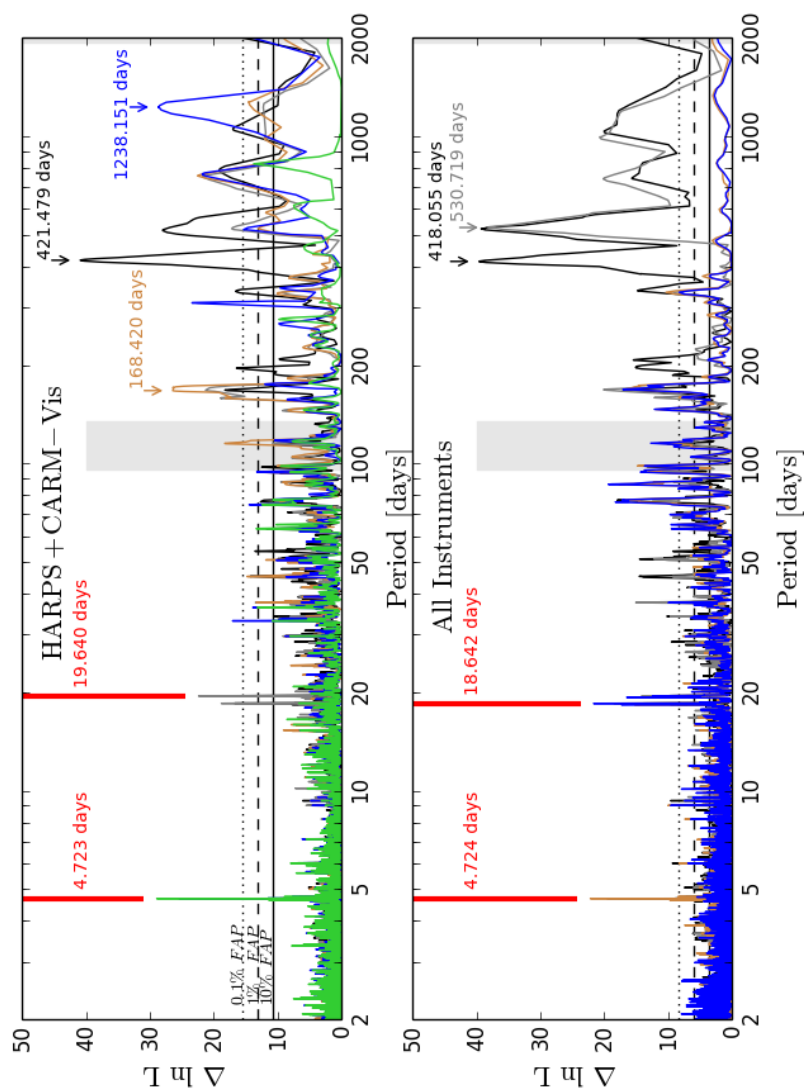
Figure 5.14: Likelihood-ratio periodogram for instruments combinations - The HARPS + CARMENES combined periodograms are shown in the top panel while a combination of all the instruments is shown at bottom. Some spurious signals were cleaned, on the contrary, the signals of the candidate planets remained.

5.1.2.2   Chromospheric activity time-series
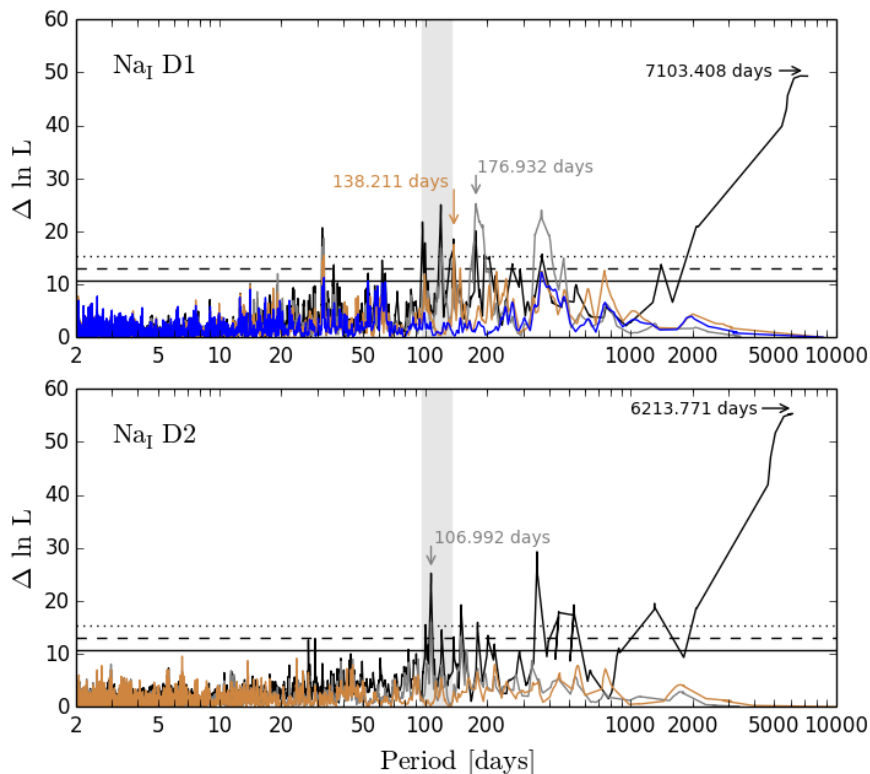
Figure 5.15: Likelihood-ratio periodograms of chromospheric activity indices I
- The Na I D1 (upper panel) and Na I D2 (bottom panel) periodograms revealed long-term signals in the long term. The lack of peaks in the short-term support the planetary origin of the ~ 4.7 and ~ 18.6 days signals detected in the RVs.

The analysis of the chromospheric activity indices revealed no signals at the periods of the planet candidates (see Fig. 5.15 and 5.16). On the contrary, periodograms show many signals in long-term which indicates that GJ 273 is not a quiet star. The excess of $\Delta \ln \mathcal{L}$ in the range of thousand days points to an activity cycle. Among them, the 1929 days peak in the S-index is the signal better fitting within the range predicted by Suárez Mascareño *et al.* (2016). Furthermore, the Na I D1 and D2 periodograms show several peaks in the range predicted for the stellar rotation period. Additionally, all periodograms show peaks close to 1-year aliases and its submultiples (e.g. 382.4 days in the Ca II H+K, or 176.9 days in the Na I D1). These, and many of the other signals, most probably arise due to the convolution of the stellar activity with the observational cadence (see the spectral window function in Fig. 5.17). Consequently, the analysis of these indices revealed that the activity of Luyten's star is not as low as for other stars of the same spectral type. This result questioned the origin of the $\sim$400 days period detected also by Bonfils *et al.* (2013). However, the lack of peaks at shorter periods support

the planetary origin of the ~ 4.7 and ~ 18.6 days signals.
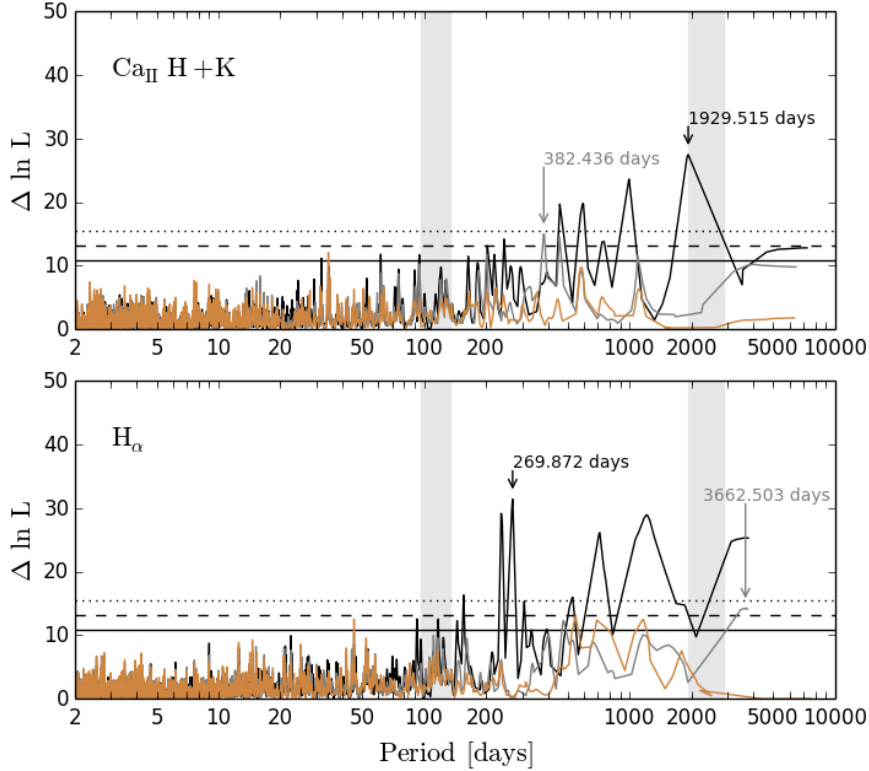
Figure 5.16: Likelihood-ratio periodograms of chromospheric activity indices II - The *S*-index (upper panel) and the H $_\alpha$ (bottom panel) periodograms present also long-term variability while are clean in the range of the predicted planets.

5.1.2.3   Mean line profiles time-series

The periodograms of the indices accounting for changes in the mean-line profiles shapes did not show any signal compatible with the planet candidates. Similarly to the chromospheric indices no peaks with P < 20 days arose in the periodograms (see Fig. 5.18 and 5.19). The periodogram of the FWHM revealed also long-term variability compatible with the Suárez Mascareño *et al.* (2016) activity cycle. The BIS time-series resulted to be very stable, however, it also show hints for a long-term period. The m_2 and m_3 time-series, which have demonstrated to trace the photometry variability in Proxima b (Anglada-Escudé *et al.*, 2016a), show peaks in the range of ~ 100 days possibly related with the stellar rotation period. However, they could also be tracing the same variability that the strong 355.56 days peak detected in the m_2, since its third submultiple fits in the rotation period range. We do not know the origin of this very strong signal that 1-year alias present in the spectral window.
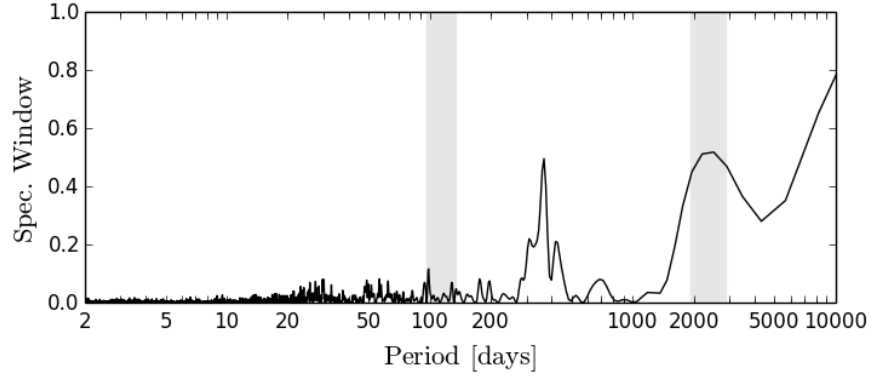
Figure 5.17: Spectral Window Function - This periodogram shows the peaks arising only due to the time span of the complete HARPS dataset observations.
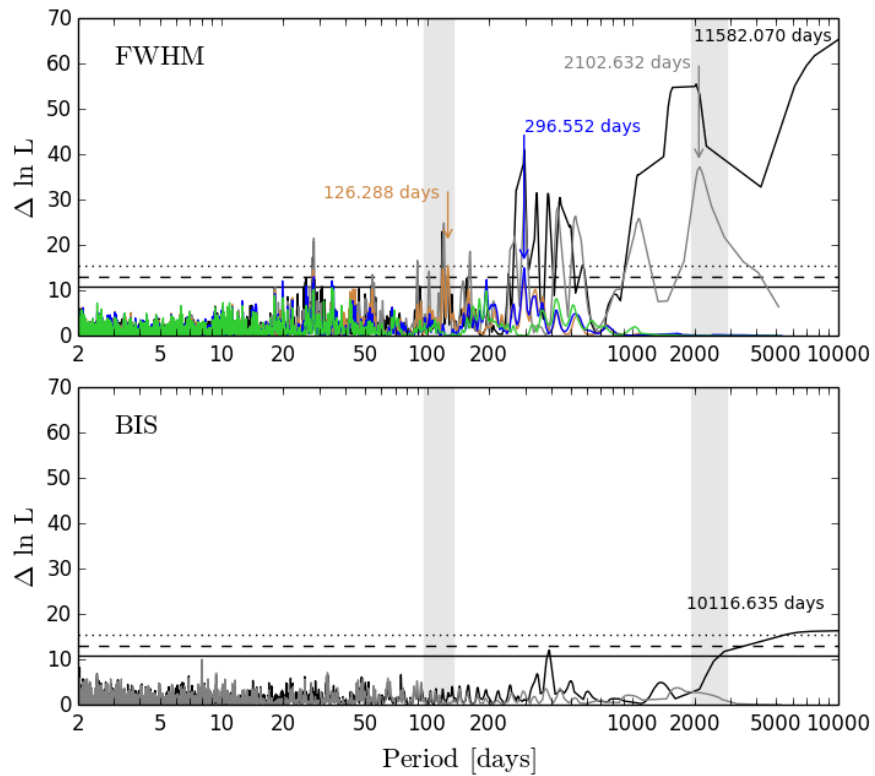
Figure 5.18: Likelihood-ratio periodogram of the mean-line profile shape I - Either the FWHM (top panel) or the BIS (bottom panel) DRS indices have signals in the short term. The BIS shows hints of a long-term. The FWHM show clear long period besides a peak in the rotation range. A set of peals is also detected close to the 1-year alias and in the range of the $\sim 400 - 500$ days signal form the RVs.
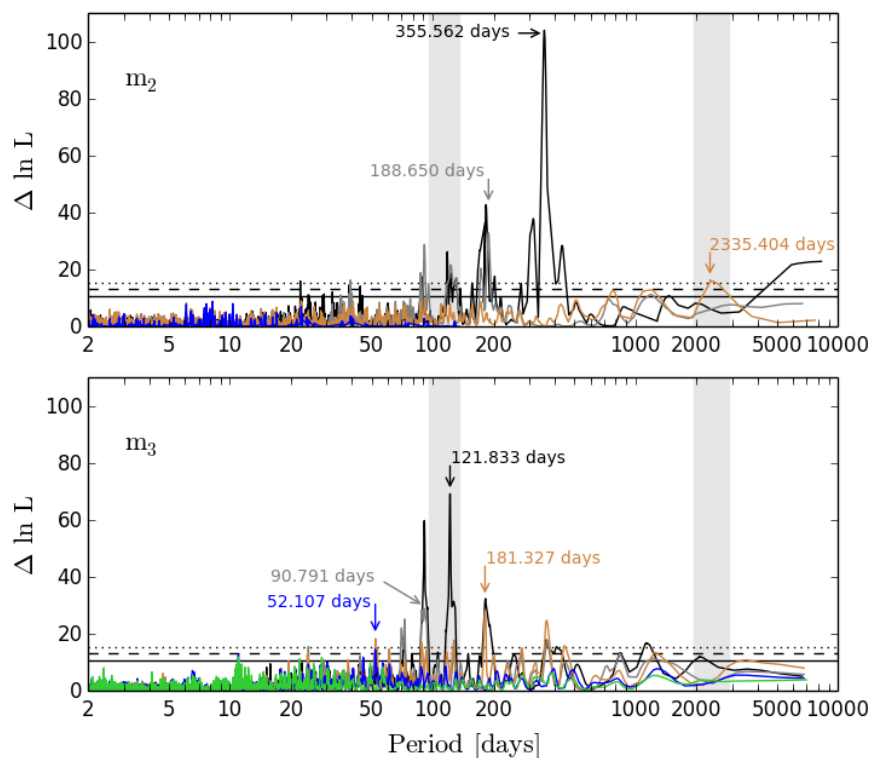
Figure 5.19: Likelihood-ratio periodogram of the mean-line profile shape II - The m_2 (top panel) and m_3 (bottom panel) have not variability in the short term. The peaks in the shaded area corresponding with the rotational period prediction could also be third submultiples of the strong 355.56 days signal.

5.1.2.4   Photometric time-series

The OSN and ASAS photometry did not revealed any significant variability. Due to the length of the original series, this result was expected in the case of the nightly binned OSN data, but not in the case of ASAS. The uncertainties given in the ASAS survey database seem to be overestimated. We deduced that by comparing the averaged value of the GJ 273 photometry, 0.039 mag, with their standard deviation, 0.019 mag. For this reason, we decided to repeat the analysis using the standard deviation instead of the original values given. Even if peaks increased their significance in the resulting periodogram none passed the 0.1%-FAP criteria. Only one peak at ~ 2500 days is compatible with the activity cycle range predicted by Suárez Mascareño *et al.* (2016), but it only reaches the 10%-FAP. In Fig. 5.20 I show in the upper panel the OSN photometry and at bottom the ASAS periodograms obtained with the original (purple line) and with the standard deviation uncertainty (black line). This apparent contradiction between populated chromospheric periodograms and the lack of signal in the photometry was previously reported for other M stars (e.g. Barnard's star; Kürster *et al.* 2003, and GJ 581;Robertson *et al.* 2014). Kürster *et al.* (2003) attributed this behaviour to localized regions on the stellar surface where magnetic fields inhibits the convection without creating dark spots.

5.1.3   The planetary system characteristics

The analysis of the chromospheric, mean-line profile shape, and photometric periodograms indicate that the 4.72 and 18.64 days RV signals can not be explained by stellar activity. The signals arise only in the Doppler time-series and thus, their simplest interpretation is the presence of two planet candidates orbiting Luyten's star. On the contrary, the activity nature of the $\sim$400-500 days signals can not be ruled out.

Once we had confident period detection from the *ln-$\mathcal{L}$* periodogram analysis, we used a Bayesian Markov Chain Monte Carlo (MCMC) approach to calculate the planet parameters and their uncertainties from the posterior distributions (Ford, 2005). With this aim, we used the same likelihood model as for the frequentist search with the *ln-$\mathcal{L}$* periodogram, whereas the prior distributions for these parameters where obtained as in Rodigas *et al.* (2016). The planet parameters shown in Table 5.2 where obtained as the average of the posterior distributions, and their uncertainties as the standard deviation.

With a period of 4.72 days Luyten b lies outside the habitable zone of its host star (see Tab. 5.2). However, Luyten c, which has a period of 18.64 days, lies out of the inner edge of the classic HZ but within the optimistic HZ (i.e. in the range of distances defined between a recent Venus and a late Mars; Kopparapu *et al.* 2013). Planet candidates have similar 1.14 and 1.46 m s^{-1} Doppler semi-amplitudes (see Fig.5.21). These signals, which are larger than the ~ 0.8m s^{-1} HARPS limit, are not particularly small compared with other previous detections (Pepe *et al.*, 2011). The minimum masses predicted for Luyten b and c are 1.11 and 2.13 M$_{\oplus}$, respectively. With corresponding semi-major axis of 0.0338 and 0.0843 AU, the orbits are barely circular as is commonly the case for compact planet systems. In fact, we have measured
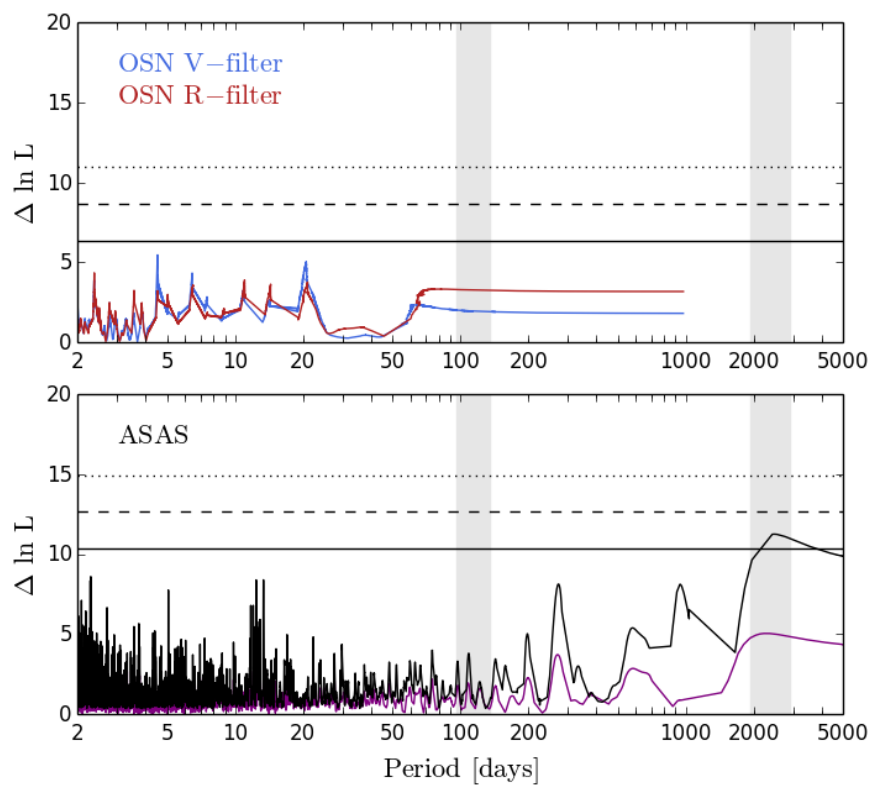
Figure 5.20: Likelihood-ratio periodograms of photometric time-series - No signals were found in the OSN nightly binned time-series (top panel). Neither the ASAS periodogram shows significative signals (bottom panel). This result is independent of using the original overestimated uncertainties (purple line) or the standard deviation (black line).

Table 5.2:   GJ 273 stellar properties, Keplerian parameters, and derived quantities.

Stellar properties		refs.
AR [hh:mm:ss]	+07:27:25	[VL07]
DEC [dd:mm:ss]	+05:12:29	[VL07]
Spectral Type	M3.5V	[RE95]
V_{mag}	9.872	[KO10]
Distance [pc]	3.80 [3.78, 3.82]	[KO10]
Mass [$M_\odot$]	0.23 [0.15, 0.31]	[GA14]
Radius [$R_\odot$]	0.25 [0.19, 0.31]	[GA14]
Luminosity [$L_\odot$]	0.008 [0.004, 0.012]	[GA14]
T_{eff} [K]	3317 [3244, 3390]	[GA14]
P_{rot} [days]	115.6 [96.2, 135]	[SU11]
$v \sin i$ [km s^{-1}]	< 2.5	[BR10]
[Fe/H] [dex]	-0.01 [-0.1, 0.08]	[NE14]
Classic HZ range [AU]	$0.0959 - 0.1826$	[KOP13]
Classic HZ period [days]	$22.60 - 59.39$	*
Optimistic HZ range [AU]	$0.0727 - 0.1933$	[KOP13]
Optimistic HZ period [days]	$14.92 - 64.68$	*

Keplerian fit	Planet b	Planet c
Period [days]	4.72356 [4.72322, 4.72391]	18.63408 [18.63395, 18.63421]
Amplitude Doppler [m s^{-1}]	1.145 [0.987, 1.303]	1.461 [1.262, 1.660]
Eccentricity [$-$]	0.16 [0.05, 0.27]	0.35 [0.25 , 0.46]
Mean Longitude $\lambda = \omega + M_0$ [deg]	304 [182, 426]	64 [43, 86]
Argument of periastron ω [deg]	31 [-]	24 [-]

Statistics summary	Planet b	Planet c
False Alarm Probability	8.4×-6	1.6×-5
Trend $\dot{\gamma}$ [m s^{-1} yr^{-1}]	0.85 [0.53, 1.17]	
Offsets γ [m s^{-1}] (HARPS-N, HARPS, CARM-Vis)	-0.99 [-1.90, -0.09], -0.02 [-0.20, 0.17], -25.14 [-30.92, -19.37]	
Offsets γ [m s^{-1}] (APF, HIRES, PFS)	-15.90 [-21.73, -10.06], -14.86 [-20.67, -9.03], -15.96 [-21.79, -10.14]	
Jitter [m s^{-1}] (HARPS-N, HARPS, CARM-Vis)	1.19 [0.85, 1.53], 1.22 [1.18, 1.26], 1.23 [1.13, 1.32]	
Jitter [m s^{-1}] (APF, HIRES, PFS)	0.55 [0.21, 0.88], 1.15 [1.02, 1.28], 1.05 [0.87, 1.23]	

Derived quantities	Planet b	Planet c
Orbital semi-major axis a [AU]	0.0338 [0.0282, 0.0393]	0.0843 [0.0705, 0.0981]
Minimum mass $m_p \sin i$ [$M_\oplus$]	1.11 [0.81, 1.42]	2.13 [1.55, 2.71]
Irradiance compared to Earth's	700%	112%
Geometric transit probability†	$\sim 3.4\%$	$\sim 1.4\%$

Note. — The estimates are a posterior estimates and the uncertainties are expressed as 68% intervals (the standard deviation of the parameter). [∗] Derived with the third Kepler's law from the value in AU. [†] Assuming planet radii of 1 R$_\oplus$. Refs.: [BR10] Browning *et al.* (2010), [GA14] Gaidos *et al.* (2014), [KO10] Koen *et al.* (2010), [KOP13] Kopparapu *et al.* (2013), [NE14] Neves *et al.* (2014), [RE95] Reid *et al.* (1995), [SU15] Suárez Mascareño *et al.* (2015), [VL07] van Leeuwen (2007).

eccentricities below 0.27 and 0.46 for planet b and c. The radius of the planet, and thus its density can be derived from its transit signature. However, our search for transit from the OSN was unfruitful so far. Aiming at filling the gaps in the photometric windows, we plan to keep observing GJ 273.
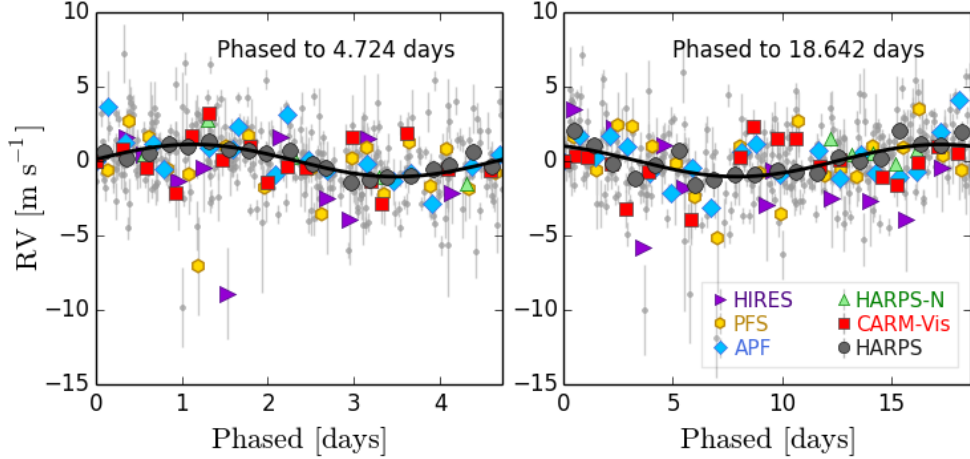
Figure 5.21: Phased-folded Doppler curves - Radial velocities measurements phased folded at the 4.72 and 18.64 day periods of the planets b and c. The maximum likelihood solution is marked with a black line. The original data (grey dots) were binned (colored markers) to improve the visualization of the different instruments RV.

We also performed dynamical studies to test the 2-planet system stability. In particular, we used the *Mean Exponential Growth Factor of Nearby Orbits* (MEGNO $Y(t)$ parameter; Cincotta & Simó, 2000) which has been previously used with this aim in other systems (e.g. Bois *et al.*, 2003; Hinse *et al.*, 2015). MEGNO is a chaos indicator that evaluates the stability of the body trajectories after small perturbations of the initial conditions[1] This analysis indicates that this system is stable when we consider the planet minimum masses and low eccentric orbits (case a, $e_b = 0.05$, $e_c = 0.25$). In contrast, the stability decreases for higher eccentricities (case b, $e_b = 0.27$, $e_c = 0.46$) resulting in chaotic scenarios nearby. Besides checking the 2-planet system stability, we can use the MEGNO maps to give a picture of the stable regions in the planet vicinity. That is, of the resonant structures and areas where particles would have stable periods orbits. The blue areas in Fig. 5.22 point to three main stable regions (A,B,C in panel a). This areas could be the hosts of minor bodies such as comets or asteroids (e.g. zones like the Oort Cloud, the Main Asteroid Belt or Kuiper belt in the Solar System). On the contrary, yellow areas highlight unstable regions. It is clear from this plots that stable regions change their shapes and even almost disappear (i.e. region B) when the eccentricity increases (case a corresponds to low-eccentric orbits and case b to higher ones). Thus, a system with higher-

---

[1]The system is chaotic if $\langle Y(t) \rangle \to \infty$ for $t \to \infty$, whereas the motion is quasi-periodic if $\langle Y(t) \rangle \to 2$ for $t \to \infty$.

eccentricities as the case *b* would be less prone to harbor minor bodies reservoirs. The abrupt changes between instability-stability regions present in both maps correspond to two body main motions resonant configurations (see some marked with arrows in *a*).

Due to their proximity to the host star, the planets receive more radiation compared to the Earth. The surface temperatures estimated were ~ 453 K for Luyten b and of ~ 287 K for the outer Luyten c. However, to calculate these numbers we assumed the planets to be blackbodies, that is, to have no atmosphere (we assume zero-albedos). Luyten b is too close to the star to hold water in its surface, but Luyten c is a difference case: it could more easily maintain water reservoirs if it had an atmosphere. As an example, the average Earth surface temperature, that is 288 K (14.85°C), would be 255 K (-18.15°C) without the warming of the atmosphere greenhouse gases.

The X-ray UV radiation from the star can heat, erode and even eliminate the planetary atmospheres but it can also led to pre-biological molecules due to photochemical reactions. The habitability potential of these compact planets is a matter of debate (e.g. Vidotto *et al.*, 2013; Leconte *et al.*, 2015). However, little or nothing is known about their atmosphere composition, and this is needed to constrain the solutions given by the theoretical models. Nevertheless, this is about to change. Occurrence rates indicate that $\sim 15 - 25\%$ of the red dwarfs host planets in their HZ (Dressing & Charbonneau, 2013, 2015). Following these statistics, we can predict in the solar vicinity (within ~ 10 pc) between 30 and 50 potentially habitable terrestrial planets orbiting around M stars. All these objects, including Luyten c, would be primary targets for the upcoming instrumental projects aiming at detecting bio-molecules on their feasible atmospheres, such as the E-ELT, *TESS* or the *James Webb Space Telescope*,

5.1.4   Results

In summary, combining Doppler time-series from several instruments, we have detected two planet candidates orbiting Luyten's star. Luyten's star is one of the targets of the CTB survey and was observed also with CARMENES during the commissioning of the instrument. Luyten c has a 18.64 day period, 2.13 $M_{\oplus}$ minimum mass, and lies at the outer edge of the classic HZ and within its optimistic estimation. Luyten b is more compact and has a period of 4.72 days and a minimum mass of 1.11 $M_{\oplus}$. We can not rule out the presence of an outer planet at $\sim 400 - 500$ days. However, the stellar activity prevents us from a firm confirmation. Our dynamical studies concluded that this 2-planet system is an stable configuration. Due to its proximity (d=3.0 pc), Luyten's star would be one of the primary target of future missions to explore the planet's atmospheres such as the JWST. Meanwhile, we will keep observing GJ 273 with the aim of measuring transit signatures.
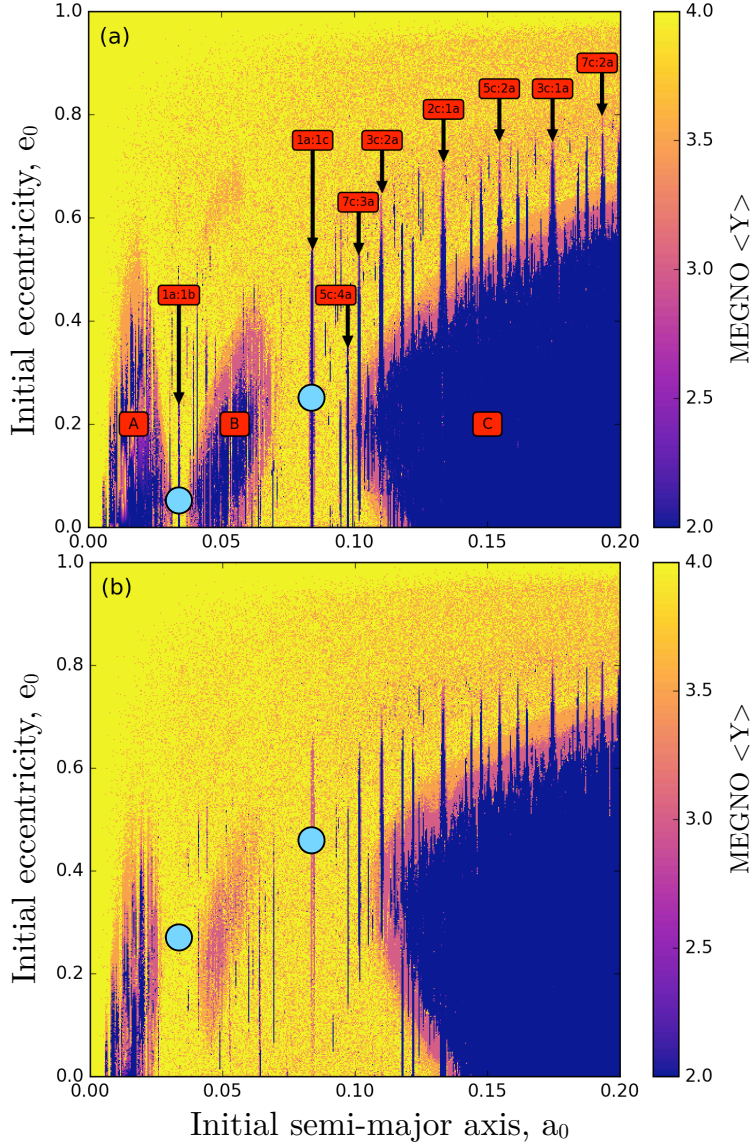
Figure 5.22: Dynamical stability MEGNO maps - The maps account for different scenarios considering minimum ($e_b = 0.05$, $e_c = 0.25$) and maximum values of eccentricities ($e_b = 0.27$, $e_c = 0.46$) in panels (a) and (b), respectively. In both cases: $\langle Y(t) \rangle \to 2$ for stable orbits (blue) and $\langle Y(t) \rangle \to 4$ for chaotic (yellow). In panel (a) the areas labelled as A, B, and C highlight the regions where minor bodies could exits. The principal mean motion resonances are shown also in panel (a). Blue dots highlight the planets assumptions of the planet parameters for each case.

5.2 A cold and a temperate super-Earths around the halo Kapteyn's star

In 2014, we confirmed the presence of two super-Earth mass planets orbiting the closest halo star to the Sun, Kapteyn's star (Anglada-Escudé *et al.*, 2014). This result made of Kapteyn b –that is within the circumstellar habitable zone– the oldest potentially planet know to date. Milky Way evolution theories suggest streams of halo stars like the retrograde Kapteyn's group were originally satellite dwarf galaxies that the early Milky Way engulfed. The longevity of M dwarfs make them key targets for planet-formation processes, but in this scenario, Kapteyn b and c set up the possibility of long-term planets surviving intergalactic merges. Tab. 5.4 shows the system main characteristics, Fig.**??** shows the likelihood periodograms.
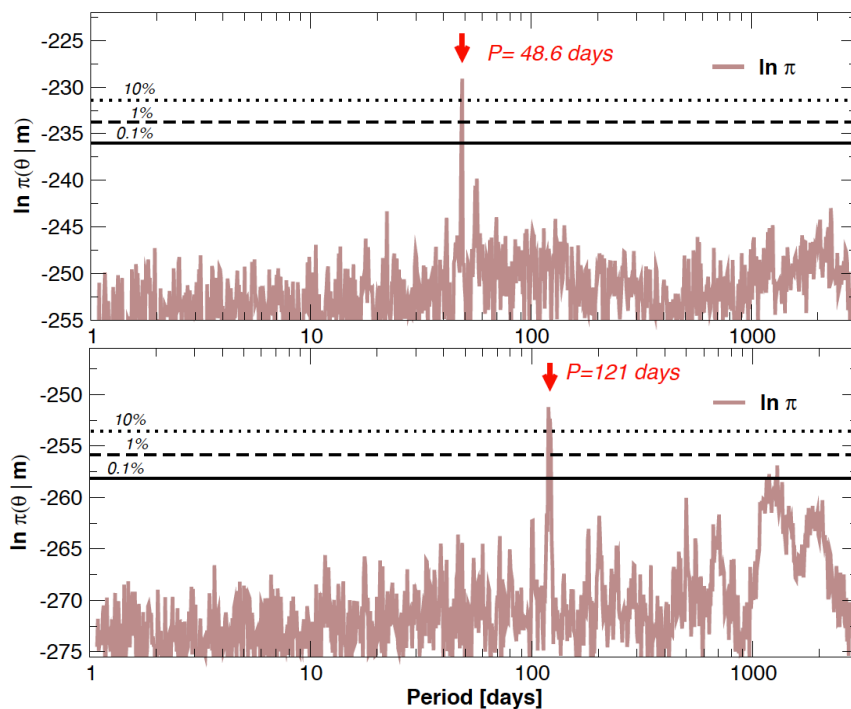
Figure 5.23: Periodograms for Kapteyn RVs. - Brown periodograms correspond to the posterior probability contour considering one (top panel) and two Keplerian (bottom panel) signals and using the Bayesian approach. Red triangles indicate the best likelihood function solutions. From Anglada-Escudé *et al.* (2014)

In this study we combined RVs from HIRES (30 spectra) and from HARPS (66 spectra from the CTB survey and 30 from the HARPS-GTO survey), and we used both likelihood periodograms and Bayesian approaches (see Chapter 2 for further details). In order to rule out masquerading stellar activity effects, we used the same techniques to investigate for correlations with several indices. Results indicated no significant correlations between the RVs and either

Table 5.3:   **Kapteyn b and c parameters and derived quantities.**

Parameters	Kapteyn b	Kapteyn c
P [days]	48.616 [48.584, 48.652]	121.54 [121.29, 121.79]
K [m s^{-1}]	2.25 [1.94, 2.56]	2.27 [2.01, 2.55]
e [$-$]	0.21 [0.11, 0.32]	0.23 [0.11, 0.33]
$\lambda = \omega + M_0$ [deg]	350.0 [331.3, 369.1]	1.6 [-18.5, 22.1]
ω_0 [deg]	80.4 [51.5, 111.1]	3.9 [-20.3, 32.8]
a [AU]	0.168 [0.160, 0.174]	0.311 [0.297, 0.349]
$m_p \sin i$ [M$_\oplus$]	4.8 [3.9, 5.7]	7.0 [6.0, 8.2]
HZ [AU]	$\sim 0.126 - 0.236$	

Note. — From Anglada-Escudé *et al.* (2014)

the BIS, the FWHM, the *S*-index, or the ASAS V-band photometry.

Nevertheless, this result was challenged a year later by Robertson *et al.* (2015). This team claimed the detection of a 143-day stellar rotation period. As a consequence, they refuted Kapteyn b for having a period third of this rotation period (P=P$_{rot}$/3). They also questioned Kapteyn c for being close to the rotation period. Moreover, the team concluded that there was a strong correlation between their H$_\alpha$ (Robertson *et al.*, 2013) index and the RVs from planet b (i.e. after removing other contributions). However, in a posterior study (Anglada-Escudé *et al.*, 2016b) we showed that selection of the 143-day period was premature since other peaks in the periodograms of the activity indices had equal or higher significances. Additionally, this work set the significance of the (Robertson *et al.*, 2013) activity-RV correlation and showed that, when including the data uncertainties, the correlation is notoriously underestimated. Even when detected planet candidates are of intense debate when orbiting active stars, this controversy brought to light the importance of using sophisticated global fitting analysis techniques. This fact is currently broadly accepted by the scientific community, and Kapteyn b and c are still considered strong planet candidates.

5.3   Proxima b: our closest terrestrial neighbour.

In August 2016 we reported the presence of a 1.3 M$_\oplus$ planet orbiting within the liquid water habitable zone of Proxima Centauri. Our previous analysis using CTB data and public HARPS and UVES data pointed to a 10-20 day period. However, misleading signals driven by stellar activity and/or instrumental issues prevented us from a solid confirmation. In January 2016, we started a new campaign called "Pale Red Dot" (PRD)[1], in which we appropriately combined new HARPS spectra with simultaneous photometry. The new 54 PRD epochs (observed during 60 nights almost consecutive) were enough to constrained a 11.2-day period and then confirm the

---

[1]Visit https://palereddot.org

Table 5.4: **Proxima b parameters and derived quantities.**

Parameters	Proxima b
P [days]	11.186 [11.184, 11.187]
K [$\mathrm{m\,s^{-1}}$]	1.38 [1.17, 1.59]
e [−]	< 0.35
$\lambda = \omega + M_0$ [deg]	110 [102, 118]
ω_0 [deg]	310 [-]
a [AU]	0.0485 [0.0434, 0.0526]
$m_p \sin i$ [$\mathrm{M_\oplus}$]	1.27 [1.10, 1.46]
HZ [AU]	$\sim 0.0423 - 0.0816$

Note. — From Anglada-Escudé *et al.* (2016a)

terrestrial planet (see in Tab. 5.4 some of the planet properties). A extra signal at 60-500 days was also detected but its nature is still unclear. As for Kapteyn's star, the significances were assessed with both frequentist and Bayesian methods (see periodograms in Fig. 5.24).

Proxima is know to be a flare star, thus the PRD simultaneous photometry was key to monitor stellar activity. But the activity monitoring was also done through spectral indices. My contribution to this discovery consisted in calculating the m_2 and m_3 mean-line profile indices, that were detrended from the SED effect previously discussed in Chapter 3 (see an explanation of the detrending procedure in Chapter 4). These m_2 index accounts for the mean-line variance, that is, it measures symmetric width distortions. This index resulted to resemble the photometric curves as Bonfils *et al.* (2007) previously suggested for other M-stars (see Fig. 5.25).

Very recently, Turbet *et al.* (2016) analyzed different atmospheres and water's cycles of Proxima b concluding that the habitability of Proxima b is possible for a broad range of atmospheric pressures and compositions (for both tidally-locked or non-synchronous rotation modes). But, the keys to constrain the different atmosphere solutions are: a) the ability of the planet to retain volatiles (i.e. water and non-condensible gases) and, b) its initial budget of water. Ribas *et al.* (2016) modeled the flux received from the star during the planet lifetime and concluded that, even when Proxima b might has lost large amounts of water during its hotter past, it could have retain enough to be considered a habitable planet. However, the current size of the feasible Proxima b oceans depend of the initial water budget, and this is constrained by the planet formation and evolution. Coleman *et al.* (2016) studied four possible formation scenarios: i) in-situ formation, ii) formation via giant impacts between migrating embryos, iii) a single embryo formation in the protoplanetary disk that migrated inwards while accreting planetesimals, and iv) formation via pebble accretion. Scenario i) derived in the formation of dry eccentric planets. However, the study concluded that scenarios ii), iii) and iv) could produce a water-rich planet.
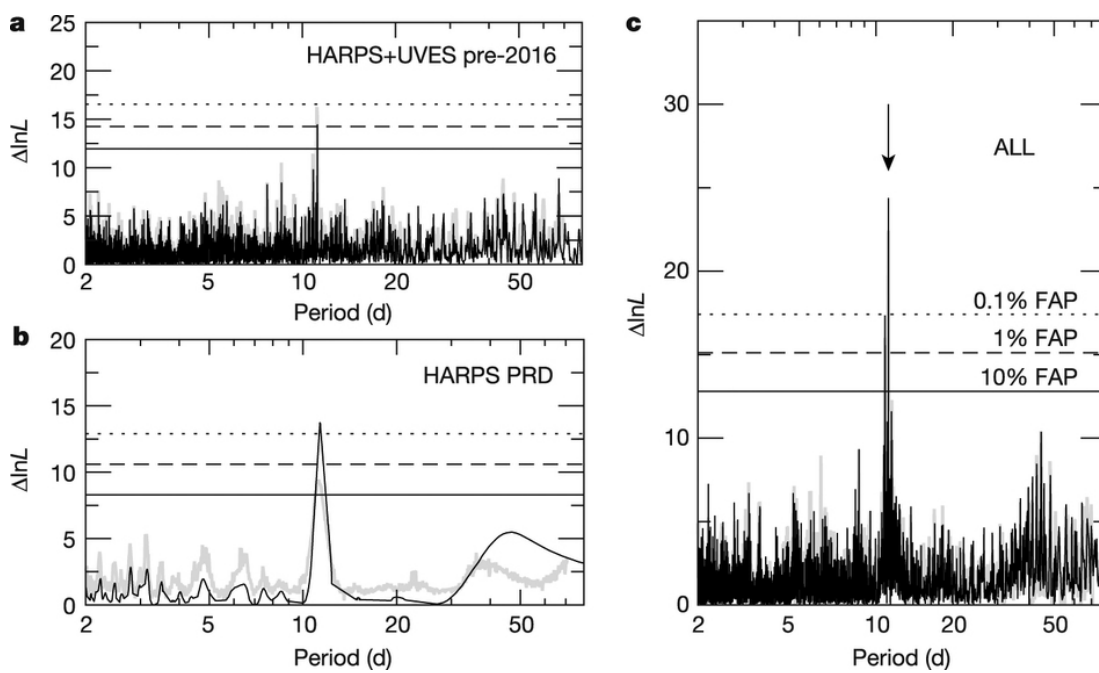
Figure 5.24: Proxima Periodograms - The UVES and HARPS pre-2016 data (top left) gave hints of a signal that again suggested by the PRD campaign (bottom left). The signal is clearly confirmed when combined all the data (right panel). From Anglada-Escudé *et al.* (2016a)
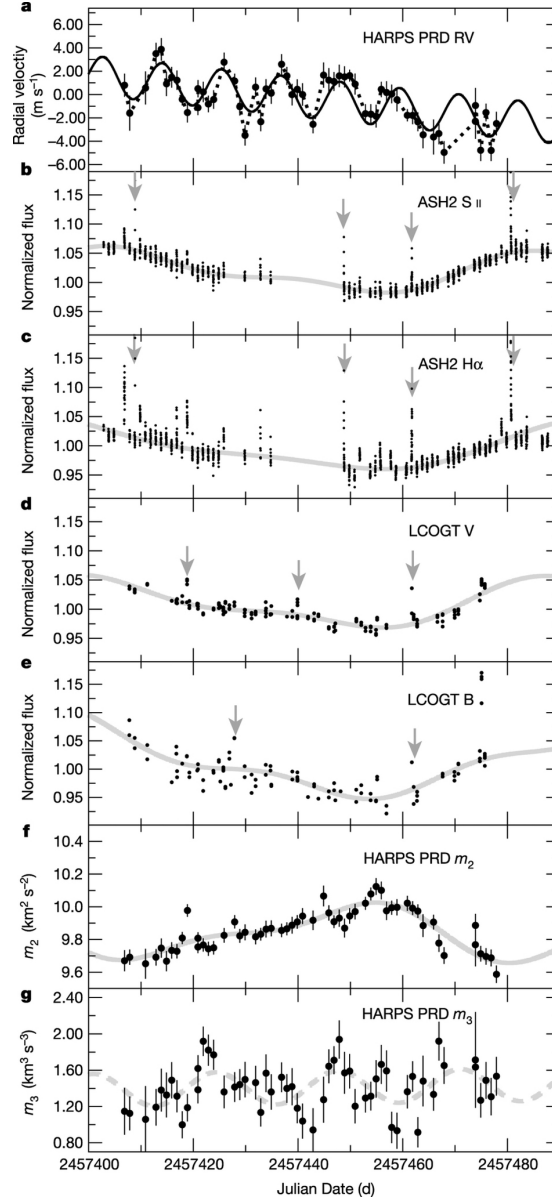
Figure 5.25: Proxima time-series - The m_2 index (panel f) follows the ASH2 (SII and H_α narrow filters) and LCOGT (V and B bands) photometry (panels from b to e). The flares detected in ASH2 photometry do not affect the RVs (panel a). The long trend in the RVs correspond to the unclear 20-500-day signal. From Anglada-Escudé *et al.* (2016a)

Statistic studies predicts that planets in the HZ of M-stars are common. However, Proxima b, at only 4.2 ly, offers rather unique exploration and further characterization opportunities that will allow us to constrain the solutions of the previous habitability studies. For example, depending on the relative contrast (i.e. depending on the planet radius and surface albedo), and thanks to its proximity to the Sun, we will be able of resolving the star-planet separation with direct imaging from the E-ELT. Also with E-ELT instrumentation, we will have chances of monitoring bio-signatures (e.g. O_2, H_2O, CO_2 or CH_4) combining high-resolution spectroscopy with high-contrast images (Snellen *et al.*, 2015). Additionally, the thermal phased curves can possible be attempted from the space with the *James Webb Space Telescope* (launch scheduled in 2018). But the most ambitious initiative is *StarShot*[1] that aims an in-situ exploration within ∼50 years. Meanwhile this technology is developed, we will keep searching for a transit signature to measure the radius and constrain the planet density.

5.4 Summary

The Chapter is focused in the search of compact planets signatures through Doppler spectroscopy. In particular, we present a detailed study of Luyten's star. Last two Sections describes other "Cool Tiny Beats" results in which I have been involved. In particular, the detection of two super-Earth orbiting Kapteyn's and the recent discovery of Proxima b. This is the summary for our study:

1. We have solid arguments to claim that there are two Earth-mass planets orbiting Luyten's star. The periods of Luyten b and c candidates are 4.7 and 18.6 days, respectively. Luyten c is at the outer edge of the classic habitable zone but within the optimistic HZ estimation.

2. Our CTB data gave us first hints of the signals, that were later confirmed using nightly bins of HARPS public data. The brand new CARMENES spectrograph supported also these signals, using only 42 nightly binned RVs. This result brought to light the well performance of the CARMENES data, commissioned in December 2015-January 2016.

3. Combining the complete HARPS dataset with data from CARMENES and from other four instruments (HARPS-N, HIRES-Keck, PFS and APF) we validated the two planets signals. Moreover, we cleaned long-term peaks caused by instrumental and observational effects. Two peaks clearly remained at 410 and 530 days. Whilst they could be long-period planets, it is not possible to rule out a stellar activity origin.

4. Stellar activity is the most plausible origin of the large amount of long-period signals arising in the periodograms of the chromospheric activity (NaI D1+D2, H_α and *S*-index) and mean-line profile indices (FWHM, BIS from the CCFs, and m_2 and m_3 from the LSD profiles detrended from SED variability). However, all indices were rid of signals with

---

[1] `http://breakthroughinitiatives.org/Initiative/3`

periods P<20 days. This result supports the planetary nature of the 4.7 and 18.6 days Doppler signals.

5. No significative peaks were found in the ASAS and OSN photometry, a behaviour previously observed in other M-stars. Our search for transit did not produce any positive result, but more observations are needed to cover the transit phased window.

6. In the last two sections we summarize two discoveries that used CTB data. The Kapteyn two planet system, and the discovery of a temperate terrestrial planet orbiting Proxima Centauri.

6
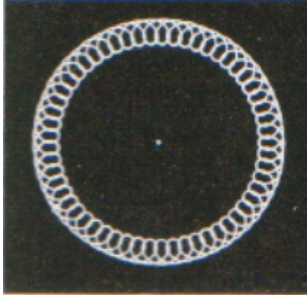
RadiCa2D: an alternative to scrambling methods

Mᴏʀᴇ precise high-resolution spectrographs are required to confidently confirm the signal of an Earth twin with radial velocities. Improving the state of the art of current technology sets the pace for the increasing precision of future échelle spectrographs. Nowadays, we can identify several factors limiting the overall radial velocity precision. The stability of the spectrograph illumination is a well-known detriment. This Chapter is based on an instrumental project for which I have dedicated a significant part of my thesis. Here I present the Radiance Characterizer 2D (RadiCa2D), an original alternative set-up which aims at reducing the total error in radial velocities. The scientific motivation is further explained in Section 6.1, while Sections 6.2 and 6.3 outline the instrument concept and current integration status, respectively. Finally, the conclusions and future plans are included in Section 6.4.

6.1   Scientific motivation

It is important to distinguish between the intrinsic precision of a single measurement and the precision the whole series. The first one refers to the range of values in which a single measurement is unknown (e.g. the error bars of the individual data points in Fig 6.1). Contrarily, the

second one refers to the dispersion of the cloud of data (e.g. the dispersion between the data points and the solid in Fig 6.1). The uncertainty of a single RV measurement is expected to be dominated by the *photon noise*. On the other hand, many sources of noise can contribute to the overall precision of a RV curve. The identification of these sources of noise and their relative contribution is of great importance to reach better RV precisions, and thus to model more accurately the planetary signals.
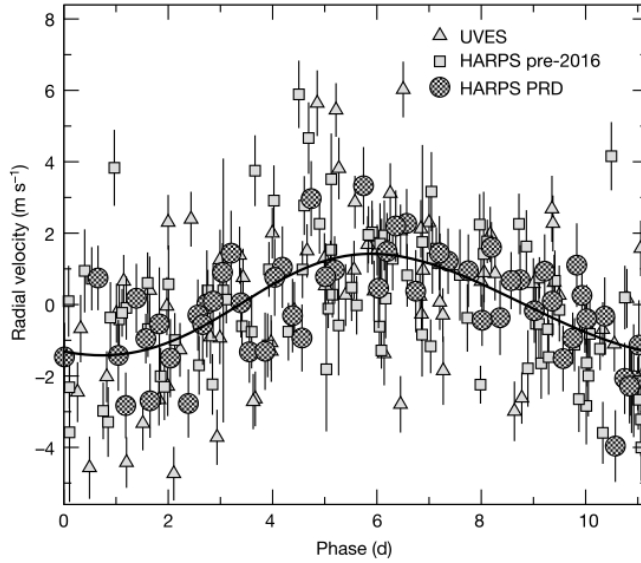
Figure 6.1: RV curve of Proxima b - The individual datapoints obtained during 16 years of observations phase-folded to the planet period ($P = 11.2$ days). The black solid line is the best model fitted, and has a semi-amplitude of $1.4\mathrm{m\,s}^{-1}$. Improving the overall RV precision of the spectrograph means to reduce the global dispersion around the planetary signal. *From Anglada-Escudé et al. (2016a).*

6.1.1 The RV error budget

The uncertainty of a single spectrum (i.e. of a single RV data point) is generally limited by **photon noise**. In particular, it depends on: i) the signal-to-noise ratio, SNR, ii) the spectral coverture, $B(\text{Å})$, iii) the spectral resolution, $R = \lambda/\delta\lambda$, and iv) the projected rotational velocity of the star, $v \sin i$. Hatzes *et al.* (2010) performed simulations and concluded the final RV precision of a single measurement can be written as:

$$\sigma_v(m/s) = \frac{2\,C}{\mathrm{SNR}\ v \sin i\ \sqrt{R^3\,B\,f(\mathrm{SpT})}} \tag{6.1}$$

where, $f(\text{SpT})$ represents the relative line density as a function of the spectral type[1], and C is a constant of proportionality[2,3]. In numbers, $1\,\mathrm{m\,s^{-1}}$ is the HARPS photon-limited RV precision if we assume a one minute exposure on a G2V star of magnitude V=7.5. However, the extra Doppler information contained in the spectrum of a cooler K-type star makes this number go down to $0.8\,\mathrm{m\,s^{-1}}$ under the same assumptions (Lovis *et al.*, 2006). In CARMENES, the averaged estimated value is also $0.8\,\mathrm{m\,s^{-1}}$ (*priv. consortium documentation*).

Nevertheless, if we aim at distinguishing the amplitude of an Earth-like planet signal beyond the noise, we need comparable levels of accuracy in the long-term. That is, in a time span sampling several orbital periods of the planet. HARPS has demonstrated to keep the noise below $\sim 0.8 - 1\,\mathrm{m\,s^{-1}}$ in the long-term (Pepe *et al.*, 2011). To reach this goal, a number of limiting factors needs to be controlled. Among them, we can distinguish between **stellar** (e.g. the RV variability arising from stellar activity or seismology events), **external contamination** (e.g. spurious RVs induced by telluric lines, moonlight or close-by objects), and **instrumental** sources of noise. First two are difficult to avoid and usually targets with known low jitter rates or specific exposures times are chosen to minimize the effects. Additionally, other effects can be controlled by identifying the signals they produce (e.g. the 1-year periods arising from telluric line shifts). In any case, the instrumental effects encompass the limiting factors that can be enhanced from a technical point of view. Among the variety of instrumental effects, the most limiting ones are:

- **Mechanical stability:** The point-spread-function (PSF) of the instrument depends on the instrument stability. Optical and mechanical elements react to different temperature and pressure conditions producing spurious shifts of the light reaching the detector. Depending of the instrumental design and the ambient conditions, such effects may account for several tens to hundreds of $\mathrm{m\,s^{-1}}$ (Lovis & Fischer, 2010). Consequently, high-precision spectrographs like HARPS are highly stabilized. Even though, changes of 0.01 K and 0.01 mbar in temperature and pressure, respectively, are enough to cause $1\,\mathrm{m\,s^{-1}}$ shifts on the spectrum. In CARMENES, the thermal simulations predict that 0.01 K changes will result in maximum drifts of $0.2\,\mathrm{m\,s^{-1}}$ during 24 h (*priv. consortium documentation*).

- **Wavelength calibration:** Since the RVs are calculated against a calibrated reference, their final precision directly relies on the quality and stability of the wavelength reference. The ideal reference is the one that meet two criteria: to have a large number of identical spectral lines, and to have lines evenly spaced over the the largest possible wavelength range. ThAr lamps are the solution most commonly used nowadays. They have demonstrated long-term stabilities of $\sim 0.3\,\mathrm{m\,s^{-1}}$ in HARPS (Lovis & Fischer, 2010)

---

[1]Assuming $f = 1$ for a G-type star we can scale $f \sim 10$ for a M-type star.

[2]Taking the HARPS values (R=110000 and B=2000Å) and assuming SNR=150 and a σ_v of $1\,\mathrm{m\,s^{-1}}$, we obtain for a G-type star $C \sim 2.4 \times 10^{11}$.

[3]Note the projected stellar rotation ($v \sin i$) is scaled to a nominal equatorial velocity of $2\,\mathrm{km\,s^{-1}}$ (origin of the number 2 in the numerator).

(CARMENES predicts the total wavelength calibration error of $\sim 0.1\,\mathrm{m\,s^{-1}}$). However, ThAr lamps present blends among contiguous lines, line drifts as a function of the lamp age, and lines in a large dynamical range of intensities.

- **Slit illumination:** Fiber-fed spectrographs produce on the detector multiple dispersed images of the fiber. Consequently, any variability in the slit illumination results in a variability of the instrumental profile and thus of the spectrum on the detector. There are three main types of time-dependent distortions, which are: (i) displacements of the image photocenter, (ii) changes of the image width and contrast, and (iii) wavelength dependent combinations of both. For example, the *airmass* or *telescope tracking* changes move the image photocenter, whereas *seeing* and *telescope focus*[1] variability during the night can also distort the image shape. Photocenter displacements from the center to the edge of a fiber with 1 arcsecond diameter lead to $\sim 3\ \mathrm{m\,s^{-1}}$ RV shifts in a R=100000 spectrograph (Lovis *et al.*, 2006; Boisse *et al.*, 2010a). And this value is even higher at lower R and larger fiber diameter. In general, a good compromise consists in using the scrambling properties of the fibers to maintain this shift below $\sim 1\,\mathrm{m\,s^{-1}}$. But the image photocenter displacements introduced by the *airmass* are wavelength dependent[2]. The atmospheric dispersion corrector (ADC) has the objective of regrouping all the wavelength dispersed photocenters at the center of the fiber. However, the ADC will not completely recover the far blue and red images if they suffer vignetting. Moreover, the ADC is designed to correct either the telescope image or the telescope pupil, then one will remain chromatically affected. Additionally, the *seeing* is also wavelength-dependent with the airmass. Thus, a chromatic dependence in the fiber illumination may couple with scrambling efficiency and produce variations in the spatial illumination of the optics in a wavelength dependent manner.

The quadratic addition of all the errors yield the overall instrument precision. Therefore, the improvement of these three limiting factors is of great importance regarding the sub-$\mathrm{m\,s^{-1}}$ precision goal of next generation spectrographs. The wavelength reference system has been considered the element requiring a larger investment. The laser frequency comb, that aims at producing uniformly spaced spectral lines locked with an atomic clock, is the most promising approach. However, many studies highlight the impact of the illumination as one of the main limiting factors (e.g. Lovis & Pepe, 2007; Lovis *et al.*, 2008; Boisse *et al.*, 2010a; Avila *et al.*, 2010; Perruchot *et al.*, 2011). This is the effect RadiCa2D aims at improving.

---

[1] When observing with HARPS-N at the TNG, the focus is usually fitted in the beginning of the night, later an active M2 mirror corrects the variations within the night. Other telescopes lack of this simultaneous correction and apply a pre-calculated focus.

[2] The star light is dispersed at different refraction index by the atmosphere as a function of the elevation.

6.1.2   Scrambling and fibers

The use of optical fibers to feed the spectrograph is of great benefit. The reasons are, for example, the large flexibility they offer to carry the light from the telescope to the spectrograph, or because they are natural stabilizers of the slit illumination. Inside a multi-mode fiber, several propagation modes travel though multiple reflections at the fiber core, resulting in a natural scrambling of the input light pattern. The light distribution at the fiber output is described by the *near* and *far fields*. The *near field* (NF) accounts for the spacial distribution at the fiber exit surface, whereas the *far field* (FF) accounts for the angular distribution of the output beam.

Therefore, the NF and FF distributions are completely homogeneous if the scrambling effectiveness of the fiber is perfect. Nearly always this turns out to not be the case. Usually, the modes traveling inside the fiber result to be coupled to each other, producing interference patterns in both the NF and the FF. Consequently, even when fibers are natural scramblers, they cannot mimic the time-dependent variably at the fiber input on their own. Inhomogeneities in the NF lead to fluctuations of the spectrum features; in the FF lead to distortions of the instrument profile (i.e of the PSF). Both fields have to be stabilized to avoid spurious RV shifts.

Avila & Singh (2008) indicated that the variability of the NF due to photocenter displacements at the fiber entrance can be quantified by:

$$G = \frac{d/D}{f/F} \tag{6.2}$$

where d is the star shift, D is the fiber diameter, f is the shift of the PSF on the detector, and F the final full-width-at-half-maximum of the PSF (see panel *a* in Fig. 6.2). Consequently, this ratio known as the *scrambling gain* (G) simply relates the fiber input and detector distortions. G∼1000 is the minimum requirement of future ESPRESSO/VLT and HIRES/E-ELT fiber-fed spectrographs (Avila *et al.*, 2010). CARMENES simulations indicate also G≥1000 is needed to maintain the tracking displacements below <0.12 arcseconds (*priv. consortium documentation*).

Current and future plans to prevent the slit-illumination variability are based in using the different scrambling properties of the optical fibers. Circular fibers are good in scrambling the azimuthal direction of the NF, but they poorly scramble both the NF radial axis and the FF (e.g. Boisse *et al.*, 2010a; Avila *et al.*, 2010). Circular fibers reach only G≤200. On the contrary, non-circular core fibers can break the spherical symmetry and increase the final scrambling in 3-5 times (i.e. fibers with octagonal cores can reach up to G∼1000; Feger *et al.*, 2012). However, they still present patterns in the FF (e.g. Boisse *et al.*, 2010a; Chazelas *et al.*, 2010). See a comparison in Fig. 6.3.

Current most precise instruments like HARPS and HARPS-N use a combination of octagonal fibers and *double image scramblers* (Hunter & Ramsey, 1992) which leads to G>10000 (Feger *et al.*, 2012). This system improve the FF stabilization by converting it into the NF of a secondary fiber (see panel *b* in Fig. 6.2). However, optical scramblers are far away from being the ideal option to stabilize the spectrograph PSF since they often show transmission losses of at least 20%. Other mechanical scramblers such as *fiber squeezers* (e.g. Avila & Singh, 2008)
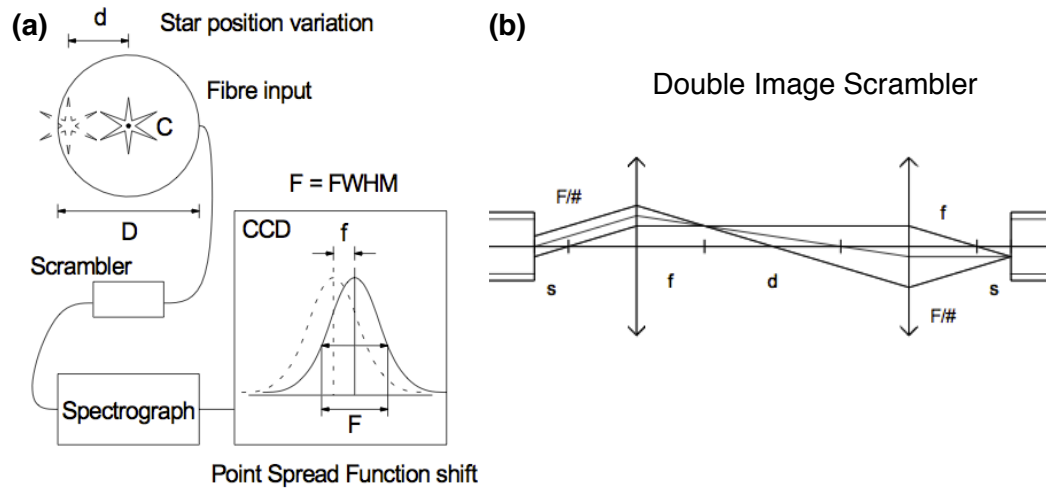
Figure 6.2: Fiber scrambling - (a) A star shift at fiber input, d, is directly related with a PSF shift on the detector, f. How this distortion affects the NF is quantified by the *scrambling gain*, G. (b) A *double image scrambler*. Two lenses invert the NF and FF between two identical fibers to increase the overall stabilization. *From Avila & Singh (2008).*
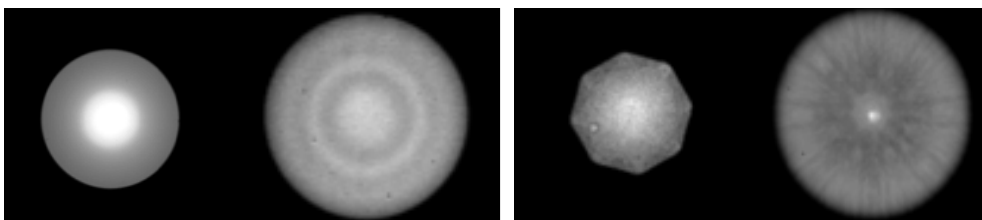
Figure 6.3: Circular versus octagonal fibers - Near and far fields of a circular fiber (left panel) compared to an octagonal one (right panel). *Adapted from Avila* et al. *(2010).*

or *fiber shakers* (e.g. Stürmer *et al.*, 2014) have been proposed as an alternative, but they usually downgrade the focal-ratio-degradation (FRD) performance. A great approach to prevent the "modal noise" is use single-mode fibers. The challenge consists in coupling the telescope beam in their typical small cores ($\sim 5\,\mu$m, compared with the core of $70\,\mu$m of the HARPS multi-mode fiber).

In summary, the ideal system would be one with high throughput and well-scrambled output in both the NF and the FF. But this system remains to be invented. Currently, best solutions imply to reach an agreement between throughput and illumination stability.

6.2 RadiCa2D instrument concept

RadiCa2D is an instrumental adaptor which aims at simultaneously monitoring and correcting the RV errors derived from a non-homogeneous illumination. RadiCa2D extracts the near and far field images in real-time simultaneously to the science image (see Fig. 6.4). Later, we use the optical model of the spectrograph to simulate the RV error caused by illumination issues. In that way, the instrument philosophy consists in measuring the RV error caused by slit-illumination variabilities instead of mimicking them with scrambling methods.
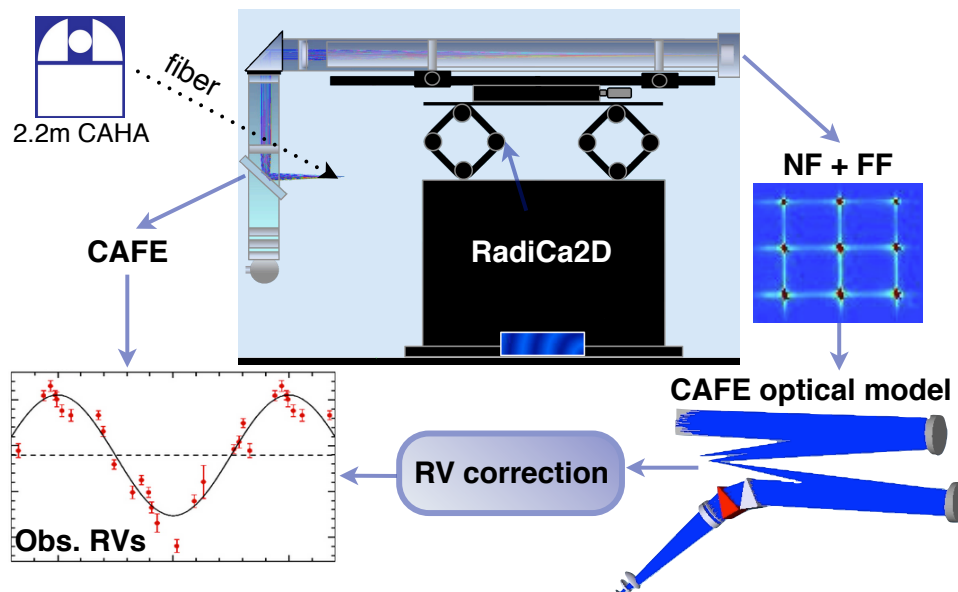
Figure 6.4: RadiCa2D concept - RadiCa2D was designed to work at the CAFE spectrograph. It uses a beam-splitter to divert 8% of the light and get the NF and FF images. Both images are recorder in a single detector. The ray tracing with the optical model of CAFE gives the final correction to be subtracted to the observed RV.

The concept born as part of the CARMENES project. However, the new technology risk along with the tight deadlines of CARMENES caused that RadiCa2D evolved separately. Rad-

6. RADICA2D: AN ALTERNATIVE TO SCRAMBLING METHODS

iCa2D is the second prototype of the "Radial Velocity Corrector" (RVC) project, being its predecessor a simple dual camera system designed to record the NF and FF at the laboratory.

The RadiCa2D prototype was design to be tested at CAFE: a high-resolution (R∼67000) non-stabilized fiber-fed spectrograph working at the 396–950 nm range (Aceituno *et al.*, 2013). A circular 100 μm fiber coupled to a mechanical shaker carry the light from the 2.2 m telescope of the Calar Alto Observatory to CAFE, which is placed at the Coudé room. CAFE is temperature controlled, but it is not highly stabilized inside a thermal and vacuum enclosure. The reported CAFE overall RV precision is of ∼ 19 m s^{-1} (Aceituno *et al.*, 2013). Thus, RadiCa2D could be a simple and affordable approach to decrease this limit.

6.2.1 Optical layout

The 100 μm fiber arrives at the CAFE spectrograph entrance where a microlens is glued to its exit providing a F#10 beam[1]. Behind the microlens, there is a rectangular slit of $270 \times 100\,\mu$m. This is the object of CAFE and it would be also the object of RadiCa2D[2] (see Fig.6.5).
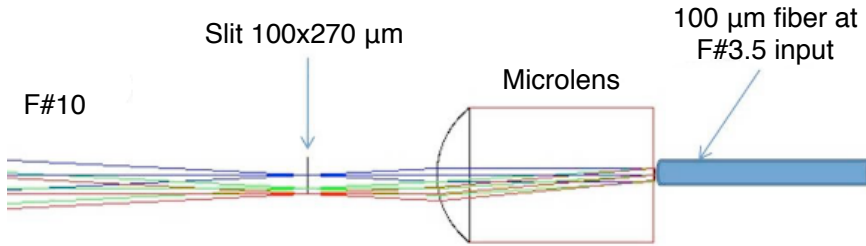
Figure 6.5: CAFE fiber exit - A rectangular slit and a microlens (glued to the fiber that comes from the telescope) define the CAFE (and RadiCa2D) object to be a $270 \times 100\,\mu$m object at F#10 with the pupil image set at infinity.

RadiCa2D is placed a few centimeters far from the slit of CAFE. At this position, the RadiCa2D first optical element, a pellicle beam-splitter[3] (BS), diverts 8% of light from the science beam. This small amount of light would be enough to analyze the NF and FF images. The light beam removed from the science is then magnified inside RadiCa2D by two lenses[4] (see Fig. 6.6). The RadiCa2D nominal position is such that sets the slit object at the focal distance of the first lens ($F_{L1} = 100$ mm). In that way, we get an image of the slit four times larger (i.e. of 1.08×0.4 mm) at the focal plane of the second lens ($F_{L2} = 400$ mm). At this

---

[1]The F-number (F#) defines the beam angular size after an optical element. For a lens completely illuminated it can be calculated as its focal length divided by its diameter.

[2]Reducing the object size in the spectral direction increases the final resolution. The goal of the $0.1\,\mu$m side of the slit is to reduce the $270\,\mu$m given by the fiber.

[3]The beam-splitter is uncoated to be thin and thus do not introduce any extra optical path in the science beam.

[4]AC254-100 and AC254-400, from Thorlabs catalog.

position, there is an orthogonal array of 3×3 microlenses (Fig. 6.7), each of which generate a pupil image on the detector (see in Appendix D the detailed ray tracing).
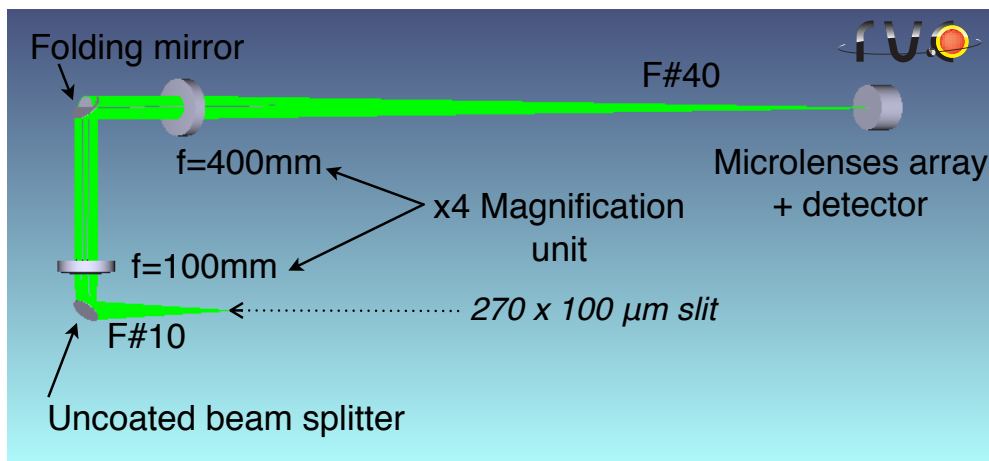
Figure 6.6: RadiCa2D optical layout - A beam-splitter removes a fraction of the science beam. RadiCa2D magnifies a factor 4 the size of the CAFE slit over a focal plane where there is an array of 3x3 microlenses. Each microlens gives an image of the pupil on the detector.

6.2.2 Near field and far field acquisition

Pupil images contain specific information about the angular distribution of the illumination. In other words, the image produced by each microlens is a far field (see panel *b* in Fig.6.8). RadiCa2D calculates only a FF image per science exposure. The final FF has 20×20 pixels and results from averaging the individual pupil images in order to increase the SNR. On the contrary, the NF image has only 3 pixels, one for each microlens that is illuminated (see panel *c* in Fig.6.8). The NF is calculated as the flux at the individual pupil centroids weighted by the total number of counts of the pupil. Consequently, the array of microlenses provides several images of the FF while samples different spatial sections of the illumination pattern. The larger the number of illuminated microlenses, the better the NF sampling is. However, the narrow slit makes blind six of the microlenses (see panel *a* in Fig.6.8). This configuration not only decreases the NF sampling, but also complicates the alignment of the instrument.

6.2.3 Calibration unit

RadiCa2D has an integrated calibration unit to correct instrument illuminations instabilities. The system is formed by a LED coupled to the input port of an integrating sphere (see Fig. 6.9). The sphere output port sets the system aperture. Later, a F#10 beam is injected into the main instrument thanks to a doublet lens of 25 mm focal length (placed at its focal distance from the
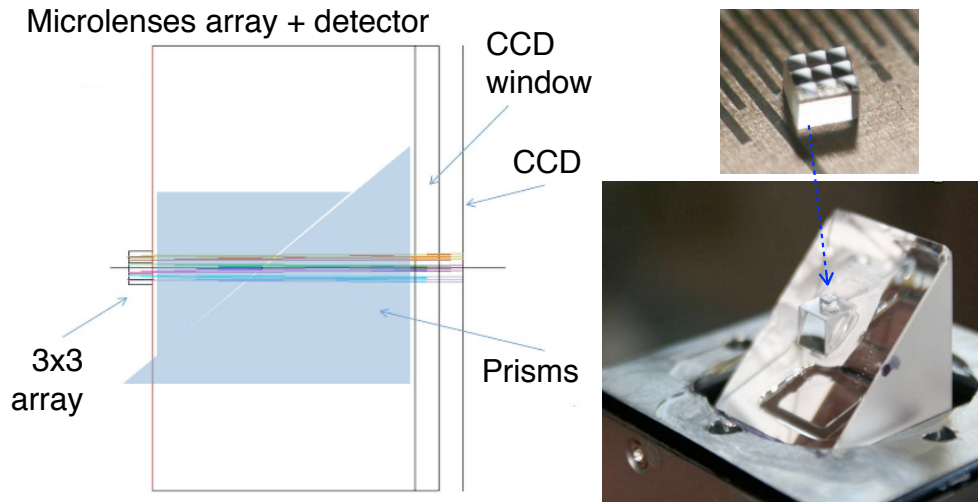
Figure 6.7: Detail of the microlenses–detector interface - Two prisms are used to assemble the array in such a way that the detector is at 98 mm, the focal distance of the array. The bigger prism was glued to the CCD window. We used UV curing glue dried.
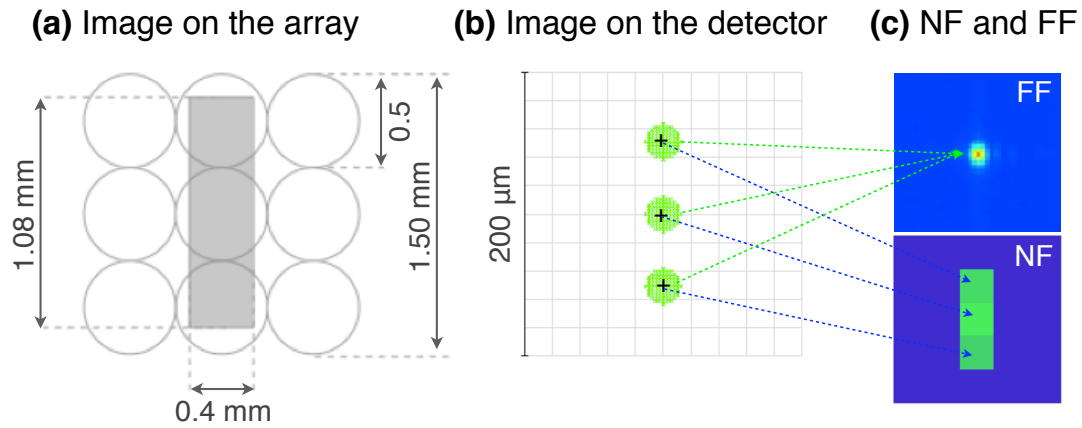
Figure 6.8: NF and FF given by RadiCa2D - (a) Microlenses have a size of 0.5×0.5 mm, thus the magnified 1.08×0.4 mm slit illuminates only three of them. (b) Shape of RadiCa2D image at the CCD. Each circle is a pupil image. (c) Near and Far field images calculation. Microlens give equivalent FF images while sample different sections of the NF.

system aperture) and a 1 mm field aperture. The beam is injected through the beam-splitter (see Fig. 6.10).
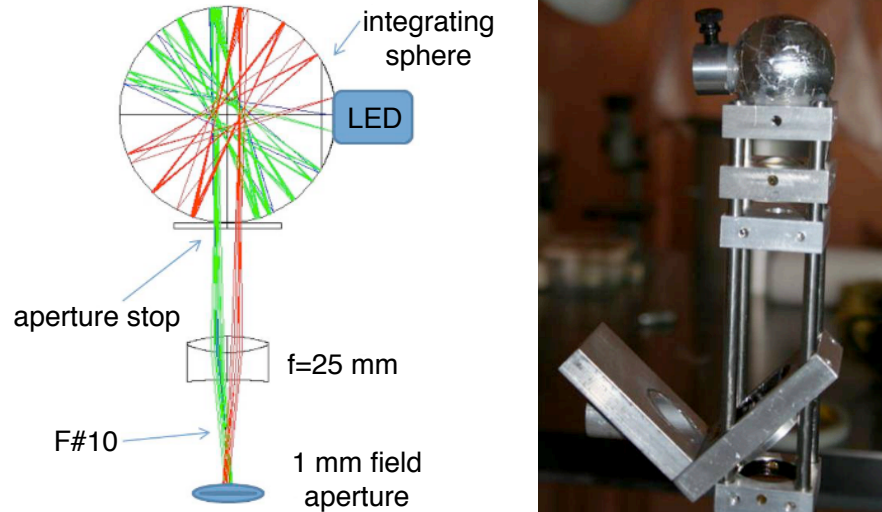
Figure 6.9: RadiCa2D calibration system - (Left panel) optical layout of the calibration unit. (Right panel) calibration unit assembled in RadiCa2D.

The object of RadiCa2D when it is illuminate through the calibration unit is a 1 mm circular aperture. The larger aperture of the calibration unit (compared with the $270 \times 100 \, \mu$m object of the science beam) results in a larger 4 mm image at the array position (see Fig. 6.11). In this case, the microlenses are completely illuminated and we can use all to get the NF and FF images.

The calibration lens is not achromatic, consequently its focal plane is wavelength dependent. We used the calibration unit optical model to optimize its output at F#10. Considering the LED illumination range to be 450–700 nm, the optimal solution was to place the calibration unit lens at 22.7 mm from a sphere aperture of 2.2 mm of diameter. The average back focal length resulted to be 17.44 mm. We placed the 1 mm field aperture at such distance from the lens (see in Appendix D the ray tracing).

Finally, we show in Figure 6.12 a 3-dimensional model of RadiCa2D. This model includes all the optical and mechanical devices described and shows the instrument in its nominal position inside the CAFE spectrograph.

6.2.4 The acquisition software

A MATLAB interface was designed for the RadiCa2D initialization, data acquisition, and NF and FF calculation (see software interface in Fig.6.13). Either the calibration or science images can be acquired from the interface. Additionally, it allows to turn on the calibration lamp. This command sends the order to an Arduino that controls the LED as well as temperature, pressure, and humidity sensors installed inside the spectrograph.
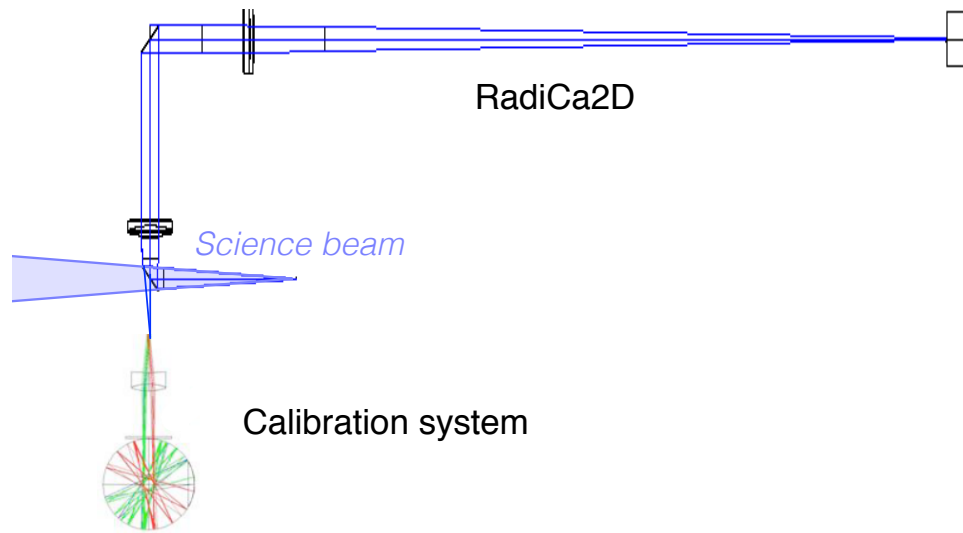
Figure 6.10: Calibration unit in context with RadiCa2D - Either the calibration unit or the science beam feed RadiCa2D through the beam-splitter.
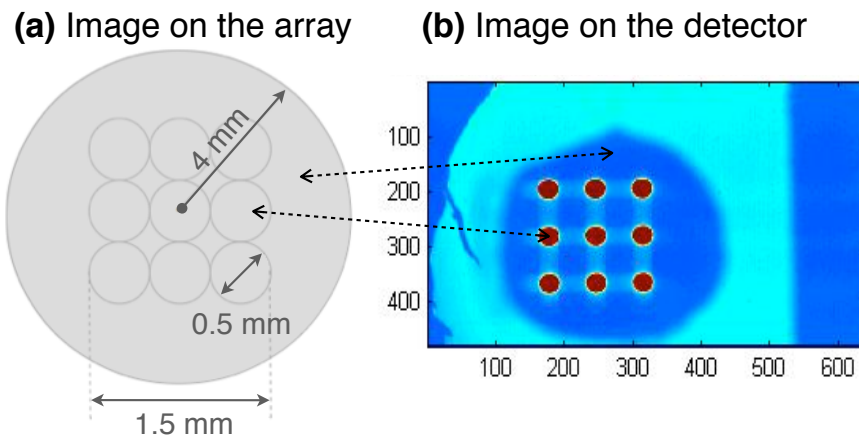
Figure 6.11: Calibration image - (*a*) The larger object of the calibration unit (a 1 mm circular aperture) result in the illumination of all the microlenses. (*b*) Red circles are the 3x3 pupil images. The external blue circle is the image of the 1 mm pinhole through the prisms.
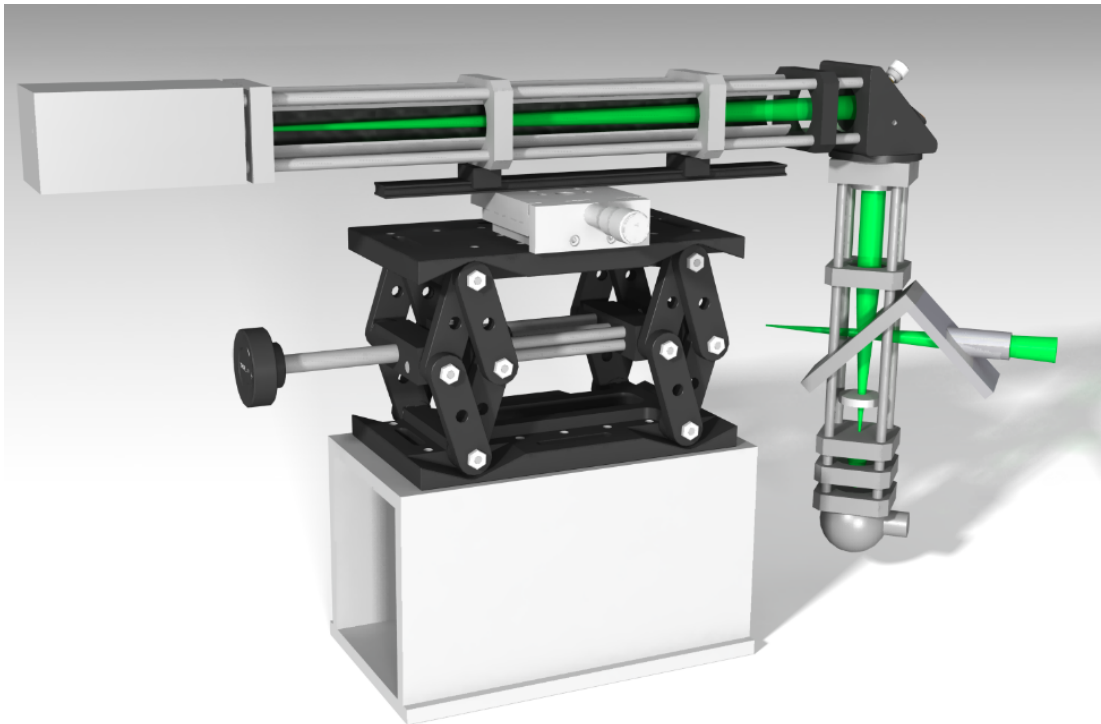
Figure 6.12: 3D model of RadiCa2D - Instrument model showing all the optical and mechanical elements. The instrument is shown in its nominal position inside the CAFE spectrograph. Green beams indicate both the calibration and science beams. The science beam coming from CAFE's slit is the horizontal one that is at the left of the BS. After removing a 8% of the light, the science beam at the right of the BS continues to the spectrograph.
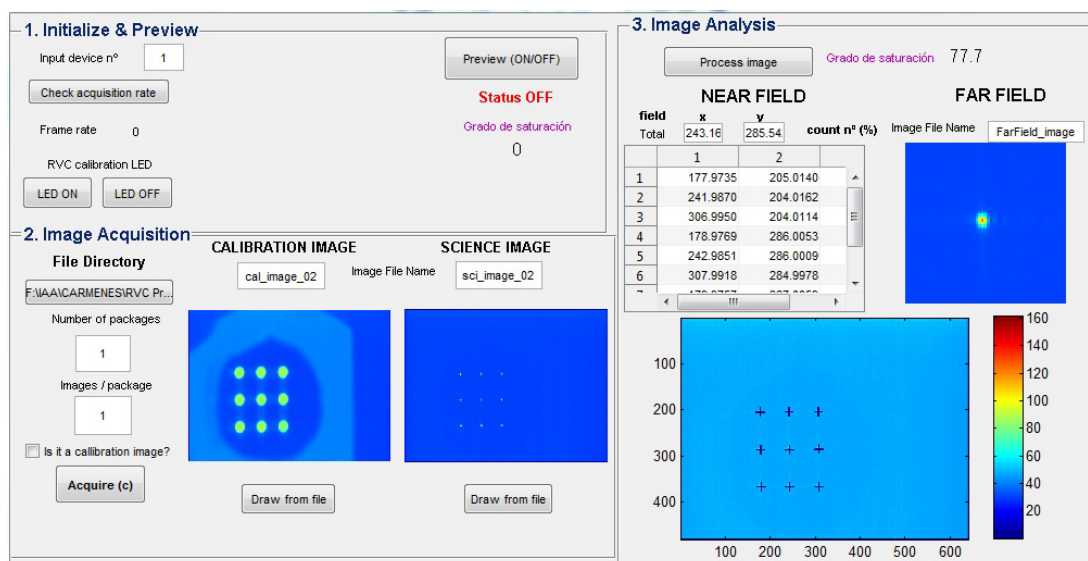
Figure 6.13: RadiCa2D acquisition software - The three main tasks controlled by the interface are: 1. Initialization and Preview (upper left part), 2. Image Acquisition (bottom left part), and 3. Image Analysis (right part). The last one refers to the calculation of the 3×3 pupil images centroids (NF), and of the average pupil (FF).

The RadiCa2D detector (a Sony B&W CCD of 1/3 inches) has 640×480 pixels and covers $\sim 6.5 \mu$m/pixel. The CCD output is digitalized by a 8-bits capturer (SVEON STV40) connected to a laptop which has the acquisition software. The capture works only at 25 fps. This means the exposure time is not tunable. Images are always the result of 40 ms integrations. Larger integration times images are defined as combinations of individual 40 ms images. However, a 15 min CAFE exposure would lead to 22500 individual images of 40 ms that require 150 GB of storage. Consequently, RadiCa2D operates by *image packages*. That is, image are combined on-the-fly by the acquisition software, avoiding the storage of the individual sub-images. The number of *image packages* to be acquired, as well as the number of 40-ms images per package, can be defined in the RadiCa2D acquisition interface (see the "Image Acquisition" part in Fig. 6.13.)

6.2.5   CAFE optical model

Once RadiCa2D has recorded the NF and FF images, we can use the CAFE optical model to account for their performance. The optical model allows us to recover on the CAFE detector the centroids of wavelengths traced (see Fig. 6.14). Consequently, with this model we can associate each ray (of a particular wavelength) with a weight, which contains the illumination information. Thus, after normalizing the NF and FF, two weight matrixes are created with a number of elements equal to NF and FF pixels, respectively. Then, depending on which pixels are crossed by the ray, we link the ray with a final weight. In others words, we add at each

ray the variability induced by the inhomogeneities at the CAFE fiber exit (i.e. NF) and at the CAFE slit position (i.e. FF). Comparing the centroids position that result in the CAFE detector with the case of homogeneous illumination we can measure the relative shifts introduced in the spectrum. Finally, the RV error due to illumination distortions can be calculated from the centroid shifts.

This part of the project is still in development. So far, preliminary tests were done with simulated NF and FF images with the aim of quantifying the RV errors that RadiCa2D could correct. Fig. 6.15 shows some of the FF patterns tested. They correspond to the external and internal FF occultation that can be associated to telescope pupil vignetting or to seeing changes depending on wether there are double image scrambler (Boisse *et al.*, 2010a; see more details in Chapter 4 about the *seeing effect*). Preliminary results point to RV displacements of 3 mpixels (RV $\sim$5-6 m s^{-1}). That would be the RV error that RadiCa2D would aims at correcting.
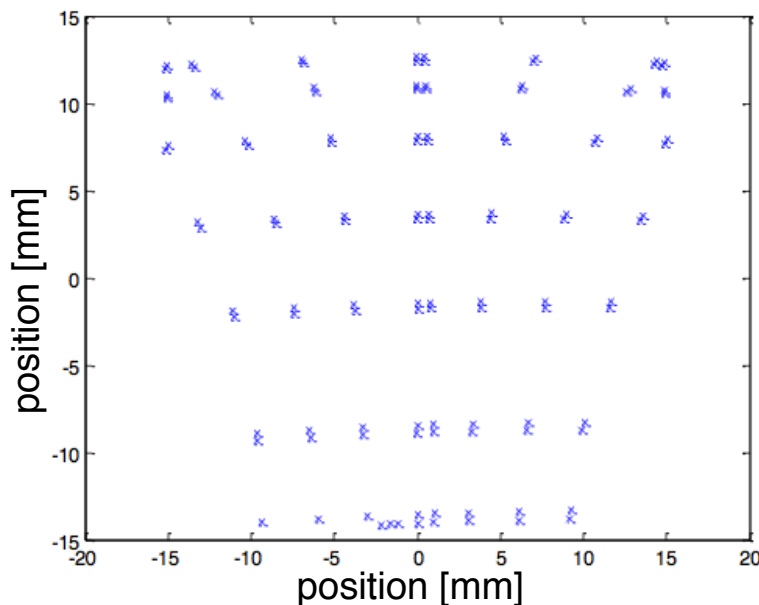
Figure 6.14: Detector image of the CAFE optical model - This is the output of the CAFE optical model. Crosses are the centroids of the ray traced by the model. Their location depends on the wavelength and on the NF and FF patterns recorded with RadiCa2D.

6.3 Instrument integration

RadiCa2D was fully assembled and aligned at the UDIT optics laboratory (see Fig. 6.16). Here, we used a set of lenses, a lamp, a diaphragm, a pinhole, and an integrating sphere to simulate the CAFE object. RadiCa2D in real operation has to be placed close to the CAFE slit position. This is a very delicate and crowded part of the spectrograph. For this reason,
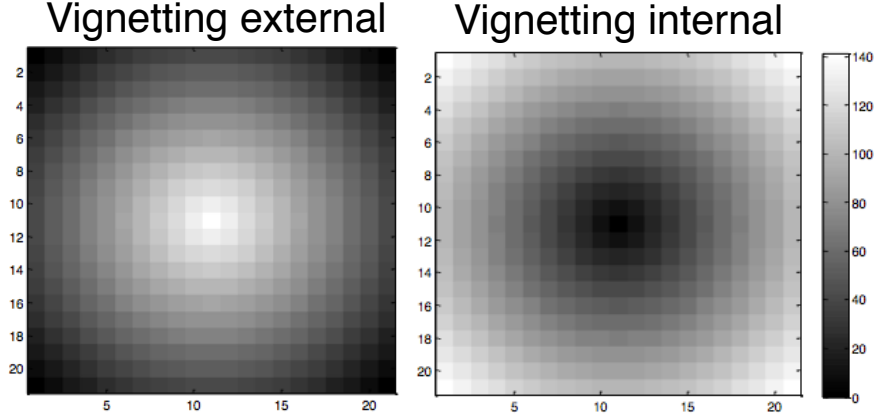
Figure 6.15: Simulated FF images - Simulation of the 20×20 pixels FF images that would result in case of vignetting the telescope pupil in CAFE.

the best RadiCa2D nominal position was chosen to be suspended in a vertical position. In that way, we can carry most part of the instrument to the backside or the slit reducing undesirable distortions with the science beam. Additionally, an angle has to be added between RadiCa2D vertical and horizontal arms to better adjust the instrument to the available space. The angle is introduced with a folding flat mirror placed at the two arms interface. RadiCa2D suffered two mayor redesigns before ending at this suspended position. In Fig. 6.17 I show RadiCa2D as it looks in CAFE during an in-situ test operation in CAFE performed on May 8, 2014.

6.3.1 CAFE first image

During the first test in CAFE, the best images we could obtain were similar to that shown in Fig. 6.18. The image resulted to be tilted and, besides the central column, some light also reached the adjacent microlenses. Our simulations discarded a tilt of the BS as the origin. Tilts larger than 5° would be required, something that is unlikely since the BS is fix in a aluminum holder. However, we could reproduce the real image by tilting the vertical arm with respect to the horizontal arm by an angle of 5° (see Fig. 6.19). This explanation is feasible due to the loose-fitting plastic holder that supports both arms along with the folding mirror.

In addition to the tilt, it is clear that the image is larger than the size of the central microlenses. Using the RadiCa2D Zemax model, we realized that this effect could be explained by the chromaticity of the image (see Fig. 6.20). This happens because the system is not telecentric and thus changes in focus produce changes in the plate scale[1]. Although this result complicates the analysis, if the tilt was corrected, we will be able of delimiting the NF and FF analysis to the central microlenses.

---

[1]Making the system telecentric is straightforward, it implies to place L2 at 500 mm from L1 (i.e. at $F_{L1} + F_{L2}$). However, the instrument size increment can not be assumed (see Appendix D).
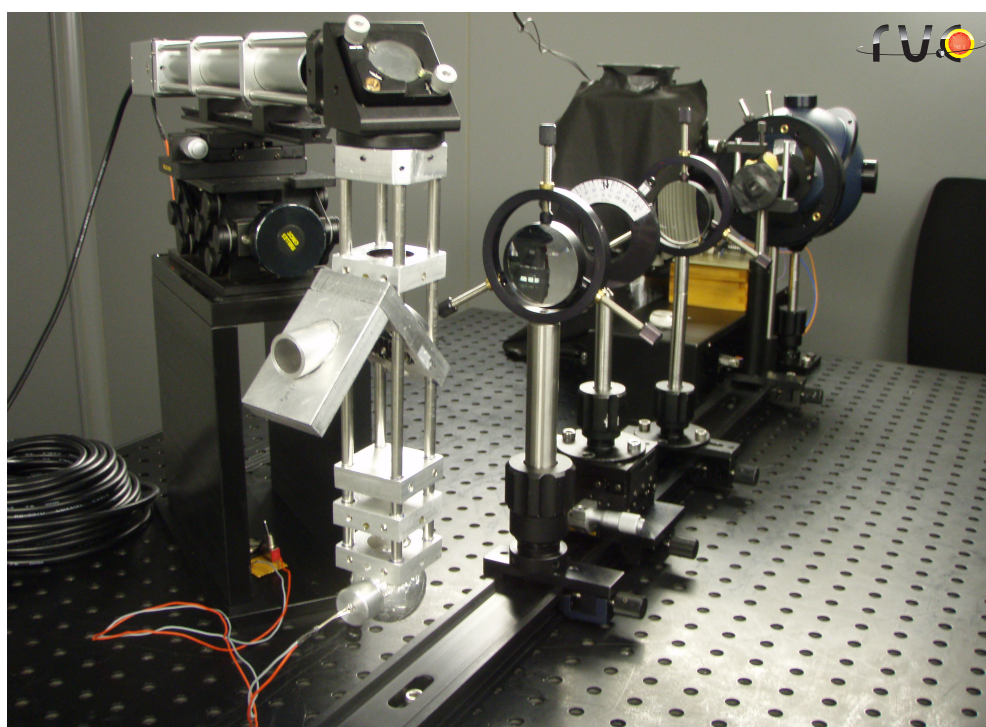
Figure 6.16: RadiCa2D at the UDIT laboratory - The laboratory set-up is used to simulate the slit of CAFE and thus to test the prototype.
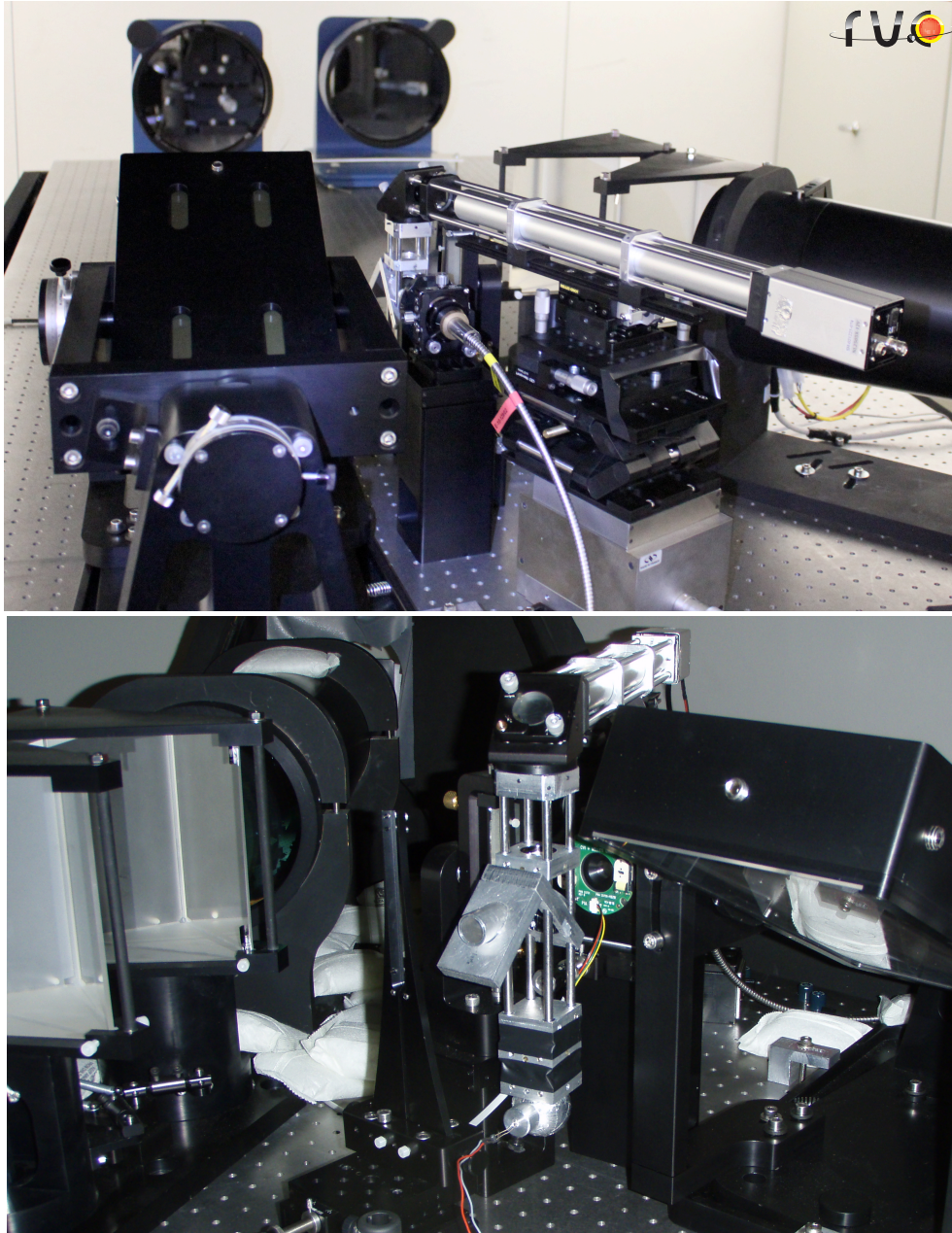
Figure 6.17: RadiCa2D in CAFE - The image show the nominal position of RadiCa2D inside CAFE. Image taken during the in-situ test operation of May 8, 2014.
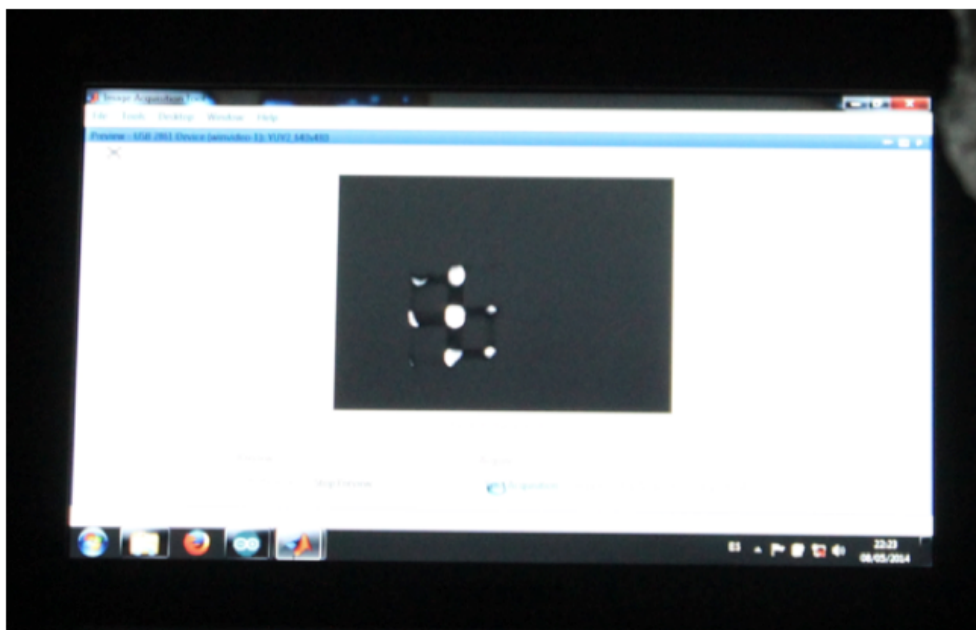
Figure 6.18: Image in real operation - The images recorded by the RadiCa2D during the in-situ test of May, 2014. The image is tilted and thus not only the central microlenses are illuminated.
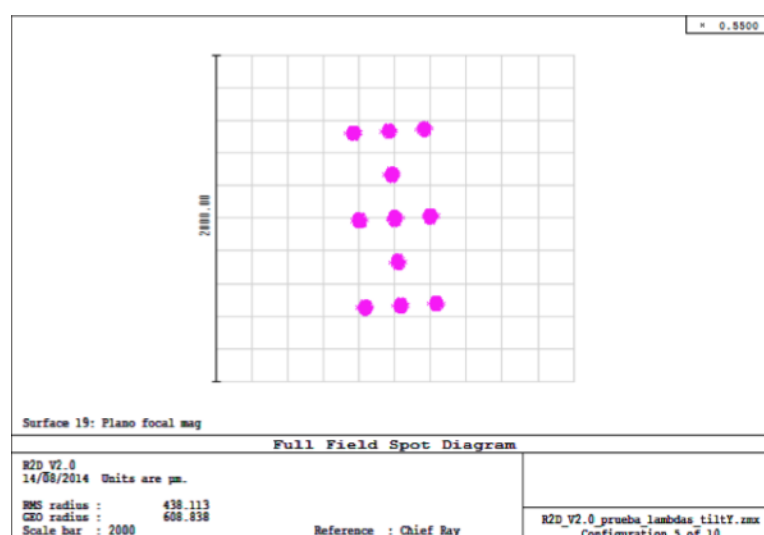
Figure 6.19: Simulated tilt - Spot diagram considering a tilt of 5° between the vertical and horizontal arms.
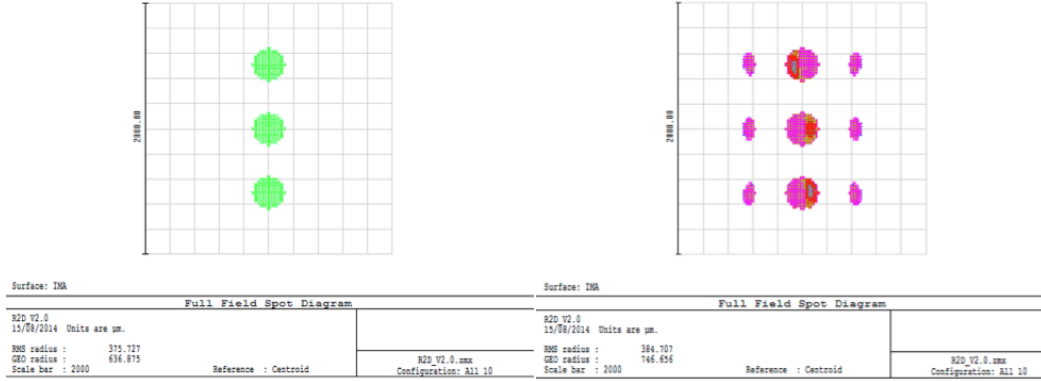
Figure 6.20: Simulated wavelength response - Image of a $270 \times 100 \, \mu$m slit on the detector for a single 520 nm wavelength (left) and for the whole 396-880 nm CAFE range (right). The number of the illuminated microlenses varies in a wavelength dependent manner.

6.4 Summary and next steps

This work is focused on the instrumental development of RadiCa2D. This instrument aims at correcting the RV errors derived from slit illumination inhomogeneities, one of the main contributors to the total RV error budget. RadiCa2D monitors in real time the near and far field images which account for the illumination distribution. The instrument (explained in detail in this Chapter) was already assembled and aligned. However, its final performance still needs to be demonstrated. Consequently, the project is still under development. Currently, we are testing the CAFE model performance, and in particular, we are optimizing the RV calculation. Once the tilt between arms is solved, the next step will be use the CAFE optical model to estimate the RV correction that RadiCa2D can provide. With this objective, we will test the performance of NF and FF images taken at the laboratory. Some of the aspects already identified to be potentially improved in future RadiCa2D prototypes are:

1. Increase the overall mechanical stability of the instrument paying special attention to the interface between both in order to avoid tilted images.

2. Use a capture device allowing tunable exposure times and a detector with a larger wavelength range.

3. Select a pellicle beam-splitter with a quality better than $\lambda/8$-10 (CAFE works with $\lambda/20$).

4. The prototype should be anodized to avoid reflections inside the spectrograph.

5. Use an array with a higher density of microlenses to improve the NF sampling.

6. Choose and adequate distribution of the microlenses in the array.

7. Make the system telecentric to avoid changes in the plate scale.

8. Resize the calibration unit field aperture to fit the size of the science object.

*O verdadeiro heroísmo consiste
en trocar os anceios en reali-
dades, as ideias en feitos.*

Sempre en Galiza, Castelao
(1886-1950)

7
Conclusions

THROUGHOUT this thesis, I have presented the results of the "Cool Tiny Beats" (CTB) project focused on unveiling the short-time domain of M dwarf stars using high-precision radial velocities. From the thorough characterization of sub-day instrumental effects, to the main scientific results regarding planets and stellar pulsations, and even to the description of a new radial velocity (RV) corrector instrumental prototype; the main conclusions of this dissertation are:

- We have analyzed the main sources of noise of the high-cadence and high-resolution data obtained with the CTB survey on HARPS and HARPS-N spectrographs. With the aim of delving into the not very-well known sub-night response we have alternated HARPS-N observations of the well-suited pair of M dwarfs GJ 725A+B. Our results show that the measured spectral energy distribution (SED) is wavelength and time-dependent and that this variability is correlated with flux losses at the fibre input. We have also shown that the SED variability correlates with the FWHM-index given by the HARPS pipeline (the DRS), which is generally used as a proxy of the Doppler variability caused by the star magnetic activity. Further tests indicate that the input flux losses do not seriously affect the shape of the point spread function of HARPS-N. We have identified an inefficient fitting of the continuum as the most likely source of the systematic variability observed in the FWHM index. Contrarily, we have shown that the RVs calculated using the template matching technique as implemented in the technique of TERRA software –which self-consistently corrects for changes in the blaze functions– are insensitive to

changes in the slope of the SED. As a consequence, we conclude that the optimal way to proceed to achieve robust and reliable measurements of the RV, and true changes in the shape of the mean-line profiles, are modeling techniques measuring moments of the line profile which are self-consistently adjusted with continuum corrections across the spectrum (e.g. our moments of the LSDs profiles).

- We have also identified in our data other previously known instrumental and/or reduction-process effects causing both intra-night and night-to-night variabilities. Using GJ 588 and GJ 699 high-cadence data we detailed a way to characterize and mitigated them. To correct the CTI effect, that cause the RVs to correlate with the SNR, we have used a logarithmic function defined from the observation of GJ 887 at different exposure times (i.e. at different SNR). This correction should at least be valid for M dwarfs observed with HARPS. We have also detected $\sim 0.5 - 1.5\,\mathrm{m\,s^{-1}}$ night-to-night jumps in the RVs, that are associated to systematic errors in the wavelength solution. Given the short time-baseline of our typical high-cadence runs (3-4 days) we have accounted for this effect using the same wavelength solution from one-night calibrations as the reference for the whole run. Finally, we have corrected with a linear function the seeing effect that causes the RVs to linearly decrease when the seeing value of the observations is lower than the fiber size (~ 1 arcsecond).

- We have analyzed the GJ 588 and GJ 699 (Barnard's star) Doppler time-series with the aim of detecting, for the first time, periodic signals compatible with stellar pulsations. These data were obtained with HARPS as part of the CTB project. The targets were selected among the CTB sample in terms of their long-term stability. Stellar pulsations are common across the Hertzsprung-Russell diagram, and they have also been theorized in M dwarfs with periods ranging from 20 min up to 3 h due to either the *flux-blocking* or the ϵ thermodynamical mechanisms. Our analysis did not revealed any confident detection in the predicted range of pulsations. Nevertheless, our analysis of both the *ln-$\mathcal{L}$* periodogram and power spectra revealed some excess of power that does not seem to be compatible with pure white noise. Comparing the most prominent periodogram peaks with the stellar theoretical models, we found the 12 d^{-1} ($\sim$2 h) putative signal of GJ 588 to be compatible with low-radial, low degree ℓ=1 and ℓ=2 g-modes. Contrarily, the GJ 699 putative signals were not compatible with any pulsation mode with the physical parameters of the star. Finally, we derived an upper limit of $\sim 0.5\,\mathrm{m\,s^{-1}}$ (90% completeness level) to the presence of signals in the regime where stellar pulsations would be expected. Next generation spectrographs (and possibly larger telescope apertures) are needed to detect pulsational signatures below this value. Nevertheless, due to the reduced size of the analyzed sample, it is still feasible that pulsations above this limit exist and have not been detected yet. This motivates further work on a larger sample with HARPS, CARMENES and possibly ESPRESSO when it becomes available (2017+).

- Combining Doppler measurements from HARPS, HARPS-N, HIRES, APF PFS and CARMENES spectrographs show very strong evidence for two planet candidates orbit-

ing Luyten's star. We used *ln-$\mathcal{L}$* periodograms to establish the significance of the signals and a Bayesian approach to calculate the credibility intervals for the planet parameters. Even though CARMENES data alone cannot confirm the signals, its results are in well-agreement with the previous HARPS data (archival and obtained by us). These results give support to the CARMENES performance as a new planet finder spectrometer. Our results indicate that Luyten b has a 1.11 $M_\oplus$ minimum mass and a 4.7-day orbital period, being too close to the star to be in the classic habitable zone (HZ). On the other hand, Luyten c has a 18.6-day period and a 2.13 $M_\oplus$ minimum mass, and lies at the outer edge of the classic HZ, but within its more optimistic definition. We have also checked the system dynamical stability. Periodograms indicate additional long-term ∼400-500 days Doppler signals of an unknown origin. Besides the radial velocities, we have also studied other spectroscopic (i.e. individual chromospheric lines and profiles moments) and photometric indices (ASAS and OSN follow-up time-series). Our analysis indicated that, while long-term Doppler signals could arise from the star's activity, their long periods are well out of the range of those of the planet candidates. In the future, astrometric missions like *Gaia* could shed light in the origin of these long-term signals (the astrometric signal is favored by large star-planet distances). Finally, the proximity (d=3.0 pc) of Luyten's star makes it an ideal target for future missions to explore planet atmospheres.

- We have summarized the report of two additional planetary systems discovered by our team: The Kapteyn's star b and c planets, and our recently discovered Proxima b. Kapteyn b and c correspond to two super-Earth mass planets of 4.8 $M_\oplus$ and 7.0 $M_\oplus$, respectively. Kapteyn's star is an old star located in the halo of our Galaxy. Thus, Kapteyn's b, which is within the HZ of the star, is the oldest potentially habitable planet known to date. Kapteyn's star may be part of a satellite dwarf galaxy that was engulfed by the Milky Way. If this is the case, this discovery would support the planet?s survival to intergalactic merges. We have also presented a summary of our recent discovery of Proxima b, an Earth-mass planet that orbits within the HZ of our closest neighbor Proxima Centauri (minimum mass of 1.3 $M_\oplus$ and orbital period of ∼11.2 days). In particular for Proxima, we have incorporated the experience acquired in characterizing the instrumental effects in the short period domain including CTI and wavelength solution effects and consistent recomputation of line-profile shape measurements (moments of the LSDs profiles). Among them, the index accounting for the width of the line-profile resulted to be in good agreement with the photometric measurements of the stellar flux. Our results, together with the most recent studies that conclude that the presence of liquid water in the surface of Proxima b is feasible, depending on its formation and evolution story, open exciting unique exploration and characterization opportunities, mostly thanks to its proximity to the Sun and more favorable star-planet contrast when compared to Sun-like stars.

- We have described the main sources of error that limit the overall precision of the RV series obtained with échelle fiber-fed spectrographs. Those are: the instrument mechan-

ical and thermal stability, the wavelength calibration accuracy, and the slit illumination stability. Regarding the last source, we have described how optical fibers are used to homogenize the light distribution, thus correcting the effects derived from its instabilities. We presented also the "Radial Velocity Corrector" project which is conceptually based on simultaneously monitoring the light instability and correcting its error contribution to the final RV measurement. In particular, we described RadiCa2D, the first prototype developed to be installed inside the CAFE spectrograph. We have already integrated and aligned this small corrector of RVs. Additionally, we have also developed the controlling, acquisition and reduction software. Our first tests in CAFE already stressed some of the most limiting sub-systems in terms of mechanical stability and near field monitoring. Nevertheless, this is still an undergoing project and the final performance of the corrector needs yet to be confirmed.

The Earth is the cradle of mankind. But one does not live in the cradle forever.

Konstantin Eduardovich
Tsiolkovskii (1857-1935)

8

Future perspectives

In the short-term, my aim is to complete and publish our work about Luyten's star Earth-mass planets. Besides a publication reporting the planet detection, we are also working in a second paper focused on a dynamical study of the system. This second work will analyze the influence of effects such as tidal forces, resonance configurations, or the system stability in the presence of an outer ∼400-500-day planet, among others.

Additionally, in a medium term I also aim at finally testing the RadiCa2D performance. Besides that, there are other medium-term projects in which in which I am already involved. These projects are directly linked with the study of M dwarfs planetary systems and represent the natural evolution of this thesis. I summarize them as follows:

- **Red dots collaboration** - This is a Proxima b legacy project. It consists in using HARPS and HARPS-N to identify exoplanets around our closest M dwarfs neighbors (initially < 5 pc), that may be appropriate primary targets for future atmosphere characterization. In fact, the properties of this likely sample will help to constrain the design of future instruments, like HIRES/E-ELT (e.g. to combine chronography and high-precision spectroscopy capabilities). Our experience indicates that stellar activity is now the main limiting factor towards detecting lower mass planets. For this reason, classic survey observing strategies (i.e. targets with random time cadences) are not valid anymore for deep high-precision searches. An specific observing cadence has to be selected adequately adequately to the probed period. Therefore, the success of this project relies on both the cadence selection as well as in the pre-selection of targets with currently

known unambiguous signals. Additionally, we will obtain simultaneous millimagnitude photometry from different medium-sized telescopes. This approach have demonstrated to be essential with Proxima b, since it allowed us to seek for traces of the photometric variability in the spectral indices. For example, the correlation of the second order moment m_2 accounting for the spectral line width with the photometric curve. We have already submitted a proposal to the ESO 99A period and to ORM 2017A semester to study three and 2 M dwarfs, respectively (co-I: Z. M. Berdiñas).

- **M dwarfs beats** - We have study in detail the very short domain of two M dwarf stars searching for stellar pulsations with unfruitful results. Nevertheless, such result is not statistically significant due to the reduced size of the sample. In fact, our knowledge about pulsation instability strips in the HR diagram of other spectral types indicate that pulsating and non-pulsating stars can be found coexisting with in the strip. These reasons motivate us to continue our high-cadence survey of M dwarfs with HARPS and HARPS-N. Indeed, our simulations and observational results agree with the fact that stellar pulsations in the range of periods up to 3 h can be detected with amplitudes greater than $\sim 0.5\,\mathrm{m\,s^{-1}}$ if targets are monitored for four consecutive nights. We have already applied for a total of 4 nights from HARPS-N to monitor one of the targets of the CTB sample at high-cadence during 2017 A (co-I: Z. M. Berdiñas). With the aim of getting the most out of our search of pulsations, we also plan to make use of the extreme precision and sensitivity of ESPRESSO. We will apply for time as soon as the instrument is offered and the observations will be also used to test the instrumental response in the sub-night domain, as we have already done with HARPS spectrographs. Additionally, we also plan to apply for observing time with CARMENES. Pulsation signals in other spectral types have demonstrated to have different amplitudes as a function of wavelength. CARMENES will extent the wavelength range into the NIR, which will allow us to explore a new range where the amplitudes of the pulsation signals could be larger and thus more easily detected. However, as this science case is very demanding in terms of RV precisions, we will apply for telescope time as soon as CARMENES reaches a $1 - 2\,\mathrm{m\,s^{-1}}$ precision in the NIR.

- **Planet atmospheres with CARMENES and CRIRES+/ESPRESSO** - High-resolution spectroscopy has demonstrated to be the best way of obtaining spectroscopic signatures of the planets? atmosphere from the ground. This technique has now proved to be able to resolve molecular bands and individual lines with 4-m class telescopes. For example, when resolved, the wings of the $\mathrm{Na_I}$ D1 and D2 lines give us information of the pressure profile of the atmosphere, whereas the centers of the line inform about the temperature profile. Besides the high-resolution spectroscopy, the chromaticity of the Rossiter-McLaughlin (RM) effect can also be used to perform atmospheric studies. That is, the modulation of the RV amplitude (RV effect) varies chromatically during a transit due to the differential absorption in the planetary atmosphere. This effect gives us information about the atmosphere composition and can be also addressed with high-

resolution spectroscopy. CARMENES is already performing optical-NIR high-resolution spectroscopic observations of individual hot jupiter targets. I plan to work with this collaboration, as well as to help in extending this study to CRIRES+ and ESPRESSO from the Southern Hemisphere.

- **CARMENES survey** - Finally, and as part of the CARMENES Consortium, I also plan to work on the data analysis from the CARMENES survey. In particular, I will be contributing in more activity related measurements and ways to monitor the spectral line profile as a function of time. This should enable deeper searches towards smaller planets.

Despite evolving incredible fast, there are many open questions in the field of exoplanets hosted by M dwarfs. Forthcoming instruments like ESPRESSO and HIRES from the ground, and like $PLATO$, $TESS$ and the $JWST$ from space are equipped to finally unveil biomarkers in the atmospheres of such planets. Without any kind of doubt, if the Proxima b discovery was a resounding success, the detection of biosignatures in an exoplanet atmosphere would be a complete scientific and philosophical revolution.

A

List of publications related to this Thesis

1. **Z. M. Berdiñas**, P. J. Amado, G. Anglada-Escudé, C. Rodríguez-López. (2016a). High-cadence spectroscopy of M dwarfs - I. Analysis of systematic effects in HARPS-N line profile measurements on the bright binary GJ 725A+B. *MNRAS*, **459**, 3551.

2. **Z. M. Berdiñas**, C. Rodríguez-López, P. J. Amado, G. Anglada-Escudé. (2016b). High-cadence spectroscopy of M-dwarfs - II. Searching for stellar pulsations with HARPS. *Submitted to MNRAS.*

3. G. Anglada-Escudé, P. J. Amado, J. Barnes, **Z. M. Berdiñas**, R. P. Butler, G. A. L. Coleman, I. de la Cueva, S. Dreizer, M. Endl, B. Giesers, S. V. Jeffers, J. S. Jenkins, H. R. A. Jones, M. Kiraga, M. Kürster, M. J. López-González, C. J. Marvin, N. Morales, J. Morin, R. P. Nelson, J. L. Ortiz, A. Ofir, S. J. Paardekooper, A. Reiners, E. Rodríguez, C. Rodríguez-López, L. F. Sarmiento, J. P. Strachan, Y. Tsapras, M. Tuomi, M. Zechmeister. (2016a). A terrestrial planet candidate in a temperate orbit around Proxima Centauri. *Nature*, **536**, 437.

4. G. Anglada-Escudé, M. Tuomi, P. Arraigada, M. Zechmeister, J. Jenkins, A. Ofir, S. Dreizler, E. Gerlach, C. J. Marvin, A. Reiners, S. V. Jeffers, P. R.

BUTLER, S. S. VOGT, P. J. AMADO, C. RODRÍGUEZ-LÓPEZ, **Z. M. BERDIÑAS** ET AL. (2016b). No Evidence for Activity Correlations in the Radial Velocities of Kapteyn's star. *ApJ*, **830**, 74.

5. E. RODRÍGUEZ, C. RODRÍGUEZ-LÓPEZ, M.J. LÓPEZ-GONZÁLEZ, P.J. AMADO, S. OCANDO, **Z. M. BERDIÑAS**. (2016). Search for pulsations in M dwarfs in the Kepler short-cadence data base. *MNRAS*, **457**, 1851.

6. G. ANGLADA-ESCUDÉ, P. ARRAIGADA, M. TUOMI, M. ZECHMEISTER, J. JENKINS, A. OFIR, S. DREIZLER, E. GERLACH, C. J. MARVIN, A. REINERS, S. V. JEFFERS, P. R. BUTLER, S. S. VOGT, P. J. AMADO, C. RODRÍGUEZ-LÓPEZ, **Z. M. BERDIÑAS** ET AL. (2014). Two planets around Kapteyn's star : a cold and a temperate super-Earth orbiting the nearest halo red-dwarf. *MNRAS*, **443**, L89.

In preparation:

6. P. J. AMADO, **Z. M. BERDIÑAS**, M. TUOMI, G. ANGLADA-ESCUDÉ ET AL. (2016). Two rocky planets orbiting Luyten's star. *In preparation.*

Proceedings:

7. **Z. M. BERDIÑAS**, P. J. AMADO, G. ANGLADA-ESCUDÉ. (2015). The Cool Tiny Beats Project - A High-cadence HARPS Survey Searching for Short-period Planets, Pulsations and Activity Signatures in M stars. *Cambridge Workshop on Cool Stars, Stellar Systems, and the Sun*, **18**, 723.

8. F. J. ALONSO-FLORIANO, D. MONTES, J. A. CABALLERO, A. KLUTSCH, S. JEFFERS, A. REINERS, M. ZECHMEISTER, A. LAMERT, V. M. PASSEGGER, R. MUNDT, P. J. AMADO, **Z. M. BERDIÑAS**, E. CASAL, M. CORTÉS-CONTRERAS, J. C. MORALES, I. RIBAS, C. RODRÍGUEZ-LÓPEZ, A. QUIRRENBACH. (2015). Preparation of the CARMENES Input Catalogue: Low- and High-resolution Spectroscopy of M dwarfs. *Cambridge Workshop on Cool Stars, Stellar Systems, and the Sun*, **18**, 796.

9. A. QUIRRENBACH, P. J. AMADO, J.A. CABALLERO, R. MUNDT, A. REINERS, I. RIBAS, W. SEIFERT, M. ABRIL, J. ACEITUNO, F. J. ALONSO-FLORIANO, M. AMMLER-VON EIFF, R. ANTONIA JIMÉNEZ, H. ANWAND-HEERWART, M. AZZARO, F. BAUER, D. BARRADO, S. BECERRIL, V.J.S. BÉJAR, **Z. M. BERDIÑAS** ET AL. (2014). CARMENES. Instrument Overview. *SPIE Proceedings*, **9147**, 1.

B
"Heavens round their hub"

Diagrams at the beginning of each chapter correspond to the patterns traced by the planets on their orbits as seen from Earth. These patterns were recorded from the Munich Planetarium. The main goal of the Ptolemaic geocentric theory was to explain this observational evidence of the movement of the planets. We can find these diagrams in the Jacob Bronowski's book "The Ascent Of Man" –based on a 1973 groundbreaking TV series of the same name– under the caption: "A sense of the heavens moving round their hub, and the hub was the round earth"[1]. The patterns of Mercury, Venus, Mars, Jupiter and Saturn correspond to Chapters 3, 2, 4, 5, and 6, respectively.

---

[1]"The Ascent Of Man", Jacob Bronowski, 1973, see: `http://isites.harvard.edu/fs/docs/icb.topic782699.files/Nov_17_Bronowski_ascent.pdf`

C

Planet detection methods

The present Appendix summarizes the main methods used to detect extrasolar planets apart from the radial velocities, those are: the transit, astrometry, pulsar timing, and direct image methods. A summary of these and other methods is shown in Figure C.1. This section comprises a description of the underlying theoretical concepts and the main planet parameters provided by each method, as well as the state-of-the-art and number of detections as of 2016.

C.1 Transits

Among all the methods, transit surveys have been the most productive in terms of number of exoplanets discovered. In fact, only the space satellite *Kepler* has detected more than half of the total exoplanetary population. That is, 2692 amongst the total 3533 planet population. A transit is simply the pass of an extrasolar planet in front of its host star in the line of sight to Earth. When a planet transits, it obstructs a percentage of the starlight reaching the Earth. Therefore, as it was traditionally done for binary stars, we can obtain information about a transiting planet by analyzing the dips that it periodically causes in the star brightness. In Fig. C.2 we can see how the stellar flux (solid line at the bottom) decreases during the planet ingress (contact points 1 and 2 in the diagram), stays flat at the bottom (points 2-3), and increases again during the egress (points 3-4) up to reach again the regular stellar flux level (contact point 4). This whole process is known as *transit* and the flux dip produced during the event is called *transit curve*. The limb-darkening effect (i.e. the apparent center-to-edge stellar

brightness gradient) modulates the slope of the transit curve during the ingress and egress and makes it to be different from a box-shape curve. However, the limb-darkening effect is wavelength dependent, causing the observations at shorter wavelengths to have deeper transits and narrower central flat regions. As a consequence, a thorough modeling of the limb-darkening effect is needed to fit the transit curve.
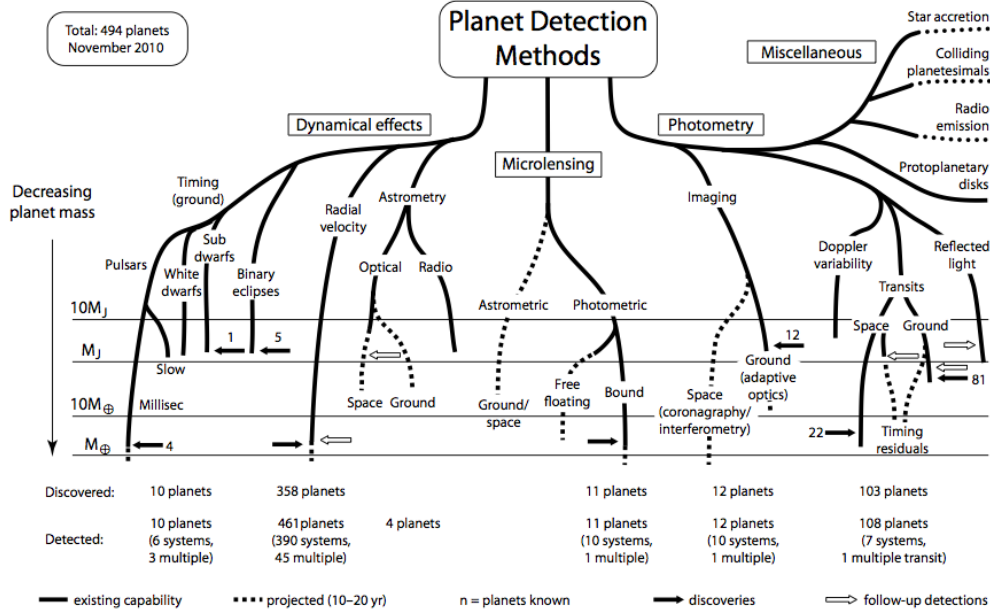
Figure C.1: Detection methods tree - The planet detection methods organized in groups depending on the main effect in which they are based. The end of the method-lines is characterized by the limiting planet masses they can detect. Dashed lines are predictions for 2020-2030. The miscellaneous branch in the upper right area groups the methods for which the mass limit in not well-constrained. Solid arrows indicate detections according to approximate mass. Hollow arrows indicate that relevant measurements of previously-detected systems have been made. Detection numbers given are for November 2010. *From Perryman (2011).*

Among all the planet detection methods, transits surveys are the only method that allows us to obtain the planet's radius, semi-major axis, and system inclination. From the observations we can measure the *transit depth* (ΔF); then, assuming a circular orbit ($e = 0$), we can roughly estimate the planet's radius from:

$$\frac{\Delta F}{F} = \left(\frac{R_p}{R_\star}\right)^2 , \tag{C.1}$$

where F is the stellar flux (i.e. the flux out-of-transit), and $R_\star$ is the star's radius, that was previously estimated with another method[1]. Then, the flux drop for and Earth-like planet

---

[1]The accuracy of the planet physical parameters relies on the star parameters estimations. As-

orbiting a Sun-like star would be $\sim 0.0084\%$, or 84 parts per million (ppm), a few times the *Kepler* precision limit. We note that the strength of the transit signal is favored by M dwarfs systems, indeed the same Earth-like planet orbiting a M4V star would lead to a signal twice more intense.

On the other hand, the transit duration (t_T), which is generally obtained from averaging several transit events, allows us to know the orbital semi-major axis. Later, we can obtain the orbital period from the third Kepler's law. In the simplest case in which a circular orbit planet ($e=0$) transits the star along its center (equatorial transit), the transit duration can be estimated as:

$$t_T \, (hours) \simeq 13 \left(\frac{R_\star}{R_\odot} \right) \left(\frac{a}{AU} \, , \right)^{1/2} \left(\frac{M_\odot}{M_\star} \right)^{1/2} \tag{C.2}$$

where $M_\star$ is the stellar mass in solar masses.

The transit method works best for edge-on systems (i.e. with an orbital inclination $i = 90°$) and equatorial transit (i.e. with an *impact factor*, the projected distance between planet-star centers at mid-transit, $b = 0$). However, such alignment is very improbable. The minimum inclination where a transit can occur can be defined (for a circular orbit) as:

$$b \, R_\star = \cos i \, a \, . \tag{C.3}$$

Then, from this relation and assuming $R_P << R_\star$, we can obtain the approximate transit probability of a randomly oriented planet in a circular orbit as:

$$prob \, (\%) = 0.5 \left(\frac{R_\star}{R_\odot} \right) \left(\frac{AU}{a} \right) \, . \tag{C.4}$$

Consequently, a quick calculation reveals that the probability of finding an Earth-like planet (1 AU) transiting a Sun-like star is of 5%; and this value is even lower for M dwarfs. Consequently, we can say that transit events occur for edge-on (or very nearly edge-on) orbits ($i = 90°$). This is the reason why transit observations are never focused on single targets; the really power of transits relies in survey searches. In that way, we increase our chances of monitoring nearly edge-on systems.

Kepler has found more than 2600 planets, but among them only ~ 600 have been later confirmed with radial velocities. One of the main drawbacks of the transit method is the large amount of noise sources that can cause misleading signals (e.g. stellar spots or low mass binary star companions), increasing the number of false positives (up to 35%; Santerne *et al.*, 2012). For this reason, transit planets remain considered as unconfirmed until they are re-observed by other planet detection method (generally with RVs). This is the reason why several thousand of exoplanets amongst the *Kepler* database remain waiting to be confirmed. Nevertheless, very recently (Morton *et al.*, 2016) defined a new method that allowed the team to statistically confirm 1284 of them.

---

teroseismology provides the most accurately determination of the star interior and of its physical parameters.
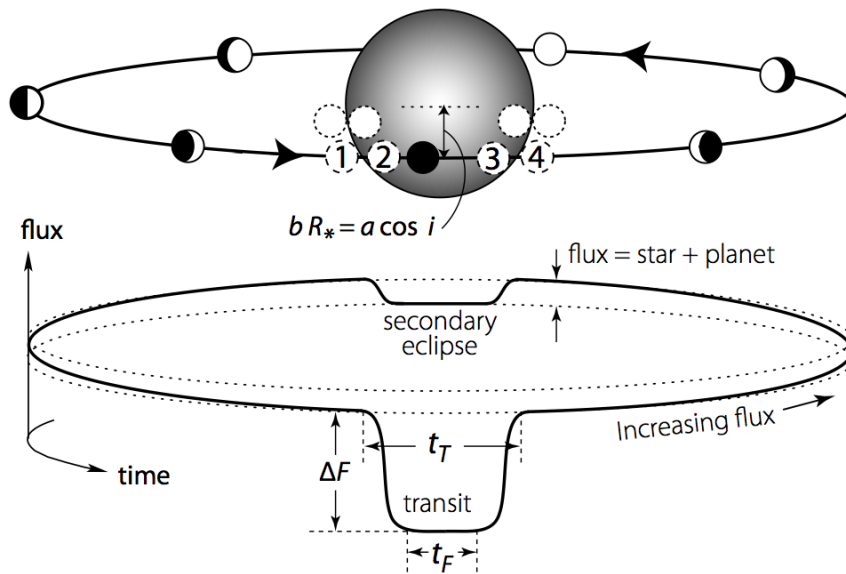
Figure C.2: Diagram of a transit - When a planet crosses in front of the star some of the starlight is blocked producing an apparent decrease of the star flux (transit) in the light curve (solid line). Circles indicate the first to fourth contact points. Dashed lines correspond to a lower impact parameter b. The transit duration is t_T between first and fourth contact points. t_F is the transit duration outside the limb-darkening area. The transit depth (ΔF) depends on the relative star/planet sizes. During a transit we obtain the transmission spectra. The emission spectra corresponds to the starlight reflected by the planet. The secondary eclipse occurs when the star blocks the planet at the point we only receive light from the star. *From Perryman (2011), who adapted it from Winn (2010).*

When a transit planet is reconfirmed with RVs we know the planet radius and mass. This implies that we can calculate the planet density which is essential to unveil the planet composition. However, we first need to know the system inclination that gives us the real planet mass (the radial velocity method only provides a lower limit). The inclination of the planet orbit with respect to the star's spin axis can be obtained through the Rossiter-McLaughlin (RM) effect during the transit[1].

Besides the planet orbital parameters, transits can give us information about the planet's atmosphere. During a transit the starlight crosses through the planet atmosphere. Thus, we can measure the planet imprints in the spectra by comparing the in and out-of-transit spectra. This gives us the *transmission spectra* of the planet wit a technique known as *transmission spectroscopy*. Moreover, if the planet's atmosphere reflects starlight, the total albedo will change during an orbital period (see bright and dark planet phases during an orbital period in the upper part of Fig. C.2). The light reflected by the planet gives the *emission spectra*. We can obtain information about the planet's atmosphere by comparing the spectra received before (or after) and during a secondary transit, where the planet is blocked by the star and only the star spectra is received.

C.2 Astrometry

Astrometry was traditionally used to calculate parallaxes and star proper motions and was the first method used with the aim of detecting extrasolar planets. Paradoxically, it has been also the less productive; only one astrometric massive planet was discovered to date (HD 176051 b; Muterspaugh *et al.*, 2010). Nevertheless, astrometry has demonstrated to be very useful giving upper limits to the minimum mass of the planets detected with radial velocities (Han *et al.*, 2001). The astrometric method is based on resolving the star wobbling produced by the presence of a planet. The difference with the RVs is that astrometry aims at measuring the star spatial displacement in the sky projection, whereas RVs measure the spectroscopic signature produced by the transverse component of the star displacement. See as an example in Fig. C.3 the movement of the Sun around the barycenter of the Solar System. Therefore, and opposite to the RVs, astrometric signatures are favored by face-on systems. With astrometry we can obtain orbital parameters such as the semi-major axis or the inclination.

The main limitation of astrometry is the extreme needed precision. The *astrometric signature* produced by a planet in a circular face-on orbit scales as:

$$\alpha \, (\text{arcseconds}) = \frac{M_p}{M_\star} \frac{a}{\text{D}} \tag{C.5}$$

where M_p and $M_\star$ are the planet and host star true masses, respectively, a is the star-planet distance in AU, and D is the star distance in parsecs (Sozzetti, 2005). Thus, ~ 1 mas would be

---

[1]During a transit, the planet blocks firstly blueshifted and later redshifted starlight when moving in the same direction that the stellar rotation. The blueshifted and redshifted light ratio gives as the inclination.
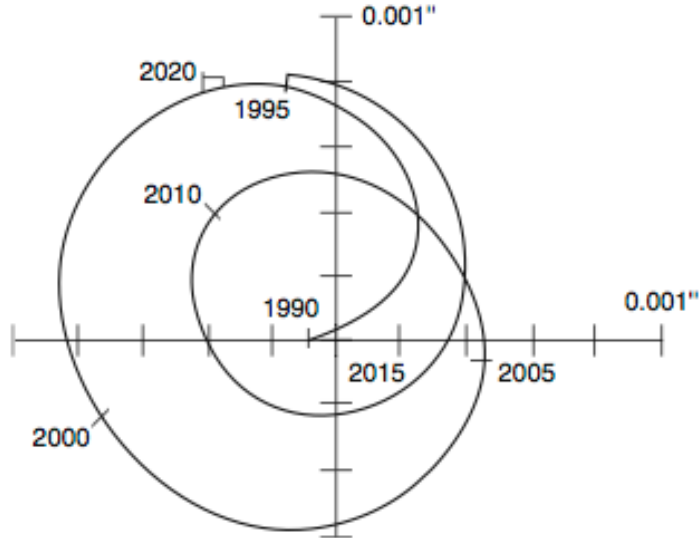
Figure C.3: Sun motion around the Solar System barycenter - Movement during 30 yr seen from 10 pc away and perpendicular to the plane of the ecliptic. Massive planets are the major responsible of the movement. *From Ollivier* et al. *(2009).*

the astrometric signature of a Jupiter-mass planet orbiting at 10 AU a Sun-mass star at 10 pc, and $\sim$3 μas that of Earth-mass under the same conditions. Consequently, while precisions of milliarcseconds are enough to detect massive nearby planets, microarcsecond precision is required to detect lower mass planets. This is the objective of the space mission *Gaia* whose first data were made public very recently (last 14th September 2016). Perryman *et al.* (2014) estimated with a $\sim$20-25 μas astrometric precision *Gaia* can discover roughly 21000$\pm$6000 long-period massive $(1-15\,M_{\mathrm{J}})$ planets out to distances of 500 pc during a 5 yr mission. Among them, at least 1000-1500 planets are estimated to orbit M-dwarf stars out to 100 pc.

C.3 Microlensing

In contrast to other methods, microlensing is sensitive to a wide range of planet masses and separations. The lensing effect was first described by Einstein's General Theory of Relativity. According to Einstein, the light from a background star blends when it passes very close to a massive foreground object on its way to an observer on Earth (Einstein, 1936). As a result, the observer can see multiple images of the background object, or a ring of unresolved images, around the foreground object. The case in which the images are not resolved is known as a microlensing event. Thus, the gravitational attraction of a planet orbiting around the foreground star can produce a secondary peak in the light curve of the microlensing event (see Fig. C.4). From this deviation of the standard event (i.e. without a planet) we can obtain the mass, period and semi-major axis of the planet. However, the effectiveness of microlensing does not rely on

the planet mass, favoring the detection of low-mass planets less accessible with other methods. The complete event can have a duration from a few hours to several days. By the end of 2016, 51 exoplanets had been discovered through gravitational microlensing. Most of them, including the first planet detected OGLE-2005-BLG-390L b Beaulieu *et al.* (2006), were discovered with the OGLE experiment Udalski *et al.* (2002), which aims at detecting dark matter using the microlensing technique.
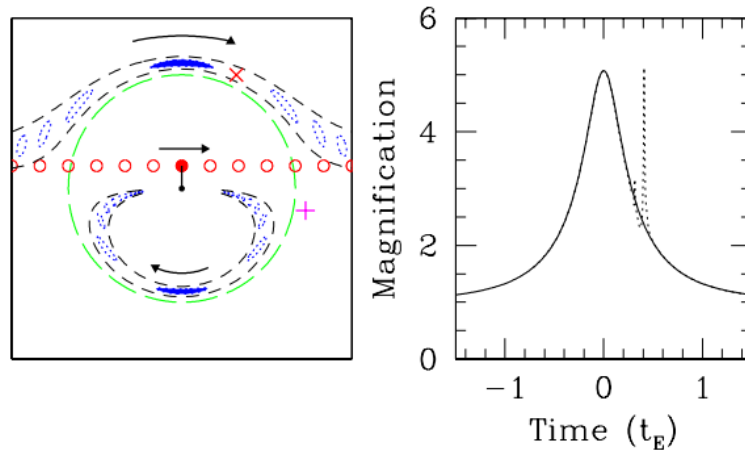
Figure C.4: Microlensing method - (Left panel) Different images of the background star (blue ovals) correspond to different positions of it (red dots) with respect to the foreground star. The green line indicates the Einstein ring. (Right panel) Light curve of the event (solid line) and the peak caused by a planet at the position "X" in the right plot (dashed line). If the planet was located at "+" (i.e out region delimited by the black dashed lines) any perturbation will appear in the light curve. *From Gaudi (2010).*

One of the main disadvantages of the microlensing events is their low occurrence. An extreme alignment is required between the observer and the background and foreground objects. Indeed, the planet signature becomes evident in the light curve only if the planet fits within the continuous ring of images of the background star. For this reason, experiments like OGLE monitor sky regions like the Galactic Bulge crowded of stars to statistically increase the number of events. This characteristic makes the planets detected by microlensing very difficult to be re-confirmed, the probability of another alignment is close to zero. On the other hand, microlensing allows us to detect planets at large distances from Earth (e.g. in the bulge of the Milky Way of even in M31; Ingrosso *et al.* 2009), not accessible with any other methods.

C.4   Pulsar timing

The first exoplanet ever detected, PSR1257+1 (Wolszczan & Frail, 1992), was discovered with the pulsar timing method (see Fig. **??**). Pulsar are rapidly rotating neutron stars that remains after a violent supernova explosion, that is, they are the remnant of the death of a massive star.

These objects emit large jets of electromagnetic radiation that reaches the Earth as periodic pulses with the regularity of an atomic clock. Alteration of this regularity can be understood as the pulsar moving back and forward due to the presence of a planet. By measuring time irregularities in the pulsar time, that typically ranges from milliseconds to a few seconds, we can infer the planet mass and orbital distance. Even though, this method has attracted less attention because the pulsar planets are thought to be non-habitable worlds as a result of the large amounts of high-energy fluxes their receive. Interesting is whether the planets survived the host star death or were captured afterwards. Nowadays, 23 planets have being discovered with this method.
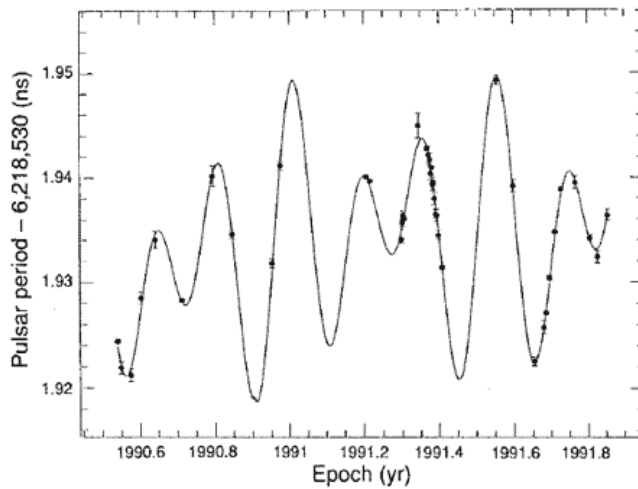
Figure C.5: Pulsar timing variations of PSR1257+12 - Each period measurement is based on observations made on at least two consecutive days. The solid line denotes changes in the period predicted by a two-planet model. *From Wolszczan & Frail (1992)*

C.5 Direct imaging

In contrast to the other methods in which the presence of an exoplanet is inferred from the star behavior, the direct imaging method consists in taking actual images of the exoplanet. This method is very challenging in terms the relative star/planet brightness. As an example, the flux of an Earth-mass planet orbiting at 0.5 arcseconds from a Sun-like star at 10 pc is $\sim 10^{10}$ times lower than the flux of the host star.

Therefore, this method is more sensitive to young brighter planets in wide orbits. Younger planets are hotter and then brighter, while wide orbital distances avoid the starlight contamination. Even though, the unfavorable flux relation requires of adaptive optics, and also of NIR wavelengths (the typical flux ratio in the NIR is $\sim 10^{-5}$). The first planet discovered with direct imaging was 2M1207 b (Chauvin *et al.*, 2004) orbiting a brown dwarf star (see Fig. C.6). To date, 72 exoplanets were found with this method, many of them orbiting A spectral type stars.
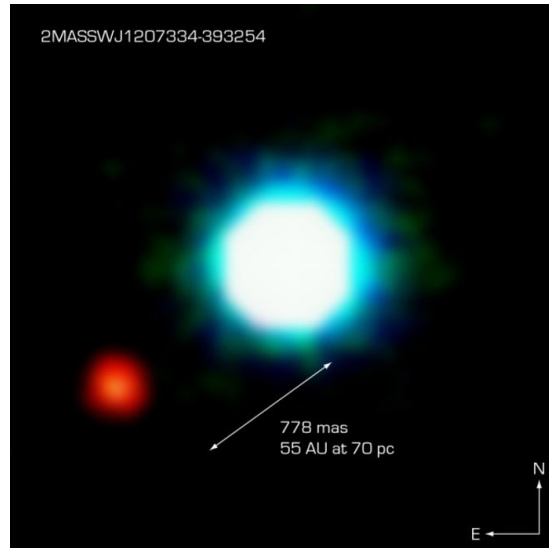
Figure C.6: Direct image of 2M1207 b - Image of the first exoplanet discovered (red dot) by direct imaging in 2004. The planet orbits the brown dwarf star 2M1207 at a distance of ~ 55 AU. The image was taken with NACO, an adaptive-optics facility at the VLT. *From ESO -* *https: // www. eso. org/ public/ spain/ images/ eso0515a/ .*

Lower stellar temperatures typical of cool K-M spectral types should favor the detectability, whereas massive stars are more prone to form planets at wide orbits. Also, the shorter life time-scales of A stars ensure young planet (≤ 5 Gyr). It is important to note that follow-up campaigns are essential in order to confirm the gravitational link of the discovered body.

D

RadiCa2D ray tracing

This Appendix explains in detail the RadiCa2D ray tracing. Two illumination set-ups are considered: the laboratory system (used to test and align RadiCa2D), and the RadiCa2D calibration unit. The first case is shown in Fig. D.1, while the second is presented in Fig. D.2. In both figures, red and blue rays account for the object and pupil ray tracing, respectively. In the laboratory system, RadiCa2D produces an image of a diaphragm (D_lab) placed at the pupil position between two laboratory lenses. The laboratory slit is proportionated to simulate a $270 \times 100 \, \mu$m slit (i.e. the slit of CAFE slit) at the RadiCa2D object location. In order to reduce the system overall size, L2 is placed at 20 mm from L1 image (D_virtual position) instead of being at the L2 focal length (i.e. 400 mm). That is, the system is not telecentric. Even when this implies the formation of virtual images, Fig. D.3 shows that the resulting image on the detector would be equivalent. Nevertheless, the system would be sensitive to changes in the focal plate at different wavelengths. This solution is a compromise to reduce the overall size of RadiCa2D.
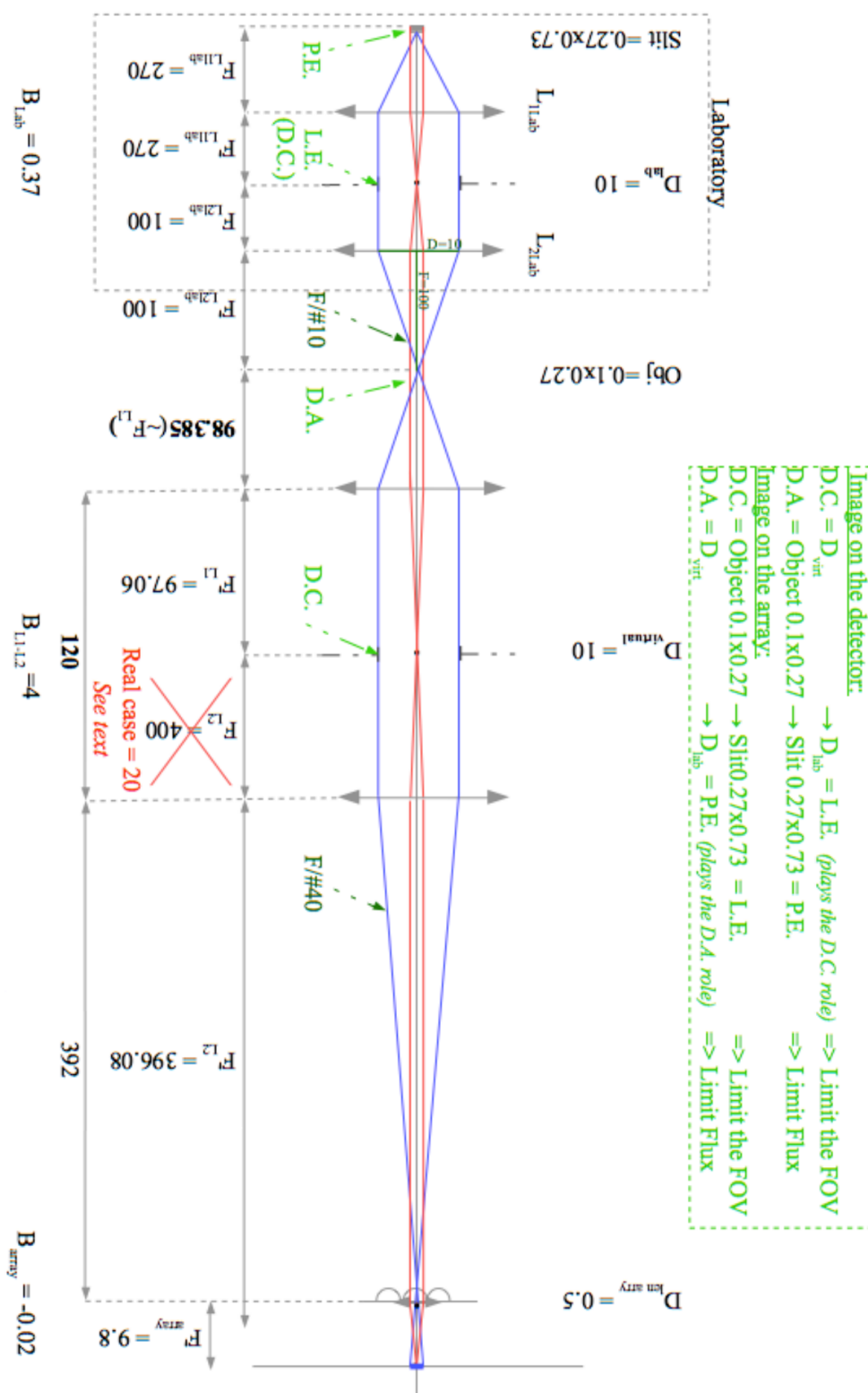
Figure D.1: RadiCa2D ray tracing–laboratory - Laboratory set-up.
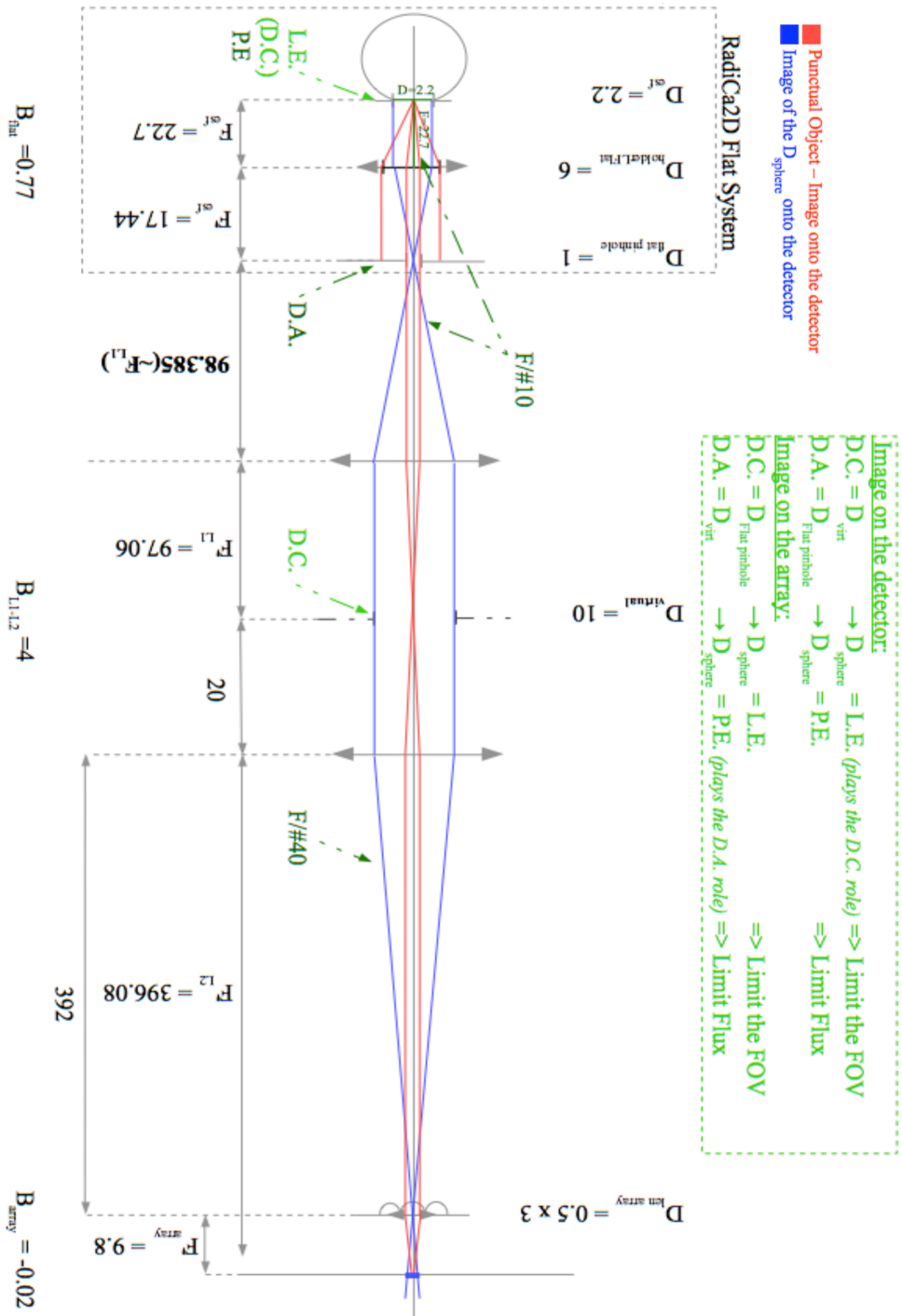
Figure D.2: RadiCa2D ray tracing–calibration unit - Paraxial raytracing illuminating RadiCa2D with the calibration unit.
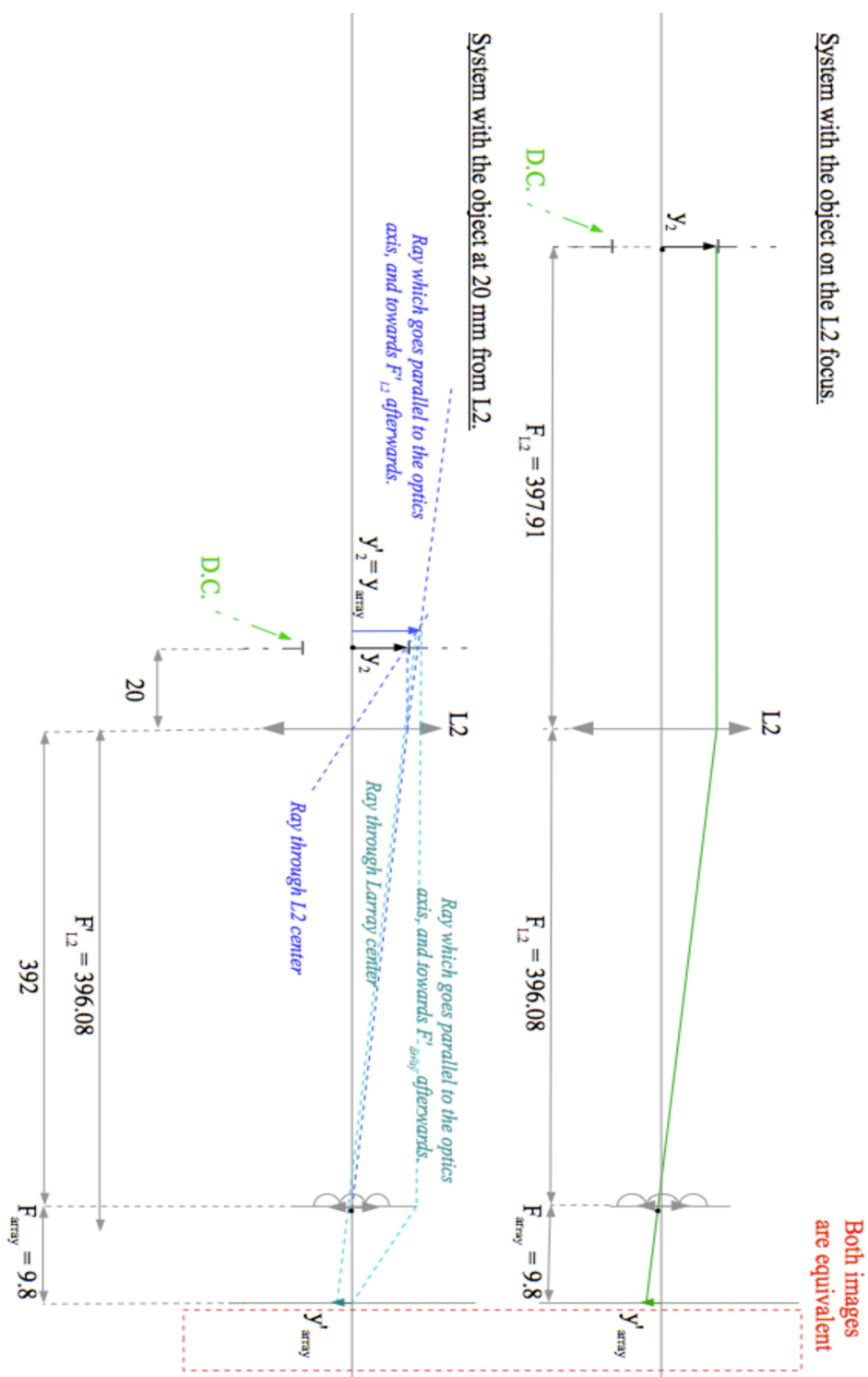
Figure D.3: RadiCa2D ray tracing–virtual L2 image - L2 virtual object produce an equivalent image onto the array than a real object placed at its focal distance.

References

Aceituno, J., Sánchez, S.F., Grupp, F., Lillo, J., Hernán-Obispo, M., Benitez, D., Montoya, L.M., Thiele, U., Pedraz, S., Barrado, D., Dreizler, S. & Bean, J. (2013). CAFE: Calar Alto Fiber-fed Échelle spectrograph. *A&A*, **552**, A31. 150

Ahrens, T.J. (1994). The origin of the Earth. *Physics Today*, **47**, 38–45. 12

Alibert, Y., Mordasini, C., Benz, W. & Winisdo-erffer, C. (2005). Models of giant planet formation with migration and disc evolution. *A&A*, **434**, 343–353. 18

Alibert, Y., Mordasini, C. & Benz, W. (2011). Extrasolar planet population synthesis. III. Formation of planets around stars of different masses. *A&A*, **526**, A63. 17

Alonso-Floriano, F.J., Morales, J.C., Caballero, J.A., Montes, D., Klutsch, A., Mundt, R., Cortés-Contreras, M., Ribas, I., Reiners, A., Amado, P.J., Quirrenbach, A. & Jeffers, S.V. (2015). CARMENES input catalogue of M dwarfs. I. Low-resolution spectroscopy with CAFOS. *A&A*, **577**, A128. 41

Amado, P.J. & CARMENES Consortium (2015). CARMENES: searching for exoplanets and much more. In A.J. Cenarro, F. Figueras, C. Hernández-Monteagudo, J. Trujillo Bueno & L. Valdivielso, eds., *Highlights of Spanish Astrophysics VIII*, 701–711. 41

Anderson, E. & Francis, C. (2012). XHIP: An extended hipparcos compilation. *Astronomy Letters*, **38**, 331–346. 54

Andrews, S.M., Wilner, D.J., Zhu, Z., Birnstiel, T., Carpenter, J.M., Pérez, L.M., Bai, X.N., Öberg, K.I., Hughes, A.M., Isella, A. & Ricci, L. (2016). Ringed Substructure and a Gap at 1 au in the Nearest Protoplanetary Disk. *ApJ*, **820**, L40. 14

Anglada-Escudé, G. & Butler, R.P. (2012). The HARPS-TERRA Project. I. Description of the Algorithms, Performance, and New Measurements on a Few Remarkable Stars Observed by HARPS. *ApJS*, **200**, 15. 43, 46, 55, 85

Anglada-Escudé, G., Arriagada, P., Vogt, S.S., Rivera, E.J., Butler, R.P., Crane, J.D., Shectman, S.A., Thompson, I.B., Minniti, D., Haghighipour, N., Carter, B.D., Tinney, C.G., Wittenmyer, R.A., Bailey, J.A., O'Toole, S.J., Jones, H.R.A. & Jenkins, J.S. (2012a). A Planetary System around the nearby M Dwarf GJ 667C with At Least One Super-Earth in Its Habitable Zone. *ApJ*, **751**, L16. 21, 111

Anglada-Escudé, G., Plavchan, P., Mills, S., Gao, P., García-Berríos, E., Lewis, N.S., Sung, K., Ciardi, D., Beichman, C., Brinkworth, C., Johnson, J., Davison, C., White, R. & Prato, L. (2012b). Design and Construction of Absorption Cells for Precision Radial Velocities in the K Band Using Methane Isotopologues. *PASP*, **124**, 586–597. 39, 41

Anglada-Escudé, G., Arriagada, P., Tuomi, M., Zechmeister, M., Jenkins, J.S., Ofir, A., Dreizler, S., Gerlach, E., Marvin, C.J., Reiners, A., Jeffers, S.V., Butler, R.P., Vogt, S.S., Amado, P.J., Rodríguez-López, C., Berdiñas, Z.M., Morin, J., Crane, J.D., Shectman, S.A., Thompson, I.B., Díaz, M., Rivera, E., Sarmiento, L.F. & Jones, H.R.A. (2014). Two planets around Kapteyn's star: a cold and a temperate super-Earth orbiting the nearest halo red dwarf. *MNRAS*, **443**, L89–L93. 107, 135, 136

Anglada-Escudé, G., Amado, P.J., Barnes, J., Berdiñas, Z.M., Butler, R.P., Coleman, G.A.L., de La Cueva, I., Dreizler, S., Endl, M., Giesers, B., Jeffers, S.V., Jenkins, J.S., Jones, H.R.A., Kiraga, M., Kürster, M., López-González, M.J., Marvin, C.J., Morales, N., Morin, J., Nelson, R.P., Ortiz, J.L., Ofir, A., Paardekooper, S.J., Reiners, A., Rodríguez, E., Rodríguez-López, C., Sarmiento, L.F., Strachan, J.P., Tsapras, Y., Tuomi, M.

& Zechmeister, M. (2016a). A terrestrial planet candidate in a temperate orbit around Proxima Centauri. *Nature*, **536**, 437–440. 14, 49, 95, 107, 108, 113, 126, 137, 138, 139, 144

Anglada-Escudé, G., Tuomi, M., Arriagada, P., Zechmeister, M., Jenkins, J.S., Ofir, A., Dreizler, S., Gerlach, E., Marvin, C.J., Reiners, A., Jeffers, S.V., Butler, R.P., Vogt, S.S., Amado, P.J., Rodríguez-López, C., Berdiñas, Z.M., Morin, J., Crane, J.D., Shectman, S.A., Díaz, M.R., Sarmiento, L.F. & Jones, H.R.A. (2016b). No Evidence for Activity Correlations in the Radial Velocities of Kapteyn's Star. *ApJ*, **830**, 74. 107, 136

Armstrong, D.J., Pugh, C.E., Broomhall, A.M., Brown, D.J.A., Lund, M.N., Osborn, H.P. & Pollacco, D.L. (2016). The host stars of Kepler's habitable exoplanets: superflares, rotation and activity. *MNRAS*, **455**, 3110–3125. 19

Avila, G. & Singh, P. (2008). Optical fiber scrambling and light pipes for high accuracy radial velocities measurements. In *Advanced Optical and Mechanical Technologies in Telescopes and Instrumentation*, vol. 7018 of *Proc. SPIE*, 70184W. 147, 148

Avila, G., Singh, P. & Chazelas, B. (2010). Results on fibre scrambling for high accuracy radial velocity measurements. In *Ground-based and Airborne Instrumentation for Astronomy III*, vol. 7735 of *Proc. SPIE*, 773588. 146, 147, 148

Balona, L.A. & Dziembowski, W.A. (2011). Kepler observations of δ Scuti stars. *MNRAS*, **417**, 591–601. 106

Baluev, R.V. (2009). Accounting for velocity jitter in planet search surveys. *MNRAS*, **393**, 969–978. 48, 50, 95

Baraffe, I., Chabrier, G., Allard, F. & Hauschildt, P.H. (1998). Evolutionary models for solar metallicity low-mass stars: mass-magnitude relationships and color-magnitude diagrams. *A&A*, **337**, 403–412. 101

Baranne, A., Mayor, M. & Poncet, J.L. (1979). CORAVEL - A new tool for radial velocity measurements. *Vistas in Astronomy*, **23**, 279–316. 4, 43

Baranne, A., Queloz, D., Mayor, M., Adrianzyk, G., Knispel, G., Kohler, D., Lacroix, D., Meunier, J.P., Rimbaud, G. & Vin, A. (1996). ELODIE: A spectrograph for accurate radial velocity measurements. *A&AS*, **119**, 373–390. 4, 39

Barnes, J.R., Collier Cameron, A., Unruh, Y.C., Donati, J.F. & Hussain, G.A.J. (1998). Latitude distributions and lifetimes of star-spots on G dwarfs in the alpha Persei cluster. *MNRAS*, **299**, 904–920. 47, 69, 86, 92

Barnes, J.R., Jenkins, J.S., Jones, H.R.A., Rojo, P., Arriagada, P., Jordán, A., Minniti, D., Tuomi, M., Jeffers, S.V. & Pinfield, D. (2012). Red Optical Planet Survey: a new search for habitable earths in the southern sky. *MNRAS*, **424**, 591–604. 69, 86, 92, 115

Barnes, R., Deitrick, R., Luger, R., Driscoll, P.E., Quinn, T.R., Fleming, D.P., Guyer, B., McDonald, D.V., Meadows, V.S., Arney, G., Crisp, D., Domagal-Goldman, S.D., Lincowski, A., Lustig-Yaeger, J. & Schwieterman, E. (2016). The Habitability of Proxima Centauri b I: Evolutionary Scenarios. *ArXiv e-prints*. 19

Bean, J.L., Seifahrt, A., Hartman, H., Nilsson, H., Wiedemann, G., Reiners, A., Dreizler, S. & Henry, T.J. (2010). The CRIRES Search for Planets Around the Lowest-mass Stars. I. High-precision Near-infrared Radial Velocities with an Ammonia Gas Cell. *ApJ*, **713**, 410–422. 41

Beaulieu, J.P., Bennett, D.P., Fouqué, P., Williams, A., Dominik, M., Jørgensen, U.G., Kubas, D., Cassan, A., Coutures, C., Greenhill, J., Hill, K., Menzies, J., Sackett, P.D., Albrow, M., Brillant, S., Caldwell, J.A.R., Calitz, J.J., Cook, K.H., Corrales, E., Desort, M., Dieters, S., Dominis, D., Donatowicz, J., Hoffman, M., Kane, S., Marquette, J.B., Martin, R., Meintjes, P., Pollard, K., Sahu, K., Vinter, C., Wambsganss, J., Woller, K., Horne, K., Steele, I., Bramich, D.M., Burgdorf, M., Snodgrass, C., Bode, M., Udalski, A., Szymański, M.K., Kubiak, M., Więckowski, T., Pietrzyński, G., Soszyński, I., Szewczyk, O., Wyrzykowski, Ł., Paczyński, B., Abe, F., Bond, I.A., Britton, T.R., Gilmore, A.C., Hearnshaw, J.B.,

REFERENCES

ITOW, Y., KAMIYA, K., KILMARTIN, P.M., KOR-PELA, A.V., MASUDA, K., MATSUBARA, Y., MOTO-MURA, M., MURAKI, Y., NAKAMURA, S., OKADA, C., OHNISHI, K., RATTENBURY, N.J., SAKO, T., SATO, S., SASAKI, M., SEKIGUCHI, T., SULLIVAN, D.J., TRISTRAM, P.J., YOCK, P.C.M. & YOSH-IOKA, T. (2006). Discovery of a cool planet of 5.5 Earth masses through gravitational microlensing. *Nature*, **439**, 437–440. 183

BEDDING, T.R., KJELDSEN, H., ARENTOFT, T., BOUCHY, F., BRANDBYGE, J., BREWER, B.J., BUTLER, R.P., CHRISTENSEN-DALSGAARD, J., DALL, T., FRANDSEN, S., KAROFF, C., KISS, L.L., MONTEIRO, M.J.P.F.G., PIJPERS, F.P., TEIX-EIRA, T.C., TINNEY, C.G., BALDRY, I.K., CAR-RIER, F. & O'TOOLE, S.J. (2007). Solar-like Oscil-lations in the G2 Subgiant β Hydri from Dual-Site Observations. *ApJ*, **663**, 1315–1324. 88

BERDIÑAS, Z.M., AMADO, P.J. & ANGLADA-ESCUDE, G. (2015). The Cool Tiny Beats Project - A High-cadence HARPS Survey Searching for Short-period Planets, Pulsations and Activity Signatures in M stars. In G.T. van Belle & H.C. Harris, eds., *18th Cambridge Workshop on Cool Stars, Stellar Systems, and the Sun*, vol. 18 of *Cambridge Work-shop on Cool Stars, Stellar Systems, and the Sun*, 723–732. 21

BOIS, E., KISELEVA-EGGLETON, L., RAMBAUX, N. & PILAT-LOHINGER, E. (2003). Conditions of Dy-namical Stability for the HD 160691 Planetary System. *ApJ*, **598**, 1312–1320. 132

BOISSE, I., MOUTOU, C., VIDAL-MADJAR, A., BOUCHY, F., PONT, F., HÉBRARD, G., BON-FILS, X., CROLL, B., DELFOSSE, X., DESORT, M., FORVEILLE, T., LAGRANGE, A.M., LOEILLET, B., LOVIS, C., MATTHEWS, J.M., MAYOR, M., PEPE, F., PERRIER, C., QUELOZ, D., ROWE, J.F., SAN-TOS, N.C., SÉGRANSAN, D. & UDRY, S. (2009). Stellar activity of planetary host star HD 189 733. *A&A*, **495**, 959–966. 113

BOISSE, I., BOUCHY, F., CHAZELAS, B., PERRUCHOT, S., PEPE, F., LOVIS, C. & HÉBRARD, G. (2010a). Consequences of spectrograph illumination for the accuracy of radial-velocimetry. In *European Phys-ical Journal Web of Conferences*, vol. 16 of *Euro-pean Physical Journal Web of Conferences*, 02003. 89, 91, 146, 147, 157

BOISSE, I., EGGENBERGER, A., SANTOS, N.C., LOVIS, C., BOUCHY, F., HÉBRARD, G., ARNOLD, L., BON-FILS, X., DELFOSSE, X., DESORT, M., DÍAZ, R.F., EHRENREICH, D., FORVEILLE, T., GALLENNE, A., LAGRANGE, A.M., MOUTOU, C., UDRY, S., PEPE, F., PERRIER, C., PERRUCHOT, S., PONT, F., QUELOZ, D., SANTERNE, A., SÉGRANSAN, D. & VIDAL-MADJAR, A. (2010b). The SOPHIE search for northern extrasolar planets. III. A Jupiter-mass companion around HD 109246. *A&A*, **523**, A88. 89

BONFILS, X., MAYOR, M., DELFOSSE, X., FORVEILLE, T., GILLON, M., PERRIER, C., UDRY, S., BOUCHY, F., LOVIS, C., PEPE, F., QUELOZ, D., SANTOS, N.C. & BERTAUX, J.L. (2007). The HARPS search for southern extra-solar planets. X. A m sin i = 11 M_$\oplus$ planet around the nearby spotted M dwarf <ASTROBJ>GJ 674</ASTROBJ>. *A&A*, **474**, 293–299. 18, 22, 137

BONFILS, X., DELFOSSE, X., UDRY, S., FORVEILLE, T., MAYOR, M., PERRIER, C., BOUCHY, F., GILLON, M., LOVIS, C., PEPE, F., QUELOZ, D., SANTOS, N.C., SÉGRANSAN, D. & BERTAUX, J.L. (2013). The HARPS search for southern extra-solar planets. XXXI. The M-dwarf sample. *A&A*, **549**, A109. 18, 101, 108, 125

BOSS, A.P. (1997). Giant planet formation by gravi-tational instability. *Science*, **276**, 1836–1839. 13

BOSS, A.P. (2006a). Rapid Formation of Gas Giant Planets around M Dwarf Stars. *ApJ*, **643**, 501–508. 18

BOSS, A.P. (2006b). Rapid Formation of Super-Earths around M Dwarf Stars. *ApJ*, **644**, L79–L82. 18

BOUCHY, F. & CARRIER, F. (2001). P-mode observa-tions on α Cen A. *A&A*, **374**, L5–L8. 106

BOUCHY, F. & CARRIER, F. (2002). The acoustic spectrum of alpha Cen A. *A&A*, **390**, 205–212. 106

BOUCHY, F., BAZOT, M., SANTOS, N.C., VAUCLAIR, S. & SOSNOWSKA, D. (2005). Asteroseismology of the planet-hosting star μ Arae. I. The acoustic spectrum. *A&A*, **440**, 609–614. 88

BOUCHY, F., ISAMBERT, J., LOVIS, C., BOISSE, I., FIGUEIRA, P., HÉBRARD, G. & PEPE, F.

REFERENCES

(2009). Charge Transfer Inefficiency effect for high-precision radial velocity measurements. In P. Kern, ed., *EAS Publications Series*, vol. 37 of *EAS Publications Series*, 247–253. 88

BOUCHY, F., DÍAZ, R.F., HÉBRARD, G., ARNOLD, L., BOISSE, I., DELFOSSE, X., PERRUCHOT, S. & SANTERNE, A. (2013). SOPHIE+: First results of an octagonal-section fiber for high-precision radial velocity measurements. *A&A*, **549**, A49. 91

BOURRIER, V. & HÉBRARD, G. (2014). Detecting the spin-orbit misalignment of the super-Earth 55 Cancri e. *A&A*, **569**, A65. 68, 73

BOYAJIAN, T.S., VON BRAUN, K., VAN BELLE, G., MCALISTER, H.A., TEN BRUMMELAAR, T.A., KANE, S.R., MUIRHEAD, P.S., JONES, J., WHITE, R., SCHAEFER, G., CIARDI, D., HENRY, T., LÓPEZ-MORALES, M., RIDGWAY, S., GIES, D., JAO, W.C., ROJAS-AYALA, B., PARKS, J.R., STURMANN, L., STURMANN, J., TURNER, N.H., FARRINGTON, C., GOLDFINGER, P.J. & BERGER, D.H. (2012). Stellar Diameters and Temperatures. II. Main-sequence K- and M-stars. *ApJ*, **757**, 112. 85, 86, 103

BROWNING, M.K., BASRI, G., MARCY, G.W., WEST, A.A. & ZHANG, J. (2010). Rotation and Magnetic Activity in a Sample of M-Dwarfs. *AJ*, **139**, 504–518. 19, 131

BUTLER, R.P., MARCY, G.W., WILLIAMS, E., MC-CARTHY, C., DOSANJH, P. & VOGT, S.S. (1996). Attaining Doppler Precision of 3 M s-1. *PASP*, **108**, 500. 111

BUTLER, R.P., VOGT, S.S., MARCY, G.W., FISCHER, D.A., WRIGHT, J.T., HENRY, G.W., LAUGHLIN, G. & LISSAUER, J.J. (2004). A Neptune-Mass Planet Orbiting the Nearby M Dwarf GJ 436. *ApJ*, **617**, 580–588. 13, 21

CHABRIER, G. & BARAFFE, I. (1997). Structure and evolution of low-mass stars. *A&A*, **327**, 1039–1053. 19

CHAUVIN, G., LAGRANGE, A.M., DUMAS, C., ZUCKERMAN, B., MOUILLET, D., SONG, I., BEUZIT, J.L. & LOWRANCE, P. (2004). A giant planet candidate near a young brown dwarf. Direct VLT/NACO observations using IR wavefront sensing. *A&A*, **425**, L29–L32. 184

CHAZELAS, B., PEPE, F., WILDI, F., BOUCHY, F., PERRUCHOT, S. & AVILA, G. (2010). New scramblers for precision radial velocity: square and octagonal fibers. In *Society of Photo-Optical Instrumentation Engineers (SPIE) Conference Series*, vol. 7739 of *Society of Photo-Optical Instrumentation Engineers (SPIE) Conference Series*, 47. 147

CHOI, J., MCCARTHY, C., MARCY, G.W., HOWARD, A.W., FISCHER, D.A., JOHNSON, J.A., ISAACSON, H. & WRIGHT, J.T. (2013). Precise Doppler Monitoring of Barnard's Star. *ApJ*, **764**, 131. 85

CINCOTTA, P.M. & SIMÓ, C. (2000). Simple tools to study global dynamics in non-axisymmetric galactic potentials - I. *A&AS*, **147**, 205–228. 132

COLEMAN, G.A.L. & NELSON, R.P. (2016). On the formation of compact planetary systems via concurrent core accretion and migration. *MNRAS*, **457**, 2480–2500. 21

COLEMAN, G.A.L., NELSON, R.P., PAARDEKOOPER, S.J., DREIZLER, S., GIESERS, B. & ANGLADA-ESCUDE, G. (2016). Exploring plausible formation scenarios for the planet candidate orbiting Proxima Centauri. *ArXiv e-prints*. 137

COSENTINO, R., LOVIS, C., PEPE, F., COLLIER CAMERON, A., LATHAM, D.W., MOLINARI, E., UDRY, S., BEZAWADA, N., BLACK, M., BORN, A., BUCHSCHACHER, N., CHARBONNEAU, D., FIGUEIRA, P., FLEURY, M., GALLI, A., GALLIE, A., GAO, X., GHEDINA, A., GONZALEZ, C., GONZALEZ, M., GUERRA, J., HENRY, D., HORNE, K., HUGHES, I., KELLY, D., LODI, M., LUNNEY, D., MAIRE, C., MAYOR, M., MICELA, G., ORDWAY, M.P., PEACOCK, J., PHILLIPS, D., PIOTTO, G., POLLACCO, D., QUELOZ, D., RICE, K., RIVEROL, C., RIVEROL, L., SAN JUAN, J., SASSELOV, D., SEGRANSAN, D., SOZZETTI, A., SOSNOWSKA, D., STOBIE, B., SZENTGYORGYI, A., VICK, A. & WEBER, L. (2012). Harps-N: the new planet hunter at TNG. In *Society of Photo-Optical Instrumentation Engineers (SPIE) Conference Series*, vol. 8446 of *Society of Photo-Optical Instrumentation Engineers (SPIE) Conference Series*, 1. 35, 39

CRANE, J.D., SHECTMAN, S.A. & BUTLER, R.P. (2006). The Carnegie Planet Finder Spectrograph. In *Society of Photo-Optical Instrumentation Engineers (SPIE) Conference Series*, vol. 6269 of *Proc. SPIE*, 626931. 42

REFERENCES

CUMMING, A. (2004). Detectability of extrasolar planets in radial velocity surveys. *MNRAS*, **354**, 1165–1176. 51, 57, 97

CUTRI, R.M., SKRUTSKIE, M.F., VAN DYK, S., BEICHMAN, C.A., CARPENTER, J.M., CHESTER, T., CAMBRESY, L., EVANS, T., FOWLER, J., GIZIS, J., HOWARD, E., HUCHRA, J., JARRETT, T., KOPAN, E.L., KIRKPATRICK, J.D., LIGHT, R.M., MARSH, K.A., McCALLON, H., SCHNEIDER, S., STIENING, R., SYKES, M., WEINBERG, M., WHEATON, W.A., WHEELOCK, S. & ZACARIAS, N. (2003). VizieR Online Data Catalog: 2MASS All-Sky Catalog of Point Sources (Cutri+ 2003). *VizieR Online Data Catalog*, **2246**, 0. 54

DAVID, T.J., HILLENBRAND, L.A., PETIGURA, E.A., CARPENTER, J.M., CROSSFIELD, I.J.M., HINKLEY, S., CIARDI, D.R., HOWARD, A.W., ISAACSON, H.T., CODY, A.M., SCHLIEDER, J.E., BEICHMAN, C.A. & BARENFELD, S.A. (2016). A Neptune-sized transiting planet closely orbiting a 5–10-million-year-old star. *Nature*, **534**, 658–661. 7

DAWSON, R.I., JOHNSON, J.A., FABRYCKY, D.C., FOREMAN-MACKEY, D., MURRAY-CLAY, R.A., BUCHHAVE, L.A., CARGILE, P.A., CLUBB, K.I., FULTON, B.J., HEBB, L., HOWARD, A.W., HUBER, D., SHPORER, A. & VALENTI, J.A. (2014). Large Eccentricity, Low Mutual Inclination: The Three-dimensional Architecture of a Hierarchical System of Giant Planets. *ApJ*, **791**, 89. 23

DÍAZ, R.F., CINCUNEGUI, C. & MAUAS, P.J.D. (2007). The NaI D resonance lines in main-sequence late-type stars. *MNRAS*, **378**, 1007–1018. 113

DONATI, J.F., SEMEL, M., CARTER, B.D., REES, D.E. & COLLIER CAMERON, A. (1997). Spectropolarimetric observations of active stars. *MNRAS*, **291**, 658. 47, 69, 115

DRESSING, C.D. & CHARBONNEAU, D. (2013). The Occurrence Rate of Small Planets around Small Stars. *ApJ*, **767**, 95. 5, 86, 133

DRESSING, C.D. & CHARBONNEAU, D. (2015). The Occurrence of Potentially Habitable Planets Orbiting M Dwarfs Estimated from the Full Kepler Dataset and an Empirical Measurement of the Detection Sensitivity. *ApJ*, **807**, 45. 17, 133

DUMUSQUE, X., SANTOS, N.C., UDRY, S., LOVIS, C. & BONFILS, X. (2011). Planetary detection limits taking into account stellar noise. II. Effect of stellar spot groups on radial-velocities. *A&A*, **527**, A82. 22

DUMUSQUE, X., BONOMO, A.S., HAYWOOD, R.D., MALAVOLTA, L., SÉGRANSAN, D., BUCHHAVE, L.A., COLLIER CAMERON, A., LATHAM, D.W., MOLINARI, E., PEPE, F., UDRY, S., CHARBONNEAU, D., COSENTINO, R., DRESSING, C.D., FIGUEIRA, P., FIORENZANO, A.F.M., GETTEL, S., HARUTYUNYAN, A., HORNE, K., LOPEZ-MORALES, M., LOVIS, C., MAYOR, M., MICELA, G., MOTALEBI, F., NASCIMBENI, V., PHILLIPS, D.F., PIOTTO, G., POLLACCO, D., QUELOZ, D., RICE, K., SASSELOV, D., SOZZETTI, A., SZENTGYORGYI, A. & WATSON, C. (2014). The Kepler-10 Planetary System Revisited by HARPS-N: A Hot Rocky World and a Solid Neptune-Mass Planet. *ApJ*, **789**, 154. 7

EGGENBERGER, A. & UDRY, S. (2010). Detection and Characterization of Extrasolar Planets through Doppler Spectroscopy. In T. Montmerle, D. Ehrenreich & A.M. Lagrange, eds., *EAS Publications Series*, vol. 41 of *EAS Publications Series*, 27–75. 45

EHRENREICH, D., BOURRIER, V., WHEATLEY, P.J., LECAVELIER DES ETANGS, A., HÉBRARD, G., UDRY, S., BONFILS, X., DELFOSSE, X., DÉSERT, J.M., SING, D.K. & VIDAL-MADJAR, A. (2015). A giant comet-like cloud of hydrogen escaping the warm Neptune-mass exoplanet GJ 436b. *Nature*, **522**, 459–461. 14

EINSTEIN, A. (1936). Lens-Like Action of a Star by the Deviation of Light in the Gravitational Field. *Science*, **84**, 506–507. 182

FEGER, T., BRUCALASSI, A., GRUPP, F.U., LANGBARDL, F., HOLZWARTH, R., HOPP, U. & BENDER, R. (2012). A testbed for simultaneous measurement of fiber near and far-field for the evaluation of fiber scrambling properties. In *Ground-based and Airborne Instrumentation for Astronomy IV*, vol. 8446 of *Proc. SPIE*, 844692. 147

FISCHER, D.A. & VALENTI, J. (2005). The Planet-Metallicity Correlation. *ApJ*, **622**, 1102–1117. 18

FISCHER, D.A., ANGLADA-ESCUDE, G., ARRIAGADA, P., BALUEV, R.V., BEAN, J.L., BOUCHY, F.,

REFERENCES

Buchhave, L.A., Carroll, T., Chakraborty, A., Crepp, J.R., Dawson, R.I., Diddams, S.A., Dumusque, X., Eastman, J.D., Endl, M., Figueira, P., Ford, E.B., Foreman-Mackey, D., Fournier, P., Főrész, G., Gaudi, B.S., Gregory, P.C., Grundahl, F., Hatzes, A.P., Hébrard, G., Herrero, E., Hogg, D.W., Howard, A.W., Johnson, J.A., Jorden, P., Jurgenson, C.A., Latham, D.W., Laughlin, G., Loredo, T.J., Lovis, C., Mahadevan, S., McCracken, T.M., Pepe, F., Perez, M., Phillips, D.F., Plavchan, P.P., Prato, L., Quirrenbach, A., Reiners, A., Robertson, P., Santos, N.C., Sawyer, D., Segransan, D., Sozzetti, A., Steinmetz, T., Szentgyorgyi, A., Udry, S., Valenti, J.A., Wang, S.X., Wittenmyer, R.A. & Wright, J.T. (2016). State of the Field: Extreme Precision Radial Velocities. *PASP*, **128**, 066001. 27

Fogtmann-Schulz, A., Hinrup, B., Van Eylen, V., Christensen-Dalsgaard, J., Kjeldsen, H., Silva Aguirre, V. & Tingley, B. (2014). Accurate Parameters of the Oldest Known Rocky-exoplanet Hosting System: Kepler-10 Revisited. *ApJ*, **781**, 67. 23

Ford, E.B. (2005). Quantifying the Uncertainty in the Orbits of Extrasolar Planets. *AJ*, **129**, 1706–1717. 48, 129

Fressin, F., Torres, G., Désert, J.M., Charbonneau, D., Batalha, N.M., Fortney, J.J., Rowe, J.F., Allen, C., Borucki, W.J., Brown, T.M., Bryson, S.T., Ciardi, D.R., Cochran, W.D., Deming, D., Dunham, E.W., Fabrycky, D.C., Gautier, T.N., III, Gilliland, R.L., Henze, C.E., Holman, M.J., Howell, S.B., Jenkins, J.M., Kinemuchi, K., Knutson, H., Koch, D.G., Latham, D.W., Lissauer, J.J., Marcy, G.W., Ragozzine, D., Sasselov, D.D., Still, M., Tenenbaum, P. & Uddin, K. (2011). Kepler-10 c: a 2.2 Earth Radius Transiting Planet in a Multiple System. *ApJS*, **197**, 5. 7

Gaidos, E., Mann, A.W., Lépine, S., Buccino, A., James, D., Ansdell, M., Petrucci, R., Mauas, P. & Hilton, E.J. (2014). Trumpeting M dwarfs with CONCH-SHELL: a catalogue of nearby cool host-stars for habitable exoplanets and life. *MNRAS*, **443**, 2561–2578. 79, 85, 86, 101, 103, 131

García-Gil, A., Muñoz-Tuñón, C. & Varela, A.M. (2010). Atmosphere Extinction at the ORM on La Palma: A 20 yr Statistical Database Gathered at the Carlsberg Meridian Telescope. *PASP*, **122**, 1109–1121. 59

Gatewood, G. & Eichhorn, H. (1973). An unsuccessful search for a planetary companion of Barnard's star BD +4 3561. *AJ*, **78**, 769–776. 3, 4

Gaudi, B.S. (2010). Exoplanetary Microlensing. *ArXiv e-prints*. 183

Gillon, M., Jehin, E., Lederer, S.M., Delrez, L., de Wit, J., Burdanov, A., Van Grootel, V., Burgasser, A.J., Triaud, A.H.M.J., Opitom, C., Demory, B.O., Sahu, D.K., Bardalez Gagliuffi, D., Magain, P. & Queloz, D. (2016). Temperate Earth-sized planets transiting a nearby ultracool dwarf star. *Nature*, **533**, 221–224. 7

Goldblatt, C. (2016). Tutorial models of the climate and habitability of Proxima Centauri b: a thin atmosphere is sufficient to distribute heat given low stellar flux. *ArXiv e-prints*. 20

Gomes da Silva, J., Santos, N.C., Bonfils, X., Delfosse, X., Forveille, T. & Udry, S. (2011). Long-term magnetic activity of a sample of M-dwarf stars from the HARPS program. I. Comparison of activity indices. *A&A*, **534**, A30. 113

Gomes da Silva, J., Santos, N.C., Bonfils, X., Delfosse, X., Forveille, T., Udry, S., Dumusque, X. & Lovis, C. (2012). Long-term magnetic activity of a sample of M-dwarf stars from the HARPS program . II. Activity and radial velocity. *A&A*, **541**, A9. 22

Gonzalez, G. (1997). The stellar metallicity-giant planet connection. *MNRAS*, **285**, 403–412. 18

Gray, D.F. & Desikachary, K. (1973). A new approach to periodogram analyses. *ApJ*, **181**, 523–530. 101

Greene, T. (2001). Protostars. *American Scientist*, **89**, 316. 11

Griffin, R.F. (1967). A Photoelectric Radial-Velocity Spectrometer. *ApJ*, **148**, 465. 43

REFERENCES

HAN, I., BLACK, D.C. & GATEWOOD, G. (2001). Preliminary Astrometric Masses for Proposed Extrasolar Planetary Companions. *ApJ*, **548**, L57–L60. 181

HATZES, A.P. (2002). Starspots and exoplanets. *Astronomische Nachrichten*, **323**, 392–394. 22

HATZES, A.P., COCHRAN, W.D. & ENDL, M. (2010). The Detection of Extrasolar Planets Using Precise Stellar Radial Velocities. In N. Haghighipour, ed., *Planets in Binary Star Systems*, vol. 366 of *Astrophysics and Space Science Library*, 51. 144

HAWLEY, S.L., DAVENPORT, J.R.A., KOWALSKI, A.F., WISNIEWSKI, J.P., HEBB, L., DEITRICK, R. & HILTON, E.J. (2014). Kepler Flares. I. Active and Inactive M Dwarfs. *ApJ*, **797**, 121. 113

HAYES, D.S. & LATHAM, D.W. (1975). A rediscussion of the atmospheric extinction and the absolute spectral-energy distribution of VEGA. *ApJ*, **197**, 593–601. 59

HENRY, T.J. & MCCARTHY, D.W., JR. (1990). A systematic search for brown dwarfs orbiting nearby stars. *ApJ*, **350**, 334–347. 108

HERSHEY, J.L. (1973). Astrometric analysis of the field of AC +65 6955 from plates taken with the Sproul 24-inch refractor. *AJ*, **78**, 421–425. 3

HINSE, T.C., HAGHIGHIPOUR, N., KOSTOV, V.B. & GOŹDZIEWSKI, K. (2015). Predicting a Third Planet in the Kepler-47 Circumbinary System. *ApJ*, **799**, 88. 132

HUBER, D., CARTER, J.A., BARBIERI, M., MIGLIO, A., DECK, K.M., FABRYCKY, D.C., MONTET, B.T., BUCHHAVE, L.A., CHAPLIN, W.J., HEKKER, S., MONTALBÁN, J., SANCHIS-OJEDA, R., BASU, S., BEDDING, T.R., CAMPANTE, T.L., CHRISTENSEN-DALSGAARD, J., ELSWORTH, Y.P., STELLO, D., ARENTOFT, T., FORD, E.B., GILLILAND, R.L., HANDBERG, R., HOWARD, A.W., ISAACSON, H., JOHNSON, J.A., KAROFF, C., KAWALER, S.D., KJELDSEN, H., LATHAM, D.W., LUND, M.N., LUNDKVIST, M., MARCY, G.W., METCALFE, T.S., SILVA AGUIRRE, V. & WINN, J.N. (2013). Stellar Spin-Orbit Misalignment in a Multiplanet System. *Science*, **342**, 331–334. 23

HUNTER, T.R. & RAMSEY, L.W. (1992). Scrambling properties of optical fibers and the performance of a double scrambler. *PASP*, **104**, 1244–1251. 147

IDA, S. & LIN, D.N.C. (2005). Toward a Deterministic Model of Planetary Formation. III. Mass Distribution of Short-Period Planets around Stars of Various Masses. *ApJ*, **626**, 1045–1060. 17, 18

INGROSSO, G., NOVATI, S.C., DE PAOLIS, F., JETZER, P., NUCITA, A.A. & ZAKHAROV, A.F. (2009). Pixel lensing as a way to detect extrasolar planets in M31. *MNRAS*, **399**, 219–228. 183

JARDINE, M., DONATI, J.F. & GREGORY, S.G. (2009). Stellar mass ejections. In N. Gopalswamy & D.F. Webb, eds., *Universal Heliophysical Processes*, vol. 257 of *IAU Symposium*, 201–210. 21

JENKINS, J.S., RAMSEY, L.W., JONES, H.R.A., PAVLENKO, Y., GALLARDO, J., BARNES, J.R. & PINFIELD, D.J. (2009). Rotational Velocities for M Dwarfs. *ApJ*, **704**, 975–988. 54

JENKINS, J.S., JONES, H.R.A., TUOMI, M., MURGAS, F., HOYER, S., JONES, M.I., BARNES, J.R., PAVLENKO, Y.V., IVANYUK, O., ROJO, P., JORDÁN, A., DAY-JONES, A.C., RUIZ, M.T. & PINFIELD, D.J. (2013). A Hot Uranus Orbiting the Super Metal-rich Star HD 77338 and the Metallicity-Mass Connection. *ApJ*, **766**, 67. 18

KASTING, J.F., WHITMIRE, D.P. & REYNOLDS, R.T. (1993). Habitable Zones around Main Sequence Stars. *Icarus*, **101**, 108–128. 15

KÄUFL, H.U., BALLESTER, P., BIEREICHEL, P., DELABRE, B., DONALDSON, R., DORN, R., FEDRIGO, E., FINGER, G., FISCHER, G., FRANZA, F., GOJAK, D., HUSTER, G., JUNG, Y., LIZON, J.L., MEHRGAN, L., MEYER, M., MOORWOOD, A., PIRARD, J.F., PAUFIQUE, J., POZNA, E., SIEBENMORGEN, R., SILBER, A., STEGMEIER, J. & WEGERER, S. (2004). CRIRES: a high-resolution infrared spectrograph for ESO's VLT. In A.F.M. Moorwood & M. Iye, eds., *Ground-based Instrumentation for Astronomy*, vol. 5492 of *Proc. SPIE*, 1218–1227. 41

KENNEDY, G.M. & KENYON, S.J. (2008). Planet Formation around Stars of Various Masses: The Snow Line and the Frequency of Giant Planets. *ApJ*, **673**, 502–512. 17, 18

KENYON, S.J. & BROMLEY, B.C. (2008). Variations on Debris Disks: Icy Planet Formation at 30-150 AU for 1-3 $M_{\odot}$ Main-Sequence Stars. *ApJS*, **179**, 451–483. 13

REFERENCES

KITCHIN, C.R. (1995). *Optical astronomical spectroscopy*. 37

KOEN, C., KILKENNY, D., VAN WYK, F. & MARANG, F. (2010). UBV(RI)$_C$ JHK observations of Hipparcos-selected nearby stars. *MNRAS*, **403**, 1949–1968. 85, 108, 131

KOPPARAPU, R.K., RAMIREZ, R., KASTING, J.F., EYMET, V., ROBINSON, T.D., MAHADEVAN, S., TERRIEN, R.C., DOMAGAL-GOLDMAN, S., MEADOWS, V. & DESHPANDE, R. (2013). Habitable Zones around Main-sequence Stars: New Estimates. *ApJ*, **765**, 131. 15, 79, 129, 131

KOPPARAPU, R.K., RAMIREZ, R.M., SCHOTTELKOTTE, J., KASTING, J.F., DOMAGAL-GOLDMAN, S. & EYMET, V. (2014). Habitable Zones around Main-sequence Stars: Dependence on Planetary Mass. *ApJ*, **787**, L29. 15

KOPPARAPU, R.K., WOLF, E.T., HAQQ-MISRA, J., YANG, J., KASTING, J.F., MEADOWS, V., TERRIEN, R. & MAHADEVAN, S. (2016). The Inner Edge of the Habitable Zone for Synchronously Rotating Planets around Low-mass Stars Using General Circulation Models. *ApJ*, **819**, 84. 15

KRISCIUNAS, K., GRIFFIN, R.F., GUINAN, E.F., LUEDEKE, K.D. & MCCOOK, G.P. (1995). 9 Aurigae: strong evidence for non-radial pulsations. *MNRAS*, **273**, 662–674. 84

KROUPA, P. (2001). On the variation of the initial mass function. *MNRAS*, **322**, 231–246. 17

KÜRSTER, M., ENDL, M., ROUESNEL, F., ELS, S., KAUFER, A., BRILLANT, S., HATZES, A.P., SAAR, S.H. & COCHRAN, W.D. (2003). The low-level radial velocity variability in Barnard's star (= GJ 699). Secular acceleration, indications for convective redshift, and planet mass limits. *A&A*, **403**, 1077–1087. 129

LAGRANGE, A.M., GRATADOUR, D., CHAUVIN, G., FUSCO, T., EHRENREICH, D., MOUILLET, D., ROUSSET, G., ROUAN, D., ALLARD, F., GENDRON, É., CHARTON, J., MUGNIER, L., RABOU, P., MONTRI, J. & LACOMBE, F. (2009). A probable giant planet imaged in the β Pictoris disk. VLT/NaCo deep L'-band imaging. *A&A*, **493**, L21–L25. 15

LATHAM, D.W., STEFANIK, R.P., MAZEH, T., MAYOR, M. & BURKI, G. (1989). The unseen companion of HD114762 - A probable brown dwarf. *Nature*, **339**, 38–40. 4, 43

LECONTE, J., FORGET, F., CHARNAY, B., WORDSWORTH, R. & POTTIER, A. (2013). Increased insolation threshold for runaway greenhouse processes on Earth-like planets. *Nature*, **504**, 268–271. 15

LECONTE, J., WU, H., MENOU, K. & MURRAY, N. (2015). Asynchronous rotation of Earth-mass planets in the habitable zone of lower-mass stars. *Science*, **347**, 632–635. 133

LEHMANN, H. & MKRTICHIAN, D.E. (2004). The eclipsing binary star RZ Cas. I. First spectroscopic detection of rapid pulsations in an Algol system. *A&A*, **413**, 293–299. 84

LEVISON, H.F., THOMMES, E. & DUNCAN, M.J. (2010). Modeling the Formation of Giant Planet Cores. I. Evaluating Key Processes. *AJ*, **139**, 1297–1314. 12

LIU, M.C., MAGNIER, E.A., DEACON, N.R., ALLERS, K.N., DUPUY, T.J., KOTSON, M.C., ALLER, K.M., BURGETT, W.S., CHAMBERS, K.C., DRAPER, P.W., HODAPP, K.W., JEDICKE, R., KAISER, N., KUDRITZKI, R.P., METCALFE, N., MORGAN, J.S., PRICE, P.A., TONRY, J.L. & WAINSCOAT, R.J. (2013). The Extremely Red, Young L Dwarf PSO J318.5338-22.8603: A Free-floating Planetary-mass Analog to Directly Imaged Young Gas-giant Planets. *ApJ*, **777**, L20. 14

LO CURTO, G., MANESCAU, A., AVILA, G., PASQUINI, L., WILKEN, T., STEINMETZ, T., HOLZWARTH, R., PROBST, R., UDEM, T., HÄNSCH, T.W., GONZÁLEZ HERNÁNDEZ, J.I., ESPOSITO, M., REBOLO, R., CANTO MARTINS, B. & DE MEDEIROS, J.R. (2012). Achieving a few cm/sec calibration repeatability for high resolution spectrographs: the laser frequency comb on HARPS. In *Ground-based and Airborne Instrumentation for Astronomy IV*, vol. 8446 of *Proc. SPIE*, 84461W. 88

LOMB, N.R. (1976). Least-squares frequency analysis of unequally spaced data. *Ap&SS*, **39**, 447–462. 49

LOVIS, C. & FISCHER, D. (2010). *Radial Velocity Techniques for Exoplanets*, 27–53. 27, 40, 84, 145

REFERENCES

Lovis, C. & Pepe, F. (2007). A new list of thorium and argon spectral lines in the visible. *A&A*, **468**, 1115–1121. 146

Lovis, C., Pepe, F., Bouchy, F., Lo Curto, G., Mayor, M., Pasquini, L., Queloz, D., Rupprecht, G., Udry, S. & Zucker, S. (2006). The exoplanet hunter HARPS: unequalled accuracy and perspectives toward 1 cm s $^{-1}$ precision. In *Society of Photo-Optical Instrumentation Engineers (SPIE) Conference Series*, vol. 6269 of *Society of Photo-Optical Instrumentation Engineers (SPIE) Conference Series*, 0. 145, 146

Lovis, C., Mayor, M., Pepe, F., Queloz, D. & Udry, S. (2008). Pushing Down the Limits of RV Precision with HARPS. In D. Fischer, F.A. Rasio, S.E. Thorsett & A. Wolszczan, eds., *Extreme Solar Systems*, vol. 398 of *Astronomical Society of the Pacific Conference Series*, 455. 146

Marcy, G., Butler, R.P., Fischer, D., Vogt, S., Wright, J.T., Tinney, C.G. & Jones, H.R.A. (2005). Observed Properties of Exoplanets: Masses, Orbits, and Metallicities. *Progress of Theoretical Physics Supplement*, **158**, 24–42. 6

Marcy, G.W. & Butler, R.P. (1992). Precision radial velocities with an iodine absorption cell. *PASP*, **104**, 270–277. 41

Marcy, G.W. & Butler, R.P. (1995). The Planet around 51 Pegasi. In *American Astronomical Society Meeting Abstracts*, vol. 27 of *Bulletin of the American Astronomical Society*, 1379. 5

Marcy, G.W. & Butler, R.P. (1996). Planets Orbiting Solar-Type Stars. In *American Astronomical Society Meeting Abstracts*, vol. 28 of *Bulletin of the American Astronomical Society*, 1314. 5

Martins, J.H.C., Figueira, P., Santos, N.C. & Lovis, C. (2013). Spectroscopic direct detection of reflected light from extrasolar planets. *MNRAS*, **436**, 1215–1224. 82

Matsuo, T., Shibai, H., Ootsubo, T. & Tamura, M. (2007). Planetary Formation Scenarios Revisited: Core-Accretion versus Disk Instability. *ApJ*, **662**, 1282–1292. 11, 13

Mayor, M. & Queloz, D. (1995). A Jupiter-mass companion to a solar-type star. *Nature*, **378**, 355–359. 4, 5, 107

Mayor, M., Pepe, F., Queloz, D., Bouchy, F., Rupprecht, G., Lo Curto, G., Avila, G., Benz, W., Bertaux, J.L., Bonfils, X., Dall, T., Dekker, H., Delabre, B., Eckert, W., Fleury, M., Gilliotte, A., Gojak, D., Guzman, J.C., Kohler, D., Lizon, J.L., Longinotti, A., Lovis, C., Megevand, D., Pasquini, L., Reyes, J., Sivan, J.P., Sosnowska, D., Soto, R., Udry, S., van Kesteren, A., Weber, L. & Weilenmann, U. (2003). Setting New Standards with HARPS. *The Messenger*, **114**, 20–24. 39

Mayor, M., Bonfils, X., Forveille, T., Delfosse, X., Udry, S., Bertaux, J.L., Beust, H., Bouchy, F., Lovis, C., Pepe, F., Perrier, C., Queloz, D. & Santos, N.C. (2009). The HARPS search for southern extra-solar planets. XVIII. An Earth-mass planet in the GJ 581 planetary system. *A&A*, **507**, 487–494. 21

McKee, C.F. & Ostriker, E.C. (2007). Theory of Star Formation. *ARA&A*, **45**, 565–687. 11

Meschiari, S., Laughlin, G., Vogt, S.S., Butler, R.P., Rivera, E.J., Haghighipour, N. & Jalowiczor, P. (2011). The Lick-Carnegie Survey: Four New Exoplanet Candidates. *ApJ*, **727**, 117. 44

Mizuno, H. (1980). Formation of the Giant Planets. *Progress of Theoretical Physics*, **64**, 544–557. 12

Mordasini, C., Klahr, H., Alibert, Y., Benz, W. & Dittkrist, K.M. (2010). Theory of planet formation. *ArXiv e-prints*. 13

Morton, T.D., Bryson, S.T., Coughlin, J.L., Rowe, J.F., Ravichandran, G., Petigura, E.A., Haas, M.R. & Batalha, N.M. (2016). False Positive Probabilities for all Kepler Objects of Interest: 1284 Newly Validated Planets and 428 Likely False Positives. *ApJ*, **822**, 86. 179

Muirhead, P.S., Johnson, J.A., Apps, K., Carter, J.A., Morton, T.D., Fabrycky, D.C., Pineda, J.S., Bottom, M., Rojas-Ayala, B., Schlawin, E., Hamren, K., Covey, K.R., Crepp, J.R., Stassun, K.G., Pepper, J., Hebb, L., Kirby, E.N., Howard, A.W., Isaacson, H.T., Marcy, G.W., Levitan, D., Diaz-Santos, T., Armus, L. & Lloyd, J.P. (2012). Characterizing the Cool KOIs. III. KOI 961: A Small Star with Large Proper Motion and Three Small Planets. *ApJ*, **747**, 144. 21, 107

REFERENCES

Muterspaugh, M.W., Lane, B.F., Kulkarni, S.R., Konacki, M., Burke, B.F., Colavita, M.M., Shao, M., Hartkopf, W.I., Boss, A.P. & Williamson, M. (2010). The Phases Differential Astrometry Data Archive. V. Candidate Substellar Companions to Binary Systems. *AJ*, **140**, 1657–1671. 181

Neves, V., Bonfils, X., Santos, N.C., Delfosse, X., Forveille, T., Allard, F. & Udry, S. (2013). Metallicity of M dwarfs. III. Planet-metallicity and planet-stellar mass correlations of the HARPS GTO M dwarf sample. *A&A*, **551**, A36. 101

Neves, V., Bonfils, X., Santos, N.C., Delfosse, X., Forveille, T., Allard, F. & Udry, S. (2014). Metallicity of M dwarfs. IV. A high-precision [Fe/H] and T_{eff} technique from high-resolution optical spectra for M dwarfs. *A&A*, **568**, A121. 85, 131

Newton, I. (1687). *Philosophiae Naturalis Principia Mathematica. Auctore Js. Newton.* 28

Ofir, A. & Dreizler, S. (2013). An independent planet search in the Kepler dataset. I. One hundred new candidates and revised Kepler objects of interest. *A&A*, **555**, A58. 21, 107

Ollivier, M., Roques, F., Casoli, F., Encrenaz, T. & Selsis, F. (2009). *Planetary Systems*. 29, 182

Pepe, F., Mayor, M., Queloz, D., Benz, W., Bonfils, X., Bouchy, F., Lo Curto, G., Lovis, C., Mégevand, D., Moutou, C., Naef, D., Rupprecht, G., Santos, N.C., Sivan, J.P., Sosnowska, D. & Udry, S. (2004). The HARPS search for southern extra-solar planets. I. HD 330075 b: A new "hot Jupiter". *A&A*, **423**, 385–389. 39

Pepe, F., Lovis, C., Ségransan, D., Benz, W., Bouchy, F., Dumusque, X., Mayor, M., Queloz, D., Santos, N.C. & Udry, S. (2011). The HARPS search for Earth-like planets in the habitable zone. I. Very low-mass planets around HD 20794, HD 85512, and HD 192310. *A&A*, **534**, A58. 15, 34, 39, 54, 129, 145

Pepe, F., Collier Cameron, A., Latham, D.W., Molinari, E., Udry, S., Bonomo, A.S., Buchhave, L.A., Charbonneau, D., Cosentino, R., Dressing, C.D., Dumusque, X., Figueira, P., Fiorenzano, A.F.M., Gettel, S., Harutyunyan, A., Haywood, R.D., Horne, K., Lopez-Morales, M., Lovis, C., Malavolta, L., Mayor, M., Micela, G., Motalebi, F., Nascimbeni, V., Phillips, D., Piotto, G., Pollacco, D., Queloz, D., Rice, K., Sasselov, D., Ségransan, D., Sozzetti, A., Szentgyorgyi, A. & Watson, C.A. (2013). An Earth-sized planet with an Earth-like density. *ArXiv e-prints.* 44

Pepe, F.A., Cristiani, S., Rebolo Lopez, R., Santos, N.C., Amorim, A., Avila, G., Benz, W., Bonifacio, P., Cabral, A., Carvas, P., Cirami, R., Coelho, J., Comari, M., Coretti, I., De Caprio, V., Dekker, H., Delabre, B., Di Marcantonio, P., D'Odorico, V., Fleury, M., García, R., Herreros Linares, J.M., Hughes, I., Iwert, O., Lima, J., Lizon, J.L., Lo Curto, G., Lovis, C., Manescau, A., Martins, C., Mégevand, D., Moitinho, A., Molaro, P., Monteiro, M., Monteiro, M., Pasquini, L., Mordasini, C., Queloz, D., Rasilla, J.L., Rebordão, J.M., Santana Tschudi, S., Santin, P., Sosnowska, D., Spanò, P., Tenegi, F., Udry, S., Vanzella, E., Viel, M., Zapatero Osorio, M.R. & Zerbi, F. (2010). ESPRESSO: the Echelle spectrograph for rocky exoplanets and stable spectroscopic observations. In *Society of Photo-Optical Instrumentation Engineers (SPIE) Conference Series*, vol. 7735 of *Society of Photo-Optical Instrumentation Engineers (SPIE) Conference Series*, 0. 106

Perri, F. & Cameron, A.G.W. (1974). Hydrodynamic instability of the solar nebula in the presence of a planetary core. *Icarus*, **22**, 416–425. 12

Perruchot, S., Kohler, D., Bouchy, F., Richaud, Y., Richaud, P., Moreaux, G., Merzougui, M., Sottile, R., Hill, L., Knispel, G., Regal, X., Meunier, J.P., Ilovaisky, S., Le Coroller, H., Gillet, D., Schmitt, J., Pepe, F., Fleury, M., Sosnowska, D., Vors, P., Mégevand, D., Blanc, P.E., Carol, C., Point, A., Laloge, A. & Brunel, J.C. (2008). The SOPHIE spectrograph: design and technical key-points for high throughput and high stability. In *Ground-based and Airborne Instrumentation for Astronomy II*, vol. 7014 of *Proc. SPIE*, 70140J. 88, 89

Perruchot, S., Bouchy, F., Chazelas, B., Díaz, R.F., Hébrard, G., Arnaud, K., Arnold, L.,

REFERENCES

Avila, G., Delfosse, X., Boisse, I., Moreaux, G., Pepe, F., Richaud, Y., Santerne, A., Sottile, R. & Tézier, D. (2011). Higher-precision radial velocity measurements with the SOPHIE spectrograph using octagonal-section fibers. In *Techniques and Instrumentation for Detection of Exoplanets V*, vol. 8151 of *Proc. SPIE*, 815115. 146

Perryman, M. (2011). *The Exoplanet Handbook*. 178, 180

Perryman, M., Hartman, J., Bakos, G.Á. & Lindegren, L. (2014). Astrometric Exoplanet Detection with Gaia. *ApJ*, **797**, 14. 182

Pierrehumbert, R.T. (2011). A Palette of Climates for Gliese 581g. *ApJ*, **726**, L8. 20

Plavchan, P.P., Anglada-Escude, G., White, R., Gao, P., Davison, C., Mills, S., Beichman, C., Brinkworth, C., Johnson, J., Bottom, M., Ciardi, D., Wallace, K., Mennesson, B., von Braun, K., Vasisht, G., Prato, L., Kane, S., Tanner, A., Walp, B., Crawford, S. & Lin, S. (2013a). Precision near-infrared radial velocity instrumentation I: absorption gas cells. In *Techniques and Instrumentation for Detection of Exoplanets VI*, vol. 8864 of *Proc. SPIE*, 88641J. 41

Plavchan, P.P., Bottom, M., Gao, P., Wallace, J.K., Mennesson, B., Ciardi, D., Crawford, S., Lin, S., Beichman, C., Brinkworth, C., Johnson, J., Davison, C., White, R., Anglada-Escude, G., von Braun, K., Vasisht, G., Prato, L., Kane, S., Tanner, A., Walp, B. & Mills, S. (2013b). Precision near-infrared radial velocity instrumentation II: noncircular core fiber scrambler. In *Techniques and Instrumentation for Detection of Exoplanets VI*, vol. 8864 of *Proc. SPIE*, 88640G. 41

Pojmanski, G. (1997). The All Sky Automated Survey. *Acta Astron.*, **47**, 467–481. 118

Pollack, J.B., Hubickyj, O., Bodenheimer, P., Lissauer, J.J., Podolak, M. & Greenzweig, Y. (1996). Formation of the Giant Planets by Concurrent Accretion of Solids and Gas. *Icarus*, **124**, 62–85. 12

Press, W.H. (1992). *Numerical recipes in Fortran 77 : the art of scientific computing*. Fortran numerical recipes, Cambridge University Press, Cambridge, G.B., New York, réimpressions avec corrections : 1996, 1997, 2001, 2003 as Numerical recipes in Fortran 77: the art of scientific computing. 47, 72, 115

Probst, R.A., Lo Curto, G., Avila, G., Canto Martins, B.L., de Medeiros, J.R., Esposito, M., González Hernández, J.I., Hänsch, T.W., Holzwarth, R., Kerber, F., Leão, I.C., Manescau, A., Pasquini, L., Rebolo-López, R., Steinmetz, T., Udem, T. & Wu, Y. (2014). A laser frequency comb featuring sub-cm/s precision for routine operation on HARPS. In *Society of Photo-Optical Instrumentation Engineers (SPIE) Conference Series*, vol. 9147 of *Society of Photo-Optical Instrumentation Engineers (SPIE) Conference Series*, 1. 82

Queloz, D., Mayor, M., Weber, L., Blécha, A., Burnet, M., Confino, B., Naef, D., Pepe, F., Santos, N. & Udry, S. (2000). The CORALIE survey for southern extra-solar planets. I. A planet orbiting the star Gliese 86. *A&A*, **354**, 99–102. 39

Queloz, D., Henry, G.W., Sivan, J.P., Baliunas, S.L., Beuzit, J.L., Donahue, R.A., Mayor, M., Naef, D., Perrier, C. & Udry, S. (2001). No planet for HD 166435. *A&A*, **379**, 279–287. 22

Quirrenbach, A., Amado, P.J., Caballero, J.A., Mundt, R., Reiners, A., Ribas, I., Seifert, W., Abril, M., Aceituno, J., Alonso-Floriano, F.J., Ammler-von Eiff, M., Antona Jiménez, R., Anwand-Heerwart, H., Azzaro, M., Bauer, F., Barrado, D., Becerril, S., Béjar, V.J.S., Benítez, D., Berdiñas, Z.M., Cárdenas, M.C., Casal, E., Claret, A., Colomé, J., Cortés-Contreras, M., Czesla, S., Doellinger, M., Dreizler, S., Feiz, C., Fernández, M., Galadí, D., Gálvez-Ortiz, M.C., García-Piquer, A., García-Vargas, M.L., Garrido, R., Gesa, L., Gómez Galera, V., González Álvarez, E., González Hernández, J.I., Grözinger, U., Guàrdia, J., Guenther, E.W., de Guindos, E., Gutiérrez-Soto, J., Hagen, H.J., Hatzes, A.P., Hauschildt, P.H., Helmling, J., Henning, T., Hermann, D., Hernández Castaño, L., Herrero, E., Hidalgo, D., Holgado, G., Huber, A., Huber, K.F., Jeffers, S., Joergens, V., de Juan, E., Kehr, M., Klein, R., Kürster, M., Lamert, A., Lalitha, S., Laun, W., Lemke, U., Lenzen, R., López del Fresno, M., López Martí, B., López-Santiago, J., Mall, U., Mandel, H., Martín, E.L., Martín-Ruiz, S., Martínez-Rodríguez,

REFERENCES

H., Marvin, C.J., Mathar, R.J., Mirabet, E., Montes, D., Morales Muñoz, R., Moya, A., Naranjo, V., Ofir, A., Oreiro, R., Pallé, E., Panduro, J., Passegger, V.M., Pérez-Calpena, A., Pérez Medialdea, D., Perger, M., Pluto, M., Ramón, A., Rebolo, R., Redondo, P., Reffert, S., Reinhardt, S., Rhode, P., Rix, H.W., Rodler, F., Rodríguez, E., Rodríguez-López, C., Rodríguez-Pérez, E., Rohloff, R.R., Rosich, A., Sánchez-Blanco, E., Sánchez Carrasco, M.A., Sanz-Forcada, J., Sarmiento, L.F., Schäfer, S., Schiller, J., Schmidt, C., Schmitt, J.H.M.M., Solano, E., Stahl, O., Storz, C., Stürmer, J., Suárez, J.C., Ulbrich, R.G., Veredas, G., Wagner, K., Winkler, J., Zapatero Osorio, M.R., Zechmeister, M., Abellán de Paco, F.J., Anglada-Escudé, G., del Burgo, C., Klutsch, A., Lizon, J.L., López-Morales, M., Morales, J.C., Perryman, M.A.C., Tulloch, S.M. & Xu, W. (2014). CARMENES instrument overview. In *Society of Photo-Optical Instrumentation Engineers (SPIE) Conference Series*, vol. 9147 of *Society of Photo-Optical Instrumentation Engineers (SPIE) Conference Series*, 1. 41, 82, 108

Radovan, M.V., Cabak, G.F., Laiterman, L.H., Lockwood, C.T. & Vogt, S.S. (2010). A radial velocity spectrometer for the Automated Planet Finder Telescope at Lick Observatory. In *Ground-based and Airborne Instrumentation for Astronomy III*, vol. 7735 of *Proc. SPIE*, 77354K. 42

Ragozzine, D. & Kepler Team (2012). The Very Compact Five Exoplanet System KOI-500: Mass Constraints from TTVs, Resonances, and Implications. In *AAS/Division for Planetary Sciences Meeting Abstracts*, vol. 44 of *AAS/Division for Planetary Sciences Meeting Abstracts*, 200.04. 21, 107

Raymond, S.N. & Morbidelli, A. (2014). The Grand Tack model: a critical review. In *IAU Symposium*, vol. 310 of *IAU Symposium*, 194–203. 13

Redfield, S., Endl, M., Cochran, W.D. & Koesterke, L. (2008). Sodium Absorption from the Exoplanetary Atmosphere of HD 189733b Detected in the Optical Transmission Spectrum. *ApJ*, **673**, L87. 10

Reegen, P. (2007). SigSpec. I. Frequency- and phase-resolved significance in Fourier space. *A&A*, **467**, 1353–1371. 100

Reid, I.N. & Hawley, S.L. (2005). *New light on dark stars : red dwarfs, low-mass stars, brown dwarfs.* 19

Reid, I.N., Hawley, S.L. & Gizis, J.E. (1995). The Palomar/MSU Nearby-Star Spectroscopic Survey. I. The Northern M Dwarfs -Bandstrengths and Kinematics. *AJ*, **110**, 1838. 54, 85, 131

Reiners, A., Joshi, N. & Goldman, B. (2012). A Catalog of Rotation and Activity in Early-M Stars. *AJ*, **143**, 93. 19, 85

Reiners, A., Shulyak, D., Anglada-Escudé, G., Jeffers, S.V., Morin, J., Zechmeister, M., Kochukhov, O. & Piskunov, N. (2013). Radial velocity signatures of Zeeman broadening. *A&A*, **552**, A103. 82

Reuyl, D. & Holmberg, E. (1943). On the Existence of a Third Component in the System 70 Ophiuchi. *ApJ*, **97**, 41. 2

Ribas, I., Bolmont, E., Selsis, F., Reiners, A., Leconte, J., Raymond, S.N., Engle, S.G., Guinan, E.F., Morin, J., Turbet, M., Forget, F. & Anglada-Escude, G. (2016). The habitability of Proxima Centauri b. I. Irradiation, rotation and volatile inventory from formation to the present. *ArXiv e-prints*. 19, 137

Robertson, P., Endl, M., Cochran, W.D. & Dodson-Robinson, S.E. (2013). Hα Activity of Old M Dwarfs: Stellar Cycles and Mean Activity Levels for 93 Low-mass Stars in the Solar Neighborhood. *ApJ*, **764**, 3. 136

Robertson, P., Mahadevan, S., Endl, M. & Roy, A. (2014). Stellar activity masquerading as planets in the habitable zone of the M dwarf Gliese 581. *Science*, **345**, 440–444. 129

Robertson, P., Roy, A. & Mahadevan, S. (2015). Stellar activity mimics a habitable-zone planet around Kapteyn's star. *ArXiv e-prints*. 113, 136

Rodigas, T.J., Arriagada, P., Faherty, J., Anglada-Escudé, G., Kaib, N., Butler, R.P., Shectman, S., Weinberger, A., Males, J.R., Morzinski, K.M., Close, L.M., Hinz, P.M.,

REFERENCES

CRANE, J.D., THOMPSON, I., TESKE, J., DÍAZ, M., MINNITI, D., LOPEZ-MORALES, M., ADAMS, F.C. & BOSS, A.P. (2016). MagAO Imaging of Long-period Objects (MILO). I. A Benchmark M Dwarf Companion Exciting a Massive Planet around the Sun-like Star HD 7449. *ApJ*, **818**, 106. 129

RODRÍGUEZ, E., RODRÍGUEZ-LÓPEZ, C., LÓPEZ-GONZÁLEZ, M.J., AMADO, P.J., OCANDO, S. & BERDIÑAS, Z.M. (2016). Search for pulsations in M dwarfs in the Kepler short-cadence data base. *MNRAS*, **457**, 1851–1863. 84

RODRÍGUEZ-LÓPEZ, C., MACDONALD, J. & MOYA, A. (2012). Pulsations in M dwarf stars. *MNRAS*, **419**, L44–L48. 22, 84

RODRÍGUEZ-LÓPEZ, C., MACDONALD, J., AMADO, P.J., MOYA, A. & MULLAN, D. (2014). The theoretical instability strip of M dwarf stars. *MNRAS*, **438**, 2371–2379. 22, 23, 84

SAFRONOV, V.S. (1969). Evolution of the Protoplanetary Cloud and Formation of the Earth and the Planets. *Moskow: Nauka*. 11

SANTERNE, A., DÍAZ, R.F., MOUTOU, C., BOUCHY, F., HÉBRARD, G., ALMENARA, J.M., BONOMO, A.S., DELEUIL, M. & SANTOS, N.C. (2012). SOPHIE velocimetry of Kepler transit candidates. VII. A false-positive rate of 35% for Kepler close-in giant candidates. *A&A*, **545**, A76. 89, 179

SANTOS, N.C., ISRAELIAN, G. & MAYOR, M. (2004). Spectroscopic [Fe/H] for 98 extra-solar planet-host stars. Exploring the probability of planet formation. *A&A*, **415**, 1153–1166. 18

SANTOS, N.C., SOUSA, S.G., MORTIER, A., NEVES, V., ADIBEKYAN, V., TSANTAKI, M., DELGADO MENA, E., BONFILS, X., ISRAELIAN, G., MAYOR, M. & UDRY, S. (2013). SWEET-Cat: A catalogue of parameters for Stars With ExoplanETs. I. New atmospheric parameters and masses for 48 stars with planets. *A&A*, **556**, A150. 86

SCARGLE, J.D. (1982). Studies in astronomical time series analysis. II - Statistical aspects of spectral analysis of unevenly spaced data. *ApJ*, **263**, 835–853. 49, 57

SCHOU, J. & BUZASI, D.L. (2001). Observations of p-modes in α Cen. In A. Wilson & P.L. Pallé, eds., *SOHO 10/GONG 2000 Workshop: Helio- and Asteroseismology at the Dawn of the Millennium*, vol. 464 of *ESA Special Publication*, 391–394. 106

SEGURA, A., WALKOWICZ, L.M., MEADOWS, V., KASTING, J. & HAWLEY, S. (2010). The Effect of a Strong Stellar Flare on the Atmospheric Chemistry of an Earth-like Planet Orbiting an M Dwarf. *Astrobiology*, **10**, 751–771. 19

SNELLEN, I., DE KOK, R., BIRKBY, J.L., BRANDL, B., BROGI, M., KELLER, C., KENWORTHY, M., SCHWARZ, H. & STUIK, R. (2015). Combining high-dispersion spectroscopy with high contrast imaging: Probing rocky planets around our nearest neighbors. *A&A*, **576**, A59. 140

SNELLEN, I.A.G., DE KOK, R.J., DE MOOIJ, E.J.W. & ALBRECHT, S. (2010). The orbital motion, absolute mass and high-altitude winds of exoplanet HD209458b. *Nature*, **465**, 1049–1051. 82

SOUMMER, R., PERRIN, M.D., PUEYO, L., CHOQUET, É., CHEN, C., GOLIMOWSKI, D.A., BRENDAN HAGAN, J., MITTAL, T., MOERCHEN, M., N'DIAYE, M., RAJAN, A., WOLFF, S., DEBES, J., HINES, D.C. & SCHNEIDER, G. (2014). Five Debris Disks Newly Revealed in Scattered Light from the Hubble Space Telescope NICMOS Archive. *ApJ*, **786**, L23. 14

SOZZETTI, A. (2005). Astrometric Methods and Instrumentation to Identify and Characterize Extrasolar Planets: A Review. *PASP*, **117**, 1021–1048. 181

STEFFEN, J.H. & FARR, W.M. (2013). A Lack of Short-period Multiplanet Systems with Close-proximity Pairs and the Curious Case of Kepler-42. *ApJ*, **774**, L12. 86

STRAND, K.A. (1943). 61 Cygni as a Triple System. *PASP*, **55**, 29–32. 2

STRUVE, O. (1952). Proposal for a project of high-precision stellar radial velocity work. *The Observatory*, **72**, 199–200. 4

STÜRMER, J., STAHL, O., SCHWAB, C., SEIFERT, W., QUIRRENBACH, A., AMADO, P.J., RIBAS, I., REINERS, A. & CABALLERO, J.A. (2014). CARMENES in SPIE 2014. Building a fibre link for CARMENES. In *Advances in Optical and Mechanical Technologies for Telescopes and Instrumentation*, vol. 9151 of *Proc. SPIE*, 915152. 149

REFERENCES

Suárez Mascareño, A., Rebolo, R., González Hernández, J.I. & Esposito, M. (2015). Rotation periods of late-type dwarf stars from time-series high-resolution spectroscopy of chromospheric indicators. *ArXiv e-prints*. 22, 85, 108, 118, 131

Suárez Mascareño, A., Rebolo, R. & González Hernández, J.I. (2016). Magnetic Cycles and Rotation Periods of Late Type Stars from photometric time series. *ArXiv e-prints*. 22, 108, 118, 125, 126, 129

Trilling, D.E., Benz, W., Guillot, T., Lunine, J.I., Hubbard, W.B. & Burrows, A. (1998). Orbital Evolution and Migration of Giant Planets: Modeling Extrasolar Planets. *ApJ*, **500**, 428–439. 6

Tuomi, M. & Jones, H.R.A. (2012). Probabilities of exoplanet signals from posterior samplings. *A&A*, **544**, A116. 48

Tuomi, M., Jones, H.R.A., Barnes, J.R., Anglada-Escudé, G. & Jenkins, J.S. (2014). Bayesian search for low-mass planets around nearby M dwarfs - estimates for occurrence rate based on global detectability statistics. *MNRAS*, **441**, 1545–1569. 5, 48

Turbet, M., Leconte, J., Selsis, F., Bolmont, E., Forget, F., Ribas, I., Raymond, S.N. & Anglada-Escudé, G. (2016). The habitability of Proxima Centauri b II. Possible climates and Observability. *ArXiv e-prints*. 19, 20, 137

Udalski, A., Paczynski, B., Zebrun, K., Szymanski, M., Kubiak, M., Soszynski, I., Szewczyk, O., Wyrzykowski, L. & Pietrzynski, G. (2002). The Optical Gravitational Lensing Experiment. Search for Planetary and Low-Luminosity Object Transits in the Galactic Disk. Results of 2001 Campaign. *Acta Astron.*, **52**, 1–37. 183

Udry, S. & Santos, N.C. (2007). Statistical Properties of Exoplanets. *ARA&A*, **45**, 397–439. 18

Uytterhoeven, K., Mathias, P., Poretti, E., Rainer, M., Martín-Ruiz, S., Rodríguez, E., Amado, P.J., Le Contel, D., Jankov, S., Niemczura, E., Pollard, K.R., Brunsden, E., Paparó, M., Costa, V., Valtier, J.C., Garrido, R., Suárez, J.C., Kilmartin, P.M., Chapellier, E., Rodríguez-López, C., Marin, A.J.,

Aceituno, F.J., Casanova, V., Rolland, A. & Olivares, I. (2008). The γ Doradus CoRoT target HD 49434. I. Results from the ground-based campaign. *A&A*, **489**, 1213–1224. 84

van de Kamp, P. (1963). Astrometric study of Barnard's star from plates taken with the 24-inch Sproul refractor. *AJ*, **68**, 515–521. 2, 3

van de Kamp, P. (1969). Alternate dynamical analysis of Barnard's star. *AJ*, **74**, 757–759. 2

van de Kamp, P. (1975). Astrometric study of Barnard's star from plates taken with the Sproul 61-cm refractor. *AJ*, **80**, 658. 3

van de Kamp, P. (1986). Dark companions of stars - Astrometric commentary on the lower end of the Main Sequence. *Space Sci. Rev.*, **43**, 211–327. 3

van Leeuwen, F. (2007). Validation of the new Hipparcos reduction. *A&A*, **474**, 653–664. 54, 131

Vidotto, A.A., Jardine, M., Morin, J., Donati, J.F., Lang, P. & Russell, A.J.B. (2013). Effects of M dwarf magnetic fields on potentially habitable planets. *A&A*, **557**, A67. 133

Vogt, S.S., Allen, S.L., Bigelow, B.C., Bresee, L., Brown, B., Cantrall, T., Conrad, A., Couture, M., Delaney, C., Epps, H.W., Hilyard, D., Hilyard, D.F., Horn, E., Jern, N., Kanto, D., Keane, M.J., Kibrick, R.I., Lewis, J.W., Osborne, J., Pardeilhan, G.H., Pfister, T., Ricketts, T., Robinson, L.B., Stover, R.J., Tucker, D., Ward, J. & Wei, M.Z. (1994). HIRES: the high-resolution echelle spectrometer on the Keck 10-m Telescope. In D.L. Crawford & E.R. Craine, eds., *Instrumentation in Astronomy VIII*, vol. 2198 of *Proc. SPIE*, 362. 41

Vogt, S.S., Radovan, M., Kibrick, R., Butler, R.P., Alcott, B., Allen, S., Arriagada, P., Bolte, M., Burt, J., Cabak, J., Chloros, K., Cowley, D., Deich, W., Dupraw, B., Earthman, W., Epps, H., Faber, S., Fischer, D., Gates, E., Hilyard, D., Holden, B., Johnston, K., Keiser, S., Kanto, D., Katsuki, M., Laiterman, L., Lanclos, K., Laughlin, G., Lewis, J., Lockwood, C., Lynam, P., Marcy, G., McLean, M., Miller, J., Misch, T., Peck, M., Pfister, T., Phillips, A., Rivera, E., Sandford, D., Saylor, M., Stover, R., Thompson, M., Walp, B., Ward, J., Wareham, J., Wei, M. & Wright,

REFERENCES

C. (2014). Apf - the lick observatory automated planet finder. *PASP*, **126**, 359–379. 42

Wagner, K., Apai, D., Kasper, M., Kratter, K., McClure, M., Robberto, M. & Beuzit, J.L. (2016). Direct imaging discovery of a Jovian exoplanet within a triple-star system. *Science*, **353**, 673–678. 15

West, A.A., Hawley, S.L., Bochanski, J.J., Covey, K.R., Reid, I.N., Dhital, S., Hilton, E.J. & Masuda, M. (2008). Constraining the Age-Activity Relation for Cool Stars: The Sloan Digital Sky Survey Data Release 5 Low-Mass Star Spectroscopic Sample. *AJ*, **135**, 785–795. 22

West, A.A., Weisenburger, K.L., Irwin, J., Berta-Thompson, Z.K., Charbonneau, D., Dittmann, J. & Pineda, J.S. (2015). An Activity–Rotation Relationship and Kinematic Analysis of Nearby Mid-to-Late-Type M Dwarfs. *ApJ*, **812**, 3. 19

Winn, J.N. (2010). Transits and Occultations. *ArXiv e-prints*. 180

Wolszczan, A. & Frail, D.A. (1992). A planetary system around the millisecond pulsar PSR1257 + 12. *Nature*, **355**, 145–147. 4, 14, 183, 184

Wyttenbach, A., Ehrenreich, D., Lovis, C., Udry, S. & Pepe, F. (2015). Spectrally resolved detection of sodium in the atmosphere of HD 189733b with the HARPS spectrograph. *A&A*, **577**, A62. 9, 10

Yang, J., Cowan, N.B. & Abbot, D.S. (2013). Stabilizing Cloud Feedback Dramatically Expands the Habitable Zone of Tidally Locked Planets. *ApJ*, **771**, L45. 15

Yang, J., Liu, Y., Hu, Y. & Abbot, D.S. (2014). Water Trapping on Tidally Locked Terrestrial Planets Requires Special Conditions. *ApJ*, **796**, L22. 20

Zechmeister, M. & Kürster, M. (2009). The generalised Lomb-Scargle periodogram. A new formalism for the floating-mean and Keplerian periodograms. *A&A*, **496**, 577–584. 57

Zechmeister, M., Kürster, M. & Endl, M. (2009). The M dwarf planet search programme at the ESO VLT + UVES. A search for terrestrial planets in the habitable zone of M dwarfs. *A&A*, **505**, 859–871. 85

Zerbi, F.M., Garrido, R., Rodriguez, E., Krisciunas, K., Crowe, R.A., Roberts, M., Guinan, E.F., McCook, G.P., Sperauskas, J., Griffin, R.F. & Luedeke, K.D. (1997). The gamma Doradus-type variable 9 Aurigae: results from a multi-site campaign. *MNRAS*, **290**, 401–410. 84

Zerbi, F.M., Rodríguez, E., Garrido, R., Martín, S., Arellano Ferro, A., Sareyan, J.P., Krisciunas, K., Akan, M.C., Evren, S., Ibanoğlu, C., Keskin, V., Pekunlu, R., Tunca, Z., Luedeke, K., Paparo, M., Nuspl, J. & Guerrero, G. (1999). The gamma DOR variable HR 8799: results from a multisite campaign. *MNRAS*, **303**, 275–283. 84

Zerbi, F.M., Bouchy, F., Fynbo, J., Maiolino, R., Piskunov, N., Rebolo Lopez, R., Santos, N., Strassmeier, K., Udry, S., Vanzi, L., Riva, M., Basden, A., Boisse, I., Bonfils, X., Buscher, D., Cabral, A., Dimarcantonio, P., Di Varano, I., Henry, D., Monteiro, M., Morris, T., Murray, G., Oliva, E., Parry, I., Pepe, F., Quirrenbach, A., Rasilla, J.L., Rees, P., Stempels, E., Valenziano, L., Wells, M., Wildi, F., Origlia, L., Allende Prieto, C., Chiavassa, A., Cristiani, S., Figueira, P., Gustafsson, B., Hatzes, A., Haehnelt, M., Heng, K., Israelian, G., Kochukhov, O., Lovis, C., Marconi, A., Martins, C.J.A.P., Noterdaeme, P., Petitjean, P., Puzia, T., Queloz, D., Reiners, A. & Zoccali, M. (2014). HIRES: the high resolution spectrograph for the E-ELT. In *Society of Photo-Optical Instrumentation Engineers (SPIE) Conference Series*, vol. 9147 of *Society of Photo-Optical Instrumentation Engineers (SPIE) Conference Series*, 23. 106

Zhao, F., Curto, G.L., Pasquini, L. & Zhao, G. (2014). Study of the HARPS Line Profile Using a Laser Frequency Comb. In N. Haghighipour, ed., *Formation, Detection, and Characterization of Extrasolar Habitable Planets*, vol. 293 of *IAU Symposium*, 407–409. 88

Zima, W., Wright, D., Bentley, J., Cottrell, P.L., Heiter, U., Mathias, P., Poretti, E., Lehmann, H., Montemayor, T.J. & Breger, M. (2006). A new method for the spectroscopic identification of stellar non-radial pulsation modes. II.

REFERENCES

Mode identification of the δ Scuti star FG Virginis. *A&A*, **455**, 235–246. 84

Zuluaga, J.I. & Bustamante, S. (2016). Geomagnetic properties of Proxima Centauri b analogues. *ArXiv e-prints*. 22